

The Search for Beyond the Standard Model Physics using Tau Leptons at the ATLAS Detector

Mitchell Norfolk

A thesis submitted for the degree of
Doctor of Philosophy
June 2023

The University of Sheffield
Department of Physics and Astronomy
Supervisor: Dr. Trevor Vickey



Abstract

The limitations of the Standard Model (SM) of particle physics have perplexed physicists for many years, prompting the exploration of various theoretical SM extensions. This thesis utilises data from the ATLAS experiment, obtained through proton-proton collisions with an integrated luminosity of 139 fb^{-1} at a centre-of-mass energy of 13 TeV, to search for particles predicted by these theories. Searches for Z' bosons and leptoquarks (LQ) are conducted by employing analysis techniques developed during the 2020 ATLAS search for heavy neutral Higgs boson ($H/A/h$) decays to two tau leptons, as predicted by the Minimal Supersymmetric Standard Model (MSSM). In addition, this thesis presents preliminary work on enhancing the 2020 MSSM $H/A/h \rightarrow \tau^+\tau^-$ analysis using machine learning techniques and other optimisations. Finally, the progress made by the University of Sheffield towards the mass production of strip barrel modules for the forthcoming ATLAS Inner Tracker upgrade is discussed.

No significant deviations from the predictions of the SM are observed in any of the searches. Consequently, upper limits at 95% confidence level are established for various parameters, and the observed limits are utilised to exclude mass ranges for specific models. The Sequential Standard Model (SSM) is used to define the Z' particle in this thesis, and the search results contribute to the ATLAS combination effort investigating the Heavy Vector Triplet (HVT) model. For the SSM, Z' masses below 3.06 TeV are excluded. Additional constraints are provided on the HVT model, for the fermion-Higgs $\{g_f, g_H\}$ and generation-inclusive (third-generation) quark-lepton $\{g_q, g_\ell\}$ ($\{g_{q_3}, g_{\ell_3}\}$) coupling parameter planes, assuming fermion universality and the Model A benchmark scenario ($g_H = -0.56$), respectively. In the LQ analysis, masses below 1.28 TeV (1.35 TeV) are excluded for the \tilde{S}_1 (U_1) models. By employing the machine learning and optimisation techniques to enhance the 2020 results, up to 4.2 (2.6) times improvement in the cross-section \times branching ratio upper limit as a function of signal mass is demonstrated for the b -associated (gluon-gluon fusion) production modes. Improvements of up to 3.1 (2.9) in the $\tan \beta$ upper limit as a function of m_A are shown for the hMSSM (M_h^{125}) benchmark scenarios. The improvements for the MSSM occur exclusively at lower mass points.

Acknowledgements

Firstly, I would like to express my deepest gratitude to my colleagues at the University of Sheffield for providing a remarkable working environment filled with stimulating discussions and invaluable guidance. I am especially indebted to my supervisor, Trevor Vickey, who allowed me to take on this amazing challenge, your unwavering support and constant guidance have been instrumental.

I would also like to extend my heartfelt appreciation to my colleagues, Theodore Zorbas and Nathan Readioff, whose assistance and guidance have played a significant role in my progress thus far. Additionally, I am immensely grateful to Hanfei Ye, Xiaozhong Huang, Adam Bailey, Yimin Che, Pawel Brückman de Renstrom, and Marcin Wolter, for their collaboration in the various analyses I have contributed to. I will always appreciate your generosity in sparing time for my questions.

Many thanks to my daft set of mates, including Lee, Jay, Dunstan, and the rest of the blades, thanks for never caring about anything I have to say, especially when it comes to particle physics. It is a blessing rather than a curse.

To my late parents Steven and Sharon, thank you for teaching me the value of respect, hard work and perseverance. I know for a fact that without these three ingredients I would have never have got close to completing this body of work. To my Nan Veronica, who has been a constant source of support since my childhood. I wish I possessed the necessary vocabulary to thank you enough.

Lastly, to my beloved partner Chloe and my lovely dog Winnie who have had the pleasure of living with an extremely stressed man over the last three or so years. The endless patience, love and support you have shown me has been incredible and inspiring.

Contents

1	Introduction and Contribution Statement	1
2	The Related Theoretical Concepts	3
2.1	The Standard Model of Particle Physics	3
2.1.1	The Standard Model as a Quantum Field Theory	6
2.2	Limitations of the Standard Model	11
2.3	Proposed Extensions to the Standard Model	14
2.3.1	Supersymmetry and the Minimal Supersymmetric Standard Model	14
2.3.2	Z' Bosons	17
2.3.3	Leptoquarks	20
3	The ATLAS Detector and the Extraction of Physics Data	22
3.1	The Large Hadron Collider	22
3.1.1	The Particle Beam	24
3.1.2	LHC Operation and Delivered Luminosity	24
3.2	The ATLAS Detector	26
3.2.1	The ATLAS Coordinate System	26
3.2.2	The Inner Detector	28
3.2.3	The Calorimeter	30
3.2.4	The Muon Spectrometer	31
3.2.5	The Trigger and Data Acquisition System	32
3.3	Particle Identification and Reconstruction at ATLAS	34
3.3.1	Electrons and Muons	35
3.3.2	Jets	41
3.3.3	Hadronically Decaying Taos	43
3.3.4	Missing Transverse Energy	46
3.4	ATLAS Simulation	46
3.5	Analysis Workflow at ATLAS	47
4	Searching for Neutral MSSM Higgs Bosons in the $\tau\tau$ Final State - Analysis Techniques	50
4.1	Analysis Strategy	50
4.2	Data Samples and Monte Carlo Simulation	52
4.3	Event Selection	53
4.3.1	Removal of Geometrically Overlapping Objects	53

4.3.2	Triggering and Defining the $\tau_{\text{lep}}\tau_{\text{had}}$ Signal Region	54
4.4	Reconstructing the Di-tau Mass	56
4.5	Background Estimation in the $\tau_{\text{lep}}\tau_{\text{had}}$ Channel	56
4.5.1	Estimation of the Fake Background	57
4.5.2	Constraining the t -quark Background	74
4.5.3	Fake Background Validation	77
4.6	Systematic Uncertainties	82
4.7	Statistical Analysis	85
4.7.1	Profile Likelihood Fit	85
4.7.2	Hypothesis Testing and Exclusion Limits	88
5	Search for Heavy Z' Bosons in the $\tau\tau$ Final State	92
5.1	Analysis Strategy	92
5.2	Monte Carlo Signal Samples	93
5.2.1	The Reweighting of Drell-Yan $Z/\gamma^* \rightarrow \tau\tau + \text{jets}$ Sliced Samples to Z' Signals	93
5.2.2	The Z' Sample Validation	95
5.3	Systematic Uncertainties	98
5.4	Results	98
5.4.1	Post-fit Results	98
5.4.2	Exclusion Limits	100
5.5	The ATLAS Heavy Resonance Combination	101
5.5.1	The Combination Setup	102
5.5.2	Preliminary Results for the Combination	104
5.6	Conclusion	113
6	Search for Third-Generation Leptoquarks in the $b\tau\tau$ Final State	114
6.1	Building an Analysis Strategy	114
6.2	Monte Carlo Signal Samples	117
6.3	Event Selection	118
6.4	Background Estimation in the $\tau_{\text{lep}}\tau_{\text{had}}$ Channel	121
6.4.1	Constraining the t -quark Background	121
6.5	Estimation of the Fake Background	126
6.5.1	Fake Background Validation	137
6.6	Systematic Uncertainties	140
6.7	Results	141
6.7.1	Exclusion Limits	143
6.7.2	Model-independent Interpretation in the Low and High $p_T^{b\text{-jet}}$ Regions	148
6.8	Conclusion	151
7	Efforts to Improve the Full Run-II Search for MSSM Higgs Bosons in the $\tau\tau$ Final State	152
7.1	Proposed Improvements to the Legacy Analysis	152
7.2	Efforts Towards $\tau_{\text{lep}}\tau_{\text{had}}$ Analysis Optimisation	153
7.2.1	Updating and Simplifying Analysis Inputs (n-tuples)	153

7.2.2	Updating Combined Performance Recommendations	154
7.2.3	Analysis Simplification	154
7.2.4	The t -quark Background Correction	155
7.2.5	Overlap Removal Optimisation	155
7.2.6	Multi-jet Fake Region Purity	157
7.2.7	Reconsidering the Lower τ Identification Cut	158
7.2.8	The Updated Analysis Strategy	161
7.3	Machine Learning Techniques for the Improved Run-II $H/A/h \rightarrow \tau\tau$ Analysis	161
7.3.1	Estimating Class Probability	162
7.3.2	Neural Networks	163
7.3.3	Implementation and Evaluation of a Neural Network	165
7.3.4	Creating a Parameterised Neural Network	167
7.4	Neural Network Application in the Improved Run-II $H/A/h \rightarrow \tau\tau$ Analysis .	168
7.4.1	Input Features	168
7.4.2	Model Architecture and Hyperparameters	173
7.4.3	Model Training	174
7.4.4	Statistical Fit and Binning Studies	180
7.4.5	Resulting Exclusion Limits	181
7.4.6	Conclusions	186
8	The ATLAS Inner Tracker as part of the High Luminosity - LHC Upgrade	187
8.1	The High Luminosity - LHC and the ATLAS Phase-II Upgrade	187
8.2	The ATLAS Inner Tracker Upgrade	188
8.2.1	The Pixel Detector	189
8.2.2	The Strip Detector	190
8.3	Construction of Strip Barrel Modules	192
8.3.1	Module Assembly Procedure	193
8.4	Quality Assurance of Strip Barrel Modules	196
8.4.1	Visual Inspection	197
8.4.2	Pull Testing	197
8.4.3	Metrology	198
8.4.4	Electrical Testing	202
8.4.5	Thermal Cycling	212
8.5	The ITk Production Database	213
9	Summary	214
A	Important Acronyms	236
B	The MSSM $H/A/h \rightarrow \tau\tau$ Full Run-II (Legacy) Analysis	237
B.1	Validation Region Scale Factors	237
B.2	Statistical Fit and Systematic Uncertainty Diagnostic Plots	240

C	Extra Information on Monte Carlo Samples and Triggers	242
C.1	Triggers Used	242
C.2	Monte Carlo Samples	243

Chapter 1

Introduction and Contribution Statement

The Standard Model (SM) of particle physics stands as an exceptionally successful framework for understanding the interactions and characteristics of elementary particles, which form the building blocks of matter in our observable universe. With remarkable precision, the SM has made predictions about the properties of these particles, and in the majority of cases, these predictions have been confirmed through experimental observations. However, theoretical tensions such as the hierarchy problem and experimental tensions such as the B -meson anomalies [1–5] and the $g - 2$ excess [6, 7] have challenged the particle physics community for decades. This thesis focuses on exploring potential explanations for these discrepancies by analysing proton-proton (pp) collision data from the ATLAS experiment with an integrated luminosity (L_{int}) of 139 fb^{-1} and centre-of-mass energy (\sqrt{s}) of 13 TeV. The proton beam is provided by the Large Hadron Collider (LHC) housed at the European Organisation for Nuclear Research (CERN). Furthermore, future plans for research in this area are discussed with an emphasis on the importance of developing advanced instrumentation such as the ATLAS Inner Tracker to facilitate these investigations.

This thesis commences in Chapter 2 by establishing the theoretical groundwork necessary to understand the conclusions drawn. Chapter 3 provides a breakdown of the effective tracking, identification, and triggering techniques employed by the ATLAS detector in order to store and organise the relevant pp collision data. The original work in this thesis relies on the methodologies employed in the 2020 ATLAS search for heavy Higgs bosons within the framework of the Minimal Supersymmetric Standard Model (MSSM), decaying into two tau leptons ($H/A/h \rightarrow \tau^+\tau^-$) [8]. Since the 2020 analysis was the first of its kind to employ the full Run-II ATLAS dataset, it is referred to as the legacy full Run-II analysis, or simply, the legacy analysis. The results from each relevant stage of the legacy analysis is reproduced in Chapter 4. Subsequently, the remainder of the thesis delves into original research, with each chapter corresponding to a distinct ATLAS analysis. Chapter 5 discusses the search for heavy Z boson (Z') decays into two tau leptons. Chapter 6 focuses on the search for scalar or vector leptoquarks (LQ) decaying into a b -quark and two tau leptons. Additionally, Chapter 7 presents exploratory work towards an enhanced version of the legacy analysis, throughout

this chapter this exploratory work will be referred to as the improved analysis. Finally, Chapter 8 describes the author’s involvement in the development of the next-generation ATLAS Inner Detector, known as the Inner Tracker (ITk), and the University of Sheffield’s role as a module-building site. This chapter details the author’s contributions to the construction, testing and organisation of these modules.

The original research conducted by the author was often conducted as part of an analysis team or group. Table 1.1 provides an overview of the author’s contributions to each of the results, further elaboration on the specific responsibilities stated in the table is present in the subsequent chapters. A typical analysis workload can be divided into several components, including n-tuple (sample) production, signal and control region selection, consideration of uncertainties, and statistical analysis. Therefore, the table makes reference to these stages. The analyses discussed in these chapters are categorised into two groups based on whether the tau decays hadronically or leptonically: $\tau_{\text{lep}}\tau_{\text{had}}$ and $\tau_{\text{had}}\tau_{\text{had}}$. While the author primarily focused on the $\tau_{\text{lep}}\tau_{\text{had}}$ decay mode, there was some involvement in the $\tau_{\text{had}}\tau_{\text{had}}$ channel depending on the analysis.

Table 1.1: The authors role and involvement for each analysis mentioned in this thesis and the ITk project. The current status of each project is also outlined.

Project and current status	Chapter	Role	Responsibilities
$Z' \rightarrow \tau\tau$ analysis Part of upcoming Heavy Resonance Combination publication Awaiting publication	4	Sole analyser and analysis contact (September 2022 - June 2023)	Conducted all stages of the analysis discussed in the chapter
$LQ \rightarrow b\tau\tau$ analysis Pre-published in arXiv:2305.15962 [hep-ex] Submitted to JHEP	5	$\tau_{\text{lep}}\tau_{\text{had}}$ analyser (April 2021 - June 2023)	Produced n-tuples Ran the $\tau_{\text{lep}}\tau_{\text{had}}$ side of the analysis up until the statistical analysis stage Derived the signal theory systematic uncertainties
MSSM $H/A/h \rightarrow \tau\tau$ improved analysis Findings considered for Run-III iteration of the analysis	6	$\tau_{\text{lep}}\tau_{\text{had}}$ analyser (March 2020 - September 2022) Sole analyser and analysis contact (September 2022 - November 2022)	Conducted all stages of the analysis discussed in the chapter. With the exception of $\tau_{\text{had}}\tau_{\text{had}}$ n-tuple production and the $\tau_{\text{had}}\tau_{\text{had}}$ analysis optimisation (new trigger and overlap removal)
ATLAS ITk upgrade project Concluding prototype phase	7	Group member (October 2019 - June 2023)	Contributed to prototype module builds and electrical testing Contributed to ITk database API interaction scripts for reporting and test upload

Chapter 2

The Related Theoretical Concepts

This chapter provides an overview of the SM and its theoretical basis. The necessity for Beyond-the-Standard-Model (BSM) theories is explained, these theories motivate the postulation of the MSSM Higgs bosons, Z' bosons and LQ s searched for in this thesis.

2.1 The Standard Model of Particle Physics

The Standard Model of particle physics is a powerful theoretical framework that describes the fundamental particles and their interactions. The SM has achieved remarkable accuracy and precision in predicting a wide range of observed phenomena. One of its notable successes is the prediction of the Higgs boson [9], which was subsequently discovered in 2012 by the ATLAS [10] and CMS [11] experiments. The Higgs boson's existence confirms the validity of the SM and deepens our understanding of the universe.

The SM successfully describes the electromagnetic, strong, and weak fundamental forces but falls short in explaining the gravitational force. In particle physics, the concept of spin plays a crucial role. It represents the intrinsic quantum mechanical angular momentum of a particle and determines its behaviour under spatial rotations. The absolute value of the spin is utilised to classify fundamental particles within the SM. Fermions, which include quarks and leptons, possess half-integer spin and form the matter typically encountered in everyday life. Bosons, on the other hand, possess integer spin and act as force mediators between fermions. This differentiation leads to distinct behaviours governed by Bose-Einstein statistics for bosons and Fermi-Dirac statistics for fermions. The Fermi-Dirac statistics give rise to the Pauli exclusion principle, a fundamental property of the universe. In Figure 2.1, the arrangement of fermions and bosons is illustrated, showcasing their respective mass, charge, and spin. Notably, the mass is expressed in units of MeV/c^2 , while in particle physics, the convention of setting the speed of light (c) and the reduced Planck constant (\hbar) to 1 is often employed for clarity, rendering all energies, momentum, and mass values in units of energy.

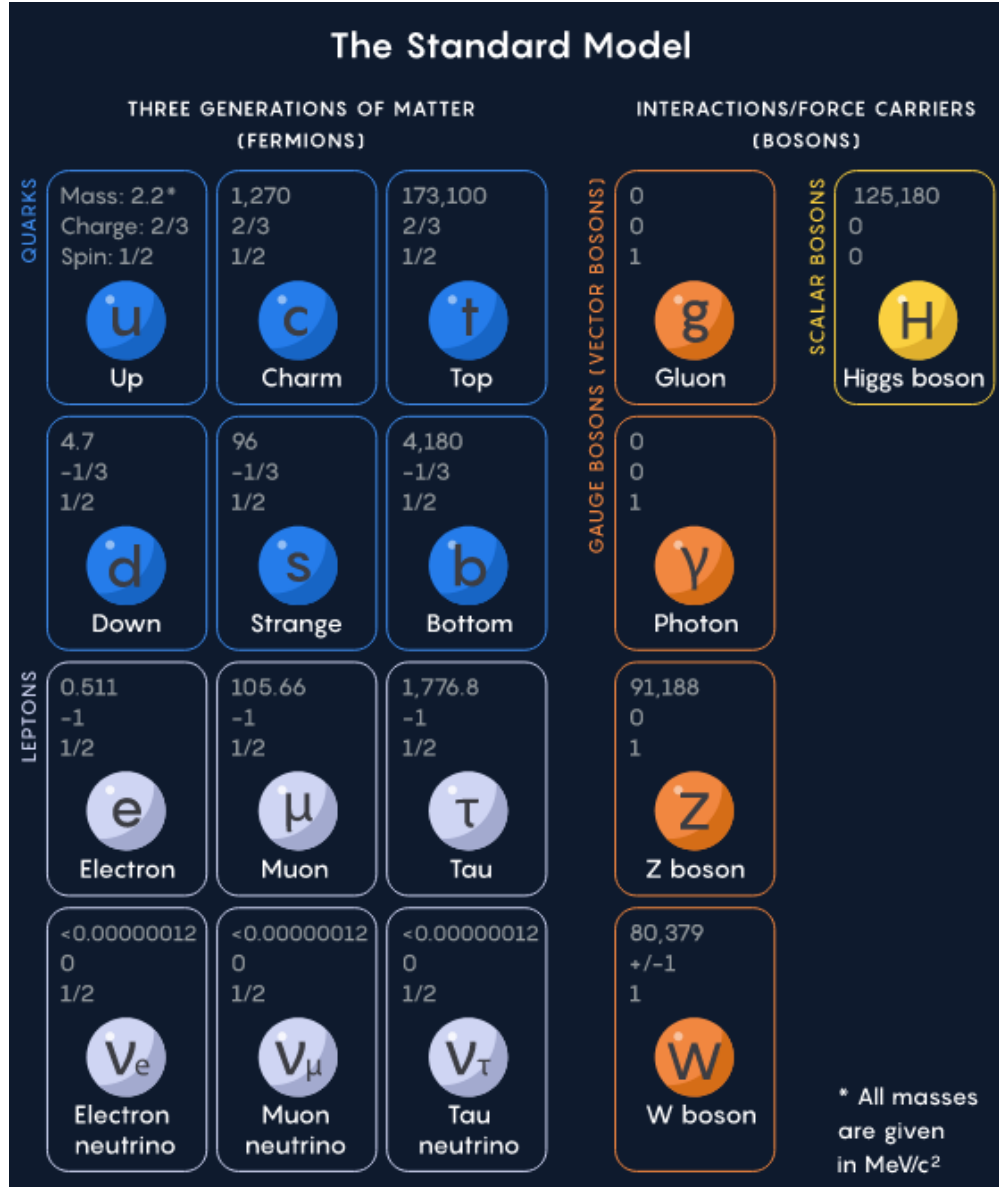


Figure 2.1: An illustration showing the arrangement of particles within the Standard Model, provided by [12]. The illustration shows the categorisation of the particles into quarks, leptons, gauge bosons and scalar bosons with respect to their mass (in MeV/c²), charge and spin.

Within the SM, the force-carrying (gauge) bosons, depicted in the orange boxes of Figure 2.1, correspond to the different force types. The strong force utilises the gluon, a massless particle, as its mediator. The strong force only acts on quarks as they possess colour charge, where each quark will have one of three available colour charges: red, green or blue. Gluons carry both a colour and an anticolour, enabling them to change the colour of quarks during interactions. In contrast, the electromagnetic force employs the massless photon as its mediator. Photons transmit forces between any particles possessing electric charge. However, the electromagnetic interaction is roughly a thousand times weaker than the strong force. The weak force exhibits some distinctions from the other forces. It involves both the weak charged current interaction mediated by the W^\pm bosons and the weak neutral current interaction mediated by the neutral Z boson. Unlike the other gauge bosons, those associated with the weak interaction act on all quarks and leptons, as they possess ‘weak isospin’. These bosons have comparatively large masses, resulting in a weak force that is approximately one hundred million times weaker than the strong force. Notably, the weak force displays a chiral nature, treating fermions differently based on whether they are left-handed or right-handed. Handedness is defined based on the orientation of the particle spin relative to its momentum. The Higgs boson, depicted in the yellow box, is unique within this context. Unlike the other particles, it does not transmit a force. It is the only observed fundamental scalar boson. The Higgs boson is associated with the Higgs field, which imparts mass to both vector bosons and fermions, as further described in the next section.

The fermions are represented by the blue and grey boxes on the left side of Figure 2.1. Each fermion has a corresponding antiparticle, which shares identical properties but has opposite sign charge. The fermions can be categorised into two groups: leptons and quarks. Both leptons and quarks come in three generations with two flavours in each generation, the generations are distinguished primarily by their mass. The tau lepton and b -quark which play a vital role in this thesis belong to the third-generation of the grey and blue boxes, respectively. The charged weak current interaction is responsible for flavour changing processes in both leptons and quarks. The Cabibbo-Kobayashi-Maskawa matrix governs the flavour changes among quark generations, allowing for transitions between different generations [13]. Within the lepton category, each lepton is accompanied by a (nearly) massless neutrino of the same flavour which interacts solely via the weak force. The implications of the chiral structure of the weak force means that only left-handed neutrinos (and right-handed antineutrinos) are predicted to exist. In the quark sector, each quark generation consists of a positively and negatively charged instance, carrying charges of $+\frac{2}{3}Q_p$ and $-\frac{1}{3}Q_p$ where Q_p is the charge of the proton. One intriguing characteristic of quarks is the concept of colour confinement associated with the strong force. At larger distances, quark interactions become stronger, making it energetically favourable to create quark-antiquark pairs. Consequently, free quarks are not observed in isolation. Instead, quarks combine and confine together to form bound states called hadrons. As a result, observable final states have no colour charge.

The SM incorporates several fundamental symmetries, namely parity (P), charge conjugation (C), and time reversal (T). Parity symmetry refers to the invariance of physical laws under the inversion of spatial coordinates. Charge conjugation symmetry relates to the invariance under the conversion of a particle to its corresponding antiparticle. Time reversal

symmetry reflects the invariance when the direction of time is reversed. However, these individual symmetries are not universally conserved in all interactions. For instance, parity is not conserved in the weak charged current interaction [14]. In addition, CP symmetry (combination of C and P) is found to be violated in weak interactions, particularly in certain processes involving quarks [15]. This observation could explain the abundance of matter compared to antimatter in the universe. Nonetheless, when all three symmetries, C , P , and T , are combined into the CPT symmetry, it is believed to be an exact symmetry of the universe that is always conserved. Any violation of CPT symmetry would have profound implications on the understanding of fundamental physics.

In practice, particle physics interactions are described by Feynman diagrams, an example of one is shown later in Figure 4.1 in which only the time axis is specified. In these diagrams, the arrows from the incoming particles and antiparticles flow through the vertex. The Feynman-Stückleberg interpretation of the negative energy solutions to the Dirac equation is used to describe antiparticles. The interpretation states that within the context of Feynman diagrams antiparticles can be thought of as positive energy states travelling backwards in time [13]. The diagrams can be used to determine scattering probabilities (cross-sections) and decay rates. Virtual particles can be generated during the interaction which can create loops corresponding to higher order diagrams. Virtual particles exist within the Heisenberg uncertainty principle and are not well defined, they can violate energy-momentum relations and have an arbitrary amount of energy. These virtual particle loops act as radiative corrections to the derived SM predictions and must be accounted for [13]. Feynman diagrams without these extra loops are referred to as tree-level or leading order (LO) diagrams.

2.1.1 The Standard Model as a Quantum Field Theory

Each of the three forces considered by the SM are described by a Quantum Field Theory (QFT), where each fermion and the Higgs boson have an associated field which permeates all of space-time. The QFTs incorporate both special relativity and quantum mechanics resulting in the quantisation of the associated fields, their excitation generates the particles observed in experiments. The strong interaction is described by Quantum Chromodynamics (QCD) [16, 17], while the electromagnetic and weak interactions are described by the Glashow-Salam-Weinberg (GSW) theory which combines the theories of Quantum Electrodynamics (QED) and Quantum Flavordynamics [18–20]. The SM as a whole is based on $SU(3)_c \times SU(2)_L \times U(1)_Y$ local gauge symmetry [21, 22], where c , L and Y represent the concepts of colour, left-handed fermions and the weak hypercharge, respectively. The role of these concepts will be described in this section. Each of the respective bosons, interactions and forces are brought about due to the requirements set by the local gauge symmetry which is best understood in the context of electromagnetism as a change in the scalar and vector potentials which has no effect on the fields.

The theory of QED provides a theoretical framework for understanding the existence and interactions of photons through local gauge invariance. The development of QED can be attributed to the groundbreaking work of Tomonaga [23], Feynman [24–26], and Schwinger [27], who were awarded the Nobel Prize in Physics in 1965. To understand the concepts of

QED an overview of the mathematical framework must be put forward starting with the Lagrangian density (known simply as the Lagrangian). This is the quantum mechanical and relativistic analogue of the classical Lagrangian used to describe the equations of motion of a given system. The Lagrangian consists of a kinetic term involving the derivatives of the fields and a potential term representing the interactions between the fields.

For a spin-half field denoted as ψ , the Lagrangian is defined as:

$$\mathcal{L}_F = i\bar{\psi}(\gamma^\mu \partial_\mu - m)\psi \quad (2.1)$$

where ψ represents a Dirac spinor, a four-component wavefunction that naturally describes the quantum spin states of fermions and satisfies the Dirac equation [13, 28]. For a non-interacting scalar field denoted as ϕ , the respective Lagrangian can be expressed as:

$$\mathcal{L}_S = \frac{1}{2}(\partial_\mu \phi)(\partial^\mu \phi) - \frac{1}{2}m^2 \phi^2 \quad (2.2)$$

where the symbols ∂_μ and ∂^μ represent the covariant and contravariant four-derivatives, respectively. In both the above equations, the Dirac γ -matrices are represented by γ^μ , and m represents the mass of the corresponding particle. The majority of the symbols are matrices and their order of operation is significant, as they act on the objects to their right in the equations.

The interaction between the photon and fermions can be extracted by requiring that the fermionic Lagrangian shown in Equation 2.1 is invariant under the following local phase transformation:

$$\psi \rightarrow \psi'(x) = e^{iq\chi(x)}\psi \quad (2.3)$$

where $q\chi(x)$ is a phase which can be different at all points in space-time. Upon substituting this transformation into Equation 2.1 and performing the necessary mathematical operations, a new field (A_μ) emerges. This new field must undergo the transformation:

$$A_\mu \rightarrow A'_\mu = A_\mu - \partial_\mu \chi \quad (2.4)$$

in order to guarantee the necessary gauge invariance. The gauge invariance would also be broken should the photon be massive, ensuring a massless photon within the theory of QED. In addition, Noether's theorem states that a symmetry of the Lagrangian is related to a conserved current, in this case it is $j^\mu = (\rho, \mathbf{J})$, the current four-vector which characterises the charge and current densities [13].

The complete Lagrangian for QED then becomes:

$$\mathcal{L}_{\text{QED}} = \bar{\psi}(i\gamma^\mu \partial_\mu - m_e)\psi + e\bar{\psi}\gamma^\mu\psi A_\mu - \frac{1}{4}F_{\mu\nu}F^{\mu\nu} \quad (2.5)$$

where e represents the electron charge, $F_{\mu\nu} = \partial_\mu A_\nu - \partial_\nu A_\mu$ is the kinetic term for a massless spin-1 field, and $\partial_\mu F^{\mu\nu} = j^\nu$ is the covariant form of Maxwell's equations for an electromagnetic field. The second term in Equation 2.5 describes the interactions between fermions

and the photon field and is most often collapsed into what is known as the covariant derivative term $\partial_\mu \rightarrow D_\mu = \partial_\mu + iqA_\mu$. The QED Lagrangian is said to be invariant under U(1) local gauge symmetry, where U(1) denotes the group of matrices that could replace $e^{iq\chi(x)}$ in Equation 2.3. In the context of QED, U(1) is simply the identity matrix. These groups are referred to as Lie groups, and their properties play a fundamental role in the SM. A Lie group can be classified as Abelian or non-Abelian based on whether the group matrices commute with each other (i.e., $AB = BA$). In the case of U(1) symmetry, there is only one generator that encapsulates the symmetry of the theory. Each generator in a Lie group corresponds to a gauge boson, and in the case of QED, the generator is associated with the photon.

The QED Lagrangian describes electromagnetic interactions with a coupling constant e and each QED vertex contributes a factor $\alpha = e^2/4\pi = 1/137$ for an infinite set of QED vertices. Experimentally however, the coupling constant varies with energy due to radiative corrections. In addition, the virtual particles carry an arbitrary amount of energy and therefore any calculation over the diagrams becomes divergent, this is accounted for using a process known as renormalisation [13].

For QCD, the Lagrangian is invariant under a non-Abelian $SU(3)_c$ Lie group local phase transformation, which are a group of 3×3 Gell-Mann matrices [29]. The $SU(3)$ symmetry leads to the existence of three massless Dirac fields, corresponding to the three colour charges. In the case of $SU(N)$ Lie groups, the number of generators is given by $N^2 - 1$. Hence, in QCD, there are eight types of gluons. The Lagrangian for QCD is represented by:

$$\mathcal{L}_{\text{QCD}} = \bar{\psi}(i\gamma^\mu D_\mu - m)\psi - \frac{1}{4} \sum_a F_{\mu\nu}^a F^{a,\mu\nu} \quad (2.6)$$

and shares similarities with that of QED, but also has distinct differences. The symbols in this equation have the same meaning as those in Equation 2.5, except for the field strength tensor and the covariant derivative. The covariant derivative is defined as $D_\mu = \partial_\mu + ig_s \sum_a G_\mu^a T^a$ using the group's generators (T^a) and g_s which is related to the strong coupling α_s by $g_s = \sqrt{4\pi\alpha_s}$. The symbol G_μ^a is the representation of the eight QCD fields which also transform under gauge invariance such that $F_{\mu\nu}^a = \partial_\mu G_\nu^a - \partial_\nu G_\mu^a - g_s f^{abc} G_\mu^b G_\nu^c$ after the transformation. Where f^{abc} are the structure constants of the $SU(3)$ group which arise due to its non-Abelian nature and describe the gluon self-interaction, this is thought to be the source of the phenomenon of colour confinement described in the previous section. The gluon field strength tensor, denoted by $F_{\mu\nu}^a$, is summed over the eight gluons and accounts for their interactions.

The weak interaction exhibits distinct behaviours compared to the interactions described by QED and QCD. This disparity primarily arises from experimental observations of P [14] and CP [15] violation, as well as the chirality (handedness) requirements which were explained in the previous section. The weak interaction remains invariant under the non-Abelian $SU(2)$ local gauge transformation. To account for this, the covariant derivative ∂_μ is modified as $D_\mu = ig_W \frac{\sigma}{2} W_\mu(x)$, where σ represents the three generators (2×2 Pauli matrices) and W_μ denotes the three gauge fields. To address the chirality requirements demanded by the

$SU(2)_L$ symmetry group, left-handed fermions are treated as weak isospin-half ($I_W = \frac{1}{2}$) doublets, while right-handed fermions are regarded as isospin-zero ($I_W = 0$) singlets. Weak isospin serves as a quantum number associated with particles that interact via the weak charged current. For instance, the left-handed electron isospin doublet is represented by:

$$\phi = \begin{pmatrix} \nu_e \\ e^- \end{pmatrix}_L \quad (2.7)$$

where the third component of isospin I_W^3 assumes a value of $+\frac{1}{2}$ for the neutrino and $-\frac{1}{2}$ for the lepton at the bottom. By adhering to the $SU(2)_L$ local gauge symmetry, three weak currents emerge, with each one corresponding to one of the Pauli matrices. Two of these currents account for the charged gauge bosons, while one suggests the existence of a weak neutral current. Since the number of generators is $N^2 - 1 = 3$, it implies the existence of three gauge fields termed W_μ^1 , W_μ^2 , and W_μ^3 . A quantum superposition of W_μ^1 and W_μ^2 is employed to generate the physical W^\pm bosons.

In the 1960s, Glashow, Salam, and Weinberg made significant contributions to the understanding of the weak interaction [18–20], introducing a theory that addressed inconsistencies with the ordinary weak interaction. Their theory proposed that the neutral weak field mixes with a photon-like field, leading to the physical Z boson and photon. This mixing phenomenon explains the Z boson’s ability to couple to right-handed chiral states. As a result, the $U(1)$ gauge symmetry is replaced by a $U(1)_Y$ local gauge symmetry. The $U(1)_Y$ symmetry introduces a new gauge field, denoted as B_μ , which couples to a type of charge known as weak hypercharge (Y). Weak hypercharge is defined as:

$$Y = 2(Q - I_W^3) \quad (2.8)$$

where Q represents the electric charge of the particle. Before the Higgs mechanism is considered, the photon field and the Z field are inherently linked in the theory, as indicated by the following relations :

$$\begin{aligned} A_\mu &= B_\mu \cos \theta_W + W_\mu^3 \sin \theta_W \\ Z_\mu &= -B_\mu \sin \theta_W + W_\mu^3 \cos \theta_W \end{aligned} \quad (2.9)$$

where the relationship between the two fields is determined by the weak mixing angle (θ_W), which is experimentally determined to be $\sin^2 \theta_W = 0.22339 \pm 0.00010$ for the on-shell scheme at the electroweak scale [18, 30]. Moreover, the theory demonstrates that under the conditions for unification, the weak coupling and electromagnetic couplings become interrelated through the equation $e = g_W \sin \theta_W$. This connection highlights the significance of the electroweak theory, which forms a part of the full SM local gauge symmetry as $SU(2)_L \times U(1)_Y$.

The introduction of the Higgs mechanism in the 1960s addressed some key issues with the SM and its local gauge symmetry. One of these issues is the presence of massive W^\pm and Z bosons, which, in the context of QED, would break the local gauge symmetry. Additionally, the weak and electromagnetic interactions exhibit distinct behaviours at lower energy scales, posing another challenge. The Higgs mechanism tackles these problems by proposing a

concept called spontaneous symmetry breaking [9, 31]. This mechanism involves modifying the non-interacting scalar field in Equation 2.2 by replacing the potential term with:

$$V(\phi) = \frac{1}{2}\mu^2|\phi|^2 + \frac{1}{4}\lambda|\phi|^4 \quad (2.10)$$

where the ϕ^2 and ϕ^4 terms represent the mass of the Higgs and the Higgs self-interaction, respectively. By choosing a negative value for μ^2 and a positive value for λ , the potential obtains a non-zero and finite minimum. The SM Higgs is a weak isospin doublet consisting of two complex scalar fields arranged as:

$$\phi = \begin{pmatrix} \phi^+ \\ \phi^0 \end{pmatrix} \quad (2.11)$$

where ϕ^+ and ϕ^0 correspond to the W and Z boson fields, respectively. For a complex scalar field (e.g., $\phi = \frac{1}{\sqrt{2}}(\phi_1 + i\phi_2)$), the potential takes the shape of a Mexican hat, exhibiting an infinite (degenerate) set of non-zero minima with a constant vacuum expectation value (ν), as depicted in Figure 2.2. Within the GWS model, the Higgs mechanism is embedded in the $SU(2)_L \times U(1)_Y$ local gauge symmetry of the electroweak sector. The choice of vacuum state ($\phi_1 + i\phi_2 = \nu$) breaks the $SU(2)_L \times U(1)_Y$ symmetry, leading to the manifestation of the electromagnetic and weak interactions observed at lower energies.

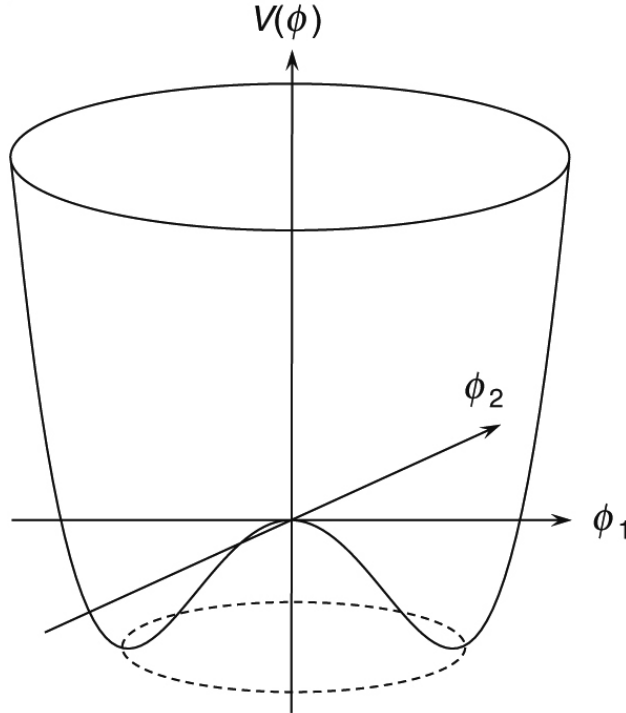


Figure 2.2: A schematic taken from [13] showing the shape of a complex scalar field with the form $V(\phi) = \frac{1}{2}\mu^2|\phi|^2 + \frac{1}{4}\lambda|\phi|^4$.

In order to understand the origin of mass for the W and Z bosons, it is necessary to consider the excitations of the Higgs field. By expanding the scalar field around its vacuum expectation value, and by imposing local gauge invariance on the Higgs Lagrangian, the theory predicts the presence of a massive scalar field, massive gauge fields (except for the photon), and Goldstone bosons. Goldstone bosons are massless scalar particles that arise as a consequence of broken symmetries, as described by Goldstone's theorem [32]. At this stage, the couplings in the theory are not physically meaningful. To address this issue, a further gauge transformation is applied, known as the unitary gauge [33], which leaves the physical predictions unchanged. In this gauge, the Goldstone field is eliminated from the Lagrangian, and the associated degrees of freedom are absorbed by the longitudinal polarisation states of the massive gauge bosons. After implementing the unitary gauge, the Higgs Lagrangian describes a massive scalar particle that interacts with the massive gauge bosons and possesses self-interaction terms.

Within the SM, the scale for the masses of the massive gauge bosons and the Higgs boson is determined by the vacuum expectation value, which is found to be approximately 246 GeV [30]. The tree-level masses of the gauge and Higgs bosons can be extracted from the derived Lagrangian. The mass expressions for the gauge bosons W^\pm and Z are given by the following relations:

$$\begin{aligned} m_H &= \sqrt{2\lambda}\nu \\ m_W &= \frac{1}{2}g_1\nu, \quad m_A = 0 \\ m_Z &= \frac{\nu}{2}\sqrt{g_1^2 + g_2^2} = \frac{m_W}{\cos\theta_W} \end{aligned} \tag{2.12}$$

where g_1 and g_2 are the couplings related to the $SU(2)_L$ and $U(1)$ gauge symmetries, respectively. However, determining the exact mass of the Higgs boson within the theory is not possible. The parameter λ is a free parameter of the SM, and radiative corrections to the Higgs mass introduce additional unknown parameters, as will be discussed in the next section. Using similar arguments to before to generate gauge invariant mass terms, it can be proven that the Higgs mechanism also provides mass to the fermions. Where the Yukawa coupling values have the form $g_f = \sqrt{2}\frac{m_f}{\nu}$, where m_f is the mass of the fermion. This shows that the Yukawa coupling of the Higgs to fermions is also dependent on the vacuum expectation value.

2.2 Limitations of the Standard Model

One of the most significant challenges to the SM arises from the observed rotational velocity of stars as they orbit their respective galactic centre, providing direct evidence of dark matter [34]. This evidence implies the existence of a new particle or an alternative BSM entity. In addition to this finding, other experimental and theoretical discrepancies have led to a prevailing sentiment within the particle physics community that the SM represents only a low energy manifestation of a more comprehensive theory known as a Grand Unified Theory (GUT), potentially characterised by a large-order local gauge symmetry such

as SU(5). When extrapolating the values of the coupling parameters related to the three forces based solely on the currently known SM particles, the values converge at energy scales (Λ_{GUT}) around 10^{15} GeV for a local gauge symmetry of SU(5). This convergence is particularly significant as it occurs below the Planck scale $\Lambda_{\text{P}} = 10^{19}$ GeV, beyond which quantum gravity effects become relevant and the previously developed gauge theories break down. While experimental investigations, such as those focused on detecting proton decay, have disfavoured a SU(5) GUT by establishing stringent limits on the proton lifetime [35], the underlying principle remains valid: a higher-order symmetry group may encompass the SM and a quantum theory of gravity.

One major theoretical challenge concerning the SM is the issue of fine-tuning in the determination of the Higgs mass, commonly known as the hierarchy problem. The mass of the Higgs is subject to quantum loop corrections, whereby both the masses of particles within the SM and BSM contribute to the Higgs mass at higher order levels. In fact, one quantum correction to the Higgs mass is proportional to Λ_{UV}^2 , where Λ_{UV} represents the ultraviolet cutoff scale [36]. This scale marks the energy level at which new physics begins to significantly affect the behaviour of the theory at high energies. Consequently, these corrections can be exceedingly large, necessitating fine-tuning to cancel out these terms and attain the observed mass at the electroweak scale [13].

Experimental evidence suggesting new physics relevant to the research in this thesis stems from anomalies observed in semi-leptonic decays of B -mesons (which contain a b -quark). Results from the BaBar [1, 2], Belle [3], and LHCb [4, 5] experiments have consistently revealed significant deviations from the expected lepton universality predicted by the SM. These B -meson decays are abundant in the aforementioned experiments. The anomalies arise from the measurement of branching ratios (\mathcal{B}). The key ratios that probe the $b \rightarrow c \ell \nu$ weak interaction using the c quark-containing D -meson and its excited state (D^*) are represented by:

$$\mathcal{R}(X) \equiv \frac{\mathcal{B}(\bar{B} \rightarrow X \tau \bar{\nu})}{\mathcal{B}(\bar{B} \rightarrow X \ell \bar{\nu})} \Big|_{X=D^* \text{ or } D} \quad (2.13)$$

where the ratios can be formed using charged or neutral D -mesons. As described in the next section, numerous physics models predict enhanced couplings to third-generation fermions. Hence, any deviation from the SM predictions suggests the presence of new physics. Multiple measurements of these ratios have been conducted, and Figure 2.3 summarises these measurements alongside the SM prediction. The SM prediction primarily relies on phase space considerations, taking into account the different masses of lepton generations. However, the SM prediction deviates from the world average by 3.2σ , indicating a substantial deviation. Nevertheless, it falls short of the 5σ threshold (corresponding to a 1 in 3.5 million chance) required to claim a discovery, as explained in Section 4.7.

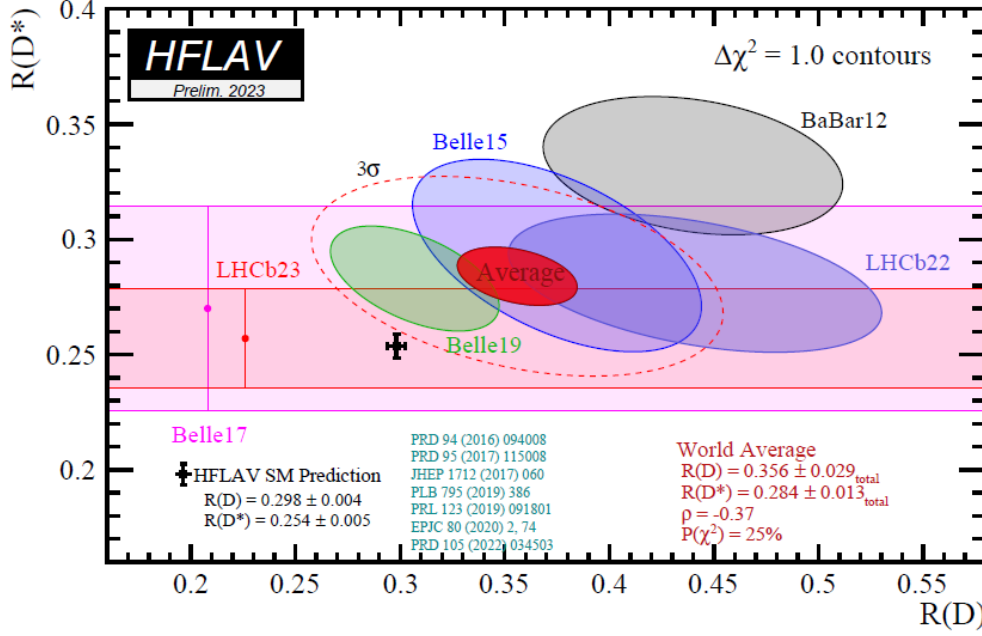


Figure 2.3: The B -meson anomalies using the combination of several experiments [37]. The SM prediction for $R(D)$ and $R(D^*)$ is shown by the black marker and the world average over all experiments is shown as the red oval.

Another interesting piece of experimental evidence which suggests BSM physics and is relevant to the work in this thesis is the muon $g - 2$ experiment conducted at Fermilab [38]. The magnetic moment of a muon can be expressed as:

$$\vec{\mu}_{\text{mag}} = g \frac{q}{2m} \vec{S} \quad (2.14)$$

where g represents the gyromagnetic ratio that describes the overall strength of the magnetic moment, and q and m denote the charge and mass of the muon, respectively. The spin vector is represented by \vec{S} . According to the Dirac formulation [28], one expects g to equal 2 [6]. However, due to quantum loop corrections involving virtual particles, the value of g deviates from the Dirac prediction at the per-mille level, representing a quantum loop correction which can be determined by theorists up to an extraordinarily high precision of tenth order in QED [39].

At Fermilab, muons are circulated around a storage ring, and the direction of their spin vector precesses around the magnetic field at a rate directly related to $g - 2$. This precession is measured by analysing the decay of muons into a positron and a neutrino. The mean energy of a resulting positron depends on the spin orientation of the muon, allowing the rate of precession to be determined through the rate of variation of the positron energy. In 2021, Fermilab reported a 4.2σ deviation from the SM prediction [7], which further confirmed the approximately 3σ excess observed at Brookhaven in 2006 [6]. While the significance of this 4.2σ excess was partially reduced by considering updated lattice QCD calculations [40], it strongly suggests the involvement of virtual BSM particles in the quantum loop corrections.

2.3 Proposed Extensions to the Standard Model

Numerous proposals have been put forward to address the issues highlighted in the previous section. These models introduce a range of novel states, a few of which are explored within this thesis. In this section, the theory pertaining to the BSM searches discussed in this thesis is outlined. Additionally, where relevant, generalised experimental results which support these theories are presented.

2.3.1 Supersymmetry and the Minimal Supersymmetric Standard Model

Supersymmetry (SUSY) stands out as one of the most renowned and promising BSM theories. It proposes the existence of sparticles, an identical partner to each known particle, but differing by half a unit of spin [36]. This concept establishes a correspondence between fermions and bosonic superpartners, presenting a potential elegant solution to the hierarchy problem. Each virtual particle correction loop from the SM would be counterbalanced by its corresponding superpartner loop, assuming an exact symmetry. Moreover, many SUSY models naturally incorporate potential candidates for dark matter. The distinction between particles and sparticles can be determined by the quantum number known as R-parity represented by:

$$R = (-1)^{3B+L+2s} \quad (2.15)$$

where B , L , and s denote baryon number, lepton number, and spin, respectively. However, the absence of observed bosonic partners at the same masses as their fermionic counterparts casts doubt on the existence of an exact symmetry. One plausible explanation is that these sparticles possess much higher masses than their partners, starting from an unknown energy scale (Λ_{SUSY}). Softly broken supersymmetric models can account for this discrepancy, and such models have been subjected to testing at the LHC for over a decade.

The MSSM is a SUSY extension of the SM that preserves R-parity. It is designed to introduce the fewest possible new particles and parameters while still incorporating supersymmetry [41]. In order to accommodate these additional particles, an extra doublet of complex scalar fields is required, giving rise to a two-Higgs doublet model (2HDM). Consequently, eight scalar fields emerge, three of which provide mass to the SM W and Z bosons, while the remaining five manifest themselves as five physical Higgs bosons: two CP-even bosons (h and H), with H typically having a higher mass, a CP-odd boson (A), and two charged bosons (H^\pm) [42]. For the purposes of this thesis, the 2HDM falls under the category of type-II, wherein each Higgs doublet (H_u and H_d) possesses a distinct vacuum expectation value. In this scenario, one doublet provides masses for the up-type quarks (the upper components of weak isospin doublets) while the other doublet couples to the down-type quarks and the charged leptons [42].

In the MSSM, at the tree-level, the masses of the neutral CP-even Higgs bosons (m_H and m_h) are determined by the mass of the CP-odd Higgs (m_A), the mass of the Z boson (m_Z), and

the ratio of the vacuum expectation values, denoted as $\tan \beta = \frac{\nu_1}{\nu_2}$. Here, $\nu_1^2 + \nu_2^2 = \nu = 256$ GeV, which represents the vacuum expectation value of the Higgs complex scalar field in the SM [43]. Consequently, at high values of $\tan \beta$, the difference in the vacuum expectation values of the two Higgs doublets becomes more pronounced. In the case of type-II 2HDMs, the coupling to down-type fermions is enhanced compared to the SM prediction for large $\tan \beta$ values. Beyond the tree-level, radiative corrections come into play, introducing additional parameters such as Λ_{SUSY} or the predicted masses of SUSY particles [44]. When testing hypotheses using MSSM signals, predictions are typically made by fixing the values of these additional parameters to reasonable values. Scanning every possible combination of parameters would be impractical. In order to explore new physics, the $\{m_A, \tan \beta\}$ plane is often scanned, as it defines the mass of the neutral heavy MSSM Higgs boson at the tree-level. This scanning process establishes exclusion regions for different models. Several benchmark scenarios have been developed for the MSSM, and they are regularly updated based on the latest information from detectors at the LHC. In the context of this thesis, the hMSSM [44] and M_h^{125} [45] scenarios are considered, they are explained below.

The hMSSM serves as a simplified approach to the MSSM, assuming CP conservation in the Higgs sector and heavy SUSY particles that do not significantly influence Higgs production and decay [44]. Given that many SUSY parameters are involved in radiative corrections, the hMSSM utilises various approximations based on the relative strengths of these corrections. This allows for a description of the heavy Higgs boson mass which is dependent on m_A , m_Z , $\tan \beta$, and m_h , with the SM Higgs boson mass of 125 GeV assigned to m_h . As a result, the mass of m_H can once again be expressed in terms of the tree-level parameters even after radiative corrections are considered. These simplifications offer advantages such as a more streamlined model and a m_h value consistent with the observed SM Higgs mass throughout the parameter space. However, the hMSSM neglects various radiative corrections, which is acceptable only in limited regions of the parameter space away from small m_A values or large $\tan \beta$ values. Despite this simplified nature, the hMSSM serves as a popular benchmark for experiments conducted at the LHC since it is somewhat model-independent (since many parameters are not fixed). Both the ATLAS and CMS experiments have conducted numerous analyses simultaneously searching for heavy Higgs bosons within the hMSSM scenario. They have released summary plots demonstrating the exclusion regions in the $\{m_A, \tan \beta\}$ plane. An example is the ATLAS experiment's hMSSM summary plot depicted in Figure 2.4, illustrating the exclusion of significant regions in the plane. The exclusion is primarily driven by the 2020 MSSM $H/A/h \rightarrow \tau^+ \tau^-$ analysis, shown in grey.

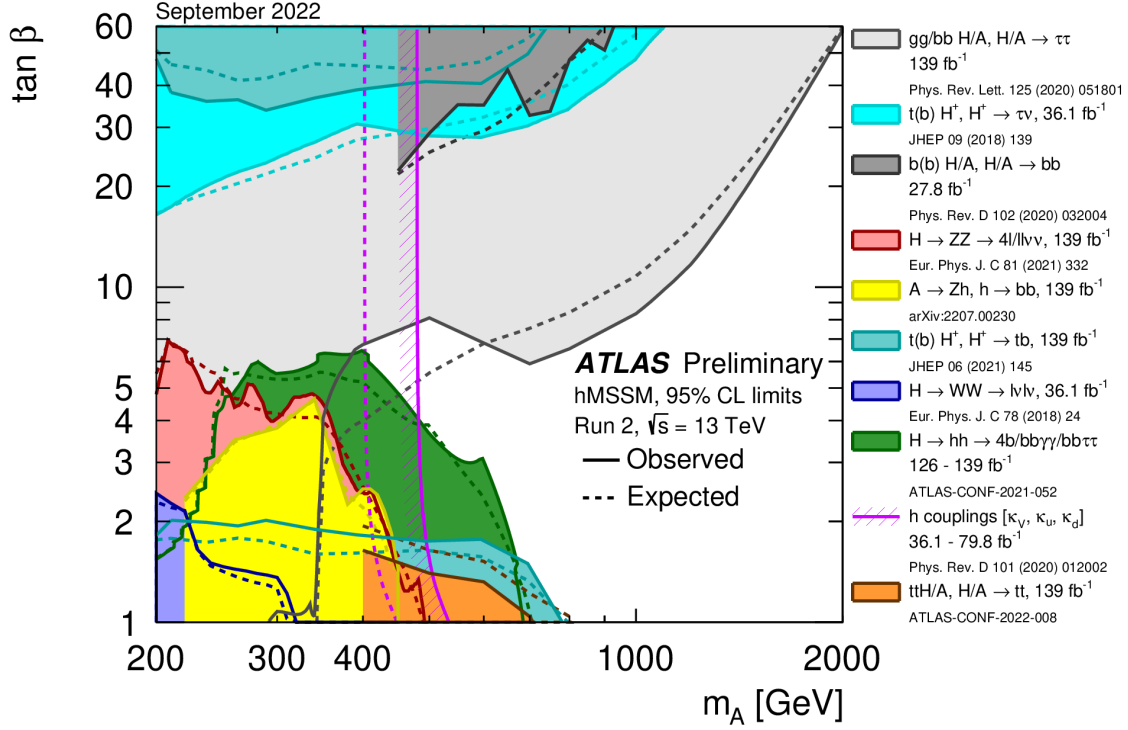


Figure 2.4: The $\{m_A, \tan \beta\}$ exclusion plane for the hMSSM benchmark scenario shown as a summary plot containing several ATLAS analyses [46].

Taking into account the findings from ATLAS and CMS experiments up until 2019, new benchmark scenarios were introduced in [45] to incorporate the impact of the radiative corrections more effectively. These benchmarks ensure that a scalar boson with properties resembling the SM Higgs boson with a mass of 125 GeV is present across a significant portion of the parameter space. Furthermore, all super-particles must conform to the experimental constraints established by the LHC up until 2019. Among the six newly defined benchmarks, this thesis focuses on the M_h^{125} scenario. In this benchmark, the SUSY parameters are set such that the MSSM Higgs bosons are only mildly influenced by the presence of super-particles, and the ones with masses below 2 TeV predominantly decay into SM particles.

2.3.2 Z' Bosons

In certain larger symmetry groups or popular GUT frameworks, the existence of an additional neutral gauge boson, referred to as Z' , is postulated [47, 48]. By introducing an extra $U(1)$ gauge group to the local gauge symmetry of the SM, it becomes possible to generate a Z' boson [49]. In many theoretical models, the Z' boson is naturally expected to have a mass around 1 TeV. Consequently, there is realistic hope that the presence of a Z' boson can be confirmed through experimental observations at the energies achievable today at the LHC. The detection of a Z' boson would impose stringent constraints on the gauge symmetry of any potential GUT. In this thesis, two specific models are employed: the Sequential Standard Model (SSM) and the Heavy Vector Triplet (HVT) model [49–53].

The SSM is a simplified model where the couplings of the Z' boson to the SM fermions are identical to those of the SM Z boson, with the only difference being the mass of the particle. The SSM cannot arise in extended gauge theories but the model is possible in composite theories which propose that certain particles, such as the Higgs boson, are composed of other fundamental constituents. One popular example of a composite theory is the technicolor theory [54–56] which proposes that the Higgs is bound state of techniquarks. The SSM serves as a valuable reference point for comparing constraints from different sources. It can also be reinterpreted for a wide range of models by examining the signal sensitivity with modifications to the required SSM Z' couplings [57]. Through experimental investigations [58], the ATLAS experiment has excluded SSM Z' masses up to 5.1 TeV using the $Z' \rightarrow e^+e^-/\mu^+\mu^- (\ell^+\ell^-)$ channel. Prior the findings mentioned in Chapter 5, the $Z' \rightarrow \tau^+\tau^-$ channel was able to exclude SSM Z' masses up to 2.4 TeV.

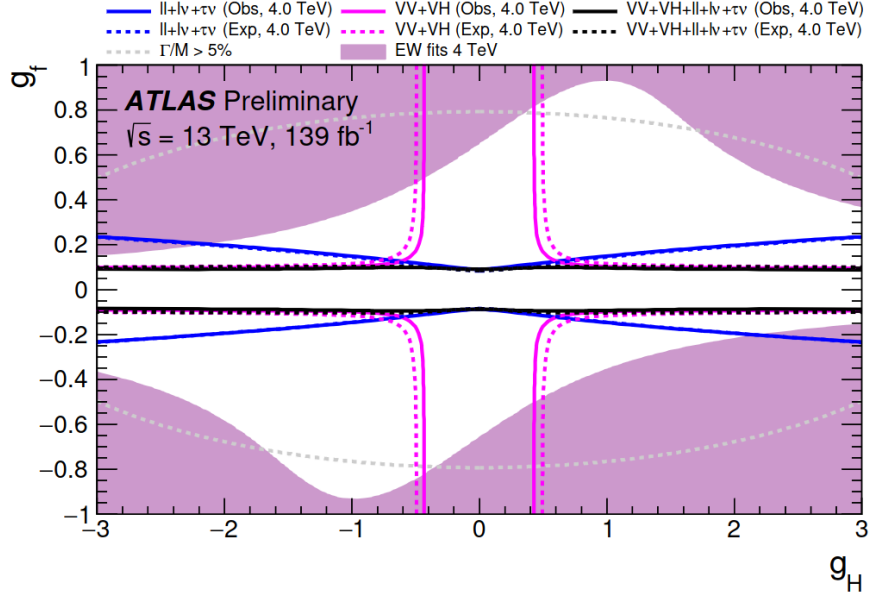
The HVT framework is another simplified model that encompasses a wide range of phenomenologies [52]. When conducting searches for narrow resonances, the focus is typically on the free parameters that govern the resonance’s mass, production, interactions and decay. Consequently, a simplified Lagrangian is employed, which retains only the relevant couplings and mass parameters. The purpose of this simplified Lagrangian is to provide a phenomenological parameterisation that encompasses a broad set of models, without being tied to any specific theoretical requirements. It adheres to symmetry constraints while allowing for easy translation of exclusion limits on the phenomenology permitted by the Lagrangian into the free parameters of any given model. This translation is achieved by computing the relationships between the free parameters of the model and the parameters of the phenomenological Lagrangian, enabling a straightforward mapping of results from the simplified framework to specific model predictions [52].

The HVT introduces a triplet of spin-1 vector bosons, denoted as \mathcal{W} , with zero hypercharge. This framework predicts the existence of a Z' boson, as well as nearly degenerate W' bosons with comparable production rates. These W' bosons are often combined into a single entity referred to as V' . The HVT adds a number of terms to the overall Lagrangian, the relevant ones for this thesis are:

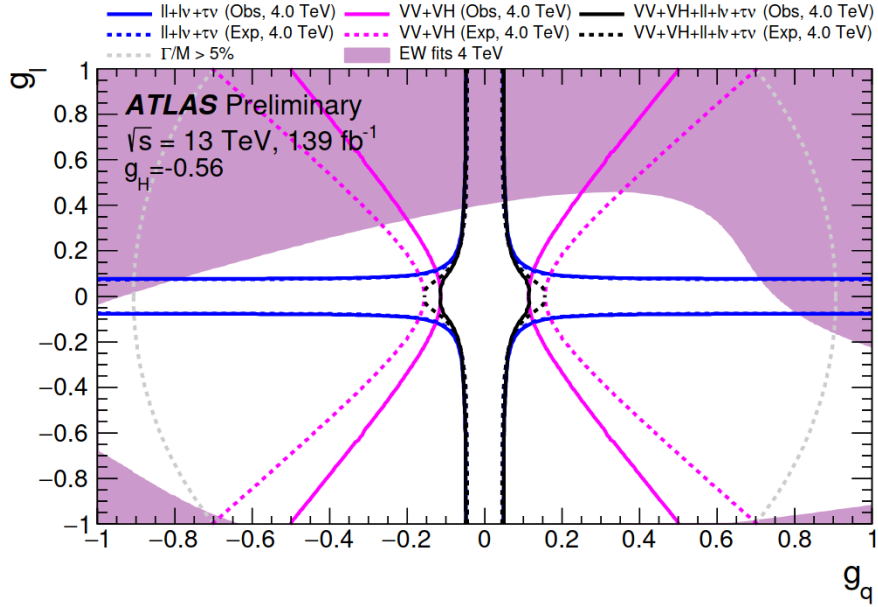
$$\mathcal{L}_{\mathcal{W}} \supset -g_q \mathcal{W}_\mu^a \bar{q}_k \gamma^\mu \frac{\sigma_a}{2} q_k - g_l \mathcal{W}_\mu^a \bar{\ell}_k \gamma^\mu \frac{\sigma_a}{2} \ell_k - g_H (\mathcal{W}_\mu^a H^\dagger \frac{\sigma_a}{2} i D^\mu H + h.c.) \quad (2.16)$$

which involve the left-handed quark and lepton doublets (q_k and ℓ_k) for the respective fermion generation k . The Higgs doublet is represented by H , and σ_a denotes the Pauli matrices. The coupling strengths between the \mathcal{W} field and the Higgs, as well as the generation-inclusive quarks and leptons, are denoted as g_H , g_q , and g_ℓ , respectively. Right-handed fermions are not predicted to participate in these interactions. The triplet field couples to the SM W and Z bosons, as well as the Higgs field, due to the equivalence theorem [59–61]. In the HVT framework, multiple benchmarks have been defined to set requirements on the phenomenology. For the purpose of this thesis, the relevant benchmark is Model A [62].

Model A is designed to describe the phenomenology of weakly coupled models based on an extended gauge symmetry [63], the production of V' is exclusively through quark-quark annihilation (qqA). The couplings in Model A are set to specific values: g_H and g_f are equal to -0.56 and -0.55 , and fermion universality is assumed, meaning $g_f = g_q = g_\ell$. In terms of branching ratios, Model A predicts relatively large couplings to fermion-antifermion final states across the resonance mass range. The branching ratio for the lepton-antilepton final state is approximately 4% over the mass range. On the other hand, the branching ratios for decays to bosonic final states are relatively low, around 2% throughout the mass range, with the VV branching ratio reaching 3% at low masses [52]. The experimental results are mainly interpreted using 2D exclusion planes. One of interest is the $\{g_q, g_l\}$ plane, assuming the Model A condition of $g_H = -0.56$. The other is the more model-independent $\{g_H, g_f\}$ plane, assuming fermion universality. These planes, obtained through a combination of ATLAS analyses, are shown in Figure 2.5, which represents the contributions of the leptonic and bosonic channels to the exclusion, as well as the combined exclusion contours for a 4 TeV V' signal [62]. These planes provide stringent constraints on the generalised coupling parameters. For a more detailed understanding of the shapes of the individual exclusion planes, further information can be found in Section 5.5.2.



(a)



(b)

Figure 2.5: The 2D generalised coupling parameter exclusion planes for a 4 TeV V' particle within the HVT framework [62]. Results are shown for the (a) $\{g_H, g_f\}$ and (b) $\{g_q, g_l\}$ sets of coupling planes. The bosonic and leptonic sub-combinations are combined as shown by the black line. Constraints already set by electroweak measurements performed by [64] are shown by the pink shaded area.

2.3.3 Leptoquarks

Leptoquarks are hypothetical particles that appear in various GUTs [65–67] and composite models [68]. They have garnered attention as a leading candidate to explain the observed lepton flavour anomalies in B -meson decays [69]. Additionally, LQ s have the potential to contribute to the radiative corrections of the muon’s anomalous magnetic moment $(g - 2)$. Leptoquarks couple to both quarks and leptons, exhibit non-zero baryon and lepton numbers, and can have fractional electric charge. The LQ characteristics depend on the proposed theoretical models which describe various plausible scenarios. In the context of this thesis, two relevant models are considered: the \tilde{S}_1 [70, 71] and U_1 [72] models. Since quarks have fractional baryon number and leptons have a lepton number of ± 1 , leptoquarks can be distinguished using the fermion quantum number defined as $F = 3B + L$. The \tilde{S}_1 model is a scalar LQ with $F = -2$, possessing an electric charge of $+\frac{4}{3}e$. On the other hand, the U_1 model is a vector LQ with $F = 0$ and an electric charge of $+\frac{2}{3}e$. The U_1 model has gained prominence as one of the favoured explanations for the B -meson anomalies [73] and was among the first LQ models to be extensively studied in the literature. It is also a constituent of the Pati-Salam model, which represents a possible GUT [70].

The coupling of LQ s to third-generation particles is expected to be large due to the indications from the B -meson anomalies [69]. As this thesis focuses on final states involving taus, it serves as a good basis for an LQ search. In the case of the \tilde{S}_1 LQ , the relevant part of the Lagrangian proposed by the theory is expressed as:

$$\mathcal{L}_{\tilde{S}_1} \supset +\lambda^{ij} \bar{d}_R^C \tilde{S}_1 e_R^j + h.c., \quad (2.17)$$

where C represents the charge conjugation operation, e_R and d_R denote the right-handed charged leptons and down-type quarks, respectively. The λ^{ij} symbol corresponds to the Yukawa couplings between the \tilde{S}_1 LQ and charged leptons and quarks for each generation. This equation plays a crucial role in designing the LQ analysis in Chapter 6.

The U_1 model is an $SU(2)_L$ singlet. The relevant part of the Lagrangian describing its interactions is represented by:

$$\mathcal{L}_{U_1} \supset -ig_s(1 - \kappa)U_{1\mu}^\dagger T^a U_{1\nu} G^{\alpha\mu\nu} + \frac{g_U}{\sqrt{2}}[U_1^\mu(\beta_L^{ij} \bar{q}_L^i \gamma_\mu \ell_L^j + \beta_R^{ij} \bar{d}_R^i \gamma_\mu e_R^j) + h.c.] \quad (2.18)$$

where $T^a = \frac{\lambda^a}{2}$ and λ^a correspond to the Gell-Mann matrices (indexed by $a = 1, \dots, 8$) as discussed in Section 2.1.1. The parameter g_s represents the QCD coupling constant, while q_L and ℓ_L denote the left-handed quark and lepton doublets, respectively, and d_R and e_R refer to the right-handed down-type quark and charged lepton singlets. The first term in the equation represents the interaction between the vector LQ and the gluon fields of the SM ($G^{\alpha\mu\nu}$). The parameter κ determines the coupling scenario, where two commonly considered scenarios are the Yang-Mills case ($\kappa = 0$), which describes nominal coupling to gluons (or colour), and the minimal coupling scenario ($\kappa = 1$), which implies the smallest possible coupling to gluons. The couplings of the vector LQ to the left-handed and right-handed charged leptons and quarks are denoted by β_L^{ij} and β_R^{ij} , respectively.

Previous leptoquark investigations from both the ATLAS [74–78] and CMS [79–81] collaborations have primarily focused on the search for leptoquarks produced in pairs with subsequent decay to a variety of final states. For the analyses which consider the third generation LQ decay into the $b\tau$ final state, the assumed LQ branching fraction to $b\tau$ ($\mathcal{B}(LQ \rightarrow b\tau)$) is important to the result. Scalar LQ masses below 1 TeV are excluded by the ATLAS search for pair produced leptoquarks decaying to the $b\tau b\tau$ final state using an integrated luminosity of 36 fb^{-1} , assuming $\mathcal{B}(LQ \rightarrow b\tau) = 1$ [82]. When considering the singly produced scalar LQ production mode or the singly produced mode in addition to the pair produced mode (named ‘singly plus pair production’ throughout this thesis, following the convention in [83]) lower limits at 95% confidence have been set by CMS for both modes. These limits are set between 0.98 TeV and 1.73 TeV depending on the LQ spin and λ , assuming that the scalar LQ can decay either into $t\nu$ or $b\tau$ final states with equal probability [84]. To date, ATLAS has not provided direct results for singly produced LQ s decaying into $b\tau$ final states, apart from the results considered in Chapter 6 [83] which considers both singly and singly plus pair produced LQ , assuming $\mathcal{B}(LQ \rightarrow b\tau) = 1$.

Chapter 3

The ATLAS Detector and the Extraction of Physics Data

The ATLAS (A Toroidal LHC Apparatus) detector [85], which forms part of the LHC [86], plays a crucial role in collecting particle physics data for this thesis. This detector is designed to capture the signals from high-energy particles produced in proton bunch collisions. The collision products generate an array of hits in the detector’s active material. By analysing the interaction between the particles and various detector components, the particle type and its properties can be determined. To calibrate the detector output and separate signal from expected background, well-modelled simulation is essential to create a reliable expectation. This chapter provides a detailed account of the relevant detector infrastructure and the techniques used to extract and store data, which will be used in subsequent chapters to conduct physics analyses.

3.1 The Large Hadron Collider

Since the first collisions in 2010, the LHC has been the largest and most powerful particle accelerator in the world. Situated around 100 m underground on the French-Swiss border near Geneva, it is designed to have the capability to perform pp collisions at $\sqrt{s} = 14$ TeV using its 26.7 km circumference beam rings. In reality, the energy limit is situated at 13.6 TeV, a trade-off between operating within the time specified and the time taken to train the magnets to routinely operate at these high magnetic fields. Additionally, the LHC has periods dedicated to heavy ion collisions, such as lead, with a design \sqrt{s} of up to 2.76 TeV per nucleon. The layout of the LHC is illustrated in Figure 3.1, many tunnels and caverns were shared between the LHC and its predecessor, the Large Electron-Positron Collider (LEP) which operated between 1989 and 2000 [87]. The highly energetic particle collisions provided by the LHC serve as the basis for thousands of particle physics publications from the four large and several smaller particle detectors. The four large experiments are situated at the four interaction points on the beamline and are shown in Figure 3.1. They are the ATLAS, CMS [88], LHCb [89] and ALICE [90] detectors, the first two are general purpose detectors whilst the latter two are highly specialised, studying B -meson decays and heavy ions, respectively.

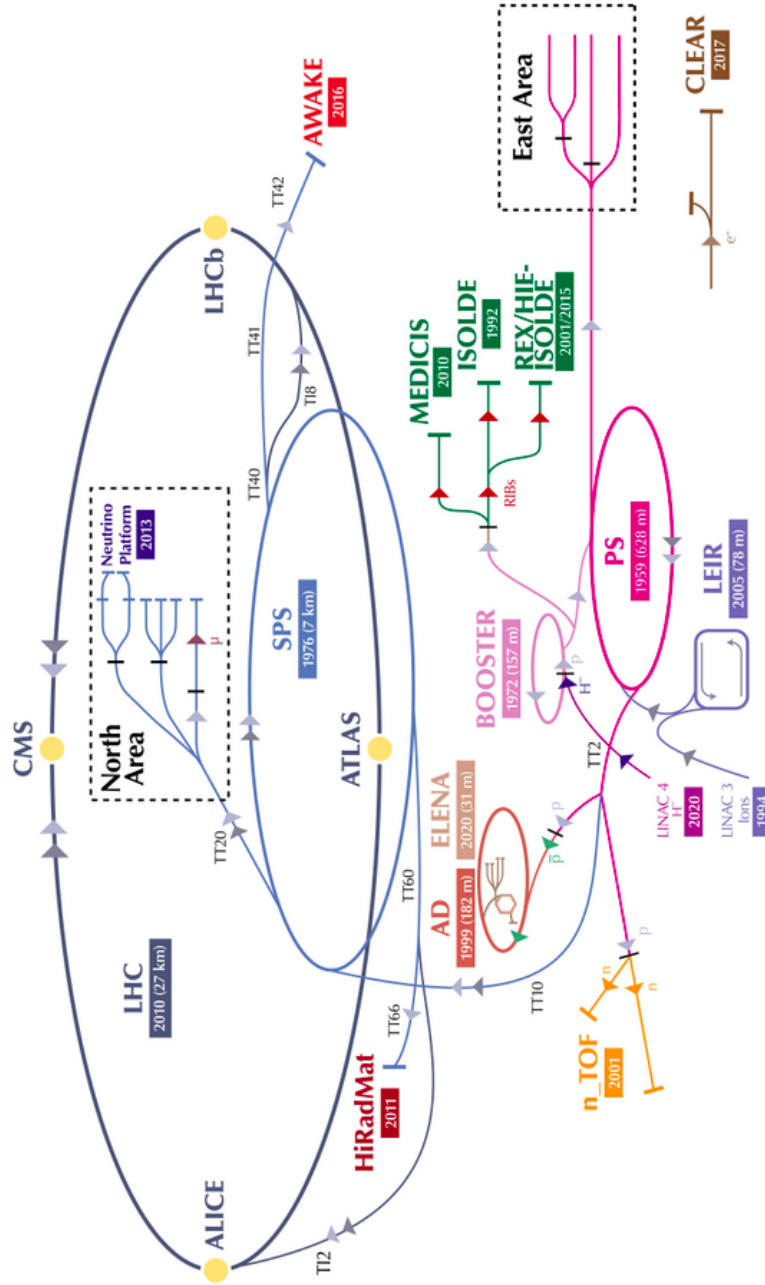


Figure 3.1: The full CERN complex showing the LHC and other smaller accelerators used to increase the beam energy prior to entry into the storage ring [91]. The four main experiments: ATLAS, CMS, ALICE and LHCb are shown along with all the other smaller experiments.

3.1.1 The Particle Beam

The LHC is a synchrotron accelerator that consists of two counter-rotating beams within a near vacuum environment. The \sqrt{s} is influenced by various factors, including the diameter of the beamline ring, the magnetic and electric fields that are applied, and the properties of the particle.

A diverse array of over 9000 superconducting magnets that are cryogenically cooled to 2 K are employed to achieve magnetic fields in excess of 8 T. The dipole magnets are typically used to bend and align both counter-rotating beams into a circular path and achieve the required \sqrt{s} . Quadrupoles are used to focus the beam at the interaction points to ensure a maximal collision rate. Higher order poles are also used to correct imperfections in the magnetic field.

To accelerate the protons to their final energy and compensate for any energy loss from synchrotron radiation, the LHC employs electromagnetic resonators called radio frequency (RF) cavities. Each direction uses eight cavities that deliver a resonant and oscillating electric field. The oscillation must be carefully timed so that a particle at maximum energy does not experience any push. In this way, the crucial role of beam splitting is conducted, allowing for the formation of over 2800 bunches, each containing approximately 1.1×10^{11} protons, with a spacing of 25 ns (corresponding to a collision rate of 40 MHz). This bunch splitting process is critical to maximise the rate of collisions and ensure the highest possible yield of data for analysis.

Before entering the LHC main (storage) ring, protons must undergo several preparatory stages. For instance, protons are initially extracted from hydrogen gas and stripped of their electrons using an electric field. Next, they are directed to LINAC 2 (or LINAC 4 after 2020 [92]) as shown in Figure 3.1, where they are accelerated to 50 MeV. The Proton Synchrotron Booster (PSB) is the next accelerator in the sequence, followed by the Proton Synchrotron (PS) and the Super Proton Synchrotron (SPS), each increasing the energy of the protons to 1.4 GeV, 25 GeV, and 450 GeV, respectively. After these stages, the protons are ready to enter the storage ring, where they are further accelerated from 450 GeV to a maximum of 6.8 TeV (7 TeV design value) per beam over approximately 20 minutes in a process known as ramping [86].

3.1.2 LHC Operation and Delivered Luminosity

The LHC operation is organised into periods of data taking called runs and periods of long shutdown used for upgrading the detector infrastructure. During Run-I which spanned from 2010 to 2013, the \sqrt{s} was 7 or 8 TeV depending on the time period. Run-II, which provided the datasets used in this thesis, took place between 2015 and 2018 and operated at a \sqrt{s} of 13 TeV for the entire run. Run-III is currently ongoing, having started in May 2022 and will continue until 2025 at a \sqrt{s} of 13.6 TeV, a world record energy for a particle collider.

The luminosity, which measures the rate of collisions per unit of time and per unit of cross-

sectional area of the colliding beams, is a crucial parameter for the performance of the LHC, it can be determined using the equation:

$$\mathcal{L}_b = \frac{\mu_{\text{pile-up}} f_r}{\sigma_{\text{inel}}} \quad (3.1)$$

for a single pair of colliding bunches, where $\mu_{\text{pile-up}}$ is the average number of inelastic collisions per bunch crossing, f_r is the LHC bunch revolution frequency (11246 Hz for protons), and σ_{inel} is the reference inelastic cross-section (80 mb for pp collisions at $\sqrt{s} = 13$ TeV) [93]. By summing \mathcal{L}_b over all the bunch pairs colliding at the interaction point, the instantaneous luminosity at a given moment can be represented by:

$$\mathcal{L}_{\text{inst}} = \sum_{b=1}^{n_b} \mathcal{L}_b = n_b \langle \mathcal{L}_b \rangle = n_b \frac{\langle \mu_{\text{pile-up}} \rangle f_r}{\sigma_{\text{inel}}} \quad (3.2)$$

where $\langle \mathcal{L}_b \rangle$ is the mean luminosity per bunch, this is equivalent to averaging the pile-up parameter across all colliding bunch pairs ($\langle \mu_{\text{pile-up}} \rangle$). During Run-II, the instantaneous luminosity peaked at $2.2 \times 10^{34} \text{ cm}^{-2}\text{s}^{-1}$, which was more than twice the design value [94].

The pile-up parameter is a crucial factor in physics analyses as it indicates the number of simultaneous pp collisions occurring within a given event. A high pile-up parameter corresponds to an event with more overlapping pp collisions, resulting in increased complexity and detector inefficiency, as the accurate reconstruction of particles becomes more challenging. Pile-up can occur in-time when multiple pp collisions occur during a single bunch crossing or out-of-time when the detector is sensitive to pp collisions from earlier bunches. Figure 3.2(b) displays the $\mu_{\text{pile-up}}$ profile for each year of Run-II data taking, with an increase in $\langle \mu_{\text{pile-up}} \rangle$ observed as the years progressed and the instantaneous luminosity rose.

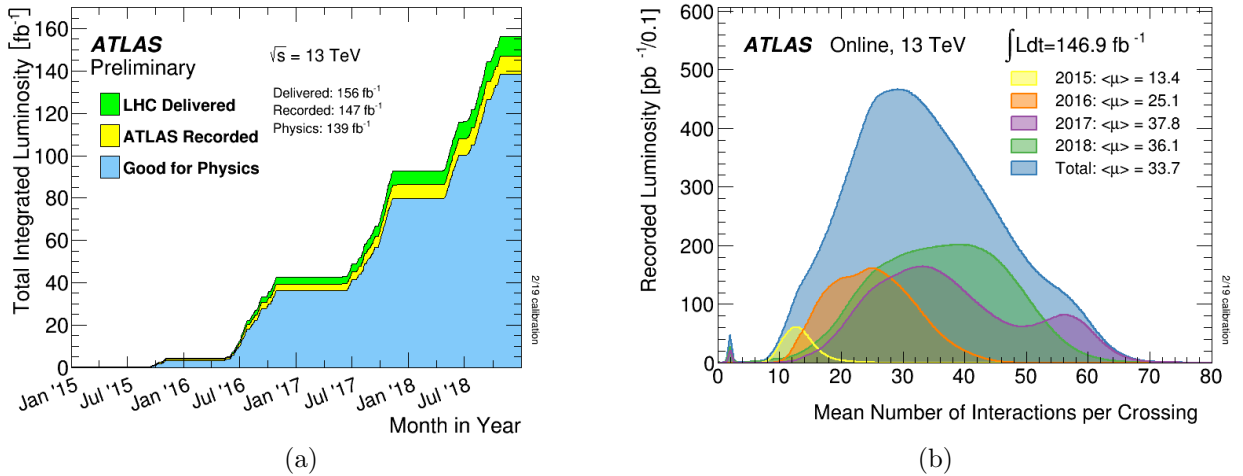


Figure 3.2: (a) The cumulative integrated luminosity for Run-II delivered by the LHC, registered by ATLAS and declared good for physics. (b) The Run-II evolution of the mean number of interactions per bunch crossing (pile-up) measured by ATLAS [94].

In practice, the instantaneous luminosity is determined by all the experiments separately. Typically, this is done by measuring the visible interaction rate per bunch crossing using dedicated sub-detectors near the collision point and various algorithms [93]. The instantaneous luminosity is assumed to be constant over approximately one minute intervals called lumi-blocks (LB). Although typically the luminosity will change over this period due to the reduced number of protons per bunch as a result of prior proton collisions.

The integrated luminosity (\mathcal{L}_{int}) is another crucial quantity that is obtained by multiplying the average $\mathcal{L}_{\text{inst}}$ with the time of each LB. By summing the $\mathcal{L}_{\text{inst}}$ over all LBs, the total integrated luminosity for the run can be determined. As shown in Figure 3.2(a), at the end of Run-II, the LHC had delivered 158 fb^{-1} of data, with 148 fb^{-1} recorded by the ATLAS detector, and 139 fb^{-1} passing stringent quality checks to be declared good for physics. The integrated luminosity is a valuable tool for describing the size of a dataset. Using the following relation:

$$N = \mathcal{L}_{\text{int}} \sigma \quad (3.3)$$

an estimate of the number of times a particular process occurred can be gathered. For example, assuming a cross-section of 390 fb , one would expect approximately 54,000 SSM $Z' \rightarrow \tau\tau$ events for a resonance mass of 1 TeV [95].

3.2 The ATLAS Detector

The general purpose ATLAS detector is composed of many subcomponents designed to detect the many experimental signatures of SM particles. Particles within the beam collide longitudinally and the collision products scatter in all directions.

3.2.1 The ATLAS Coordinate System

A right handed Cartesian coordinate system with the origin located at the collision point can be considered for the detector geometry design. The z -axis is defined as pointing in the direction of the beam and the x and y -axis are defined as pointing towards the centre of the LHC ring and directly upwards, respectively. This creates an x - y plane transverse to the beamline. The definition of this plane, leads to the derivation of the key kinematic quantities for particle physics analyses, such as transverse momentum (p_T). Since the vectorial sum of the p_T is zero to a good approximation, the missing transverse energy (E_T^{MISS}) can be derived to consider the invisible particles traversing the detector. While the transverse momentum is well-defined, the longitudinal component is not as reliable because the individual partons within the protons can have differing longitudinal momenta, making this component difficult to measure accurately. As a result, the longitudinal component is often neglected.

Due to the cylindrical geometry of the detector, cylindrical coordinates are typically more convenient to use. The radial (r) direction is defined as the direction directly outwards from the beamline ($r \in \{0, \infty\}$), the azimuthal angle (ϕ) is measured around the beam ($\phi \in \{-\pi, \pi\}$) and the polar angle (θ) is measured from the beam axis ($\theta \in \{0, \pi\}$). The

polar angle of a particle is more commonly translated to the (approximately Lorentz invariant for boosts along the beam axis) pseudorapidity (η) which is defined as:

$$\eta = -\ln(\tan(\theta/2)) \quad (3.4)$$

One can then use η and ϕ to describe the entire solid angle around the beamline. The angular variables are often used to construct a cone of size ΔR in angular space using the relation:

$$\Delta R = \sqrt{(\Delta\phi)^2 + (\Delta\eta)^2} \quad (3.5)$$

which is often used to define the distance between two objects or construct isolation cones.

The ATLAS detector, as depicted in Figure 3.3, has a forward-backward symmetric design, with concentric sub-detectors positioned around the collision point. End-caps and forward detectors are also included allowing for $|\eta| < 4.9$ coverage. However, the coverage is severely diminished in the transition region between the barrel and end-cap cryostats, this is the $|\eta|$ region between 1.37 and 1.52. The sub-detectors are arranged in the following order of proximity to the collision point: the Inner Detector, the electromagnetic (ECAL) and hadronic calorimeter (HCAL), and the muon spectrometer (MS). The magnet system is also shown in Figure 3.3, which curves the path of particles passing through it and enables the determination of their p_T . Once a particle interacts with these sub-detectors, a data acquisition and trigger (TDAQ) system is required to promptly retrieve and save the event.

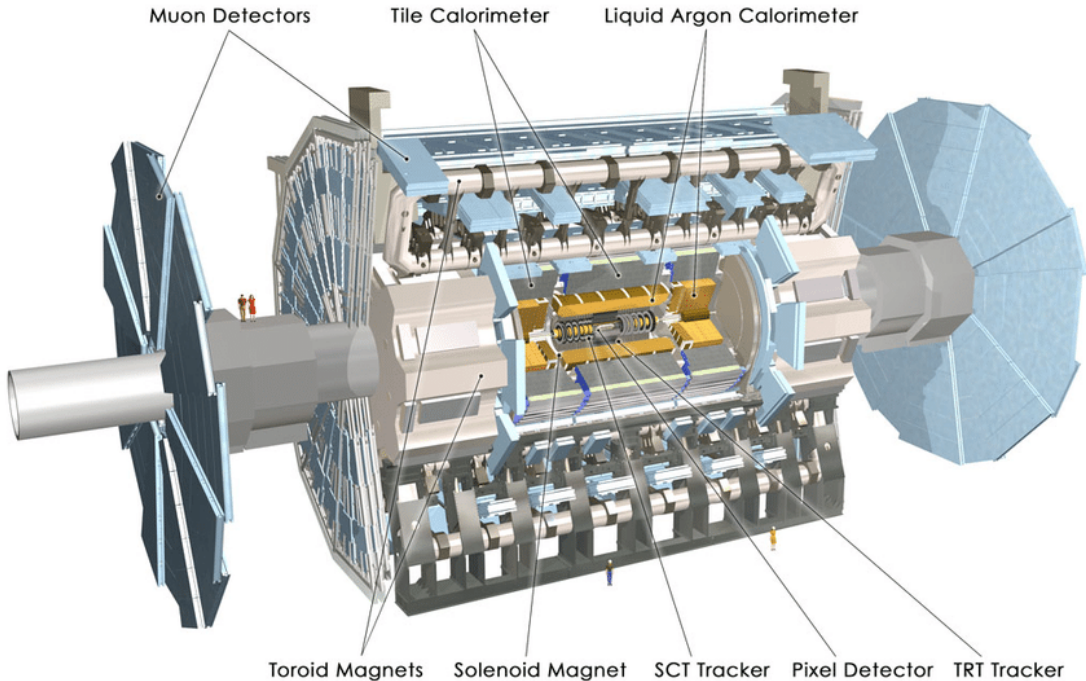


Figure 3.3: A dissected view of the ATLAS detector, a general purpose experiment on one of the LHC beamline interaction points. The Inner Detector, ECAL and HCAL, and the muon spectrometer are shown [85].

3.2.2 The Inner Detector

The Inner Detector is a highly granular sub-detector of ATLAS that operates within a 2 T axial magnetic field generated by a central solenoid made of Al-stabilised NbTi conductor cooled to 4.5 K using liquid helium. The Inner Detector has four independent components: the Insertable B-layer (IBL), the pixel detectors, the Semiconductor Tracker (SCT), and the Transition Radiation Tracker (TRT). Together, these components cover the $\eta < 2.5$ range. Figure 3.4 shows a schematic view of the Inner Detector, excluding the IBL. The Inner Detector provides the most precise momentum resolution compared to the other sub-detectors and enables primary and secondary vertex measurements for tracks with $p_T > 0.5$ GeV by default [85].

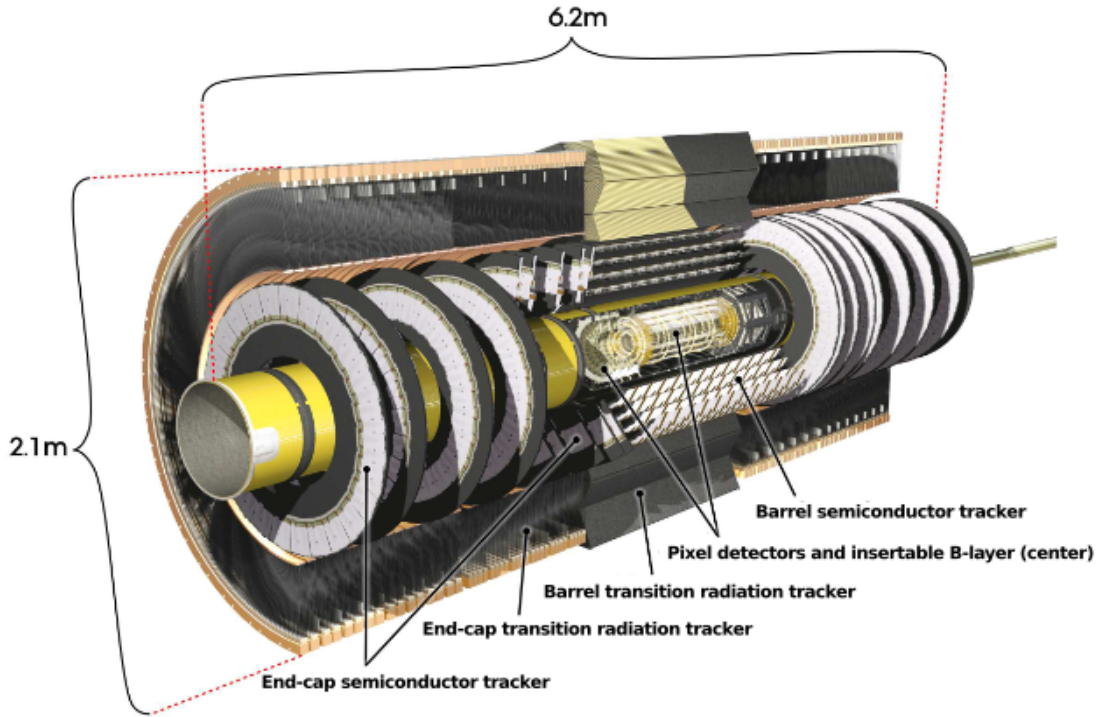


Figure 3.4: An illustration of the Inner Detector, the closest ATLAS sub-detector to the LHC beamline. The barrel and end-cap are visible for the pixel, SCT and TRT. The IBL is not shown but is situated between the beam pipe and the first pixel layer [85].

The sub-components of the Inner Detector are based on two different technologies: silicon semiconductor (IBL, pixel, and SCT) and gas-based straw (TRT). The silicon-based detectors consist of thin layers of semiconductor material doped with impurities. When a particle passes through the material, it creates electron-hole pairs that generate an electrical signal that is read-out using electronic channels. On the other hand, the straw technology is primarily based on the ionisation of gas molecules after collision with an incident particle. The resulting electrons are drifted towards an anode wire located in the centre of the straw tube. In addition, transition radiation produced when a particle passes through a boundary between two materials with different dielectric constants can be detected. This radiation

is proportional to the Lorentz factor, these factors are typically larger for electrons so the amount of radiation can be used to discriminate electrons from hadrons.

During Long Shutdown 1 (2013-2015), a reduction of the radial extension of the beam pipe and the installation of the IBL was carried out. The IBL is an additional layer of pixel based detectors that was installed to address issues related to radiation damage, pile-up, and the increased luminosity during Run-II and Run-III. By reducing the distance between the beam pipe and the lowest sensitive layer of active material to 25.7 mm, compared to the previous distance of 50.5 mm, the impact parameter resolution was maintained, leading to increased b -tagging efficiency over time [96].

The pixel and SCT (strip) detectors are arranged as concentric cylinders around the beamline and as disks perpendicular to the beamline in the end-cap region, as shown in Figure 3.4. The pixel detector is composed of three barrel layers of identically sized pixels ($50 \times 400 \mu\text{m}^2$ in $(r-\phi, Z)$ space) attached to modules ranging from 50.5 mm to 122.5 mm radially outwards from the beamline. There are also three pixel end-cap disks on either side of the barrel ranging from 495 mm to 650 mm in z along the beamline. Each module has 47,232 pixels (46,080 channels), and there are 1744 modules resulting in over 80 million channels for the pixel barrel and end-caps combined. Both the barrel and end-cap have intrinsic accuracies of $10 \mu\text{m}$ in $r-\phi$, while the accuracy in the other available direction (z for barrel, R for end-cap) is $115 \mu\text{m}$.

The SCT is made up of silicon strip modules that vary in size depending on their position. The SCT barrel is composed of four layers ranging from 299 mm to 514 mm in the radial direction and nine end-caps on either side of the interaction point ranging from 839 mm to 2735 mm in z along the beamline. For the SCT, there are 4088 modules with over 6 million read-out channels allowing for an intrinsic accuracy per barrel module of $17 \mu\text{m}$ in $r-\phi$ and $580 \mu\text{m}$ for the barrel z -direction and end-cap r -direction. In a less busy environment, there is less need for such granular precision in the SCT compared to the pixel detector.

The outermost part of the Inner Detector is the TRT, which consists of many layers of straw tubes, totalling around 300,000 tubes with a diameter of 4 mm. The tubes are made of polyimide and contain a gas mixture of xenon, oxygen, and carbon dioxide, with a gold-plated tungsten wire anode in the centre. The TRT is divided into three barrel layers of 96 modules containing up to around 700 straws of 144 cm length and 20 end-cap modules with around 6000 straws of length 37 cm, allowing for over 350,000 channels. The TRT can collect data for particles with $p_T > 0.5 \text{ GeV}$ and $|\eta| < 2.0$, with a minimum of 36 (22 crossed) straw tubes traversed per particle for the barrel (end-cap transition region $0.8 < |\eta| < 1.0$). The track information from the TRT allows for a positional resolution of $130 \mu\text{m}$ per straw tube for particles, which can be used to reconstruct the particle's path accurately.

3.2.3 The Calorimeter

The calorimeter is a critical sub-detector located just outside the Inner Detector. The geometry of the calorimeter has an accordion shape ensuring complete ϕ coverage with no gaps, which is divided into two parts: the ECAL and the HCAL calorimeters arranged as shown in Figure 3.5 [85].

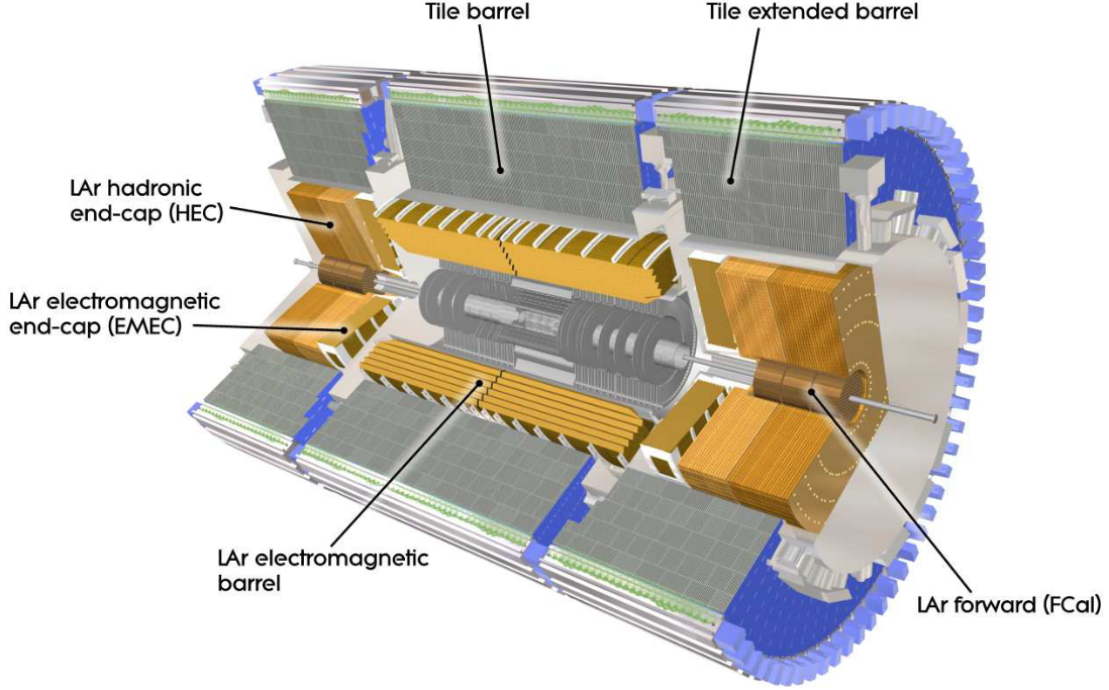


Figure 3.5: A schematic view of the ATLAS calorimeter, showing the ECAL, HCAL, FCAL and their constituent parts [85].

The calorimeter technology works similarly for both the ECAL and the HCAL. When incident particles collide with the calorimeter material, they produce a shower of secondary particles, often resulting in a cascade. An active material is used to measure the energy of the particle shower through ionisation or scintillation. For the ECAL, particles such as electrons, positrons, and photons undergo pair production and bremsstrahlung upon collision, which generates electromagnetic (EM) showers. In contrast, the HCAL detects hadrons such as protons, neutrons, pions, and kaons interacting strongly with the detector material nuclei, causing them to break apart or undergo other types of interactions. To measure the energy, successive layers of dense and active material are used. The dense material is selected to have a suitable radiation length to stop the particle within the calorimeter volume while maintaining high resolution.

The ECAL utilises lead and liquid argon (LAr) cooled to 88 K as the absorber and active material, respectively. In this case, the signal is brought about from ionisation of the active material. The ECAL barrel covers the region $\eta < 1.475$ and is composed of four layers, including a pre-sampler layer. The end-caps cover the region $1.375 < |\eta| < 3.2$ and have

between two and four layers, depending on $|\eta|$. This configuration provides high granularity over the $|\eta|$ range of the Inner Detector ($|\eta| < 2.5$) for precise measurements of electrons and photons. In contrast, coarser granularity in other regions is sufficient for jet (a spray of hadronic activity) and E_T^{MISS} reconstruction. The granularity varies depending on $|\eta|$, but the average cell size in the barrel is $|\eta| \times \phi = 0.025 \times 0.025$. The cell size increases as one moves through the layers. However, the total number of channels is over 110,000 for the barrel and 60,000 for each end-cap.

The HCAL is divided into three parts: the tile calorimeter, the hadronic end-cap calorimeter (HEC), and the forward calorimeter (FCAL). The tile calorimeter consists of a barrel region ($|\eta| < 1.0$) and an extended barrel region ($0.8 < |\eta| < 1.7$), each with three layers kept at near room temperature. Any $|\eta|$ overlap is to increase the material density in the barrel to end-cap transition regions. The active material in the tile calorimeter is plastic scintillator tiles, while the absorber is made of steel. The HEC is located behind the ECAL end-caps and covers the $1.5 < |\eta| < 3.2$ range using four layers. The FCAL is sensitive to the $3.1 < |\eta| < 4.9$ region and is composed of four layers, providing an extension to the detector's $|\eta|$ range. Both the HEC and FCAL use liquid argon as the active material and share the same cryostat with the ECAL end-cap. The absorbers used are copper for the HEC and the first layer of the FCAL (for EM measurements), while the rest of the FCAL uses tungsten as the absorber. The average granularity in the tile and HEC is 0.1×0.1 in $|\eta| \times \phi$, resulting in approximately 25,000 channels combined. The FCAL granularity varies significantly across η and r , but contributes around 7000 channels in total.

3.2.4 The Muon Spectrometer

The MS is the final layer of the ATLAS detector and is responsible for detecting muons, which are able to fully traverse the calorimeter without stopping. The MS is composed of four sections, as shown in Figure 3.6 [85]. All sections use gas mixtures that ionise when a muon passes through the detector, providing an electric signal. These sections are the Monitored Drift Tubes (MDT) (coverage $|\eta| < 2.7$), Cathode Strip Chambers (CSC) (coverage $2.0 < |\eta| < 2.7$), Resistive Plate Chambers (RPC) (coverage $|\eta| < 1.05$), and Thin Gap Chambers (TGC) (coverage $1.05 < |\eta| < 2.7$). For the $|\eta| < 1.4$ range, the barrel toroid provides a magnetic field of 0.5 T, while for $1.6 < |\eta| < 2.7$, the end-cap toroids provide a 1 T magnetic field. In the transition region, a mixture of the end-cap and barrel toroids provide the magnetic field. The MDTs provide precise measurements of the track coordinates over most of the $|\eta|$ range, while CSCs with higher granularity are used at larger $|\eta|$ to cope with the demanding background conditions. The RPCs and TGCs provide muon triggering up to $|\eta| < 2.4$ and have the capability to measure the muon kinematics in the direction orthogonal to that determined by the MDTs and CSCs.

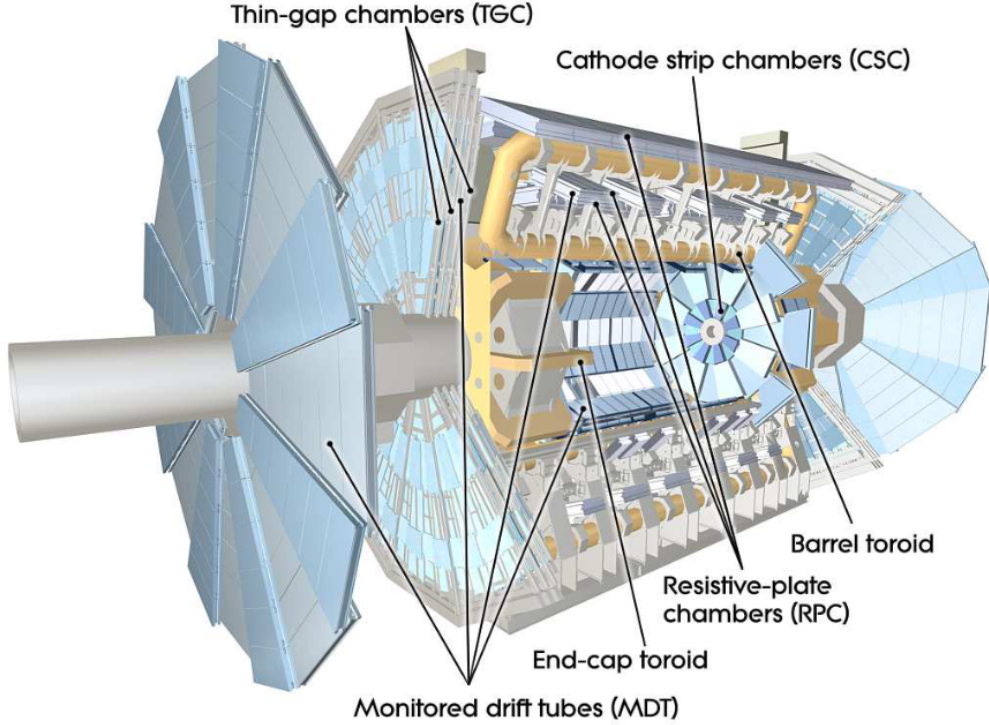


Figure 3.6: The ATLAS muon spectrometer showing the Monitored Drift Tubes and Cathode Strip Chambers used for precision tracking, along with the Resistive Plate Chambers and Thin Gap Chambers used primarily for triggering. The barrel and end-cap toroid magnets can also be seen which provide the bending magnetic field [85].

3.2.5 The Trigger and Data Acquisition System

The ATLAS detector is designed to handle an enormous rate of up to 1.7 billion collisions per second, which would be impractical to process and store entirely. Furthermore, the majority of these collisions are unremarkable low-energy inelastic scattering events. The challenge, therefore, is to effectively reduce the number of events while maintaining a high signal efficiency. The ATLAS data acquisition system accomplishes this through the use of a two-stage trigger system, which ensures quick trigger decisions, read-outs, and storage protocols for important, high-energy scattering events. The TDAQ routine is illustrated in detail in Figure 3.7, and consists of a hardware-based Level-1 (L1) trigger and a software-based High-Level Trigger (HLT).

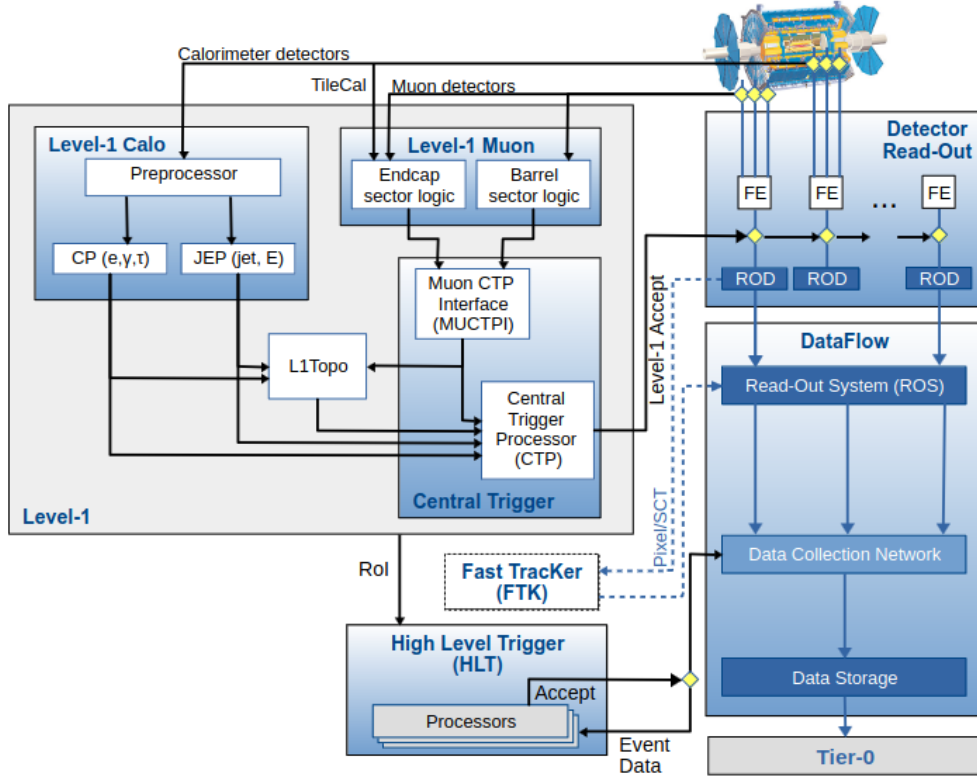


Figure 3.7: The ATLAS data acquisition and trigger system [97] showing the constituent parts of the L1 and HLT triggers used to form a decision on whether to keep the event. The FTK was designed to apply tracks to the HLT at the L1 rate of 100 kHz, this was supposed to be commissioned during Run-II but was later cancelled by ATLAS and was not used for the analyses in this thesis [98].

The L1 trigger system utilises custom electronics to make a rapid decision on whether an event should be retained, using reduced granularity information. The L1 trigger is composed of several components, including the L1 calorimeter trigger (L1Calo), the L1 muon trigger (L1Muon), the L1 topological trigger (L1Topo), and the Central Trigger Processor (CTP). The L1Calo employs signals from the calorimeter, which are calibrated by the Cluster Processor and Jet/Energy-sum Processor (JEP) to identify relevant particles above a programmable threshold. For L1Muon, the TGC and RPC trigger chambers are employed to select muons. The L1Topo trigger then uses information from L1Calo and L1Muon to calculate kinematic quantities and impose selections. The CTP combines this information and recommends a decision, while also defining a ‘region of interest’ (ROI) in $\eta \times \phi$ space for the HLT to examine. With a latency of $2.5 \mu\text{s}$, the L1 trigger system can reduce the event rate from 40 MHz (bunch crossing rate) to around 100 kHz [99]. To maintain this maximum rate, the CTP may apply ‘dead time’, during which no events can be recorded. For every accepted event, the front-end (FE) electronics export data from each sub-detector, which is then sent to the read-out driver (ROD) and read-out system (ROS) for processing, formatting, and buffering. The ROS then transmits the relevant data to the HLT, and accepted events are subsequently saved at ATLAS Tier-0 sites with high levels of disk memory [100].

The HLT decisions consist of a rapid trigger algorithm to quickly reject uninteresting events, followed by a decision based on offline (not in real time) particle reconstruction techniques (detailed in the next section). With its sophisticated algorithms, the HLT is capable of reducing the event rate even further, down to approximately 1 kHz. For analysis, the sequence of algorithms used is referred to as the trigger, which identifies particles of a particular type with a minimum threshold for a given variable, such as p_T . The ATLAS trigger menu provides access to these triggers, which are widely utilised in the analyses presented in this thesis. Appendix C.1 showcases examples of different triggers, along with the corresponding naming conventions.

3.3 Particle Identification and Reconstruction at ATLAS

ATLAS employs a variety of techniques to ensure the accurate reconstruction and identification of objects which interact with the detector. This section describes the signatures and Run-II reconstruction techniques for the main objects used in this thesis: electrons, muons, jets, hadronically decaying (hadronic) taus and E_T^{MISS} . They are reconstructed using the ATHENA offline reconstruction framework, based on the GAUDI framework [101] which is common in High Energy Physics (HEP) experiments. Once each particle candidate is reconstructed, ATLAS combined performance groups provide guidance to analysis teams under which conditions the particles are considered calibrated such that they can be used in physics analyses. The requirements are shown in Table 3.1 and will be explained in detail during this section.

Table 3.1: The basic requirements of the main core physics objects used for the analyses in this thesis, the recommendations are given by the combined performance groups which define the conditions under which the particles are considered calibrated.

Object	Baseline Calibration
e	$ \eta < 2.47$ (excluding the $1.37 < \eta < 1.52$ transition region) $p_T > 10$ GeV, $ \frac{d_0}{\sigma(d_0)} < 5$, $ Z_0 \sin(\theta) < 0.5$ mm ID WP: Medium Jet- e overlap removal applied
μ	$ \eta < 2.7$, $p_T > 10$ GeV $ \frac{d_0}{\sigma(d_0)} < 3$, $ Z_0 \sin(\theta) < 0.5$ mm ID WP: Medium
jet (b -tagged)	$ \eta < 2.5$, $p_T > 20$ GeV, $\Delta R_{\text{jet}} = 0.4$ LooseBad jet cleaning JVT (Tight) > 0.5 (EMPflow), JVT (Medium) > 0.59 (EMTopo) DL1r b -tagging algorithm (70% Eff.) (EMPflow) MV2c10 b -tagging algorithm (70% Eff.) (EMTopo) $ Z_0 \sin(\theta) < 2$ mm (EMPflow)
τ_{had}	$ \eta < 2.5$ (excluding the transition region), $p_T < 20$ GeV, 1 or 3 prongs For the seed jet: $\Delta R_{\text{jet}} = 0.4$, $p_T^{\text{tracks}} > 1$ GeV $ d_0 < 1$ mm, $ z_0 \sin \theta < 1.5$ mm, ID WP when required: Medium (RNN or BDT)
E_T^{MISS}	Objects as defined above $p_T^{\text{tracks}} > 0.4$ GeV

In general, each ATLAS event starts with a primary vertex, this is usually the one with the highest sum of p_T^{track} in the event. The primary vertex must have at least two tracks associated with it, with a minimum p_T^{track} of 0.4 GeV. One can then define the impact parameters d_0 and z_0 which are the distance of closest approach to the primary vertex in the r - ϕ plane and the longitudinal plane, respectively.

3.3.1 Electrons and Muons

The signatures of electrons and muons are very different at ATLAS. The electron should register a track in the Inner Detector and then be stopped in the ECAL displaying an EM shower in the process. Muons should leave a track in the Inner Detector, traverse the entire calorimeter depositing little energy and ultimately be detected in the MS.

Electron and Muon Reconstruction

The reconstruction of electrons takes place within the $|\eta| < 2.47$ region and involves a three-stage process, which is detailed in [102] and summarised here. The calorimeter is divided into towers of size $\Delta\phi \times \Delta\eta = 0.025 \times 0.025$ (the granularity of the second calorimeter layer) and the energy of each tower is evaluated by adding contributions from all calorimeter layers. A sliding window approach [103] is then used to group towers using a 3×5 tower window in $\eta \times \phi$. If the window's energy exceeds 2.5 GeV, it is selected as the seed cluster. The next

stage is track reconstruction, which involves seeding tracks from hits in the Inner Detector layers [104]. A pattern recognition algorithm is used, fitting procedures such as the ATLAS Global χ^2 Track Fitter [105] are employed for $p_T^{\text{track}} > 0.4$ GeV (low p_T tracking is available in ROIs [106]) and ambiguities are solved. Finally, the procedure is completed by evaluating the full size of the cluster and by matching the track candidates to seed calorimeter clusters if they are in close enough proximity in $\eta \times \phi$ space. If multiple tracks are present, an algorithm is used to consider the various properties of the track and the location of the seed cluster. Photons are also reconstructed using this process since they also undergo an EM shower. A further selection is performed based on the electron p_T , the presence of a pixel detector hit, and the secondary vertex information to determine if the particle is an electron.

The Inner Detector, calorimeter and MS are all involved in the reconstruction of muons, as detailed in [107]. The first step is to transform hits in a portion of the MS into small straight line segments, which are then transformed into 3D parabolic track candidates by combining measurements from the precision tracking stations (MDTs and CSCs) and the trigger stations (RPCs and TGCs) that provide the second coordinate. A χ^2 fit is performed on the particle trajectory to incorporate additional hit information, taking into account interactions with the detector and any misalignment, resulting in tracks that can be used in the global muon reconstruction. The tracks in the Inner Detector are reconstructed similarly to the electron case. The complementary track candidates are then combined with calorimeter information to define the five types of muons, which are listed below. If multiple instances of the same muon type are detected, a hierarchy is established with combined muons having the highest priority.

- Combined (CB): Identified by matching an Inner Detector track to an MS track and applying a fitting technique taking into account the energy loss in the calorimeter. Silicon-associated forward (SiF) muons are a subset of CB muons for $|\eta| > 2.5$, where MS tracks may be combined with reconstructed track segments from a smaller amount of pixel and SCT hits.
- Inside-out combined (IO): Reconstructed using an algorithm which extrapolates Inner Detector tracks to the MS and searches for at least three loosely-aligned MS hits. A fit is then applied taking this into account along with the calorimeter information.
- Muon spectrometer extrapolated (ME): For muons where an MS track cannot be matched to an Inner Detector track, the MS tracks are extrapolated to the beamline.
- Segment tagged (ST): Muons where the extrapolation line from the Inner Detector to the MS satisfies some angular requirements to an MS segment. The muon parameters are taken from the Inner Detector track fit for this case.
- Calorimeter tagged (CT): Inner Detector tracks are extrapolated through the calorimeter searching for energy deposits consistent with a muon, the Inner Detector track is then tagged as a muon and the parameters are taken from the Inner Detector track fit.

Electron and Muon Identification

The electron likelihood (LH) discriminant is the primary tool used to evaluate the probability of a reconstructed prompt electron within the fiducial volume of $|\eta| < 2.47$ being a true electron. The LH function is constructed for both signal (prompt electrons) and background (jets that mimic prompt electrons and non-prompt electrons from heavy flavour hadrons) by taking into account the probability distribution functions of various discrimination quantities, which can be found in [102]. The discriminant is then derived from the likelihood, and a transformation is applied to achieve a significant separation between the signal and background for different values of this discriminant. By applying a selection on the likelihood score, one can achieve a desired signal efficiency and background rejection rate. This LH score and some extra criteria on the track properties form the electron likelihood identification (ID) working points (WP): Loose, Medium and Tight.

The Medium working point, as indicated in Table 3.1, has been employed in the analyses presented in this thesis. This working point provides a signal efficiency of 88% at $E_T = 40$ GeV. The efficiency results, which have been obtained from $J/\psi \rightarrow ee$ and $Z \rightarrow ee$ events, are summarised in Figure 3.8. The figure shows that when moving from the Tight to the Medium working point, a 8% improvement in signal efficiency (from 80% to 88%) is observed, and much of the low- E_T efficiency is recovered. To ensure that the electrons are considered to be properly calibrated, two additional requirements related to the impact parameter must be fulfilled. Specifically, $|\frac{d_0}{\sigma(d_0)}| < 5$ and $|Z_0 \sin(\theta)| < 0.5$ mm. These requirements refer to the d_0 significance (d_0 divided by its error) and the shortest longitudinal distance from the track to the primary vertex, respectively.

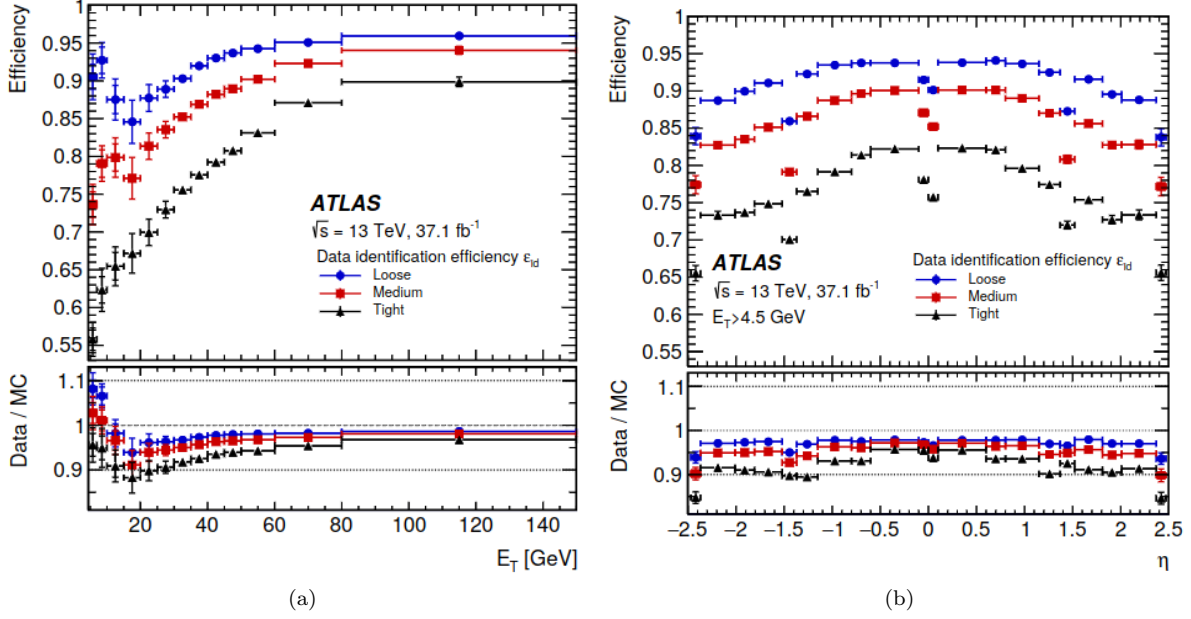


Figure 3.8: The electron identification efficiencies of the Loose (blue), Medium (red) and Tight (black) working points shown as a function of (a) E_T and (b) η for the 2015-16 dataset. The data efficiencies are calculated using $J/\psi \rightarrow ee$ and $Z \rightarrow ee$ data with $Z \rightarrow ee$ simulation. The full procedure is available in [102]. The ratio plot shows the data to simulation ratios.

The identification of muons is available for $|\eta| < 2.7$ and relies on a set of selection criteria that differ from the LH based technique used for electrons. These criteria consider various variables, such as the type of muon, the number of hits in the pixel, SCT and MS, the track fit parameters, and the compatibility of the Inner Detector and MS track. Multiple working points are defined based on these criteria, including Loose, Medium, Tight, High- p_T , and Low- p_T , with the latter two being used in extreme phase spaces. For the analyses in this thesis, the Medium working point was used, which strikes a good balance between high efficiency and small systematic uncertainties on the background rejection. This is demonstrated in Figure 3.9, which represents the efficiency as a function of p_T and $|\eta|$ for the different muon ID working points. Additionally, the impact parameter requirements are $|\frac{d_0}{\sigma(d_0)}| < 3$ and $|Z_0 \sin(\theta)| < 0.5$ mm.

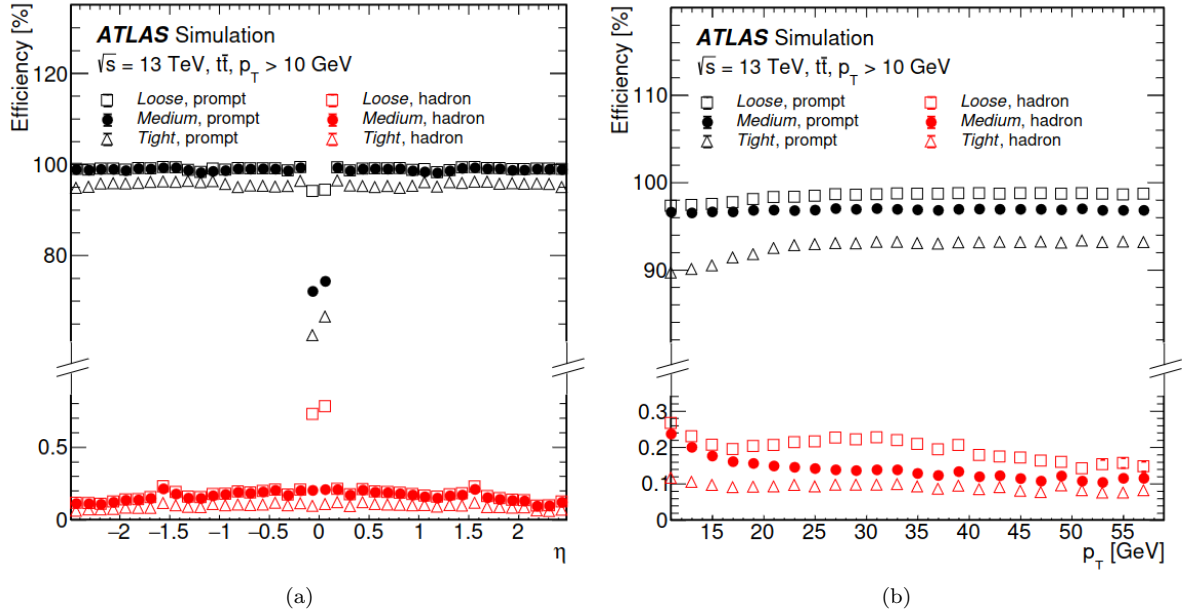


Figure 3.9: The identification efficiency of the muon Inner Detector track for the Loose (square), Medium (circle) and Tight (triangle) working points shown as a function of the (a) $|\eta|$ and (b) p_T of the ID track. The efficiencies are calculated using a sample of $t\bar{t}$ events with $p_T^{\text{tracks}} > 10$ GeV as described in [107]. Efficiencies are shown for simulations of prompt muons and for hadrons to give a representation of the rejection.

The Medium working point only accepts CB and IO muons within the fiducial range of the Inner Detector ($|\eta| < 2.5$). There must be at least three hits in at least two regions (stations) of the MDT or CSC, except for $|\eta| < 0.1$, where muons with otherwise good tracks can have at least three hits in one region. Furthermore, a muon p_T and $|\eta|$ dependent compatibility requirement based on two variables, namely q/p and ρ' , is imposed. These variables measure the compatibility between the ratio of the charge and momentum, and the p_T of the tracks in the Inner Detector and MS, respectively. In regions outside the Inner Detector fiducial range ($2.5 < |\eta| < 2.7$), ME and SiF muons may also be included. In a sample of $t\bar{t}$ events, the majority of the muons that pass the Medium ID criteria are CB muons, accounting for 98% of the prompt muons.

Electron and Muon Isolation

Effective lepton isolation is vital for distinguishing between signal and background events in HEP analyses. This is particularly important for the subsequent chapters of this thesis, as BSM particles, such as heavy Higgs bosons, tend to produce leptons with low surrounding activity. Conversely, leptons that are surrounded by a lot of activity are often not prompt and can be the result of other processes, such as pair production.

The isolation of electrons and muons is determined in a similar way, a threshold is applied on the sum of E_T or p_T^{track} within a cone of size ΔR_{iso} around the candidate cluster or track,

respectively. Where Equation 3.5 is used to determine which objects are within the cone. Calorimetric isolation uses a variable known as $E_T^{\text{topocone-}\Delta R_{\text{iso}}}$ as a threshold. This metric subtracts the energy of the candidate, the energy leakage to other cells attributed to the candidate, and the energy due to pile-up from the total energy of all the topological clusters whose barycentres overlap with a $\Delta R_{\text{iso}} = 0.2$ cone around the candidate cluster, including the candidate itself. As the Inner Detector granularity is much higher than the calorimeter, the chosen value of ΔR_{iso} can be reduced if necessary, as shown by the condition:

$$\Delta R_{\text{iso}} = \min\left(\frac{10 \text{ GeV}}{p_T [\text{GeV}]}, \Delta R_{\text{iso}}^{\text{max}}\right) \quad (3.6)$$

where $\Delta R_{\text{iso}}^{\text{max}}$ is used to set the cone size upper limit. For track isolation, the metric is called $p_T^{\text{cone-}\Delta R_{\text{iso}}}$ for ΔR_{iso} fixed to 0.2 or $p_T^{\text{varcone-}\Delta R_{\text{iso}}^{\text{max}}}$ for a p_T varying cone with maximum value $\Delta R_{\text{iso}}^{\text{max}}$ of 0.2 or 0.3. Moreover, a track-to-vertex association (TTVA) algorithm can be applied to the corresponding tracks in the cone, with a specified p_T threshold as shown in Table 3.2. In the next section, it will be mentioned that particle flow jets combine tracking and calorimeter information into one jet object. Therefore, the tracking and calorimeter cones are considered together when using this jet type, and a new variable $E_T^{\text{neflow-}\Delta R_{\text{iso}}}$ is used to denote the transverse energy of neutral particle flow objects. Table 3.2 presents the lepton isolation working points utilised in the analyses conducted in this thesis for both muons and electrons. The gradient isolation working point differs slightly from the others as it aims to achieve a fixed value for the isolation efficiency (ϵ_{iso}) that is uniform in $|\eta|$ [102].

Table 3.2: The definition of the electron and muon isolation working points used for the analyses in this thesis.

Working Point	Definition
<i>e</i> -isolation	
Gradient	$\epsilon_{\text{iso}} = 0.1143 \times p_T + 92.14\%$ (Track)
	$\epsilon_{\text{iso}} = 0.1143 \times p_T + 92.14\%$ (Calo)
	90 (99) % at 25 (60) GeV (Combined)
FCTight	$p_T^{\text{varcone-20}}(\text{TTVA}(\text{Tight}, p_T^{\text{track}} > 1 \text{ GeV}))/p_T < 0.06$ $E_T^{\text{topocone-0.2}}/p_T < 0.06$
μ -isolation	
FCTightFixedRad	(Track)
	For $p_T < 50 \text{ GeV}$: $(p_T^{\text{varcone-30}}(\text{TTVA}(\text{Tight}, p_T^{\text{track}} > 1 \text{ GeV}))/p_T < 0.04$
	For $p_T > 50 \text{ GeV}$: $(p_T^{\text{cone-20}}(\text{TTVA}(\text{Tight}, p_T^{\text{track}} > 1 \text{ GeV}))/p_T < 0.04$
PflowTightFixedRad	(Calo)
	$E_T^{\text{topocone-0.2}}/p_T > 0.15$
	(Combined)
PflowTightFixedRad	For $p_T < 50 \text{ GeV}$: $(p_T^{\text{varcone-30}}(\text{TTVA}(\text{Tight}, p_T^{\text{track}} > 0.5 \text{ GeV})) + 0.4E_T^{\text{neflow-20}})/p_T < 0.045$
	For $p_T > 50 \text{ GeV}$: $(p_T^{\text{cone-20}}(\text{TTVA}(\text{Tight}, p_T^{\text{track}} > 0.5 \text{ GeV})) + 0.4E_T^{\text{neflow-20}})/p_T < 0.045$

3.3.2 Jets

Jets are the most abundant objects that interact with the ATLAS detector. They are frequently produced from QCD interactions and are also often generated as part of interesting processes. Following high-energy collisions, quarks and gluons are produced initially in an unstable and high-energy state referred to as a parton shower. As per the concept of colour confinement in QCD, free quarks and gluons are forbidden to exist, which results in the generation of additional gluons and quark-antiquark pairs, creating a cascade of particles that leads to a spray of hadronic activity known as a jet. This process is known as hadronisation. Since jets are frequently produced in association with the interesting particles that are targeted by the analyses in this thesis, it is crucial that they are appropriately reconstructed, calibrated, and identified.

During Run-II, the definition of the jet was changed from using topological clusters in the calorimeter to using particle-flow (p-flow) objects that take into account both calorimeter and track information. Since both types of jets are used in the analyses presented in this thesis (topological for Z' studies and p-flow for LQ and the improved analysis), both are discussed in the following sections.

Jet Reconstruction and Calibration

Historically, jets at ATLAS were reconstructed by solely using topological clusters in the calorimeter using an algorithm that takes into account the calorimeter cell signal in comparison to the expected noise for a seed cell and its neighbours [108]. The derived topological clusters are then fed into the anti- k_t jet reconstruction algorithm with a predefined cone size ΔR_{jet} [109], resulting in the reconstruction of ‘EMTopo’ jets. Equation 3.5 is used to define which objects should form part of the jet. To correct for detector effects and ensure a consistent jet energy scale across the detector, the jets are calibrated using various methods. The jet energy scale (JES) is corrected to the predicted particle level energy using simulation, and a jet energy smearing (JER) is included to account for the jet energy response in regions where the simulation resolution is small. Various jet cleaning algorithms are also applied to remove spurious or anomalous signals [110]. To mitigate the effects of pile-up, the jets can be matched to a vertex using the Jet Vertex Tagger (JVT) [111], which is a multivariate discriminant that uses tracking information to segregate jets from pile-up using three defined working points corresponding to a selection of the JVT score: Loose, Medium, and Tight.

The p-flow algorithm [112] starts with a stringent tracking criteria, requiring at least 9 hits in the silicon detectors, and no missing pixel hits when they are expected. The advantage of this algorithm is that it uses the superior energy resolution of the Inner Detector for low-energy charged particles and can therefore detect particles with a minimum p_T^{track} of 0.4 GeV. These objects share many similarities with EMTopo jets as they are also calibrated at the EM scale and use the anti- k_t algorithm, they are referred to as ‘EMPflow’ jets. The change to EMPflow jets has led to an order of magnitude better suppression of pile-up and substantial improvements in angular and p_T resolution [112].

The EMPflow and EMTopo jets are defined using the $\Delta R_{\text{jet}} = 0.4$ size parameter, as shown in Table 3.1. The calibration is conducted using the methods outlined above. To further reduce fake jets, a jet cleaning algorithm with the ‘LooseBad’ working point, as defined in [113], is applied. The JVT working point used depends on the type of jet. For EMTopo jets, the Medium working point with a JVT score of 0.59 is used, while for EMPflow jets, the Tight working point with a JVT score of 0.50 is used. The calibrated jets used for b -tagging in the following sections need to have a p_T greater than 20 GeV and $|\eta| < 2.5$.

Jet b -tagging

Jets originating from the hadronisation of b -quarks (B -hadrons) can be identified based on their experimental signatures. The resulting B -hadrons have a relatively long lifetime of approximately 1 picosecond, which leads to the production of displaced vertices and large impact parameters $|d_0|$ and $z_0 \sin \theta$. The collimated nature of the quark-initiated jet and the fact that many B -hadrons decay to c -quark containing D -hadrons can also provide valuable information when selecting b -jets.

To identify jets originating from b -quark hadronisation, several low-level algorithms are utilised to exploit the signatures of the b -jets. The impact parameter based algorithms IP2D and IP3D [114] are discriminators based on $|\frac{d_0}{\sigma_{d_0}}|$ and $|\frac{z_0 \sin \theta}{\sigma_{z_0 \sin \theta}}|$. The RNNIP [115], is a neural network (described in Section 7.3.2) used for learning track-impact parameter correlations. Additionally, the SV1 [116] and JetFitter [117] algorithms are used to reconstruct the secondary vertex and the b -to- c decay chain, respectively. The output quantities of these low-level algorithms, as well as other variables such as p_T^{jet} and $|\eta^{\text{jet}}|$, are fed into multivariate classifiers, such as neural networks, to output the probability of the jet originating from a b -quark.

In this thesis, two b -tagging algorithms are used, MV2c10 [118] and DL1r [119]. The MV2c10 algorithm uses EMTopo jets as inputs, while DL1r uses EMPflow jets. Figure 3.10 illustrates a comparison between the DL1r and MV2c10 b -tagging algorithms, with DL1r showing significantly better performance. The DL1r algorithm employs a feed-forward neural network (NN) classifier, while MV2c10 utilises boosted decision tree (BDT) classifiers as described in [118]. In general, neural networks outperform BDTs for complex, non-linear data by learning its features rather than using optimised decision trees. Additionally, the inputs to each algorithm differ, with the RNNIP low-level algorithm being newly introduced as an input.

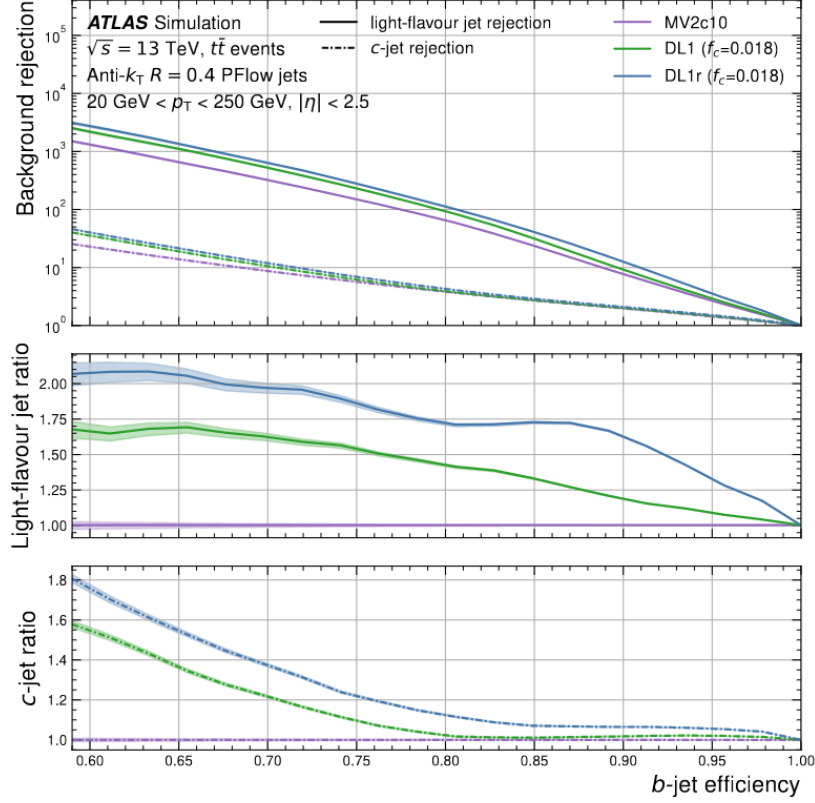


Figure 3.10: A comparison of the jet b -tagging algorithms available at ATLAS [119]. The total background, light flavour and c -jet rejection factors as a function of the b -jet efficiency tested against $t\bar{t}$ events are presented. Results are compared between the MV2c10 (purple), DL1 (green) and DL1r (blue) algorithms, where DL1 is similar to DL1r but doesn't include the RNNIP low-level input.

For this analysis, a Medium working point with a fixed efficiency of 70% is used for both MV2c10 and DL1r algorithms. The rejection factor is a commonly used figure of merit which is defined as the reciprocal of the fraction of background events which are labelled as b -tagged jets. The Medium working point provides rejection factors of 300 (9) for MV2c10 and 600 (11) for DL1r against light-jets (c -jets).

3.3.3 Hadronically Decaying Taus

Tau leptons which decay hadronically make up 65% of all tau decays, they are the main objects used for the analyses in this thesis. The tau candidate is only reconstructed based on its visible decay products and is therefore sometimes referred to as $\tau_{\text{had-vis}}$. A hadronic tau produces a narrow jet with an odd number of tracks, called prongs, emerging from a displaced common vertex. These distinctive features are used to distinguish hadronic taus from their largest background, which are quark or gluon-initiated jet fakes. However, electrons can also mimic 1-prong hadronic taus, due to their similar signature in the detector.

Tau Reconstruction

In order to act as seeds for tau reconstruction, jets must satisfy certain requirements: ΔR_{jet} must be 0.4, $p_T > 10$ GeV, and $|\eta| < 2.5$ (excluding the transition region). The tau vertex is defined as the candidate track vertex with the largest sum of p_T^{track} within a ΔR cone of 0.2 around the seed jet. To be associated with the tau vertex, tracks must have $p_T > 1$ GeV and meet a requirement for the number of Inner Detector hits. Additionally, the impact parameter requirements are $|d_0| < 1.0$ mm and $|z_0 \sin \theta| < 1.5$ mm [120]. The tracks are classified as either core tracks ($0 < \Delta R < 0.2$) or isolation tracks ($0.2 < \Delta R < 0.4$) depending on their distance from the jet. For optimal performance, the topological clusters used to derive the jets are calibrated to the local hadronic (LC) scale, which is available for some particles. This results in ‘LCTopo’ jets, which have better performance in tau reconstruction than EMTopo jets, since the EM scale has a non-linear response to hadronic activity [121]. The local calibration uses corrections based on the cluster shape, energy, and η , taking into account the effects of hadronic interactions in the calorimeter. In addition to the LC calibration with pile-up subtraction, a tau-specific calibration called ‘tau particle flow’ is used to correct for energy deposition in the detector [120]. This calibration corrects the energy to the average value carried by the visible part of the tau at the generator level. As shown in Table 3.1, to be considered calibrated by the combined performance groups, the hadronic tau candidates are recommended to have $p_T > 20$ GeV.

Tau Identification

Since the signature of a hadronic tau is a jet in its own right, the accurate and consistent separation of hadronic taus from QCD based gluon jets or quark jets is a difficult but essential requirement. For the lesser problem of electron fakes, one method to deal with these is to reject hadronic taus close to electrons which also pass the electron LH discriminant, another way is to use the ATLAS electron veto BDT [122].

Similar to the b -tagging methods discussed before, the reconstructed taus are tested using a multivariate technique. The technique employed varies depending on the specific analysis, but for some studies in this thesis, a BDT-based tau ID [123] was used. However, newer analyses have superseded this method with a recurrent neural network (RNN) [124]. The variables used in these classification models are categorised into high and low-level. Low-level variables represent the raw detector measurements, such as the cluster depths and radial or longitudinal extensions, before any algorithmic treatment. In contrast, high-level variables are typically combinations of low-level variables and are more physically meaningful to physics analyses, such as the p_T of the original seed jet or the maximum ΔR between the core tracks and the tau direction axis. The BDT method utilised an array of high-level variables, while the RNN incorporated both high and low-level variables. To improve the accuracy of tau identification, both the BDT and RNN models were trained separately for 1-prong and 3-prong taus.

The RNN is similar in some ways to the feed-forward NN discussed in Section 7.3.2, but it can process sequential data of varying length and has the ability to retain some memory of

previous inputs, as explained in [124]. The inputs to the network are high-level variables, similar to those used in the BDT, as well as sequences of up to 10 tracks and 6 clusters associated with the tau, ordered by p_T and E_T , respectively. A mixture of shared layers and LSTM (Long Short-Term Memory) layers [125] are used to incorporate contextual information from the multiple tracks and clusters. The trained neural network finally outputs a probability of a jet being a hadronic tau using the information from the input high and low-level variables.

A number of tau ID working points are defined in [123, 124] which are fixed points of true τ_{had} efficiency and background rejection for analyses to choose between based on their needs. For the analyses presented in this thesis, both the BDT and RNN algorithms use the Medium ID working point, which achieve a true τ_{had} efficiency of 55% (40%) for 1-prong (3-prong) taus for the BDT and 75% (60%) for the RNN. These efficiencies correspond to quark and gluon jet rejections of 35 (240) for 1-prong (3-prong) taus, where the rejection factors are defined in a similar way to the rejection factors mentioned in Section 3.3.2. Figure 3.11 illustrates the rejection as a function of the efficiency for a set of $\gamma^* \rightarrow \tau\tau$ signals in a di-jet background sample, demonstrating the improved RNN rejection power over the BDT. Specifically, the RNN algorithm achieves a 75% improvement over the BDT for $30 \text{ GeV} < p_T^{\tau_{\text{had}}} < 50 \text{ GeV}$ and over 100% improvement for higher values of $p_T^{\tau_{\text{had}}}$. Additionally, the figure shows the available working points.

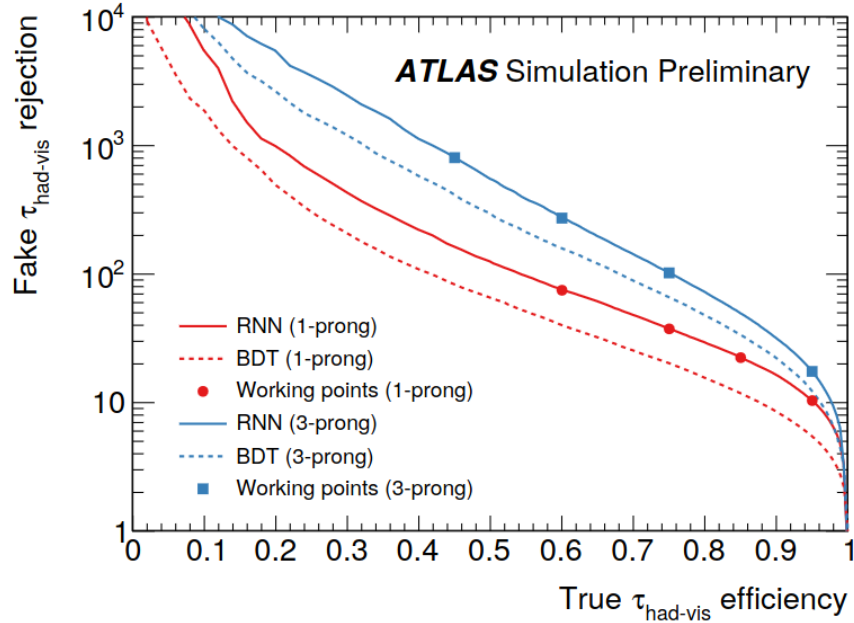


Figure 3.11: A comparison of the ATLAS tau ID algorithms [124], showing the background rejection as a function of the real hadronic tau efficiency. Results are shown for 1-prong (red) and 3-prong (blue) taus for the RNN (solid) and BDT (dashed) algorithms used for tau identification. The solid squares and circles represent the RNN Loose, Medium and Tight working points used by the analyses.

3.3.4 Missing Transverse Energy

The E_T^{MISS} associated with an event provides evidence that invisible particles, such as neutrinos or some BSM particles, have traversed the detector. However, determining E_T^{MISS} accurately is challenging as it requires the precise measurement of all objects originating from the hard scatter. The E_T^{MISS} can be derived using the following equation:

$$E_T^{\text{MISS}} = - \sum_{\substack{\text{selected} \\ e}} p_T^e - \sum_{\substack{\text{accepted} \\ \gamma}} p_T^\gamma - \sum_{\substack{\text{accepted} \\ \tau_{\text{had}}}} p_T^{\tau_{\text{had}}} - \sum_{\substack{\text{selected} \\ \mu}} p_T^\mu - \sum_{\substack{\text{accepted} \\ \text{jets}}} p_T^{\text{jet}} - \sum_{\substack{\text{unused} \\ \text{tracks}}} p_T^{\text{track}} \quad (3.7)$$

where all the terms except the last one are referred to as hard terms [126]. The final term is known as the soft term and it represents all the Inner Detector tracks from the hard scatter vertex that pass the reconstruction and kinematic selection criteria, and are not associated with any objects from the hard scatter. The soft term is obtained using the Track-based Soft Term (TST) algorithm described in [127]. To ensure the hard objects are unambiguous and prevent double counting, an ambiguity resolution procedure is implemented, which ensures that no signals are shared between objects.

3.4 ATLAS Simulation

Simulation is an indispensable tool for conducting physics analyses and has significant implications for calibration and discovery at ATLAS. In this thesis, the findings are based on physics objects that have been calibrated using simulations. However, the primary use of simulations is in the generation of SM and BSM samples, which are simulated and compared to data to draw conclusions. To achieve this, a simulation is performed for every possible background and considered signal process, typically using the Monte Carlo (MC) simulation technique. Monte Carlo simulation employs random numbers to accurately model the complex variables involved in the events, resulting in a reliable simulation when considering many events [128].

To construct a sample, event generators such as SHERPA [129, 130], POWHEG-Box [131], AMC@NLO (MADGRAPH) [132], and other similar tools are used to generate the matrix element which determines the cross-section of a decay. The matrix element is usually computed by first generating the Feynman diagrams at a certain order in perturbation theory, such as leading order, next-to-leading order (NLO), or next-to-next-to-leading order (NNLO). Parton distribution function (PDF) sets are provided to the matrix element generator to describe the parton content of the protons involved in the collisions. Next, simulations of the parton shower (PS), hadronisation, initial and final state radiation (ISR, FSR), and the additional hadronic activity from the underlying event are performed. For this thesis, the phenomenological models for these processes are typically implemented using PYTHIA 8 [133] with the A14 tune [134]. In some cases, they are also integrated into the event generator itself, as is the case for SHERPA-based samples.

After simulating the physics process at the truth level (generator level), the inefficiencies of the detector can be modelled using the GEANT4 package [135]. This package incorporates

the active material, detector geometry, and the signal output from the electronics, as if it were a real event. However, simulating samples using the full GEANT4 package (known as full simulation) can be time-consuming, especially due to the complex interactions with the calorimeter that dominates the simulation time. To speed up the process, the ATLFast-II [136] fast simulation technique can be used, reducing the simulation time by an order of magnitude. In this case, a simplified detector description is used, the default usage of fast simulation is to reduce the complexity only for the calorimeter simulation.

A typical analyser may produce a batch of fast simulation samples with different signal masses and validate these against one full simulation sample with a specific mass point. Once the full or fast simulation campaign is complete, a sample is produced and ready for particle reconstruction using the ATHENA framework utilising the principles described in the previous section.

3.5 Analysis Workflow at ATLAS

After setting up the simulation procedure, the ATLAS distributed analysis infrastructure is used to process the large amounts of simulation and data. Each instance of event processing is known as a job, the PANDA workload management system [137] takes the users job and splits it accordingly into smaller tasks ready for allocation to an ATLAS computer core. The computer node is provided by the Worldwide LHC Computing Grid (WLCG) which houses around 1.4 million cores and handles around 2 million tasks per day [137].

In order to produce usable samples for analysis, the following steps are taken. For data, triggered events are stored in a RAW data format, which is then fed directly into the ATHENA reconstruction software to generate an Analysis Object Data (AOD) sample format [138], using the ATLAS event data model (EDM) [139]. The AODs are significantly slimmed, representing only a few percent of the size of the input, but they contain everything necessary to calibrate and use the required physics objects. As shown in Figure 3.12, the AODs can be slimmed further and then used for physics analysis.

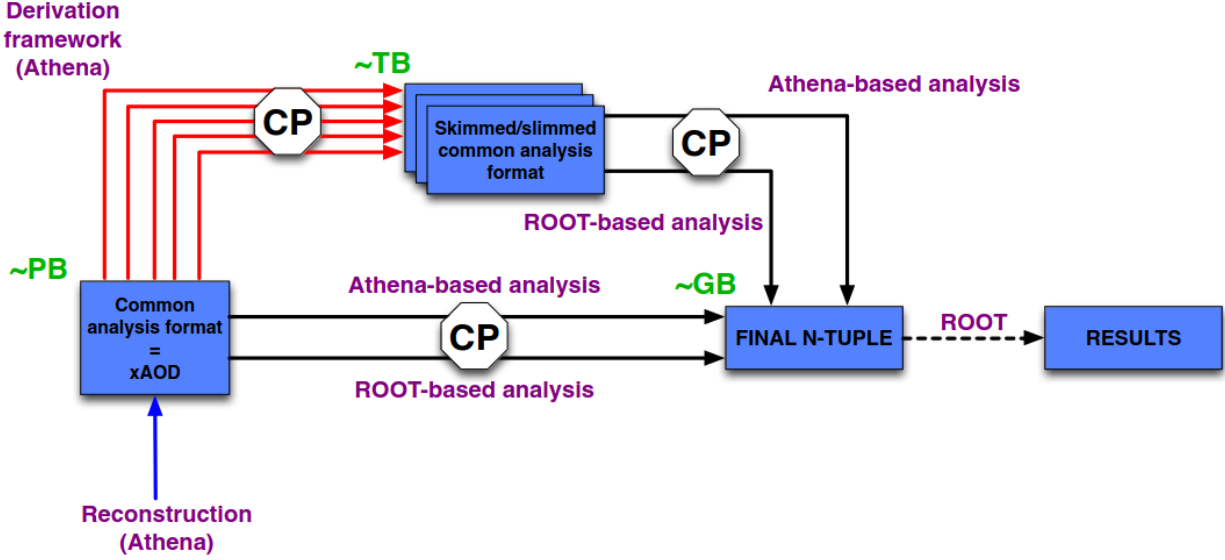


Figure 3.12: The Run-II ATLAS analysis model taken from [138]. The samples are firstly arranged as AODs and the combined performance groups recommend the calibrations at which the physics objects are useable. The calibrations are applied to either the DAOD or AOD to produce n-tuples ready for analysis.

In the case of simulation, the event generation typically generates an EVNT file containing the truth record in the standardised HepMC format [140]. Then, one can choose to simulate the detector response using GEANT4 or use only the truth information by generating a TRUTH sample (as done for systematic studies in later chapters). When simulating the detector response, the EVNT files are converted into HITS files, which include the effect of energy deposits in the detector and its resulting response. A digitisation step then takes place. After these steps, the simulated events are in a state almost identical to the RAW files from data and can therefore be passed through the ATHENA reconstruction framework.

To efficiently handle the large amount of data produced by the AOD format, a slimmer format called the Derived Analysis Object Data (DAOD) is used. The DAOD is about 1% of the size of the AOD, reducing the storage from petabytes to terabytes. The AOD and DAOD generation are handled centrally since they apply to many analyses. Once the DAOD is generated, it is fed into the xTAUFRAMEWORK software, which is a DAOD to n-tuple conversion software designed primarily for tau-based analyses. The xTAUFRAMEWORK performs a loose preselection and outputs flat n-tuples with all the necessary calibrations and systematic uncertainties recommended by the combined performance groups. The n-tuples are designed to be used within the ROOT [141] software infrastructure, which is commonly used in HEP. The n-tuples are typically several gigabytes in size and consist of TTrees [142], which are a ROOT class implementation which provide easy access to the particle kinematics for each event.

The entire chain of simulation to useable flat n-tuple can take many months, even for fast simulation. The DAOD to n-tuple step, in particular, can take around a month for all signal and background samples considered in this thesis. After the n-tuples are generated, they are fed into analysis-specific frameworks for investigation.

To address the higher integrated luminosity in Run-III and beyond, a new protocol has been developed, aimed at reducing the disk requirements and management [143]. This protocol involves reducing the size of the DAOD by removing many of the low-level variables used by some analyses for systematic studies and calibrations [143]. The number of DAOD formats will also be reduced, with two new formats named DAOD_PHYS and DAOD_PHYSLITE being introduced. DAOD_PHYS, with a disk space requirement of 70 kB per event, will have significantly less track, trigger, and MC generator information compared to the current DAOD format, which requires 100 kB per event. On the other hand, DAOD_PHYSLITE will only take up 10 kB per event and will house already calibrated physics objects, making it suitable for non-precision-based analyses such as the ones in this thesis. To address the disk space requirements of the current AOD format, which contains around 600 kB per event, they will be moved to tape storage and reintroduced using a carousel system if they are needed by an analysis. With these changes, if one translated the disk usage at the end of Run-II and replaced it with this configuration, the disk usage is reduced by around 35%. The changes required pose challenges for downstream frameworks which generate n-tuples from the reduced format. To handle the new DAOD_PHYS format, the author was involved in updating the XTAUFRAMEWORK to accommodate the new format.

Chapter 4

Searching for Neutral MSSM Higgs Bosons in the $\tau\tau$ Final State - Analysis Techniques

This chapter outlines the key techniques used to perform the original work in this thesis, these are mainly taken from the 2020 MSSM $H/A/h \rightarrow \tau\tau$ (legacy) search [8] performed on the full Run-II ($L_{int} = 139 \text{ fb}^{-1}$, $\sqrt{s} = 13 \text{ TeV}$) dataset. The legacy analysis is part of a long line of smaller dataset searches from the ATLAS, CMS, CDF and DØ collaborations which form the basis for this analysis [57, 144–148].

The primary focus of this chapter is the $\tau_{\text{lep}}\tau_{\text{had}}$ channel. However, the results from the $\tau_{\text{lep}}\tau_{\text{had}}$ and $\tau_{\text{had}}\tau_{\text{had}}$ combination are also discussed towards the end. The entire analysis chain for this channel is regenerated for explanatory purposes as many concepts from this analysis are applied to the analyses described in the upcoming chapters with only minor modification.

4.1 Analysis Strategy

As described in Chapter 2, a natural extension to the SM could involve the existence of MSSM Higgs bosons where the branching fraction to taus and b -quarks is enhanced for large $\tan\beta$. There are several reasons why searching in the $\tau^+\tau^-$ final state can be beneficial. Firstly, a relatively high percentage (6.3%) of SM Higgs Bosons will decay to two oppositely charged tau leptons, the highest branching ratio among all leptons. The di-tau signature is relatively easy to distinguish from background regardless of the resulting neutrinos escaping the detector. These factors mean that the $\tau^+\tau^-$ channel is currently the most sensitive channel when searching for MSSM Higgs bosons. The $b\bar{b}$ channel should also be enhanced in the MSSM and has a much higher SM Higgs branching ratio than the $\tau^+\tau^-$ channel. The much lower sensitivity of the $b\bar{b}$ channel is shown in Figure 2.4 and is due to the complicated background composition. One of the major backgrounds comes from QCD multi-jet events, these events easily mimic the expected signal and are produced copiously at the LHC making them difficult to model using MC simulation. As a result, the lower trigger thresholds are

also significantly increased for this analysis relative to the $\tau^+\tau^-$ channel which also reduces the impact at low signal masses.

The two LO contributions to the $H/A/h \rightarrow \tau\tau$ process relevant to this analysis are shown in Figure 4.1. The contributions are gluon-gluon fusion (ggH) and b -associated production (bbH), where bbH can be computed using two different schemes in which the b -quark can be encoded within the QCD description of pp collisions. These schemes are called the four and five flavour schemes, each one supports issues which arise in different kinematical regimes. For the four flavour scheme [149, 150], the b -quark never appears in the initial state and is considered to be a massive object where mass effects are considered at any order. For the five flavour case [151], the b -quark is treated as a light parton with a b -quark PDF, meaning it is included in the initial state with an equal footing to the other quark flavours. These distinctions are necessary since gluon splitting to $b\bar{b}$ pairs introduces logarithmic contributions to the cross section which dominate at high energy scales where mass effects become negligible. In this case, the five flavour scheme is more accurate since large logarithms are resummed into the b -quark PDF giving more stable predictions [152]. At energy scales close to the production threshold of the b -quarks, mass effects become important and the four flavour scheme is more accurate. The four flavour scheme cross section is known up to NLO and the five flavour scheme is known up to NNLO. At these precisions, the two computations often disagree by a sizeable amount over a rather wide range of energy scales [152]. As a result, the benefits of each scheme are exploited by combining them using a matching techniques known as Santander matching. This performs a weighted average between the two schemes depending on the considered Higgs mass [153–155].

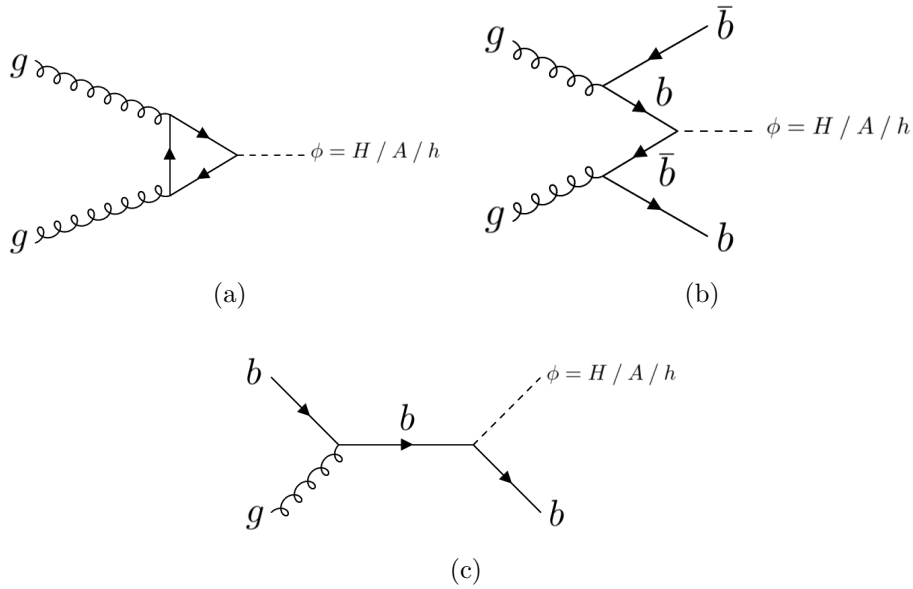


Figure 4.1: Leading order Feynman diagrams for $H/A/h$ production. Diagrams are shown for (a) gluon-gluon fusion and b -associated production in the (b) four flavour scheme [151] and (c) five flavour scheme [149, 150].

To isolate the bbH signal, the analysis is split into b -veto (no b -jet in the event) and b -tag (at least one b -jet in the event) categories. Therefore, the b -tag category will have some sensitivity to the enhanced MSSM Higgs branching fractions to b -quarks. The analysis is further divided into the purely hadronic and semi-leptonic decay modes. This leads to the $\tau_{\text{lep}}\tau_{\text{had}}$ and $\tau_{\text{had}}\tau_{\text{had}}$ channels with a branching ratio of 46% and 42%, respectively. The $\tau_{\text{lep}}\tau_{\text{lep}}$ channel has been neglected for all ATLAS Run-II MSSM $H/A/h \rightarrow \tau\tau$ analyses. In Run-I, the $e\mu$ final state was considered but it has a negligible impact on the results due to the small branching ratio [156].

To accurately estimate the background, control regions (CR) with low signal contamination are defined, as described in Section 4.5. Once the background is well understood and validated in separate validation regions (VR), a fitting technique, discussed in Section 4.7, is used to determine whether evidence of signal is present in the data.

Various software packages specific to ATLAS are employed for the analysis. The xTAUFRAMEWORK is used to slim the DAOD to flat n-tuples (described in Section 3.5) which serve as the analysis inputs. The n-tuples are then processed by the BSMTAUTAUCAF analysis framework, the analysis regions are defined and the pre-fit histograms are arranged into ROOT files using this software. These files are then used as inputs to WSMAKER, which utilises ROOFIT to perform the statistical analysis. Finally, a variety of software tools can be used to visualise the results.

4.2 Data Samples and Monte Carlo Simulation

For the ATLAS data samples, a selection criterion is applied to ensure that only data collected under favourable conditions was used. In the case of HLT timeouts or software errors, the affected data events were directed to a debug stream for further analysis. However, no such events were found to be relevant for this analysis, or for any of the analyses in the subsequent chapters.

The signal and background samples are generated using MC simulation as described in Section 3.4. Table 4.1 provides information on the chosen simulation techniques for each sample. The table columns denote the employed generator, PDF set, the underlying event, parton showering and hadronisation (UEPS) model, and the order at which the cross-section is calculated ($\mathcal{O}(\sigma)$). More information on the generation of the samples and the recipes used to calculate the cross-sections can be retrieved from the attached citations in the table. Diboson background events account for $VV/V\gamma^*$ events, where V is either a W or Z boson. All samples except for the bbH signal use the full GEANT4 software to simulate the effect of the detector [135]. The bbH generator outputs a non-negligible amount of negative weights, for example, inspection of a bbH 2500 GeV n-tuple file found around 40% of the events had negative weights. Therefore, to get an accurate yield, more events must be processed to compensate. For a 2500 GeV signal, over double the amount of bbH events are generated compared to ggH . The ATLFast-II fast simulation is utilised for the generation of bbH samples [136].

Table 4.1: The samples involved in this analysis. The table shows the event generator, PDF set, the software which provides the underlying event, hadronisation and parton showering models (UEPS), and the order at which the cross-section is determined ($\mathcal{O}(\sigma)$). The NNLL acronym stands for next-to-next-to-leading-log order.

Process	Generator	PDF	UEPS	$\mathcal{O}(\sigma)$
SM Backgrounds				
$Z/\gamma^* \rightarrow \tau\tau + \text{jets}$	POWHEG-Box v1 [131, 157–159]	CT10 [160]	PYTHIA 8.1 [161]	NNLO [162]
$W + \text{jets}$	SHERPA 2.2.1 [130]	NNPDF 3.0 NNLO [163]	SHERPA 2.2.1 [164]	NNLO [162]
$t\bar{t}$	POWHEG-Box v2 [131, 157, 158, 165]	NNPDF 3.0 NNLO	PYTHIA 8.2 [133]	NNLO+NNLL [166–171]
Single t-quark	POWHEG-Box v2 [131, 157, 158, 172–174]	NNPDF 3.0 NNLO	PYTHIA 8.2	NNLO+NNLL [175, 176]
Diboson	SHERPA 2.2.1 OR SHERPA 2.2.2	NNPDF 3.0 NNLO	SHERPA 2.2.1 OR SHERPA 2.2.2	NLO [129, 177]
BSM Signals				
bbH	MG5_AMC@NLO 2.1.2 [132, 178]	CT10	PYTHIA 8.2	NLO/NNLO [149–151, 153, 154]
ggH	POWHEG-Box v2 [131, 157, 158, 179, 180]	CT10	PYTHIA 8.1	NLO/NNLO [181–195]

For the BSM signals, the Yukawa couplings of the Higgs bosons are calculated using FEYN-HIGGS [196–202], branching ratios are determined by following the recipe outlined in [203]. The MSSM cross-sections and branching fractions are calculated using the LHC Higgs cross-sections handbook [204].

4.3 Event Selection

An event is defined as having at least one primary vertex with two associated tracks (as outlined in Section 3.3). When multiple vertices are present, the one with the highest sum of p_T among its tracks is chosen as the hard scatter vertex. The first two particles with the highest p_T are considered to have originated from the hard scatter, this is the most likely scenario after pile-up mitigation techniques are employed.

4.3.1 Removal of Geometrically Overlapping Objects

Overlap removal (OLR) is a crucial step before the selection of interesting events. A given particle in the detector can be reconstructed using multiple different algorithms and enter more than one particle container. For example, a tau particle can enter the tau container and the jet container since a jet seed is used to reconstruct a tau. For this reason, when two particles are geometrically very close in the detector, it is essential to label the particle accurately and remove the duplicate to avoid double counting. The proximity between two objects is defined by Equation 3.5, this metric is typically used across most ATLAS analyses to perform OLR by rejecting certain objects if they fall within a cone of size ΔR_{OLR} of another. This analysis employs a manually derived OLR across all channels, as detailed in Table 4.2. The OLR works with the loosest objects available in the analysis with no tau identification applied, these objects are detailed in the next section.

Table 4.2: The manually derived OLR used for this analysis, it is a crucial step in order to remove duplicate objects in an event.

Reject	Keep	Manual OLR Criteria
τ_{had}	e	$\Delta R_{\text{OLR}} < 0.2$
τ_{had}	μ	$\Delta R_{\text{OLR}} < 0.2$
e	μ	$\Delta R_{\text{OLR}} < 0.2$
j	e	$\Delta R_{\text{OLR}} < 0.4$
j	μ	$\Delta R_{\text{OLR}} < 0.4$
j	τ_{had}	$\Delta R_{\text{OLR}} < 0.2$

4.3.2 Triggering and Defining the $\tau_{\text{lep}}\tau_{\text{had}}$ Signal Region

In order to accurately model the data with simulation, it is necessary to match simulated physics objects to the HLT objects that triggered the event. In the $\tau_{\text{lep}}\tau_{\text{had}}$ channel, events are triggered using unprescaled single electron or muon triggers. Prescaled triggers are often used in ATLAS to reduce the trigger rate where necessary, the prescaling is performed by accepting 1 out of every n events, where n is the prescale. For the analyses in this thesis, un-prescaled triggers are used meaning that every event which passed the trigger was accepted. The trigger threshold varies depending on the beam conditions during data collection. The lowest p_T threshold for the electron trigger during the 2015 data taking period was $p_T^e > 24$ GeV, requiring the electron to pass the Medium LH ID requirement. During the 2016-2018 data taking period, the lowest p_T threshold was $p_T^e > 26$ GeV with a Tight LH ID requirement and Loose isolation requirement [205]. For muons, the lowest threshold was $p_T^\mu > 20$ GeV with a Loose isolation ($p_T^\mu > 26$ GeV with a Medium isolation) requirement for the 2015 (2016-2018) data taking period [206, 207]. The complete trigger list for each data taking period can be found in Appendix C.1.

In the $\tau_{\text{had}}\tau_{\text{had}}$ channel, unprescaled single tau triggers are used, with $p_T^{\tau_{\text{had}}}$ thresholds at 80 GeV and 160 GeV for the lower and higher thresholds, respectively [206, 207]. This has ramifications on the final results in Section 4.7 as it typically means the acceptance to lower resonance mass signals is reduced for the $\tau_{\text{had}}\tau_{\text{had}}$ channel compared to $\tau_{\text{lep}}\tau_{\text{had}}$.

The core physics objects in this analysis are selected based on the combined performance recommendations detailed in Section 3.3. A summary of these recommendations for each object used can be found in Table 3.1. The minimum p_T requirement for utilising calibrated physics objects is determined by the recommendations, trigger requirements, and the expected signal. For the $\tau_{\text{lep}}\tau_{\text{had}}$ channel, a $p_T^\ell > 30$ GeV requirement is set for the leading leptons. The lepton isolation working points used in this analysis are Gradient and FCTightFixedRad for electrons and muons, respectively, as defined in Table 3.2. The isolation requirement serves the purpose of suppressing non-prompt objects which can mimic any potential signal such as semi-leptonic B -decays. As isolated leptons are preferred in MSSM Higgs decays, the impact on the signal efficiency is negligible. The selected hadronic tau must pass the

Medium working point of the BDT based tau identification. Reconstructed jets are of the EMTopo type, and the b -tagging working point used is the 70% efficiency (for b -jets in $t\bar{t}$ events) provided by the MV2c10 algorithm. The transition region between the end-cap and the barrel ($1.37 < |\eta| < 1.52$) is excluded from the analysis.

Assumptions on the topologies of typical signal and background events can be used to impose kinematic selections and optimise the signal to background ratio in the SR. The most common final state is assumed to be a low p_T neutral Higgs Boson with a mass equal to or above 200 GeV decaying to two oppositely charged boosted taus that are back to back in the transverse plane.

The $\tau_{\text{lep}}\tau_{\text{had}}$ SR selections are summarised in Table 4.3. The $\Delta\phi(\ell, \tau_{\text{had}}) > 2.4$ and opposite sign of the charge (q) between the two taus $q(\ell) \times q(\tau_{\text{had}}) < 0$ are used to suppress the jet fake background and isolate the signal. To reduce the W +jets background, mass variables can be employed. For example, the transverse mass ($m_T(\ell, E_T^{\text{MISS}})$) which is defined as follows:

$$m_T(\ell, E_T^{\text{MISS}}) = \sqrt{2p_T^\ell E_T^{\text{MISS}}(1 - \cos \Delta\phi(\ell, E_T^{\text{MISS}}))} \quad (4.1)$$

can be used to remove the W +jets peak which is situated at $m_T(\ell, E_T^{\text{MISS}}) \approx 80$ GeV. As the leptonically decaying tau has one extra neutrino relative to the hadronic tau, one would expect the lepton and E_T^{MISS} direction to be aligned, minimising $\Delta\phi(\ell, E_T^{\text{MISS}})$ and giving low $m_T(\ell, E_T^{\text{MISS}})$. The majority of the signal is therefore situated at $m_T(\ell, E_T^{\text{MISS}}) < 40$ GeV, motivating the use of the rest of the $m_T(\ell, E_T^{\text{MISS}})$ parameter space for control regions. For the $Z/\gamma^* \rightarrow ll$ background in which electrons can fake taus, a di-lepton veto is enacted by requiring that any given event contains only one lepton. This is implemented by requiring that only one lepton passes the Loose ID requirement and has p_T^ℓ above a 15 GeV (7 GeV) threshold for electrons (muons). Finally, to further reduce the $Z/\gamma^* \rightarrow ee$ contribution, the invariant mass of the visible products ($m_{\text{vis}} = (E_e + E_{\tau_{\text{had-vis}}})^2 - |\mathbf{p}_e + \mathbf{p}_{\tau_{\text{had-vis}}}|^2$) of the electron and τ_{had} is used to veto the region around the Z peak ($80 \text{ GeV} < m_{\text{vis}} < 110 \text{ GeV}$) in the $e\tau_{\text{had}}$ channel.

Table 4.3: A summary of the signal region selection for the $\tau_{\text{lep}}\tau_{\text{had}}$ b -veto and b -tag signal regions (SR).

Region	Selection
$\tau_{\text{lep}}\tau_{\text{had}}$ SR	$\ell(\text{trigger, isolated}), \tau_{\text{had}}(\text{Medium BDT}), q(\ell) \times q(\tau_{\text{had}}) < 0, \Delta\phi(\ell, \tau_{\text{had}}) > 2.4,$ $m_T(\ell, E_T^{\text{MISS}}) < 40 \text{ GeV}, 80 \text{ GeV} < m_{\text{vis}}(e, \tau_{\text{had}}) < 110 \text{ GeV vetoed}, N_\ell = 1$ $N_{b\text{-jets}} > 0$ (b -tag SR only)

4.4 Reconstructing the Di-tau Mass

In many particle physics analyses, the invariant mass of a chosen system is reconstructed and investigated to search for resonance peaks in a smoothly decaying background distribution. However, when dealing with tau decays, the presence of neutrinos in the final state makes it impossible to fully reconstruct the invariant mass, since the four-momenta of the neutrinos cannot be directly determined. Only information on the E_T^{MISS} is available.

Various mass variables have been considered in past publications to discriminate between signal and background in MSSM $H/A/h \rightarrow \tau\tau$ analyses [57, 144–148]. The chosen variable M_T^{TOT} , as represented by:

$$\begin{aligned} M_T^{\text{TOT}} &= \sqrt{m_T^2(\tau_{\text{had}}, E_T^{\text{MISS}}) + m_T^2(\tau_{\text{lep}}, E_T^{\text{MISS}}) + m_T^2(\tau_{\text{had}}, \tau_{\text{lep}})} \\ &= \sqrt{(p_T^{\tau_{\text{had}}} + p_T^{\tau_{\text{lep}}} + E_T^{\text{MISS}})^2 + (\mathbf{p}_T^{\tau_{\text{had}}} + \mathbf{p}_T^{\tau_{\text{lep}}} + \mathbf{E}_T^{\text{MISS}})^2} \end{aligned} \quad (4.2)$$

has been proven to give large signal to background separation whilst also having low computation time when compared to other more complicated invariant mass reconstruction techniques. This variable is based on the visible transverse mass (m_T) which is defined similarly to Equation 4.1, but with the necessary objects swapped in.

4.5 Background Estimation in the $\tau_{\text{lep}}\tau_{\text{had}}$ Channel

The dominant background in the $\tau_{\text{lep}}\tau_{\text{had}}$ channel arises from two separate scenarios where a jet is misidentified as a hadronic tau. The first type involves cases induced by QCD multi-jet events, where both the lepton and the τ_{had} are jet fakes. The second scenario is where the lepton is genuine, but the τ_{had} is a jet fake. This scenario is dominant in the $\tau_{\text{lep}}\tau_{\text{had}}$ channel and is typically associated with W +jets ($t\bar{t}$) events in the b -veto (b -tag) category, they are referred to as W +jets/top fakes, where top collectively refers to single t -quark and $t\bar{t}$ events.

Both scenarios have large cross-section and small acceptance, simulating these events with MC is not practical as any sample would be prohibitively large. Therefore, the fake component is modelled using the data-driven techniques described in the following sections.

The $\tau_{\text{lep}}\tau_{\text{had}}$ channel also features other backgrounds that involve genuine particles in the final state. For instance, the $Z/\gamma^* \rightarrow \tau\tau$ background is irreducible and relevant for the b -veto SR, while the $t \rightarrow b\tau$ process, mainly from $t\bar{t}$ production, contributes to the b -tag SR. In addition, minor backgrounds such as $Z/\gamma^* \rightarrow ll$, diboson, and single t -quark processes are present. These backgrounds are typically well modelled using standard MC simulations.

Table 4.4 displays the partition of the control and fake regions that are typically segregated based on $m_T(\ell, E_T^{\text{MISS}})$. The background estimation is modelled and validated in these regions in the following sections.

Table 4.4: The partitioning of the control, fake and validation regions for the MSSM $H/A/h \rightarrow \tau\tau$ 2020 (legacy) analysis [8].

Region	Usage	Selection
MFR	Calculate the multi-jet fake factors	$\ell(\text{trigger}), \tau_{\text{had}}(\text{BDT score} < 0.01), N_\ell = 1, m_T(\ell, E_T^{\text{MISS}}) < 30 \text{ GeV}$ Pass or fail lepton isolation
WFR	Calculate the W +jets/top fake factors	Pass SR except: $60 \text{ GeV} < m_T(\ell, E_T^{\text{MISS}}) < 150 \text{ (110) GeV (} b\text{-tag)}$, Pass or fail τ_{had} ID (BDT score > 0.01)
TCR	Used in final fit and to normalise b -tag W +jets/top fake factors	Pass SR except: $m_T(\ell, E_T^{\text{MISS}}) > 110 \text{ GeV (} b\text{-tag only)}$
VR	Validating the background model	Pass SR except: $40 \text{ GeV} < m_T(\ell, E_T^{\text{MISS}}) < 60 \text{ GeV}$
MF-AR1	The region to apply the multi-jet fake factor to get the SR multi-jet contribution	Pass SR except: $\ell(\text{trigger, fail lepton isolation})$
MF-AR2	The region to apply the multi-jet fake factor to get the fail-ID SR multi-jet contribution, such that the W +jets/top fake contribution can be retrieved	Pass SR except: $\ell(\text{trigger, fail lepton isolation}),$ $\tau_{\text{had}}(\text{fail } \tau_{\text{had}} \text{ ID, BDT score} > 0.01)$
WF-AR	The region to apply the W +jets/top fake factor to get the SR W +jets/top fake contribution	Pass SR except: $\tau_{\text{had}}(\text{fail } \tau_{\text{had}} \text{ ID, BDT score} > 0.01)$

4.5.1 Estimation of the Fake Background

The data-driven estimation of the fake background in this analysis relies on the fake factor (FF) technique. For each fake contribution, a fake region enriched in those fakes is defined. The following equation is evaluated to derive the fake factors:

$$FF = \frac{N_{\text{data}}^{\text{pass-req}}(\mathbf{x}) - N_{\text{bkg}}^{\text{pass-req}}(\mathbf{x})}{N_{\text{data}}^{\text{fail-req}}(\mathbf{x}) - N_{\text{bkg}}^{\text{fail-req}}(\mathbf{x})} \Big|_{\text{req} = \text{ID (WFR), ISO (MFR)}} \quad (4.3)$$

where $N_{\text{data}}^{\text{pass-req}}$ ($N_{\text{bkg}}^{\text{pass-req}}$) are the number of data (background) events which pass the associated requirement. The fake factor is defined as the ratio of a set of events that pass and fail some selection criteria. The corresponding set of events is the predicted background contribution subtracted from the data in the fake enriched region. The criteria is an isolation (ISO) selection when the FF is evaluated in the multi-jet fake region (MFR) or an identification requirement for the W +jets/top fake region (WFR). The fake factor is typically parameterised in various kinematic quantities (\mathbf{x}), such as p_T , angular variables, and the number of tau charged tracks (prongs), to correct the most heavily affected variables. As an example, the equation can be evaluated to calculate the multi-jet fake factor (MFF) in the following way:

$$MFF = \frac{N_{\text{data}}^{\text{pass-ISO}}(p_T^\ell, \Delta\phi(\ell, E_T^{\text{MISS}})) - N_{\text{MC bkg}}^{\text{pass-ISO}}(p_T^\ell, \Delta\phi(\ell, E_T^{\text{MISS}}))}{N_{\text{data}}^{\text{fail-ISO}}(p_T^\ell, \Delta\phi(\ell, E_T^{\text{MISS}})) - N_{\text{MC bkg}}^{\text{fail-ISO}}(p_T^\ell, \Delta\phi(\ell, E_T^{\text{MISS}}))} \quad (4.4)$$

where the background subtracted from data is just the MC predicted background. The W +jets/top fake factor (WFF) case is similar but the determined multi-jet contribution is

also subtracted from the data along with the MC predicted background and the variables used for parameterisation are different.

The fake factor is then applied to an application region (fail-ISO and/or fail-ID) to estimate the contribution in the SR (or other interesting pass-ISO or pass-ID region). Since there are two fake contributions, one fake factor is firstly evaluated and used to calculate its contribution in the other fake region, creating an anti-correlation effect between the two fakes. This means that any fakes not assigned as multi-jet in the W +jets/top fake region are assigned as W +jets/top fakes. The multi-jet fake factor is typically evaluated before the W +jets/top fake factor because the WFR is closer to the SR in terms of event topology, so the extrapolation uncertainty from moving from one $m_T(\ell, E_T^{\text{MISS}})$ region to another is reduced. Using the calculated fake factors and the application regions defined in Table 4.4, the multi-jet and W +jets/top fake contributions can be calculated using the following relations:

$$N_{\text{Multi-jet}}^{\text{SR}} = FF_{\text{Multi-jet}} \times (N_{\text{data}}^{\text{MF-AR1}} - N_{\text{bkg}}^{\text{MF-AR1}}) \quad (4.5)$$

$$N_{W+\text{jets/top fake}}^{\text{SR}} = FF_{W+\text{jets/top fake}} \times (N_{\text{data}}^{\text{WF-AR}} - N_{\text{bkg}}^{\text{WF-AR}} - FF_{\text{Multi-jet}} \times (N_{\text{data}}^{\text{MF-AR2}} - N_{\text{bkg}}^{\text{MF-AR2}})) \quad (4.6)$$

Multi-jet Fake (Fake τ_{had} , Fake ℓ) Background

The multi-jet fake region, which is also often referred to as the lepton fake region (LFR), is designed to be enriched with gluon-initiated jet fakes that typically fake both the lepton and the tau. As gluon jets are typically less collimated than quark jets, they are easier to distinguish from taus. Therefore, the proportion of multi-jet fakes can be enhanced by requiring a very low tau ID BDT score of 0.01 or less. The MFR can be brought closer to the SR by moving to the $m_T(\ell, E_T^{\text{MISS}}) < 30$ GeV region. The MFR selection is summarised in Table 4.4.

Equation 4.4 is evaluated by using p_T^ℓ and four (three) bins of $\Delta\phi(\ell, E_T^{\text{MISS}})$ in the b -veto (b -tag) category as the parameterisation. No truth matching is applied when the MC predicted fakes are subtracted from the data, this is to give a crude estimation of the W +jets/top fake contribution in the region. The resulting fake factors are presented in Figures 4.2 and 4.3 for the $e\tau_{\text{had}}$ and $\mu\tau_{\text{had}}$ channels, respectively. The fake factors show a dependence on the b -jet multiplicity and the lepton type, leading to separate fake factors for each case. Discontinuities in the distributions are caused by reaching the threshold of a new trigger with different isolation requirements. The uncertainty bars indicate the statistical uncertainty associated with each fake factor bin. The uncertainty band is the statistical uncertainty and the assigned systematic uncertainty added in quadrature. The systematic uncertainty for the band is derived by considering the confidence in which the theoretical cross-sections are calculated and the calibration precision of the combined performance physics objects. A 10% variation to the background MC in the pass-ISO region and a more conservative 20% variation in the fail-ISO region is applied due to the poorly calibrated non-isolated lepton.

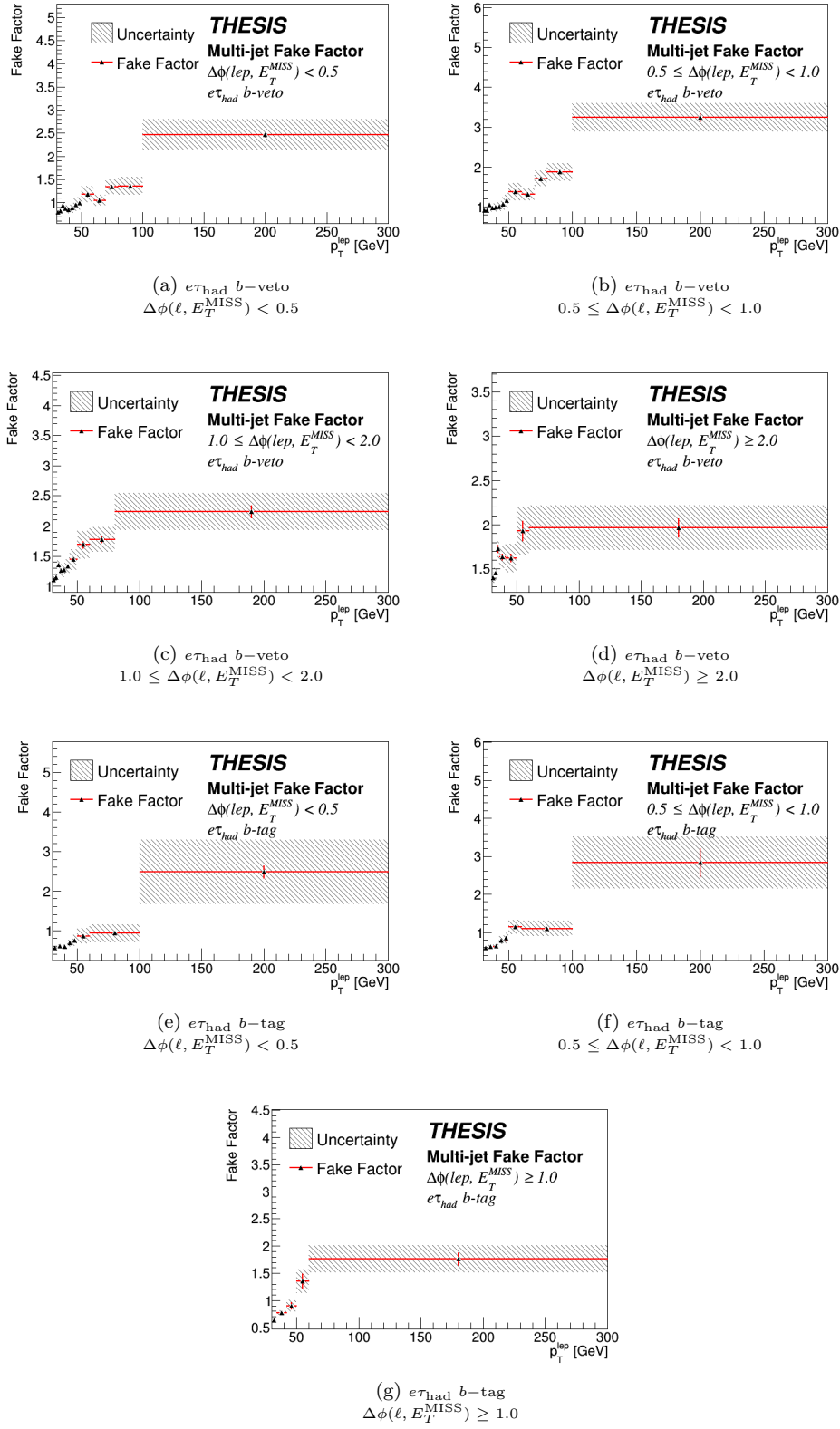


Figure 4.2: The $e\tau_{\text{had}}$ multi-jet fake factors. The uncertainty bar corresponds to the statistical uncertainty, whilst the uncertainty band also considers the assigned systematic uncertainty.

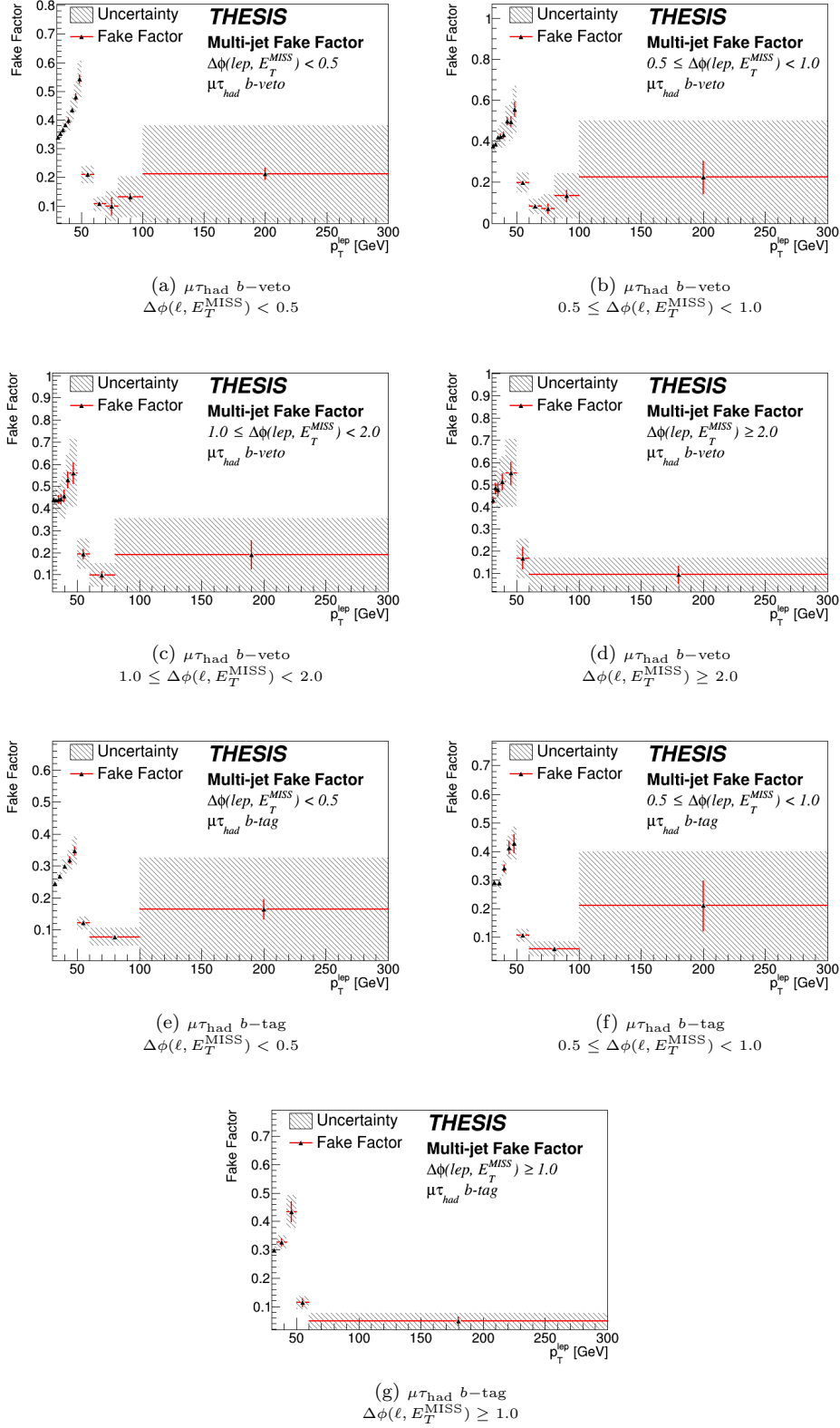


Figure 4.3: The $\mu\tau_{\text{had}}$ multi-jet fake factors. The uncertainty bar corresponds to the statistical uncertainty, whilst the uncertainty band also considers the assigned systematic uncertainty.

A validation test is performed to ensure the accuracy of the fake factor method. The fake factor is applied to an MFR application region (fail-ISO) which retrieves the estimated multi-jet contribution in the MFR. The data is inspected to ensure that it exactly matches the background for the distributions for which the fake factor was calculated. Additionally, other distributions are checked for any modelling discrepancies. The p_T^τ distribution for the $\mu\tau_{\text{had}}$ channel in both the b -veto and b -tag categories show some mismodelling. Similar discrepancies can also be observed in intervals of $\Delta\phi(\ell, E_T^{\text{MISS}})$. To correct this, a scale factor is defined and parameterised in p_T^τ and four (three) bins of $\Delta\phi(\ell, E_T^{\text{MISS}})$ in the b -veto (b -tag) category. The resulting scale factors are shown in Figure 4.4. The scale factor is then added as a correction to the original fake factor and the full amount of the correction is assigned as additional systematic uncertainty. The validation plots with the final fake factors applied now show acceptable modelling in the key distributions, as shown in Figures 4.5 and 4.6 (4.7 and 4.8) for the $e\tau_{\text{had}}$ and $\mu\tau_{\text{had}}$ channels in the b -veto (b -tag) category, where only statistical uncertainty is shown.

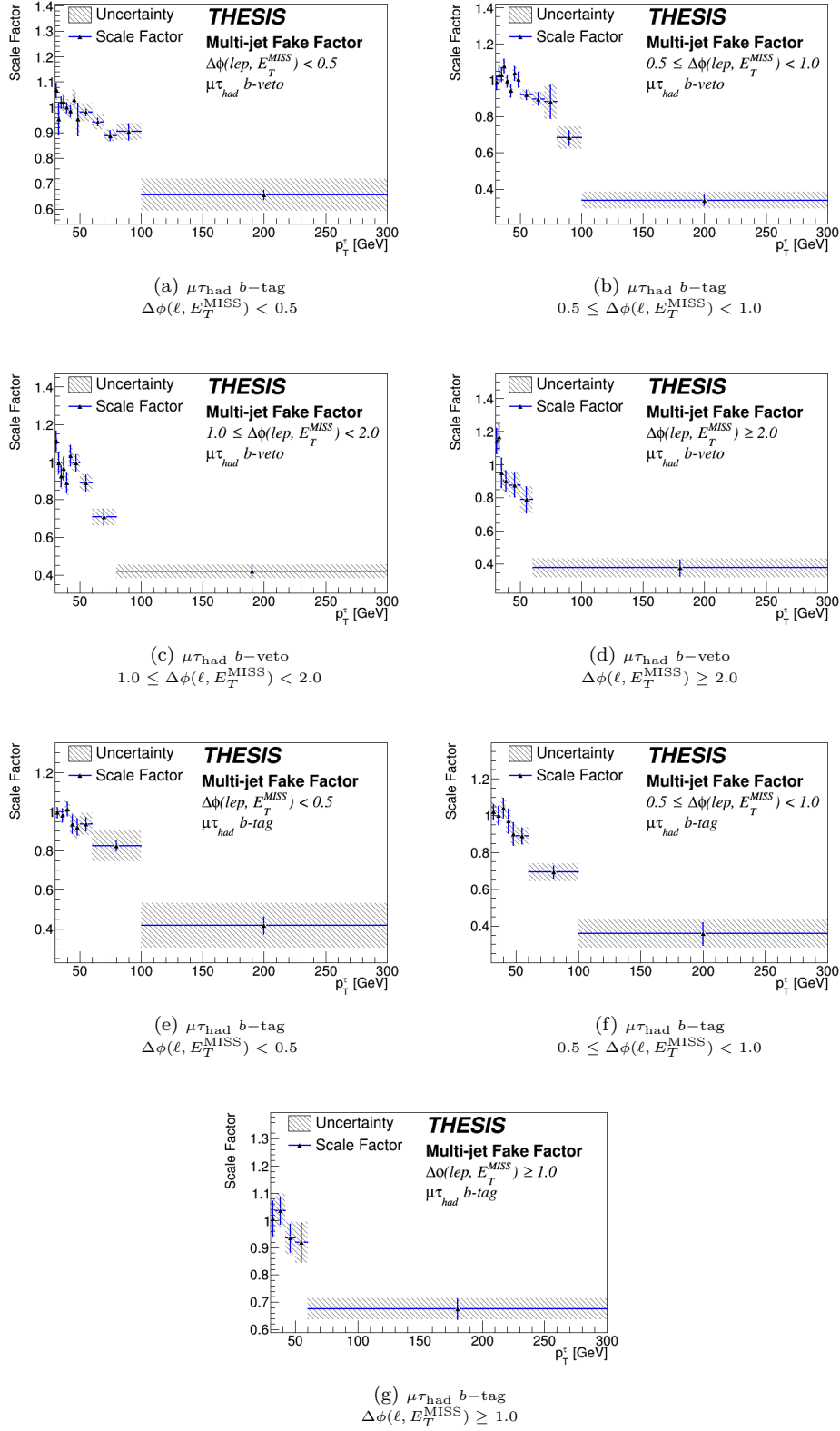
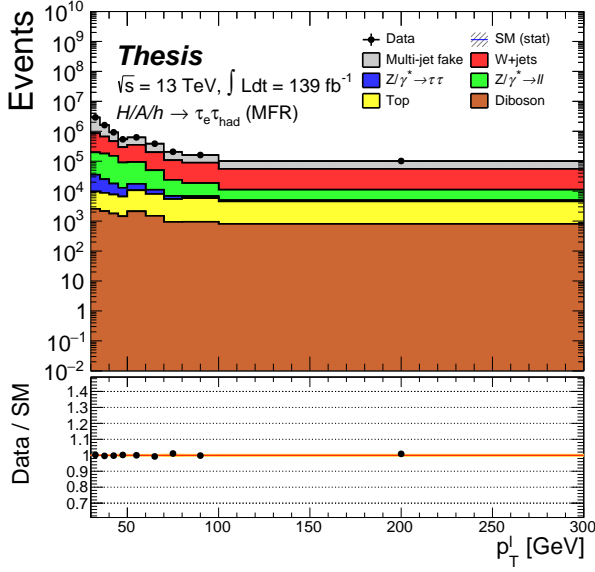
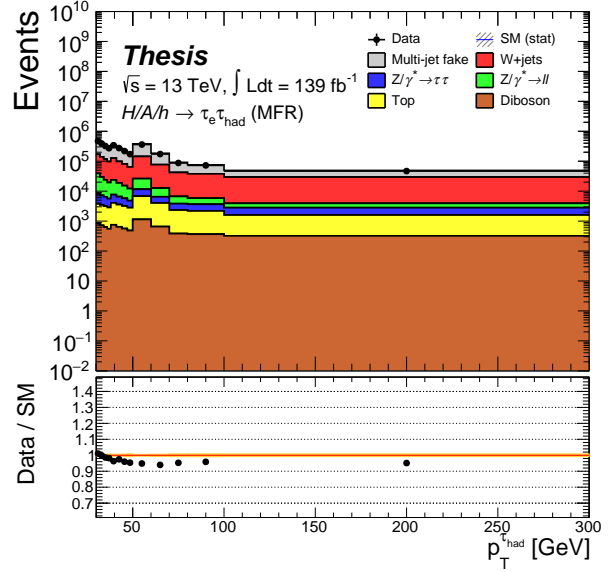


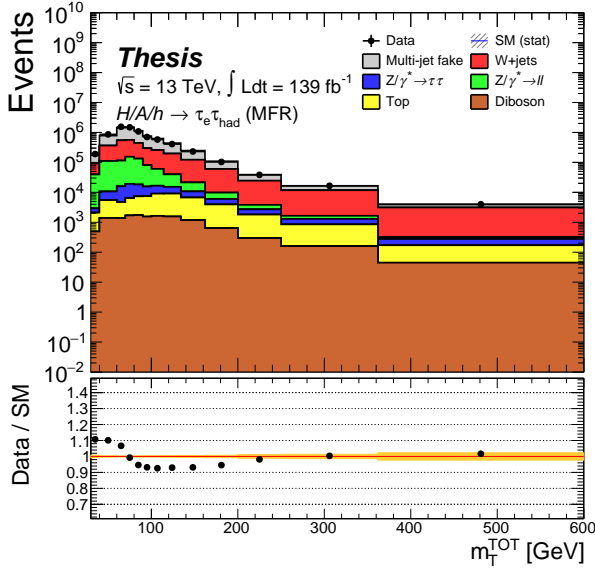
Figure 4.4: The $\mu\tau_{\text{had}}$ fake factor corrections. The uncertainty bar corresponds to the statistical uncertainty, whilst the uncertainty band also considers the assigned systematic uncertainty.



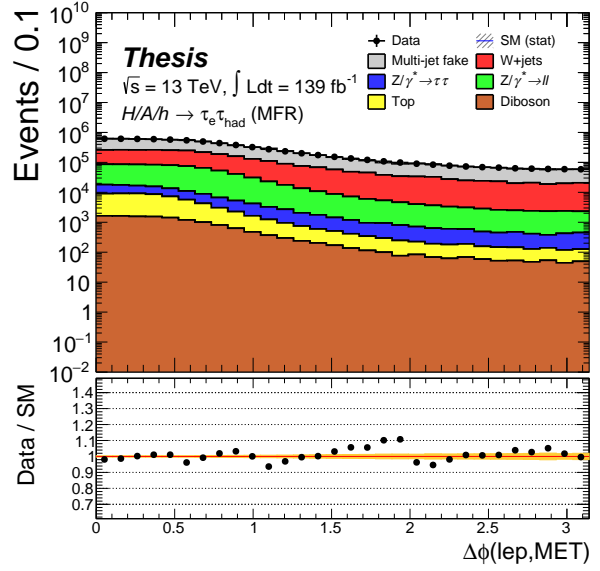
(a) $e\tau_{\text{had}} p_T^\ell$



(b) $e\tau_{\text{had}} p_T^{\tau_{\text{had}}}$

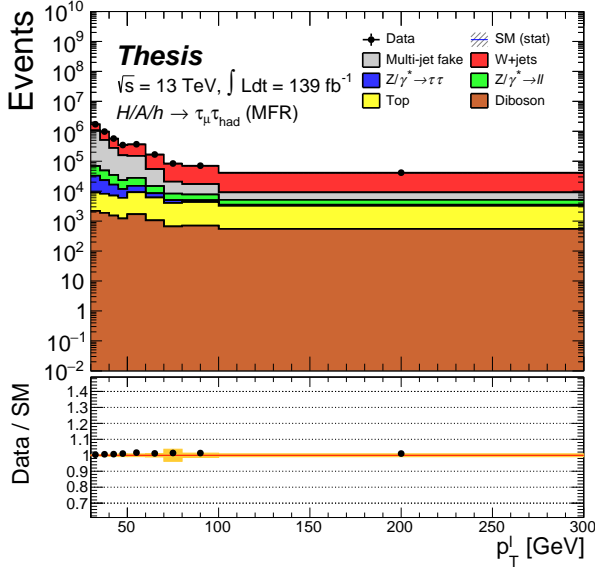


(c) $e\tau_{\text{had}} m_T^{\text{TOT}}$

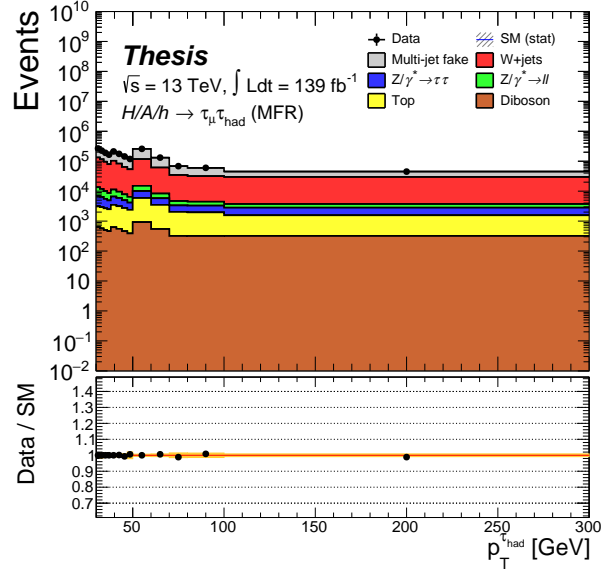


(d) $e\tau_{\text{had}} \Delta\phi(\ell, E_T^{\text{MISS}})$

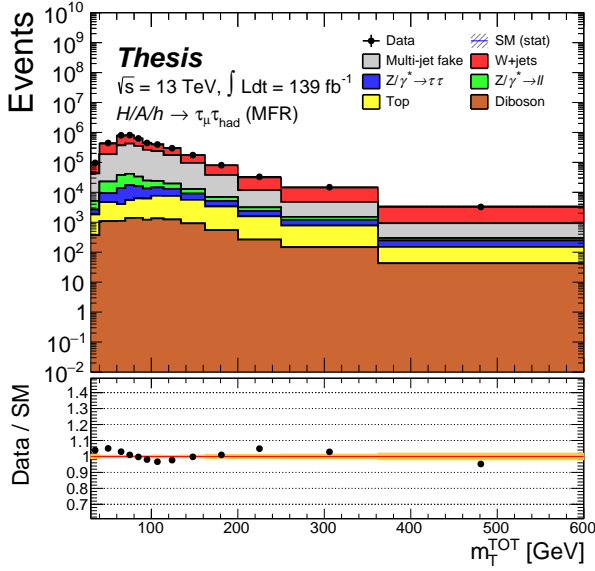
Figure 4.5: The multi-jet fake region validation plots for the $e\tau_{\text{had}}$ channel in the b -veto category. The plots show the derived multi-jet fake contribution from applying the corrected fake factors. Distributions are shown for p_T^ℓ , $p_T^{\tau_{\text{had}}}$ and m_T^{TOT} . The ratio plot shows the ratio of the data and the MC total predicted background. The uncertainty band considers only the statistical uncertainty on the background.



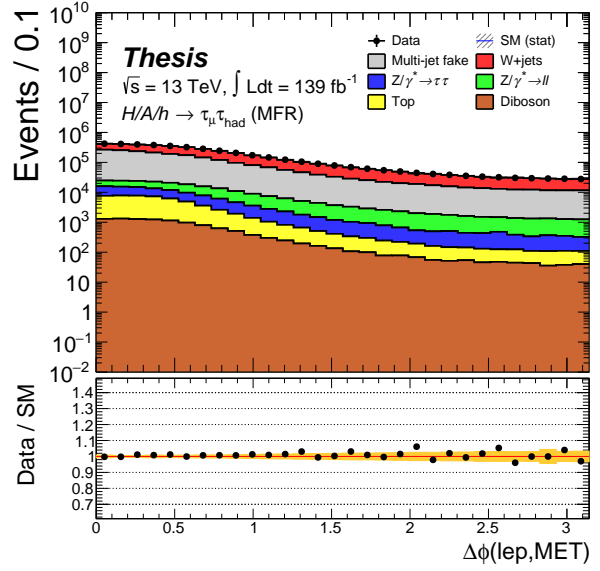
(a) $\mu\tau_{\text{had}} p_T^\ell$



(b) $\mu\tau_{\text{had}} p_T^{\tau_{\text{had}}}$

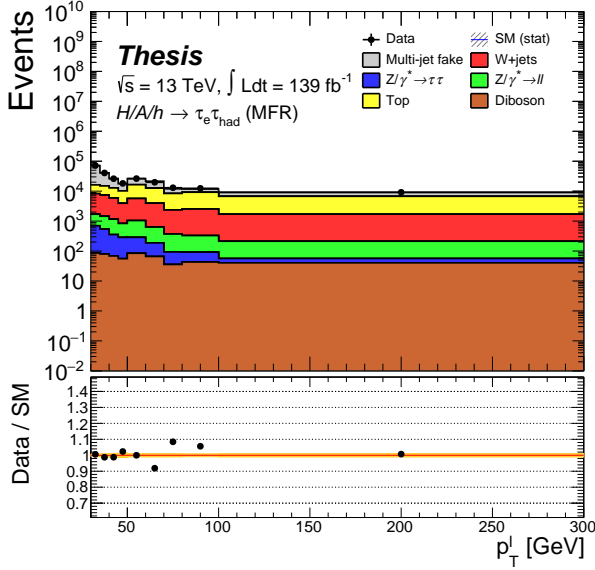


(c) $\mu\tau_{\text{had}} M_T^{\text{TOT}}$

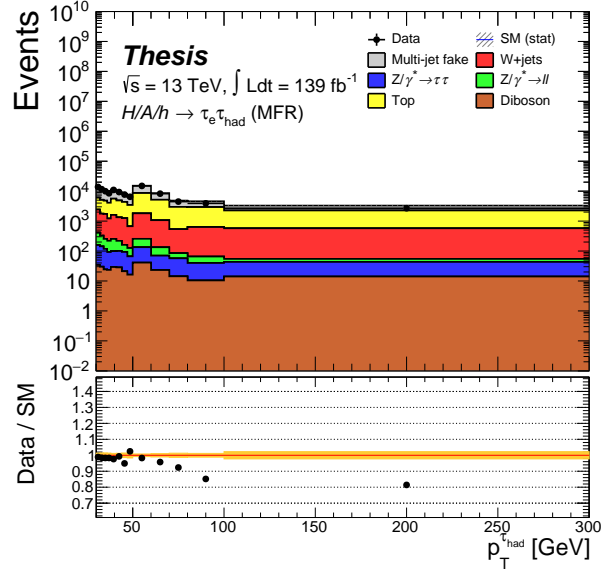


(d) $\mu\tau_{\text{had}} \Delta\phi(\ell, E_T^{\text{MISS}})$

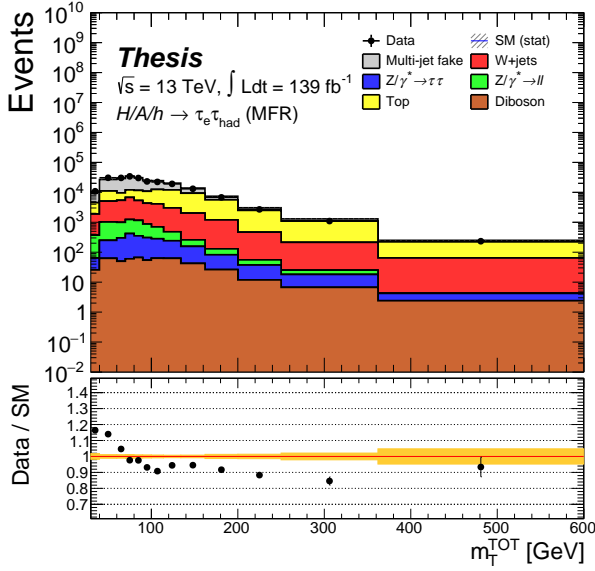
Figure 4.6: The multi-jet fake region validation plots for the $\mu\tau_{\text{had}}$ channel in the b -veto category. The plots show the derived multi-jet fake contribution from applying the corrected fake factors. Distributions are shown for p_T^ℓ , $p_T^{\tau_{\text{had}}}$ and M_T^{TOT} . The ratio plot shows the ratio of the data and the MC total predicted background. The uncertainty band considers only the statistical uncertainty on the background.



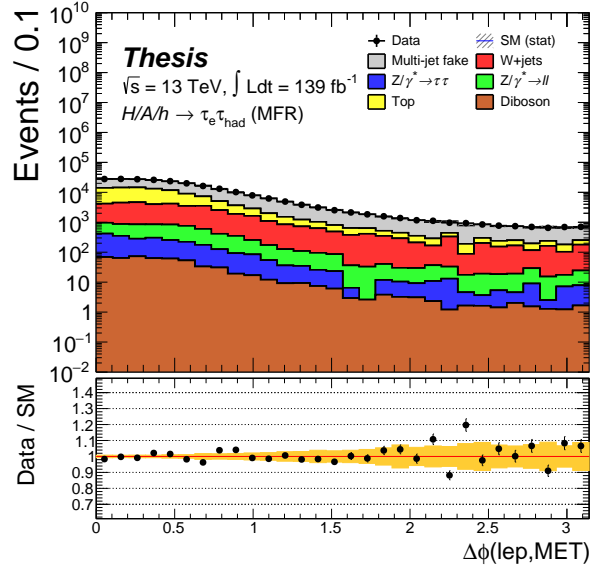
(a) $e\tau_{\text{had}} p_T^\ell$



(b) $e\tau_{\text{had}} p_T^{\tau_{\text{had}}}$

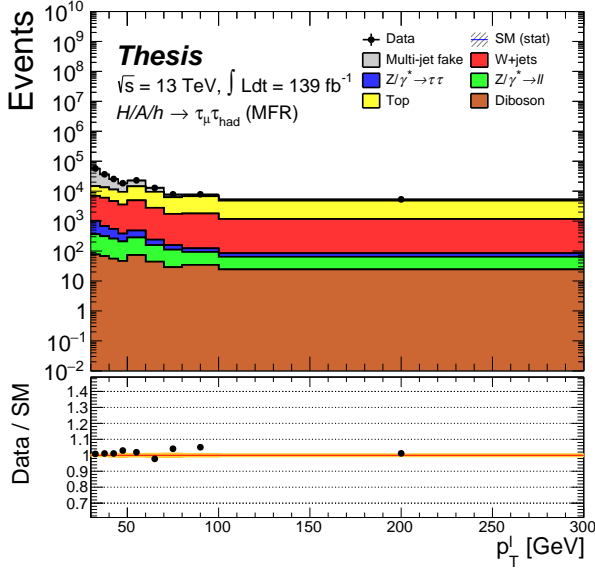


(c) $e\tau_{\text{had}} M_T^{\text{TOT}}$

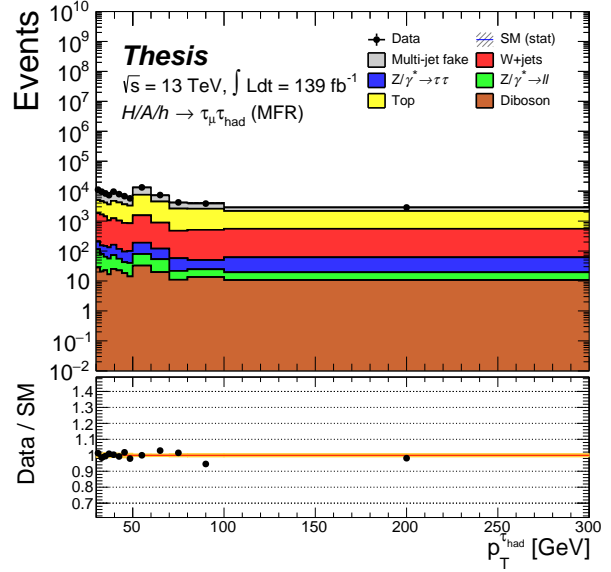


(d) $e\tau_{\text{had}} \Delta\phi(\ell, E_T^{\text{MISS}})$

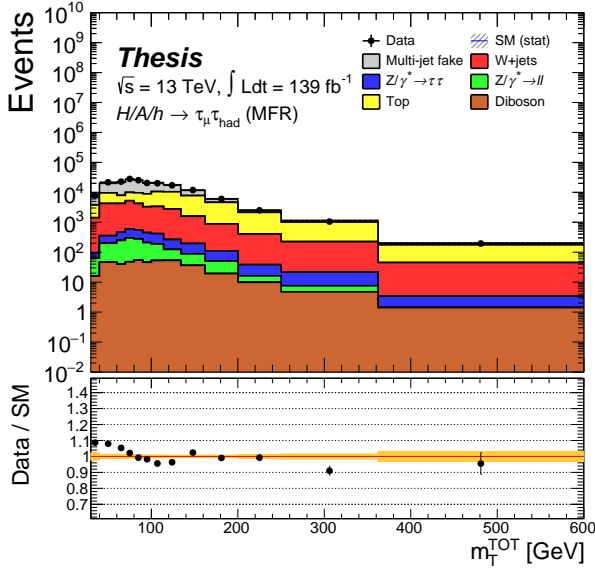
Figure 4.7: The multi-jet fake region validation plots for the $e\tau_{\text{had}}$ channel in the b -tag category. The plots show the derived multi-jet fake contribution from applying the corrected fake factors. Distributions are shown for p_T^ℓ , $p_T^{\tau_{\text{had}}}$ and M_T^{TOT} . The ratio plot shows the ratio of the data and the MC total predicted background. The uncertainty band considers only the statistical uncertainty on the background.



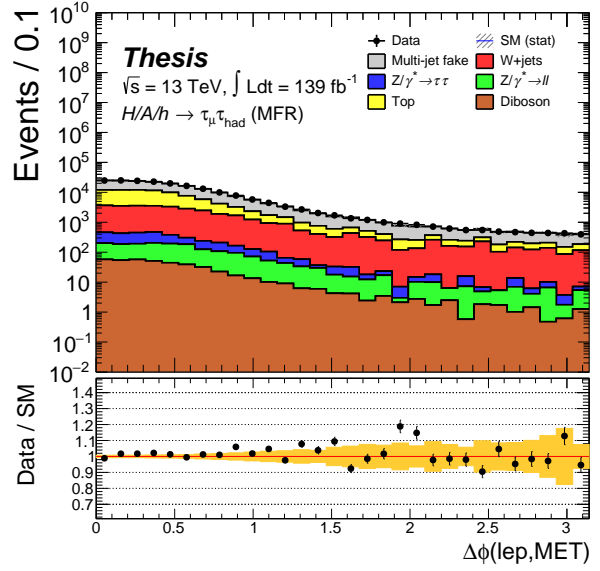
(a) $\mu\tau_{\text{had}} p_T^\ell$



(b) $\mu\tau_{\text{had}} p_T^{\tau_{\text{had}}}$



(c) $\mu\tau_{\text{had}} m_T^{\text{TOT}}$



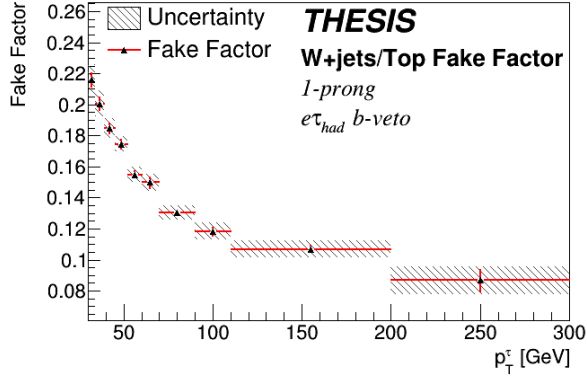
(d) $\mu\tau_{\text{had}} \Delta\phi(\ell, E_T^{\text{MISS}})$

Figure 4.8: The multi-jet fake region validation plots for the $\mu\tau_{\text{had}}$ channel in the b -tag category. The plots show the derived multi-jet fake contribution from applying the corrected fake factors. Distributions are shown for p_T^ℓ , $p_T^{\tau_{\text{had}}}$ and m_T^{TOT} . The ratio plot shows the ratio of the data and the MC total predicted background. The uncertainty band considers only the statistical uncertainty on the background.

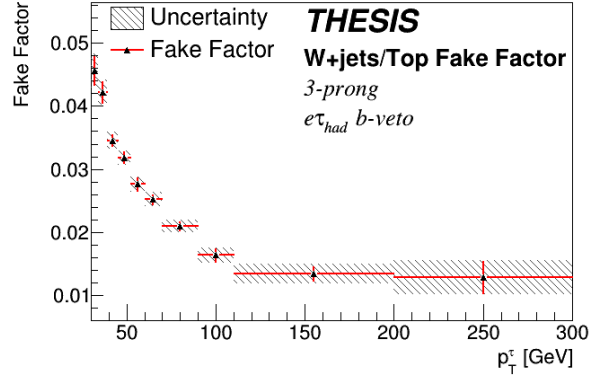
W +jets/top Fake (Fake τ_{had} , Genuine ℓ) Background

The WFR summarised in Table 4.4 is designed to address quark-initiated jet fake contributions. To achieve this, the SR is modified by imposing a requirement of $60 \text{ GeV} < m_T(\ell, E_T^{\text{MISS}}) < 110 \text{ (150) GeV}$ for b -tag (b -veto). Additionally, a low tau ID score cut (score > 0.01) is applied in the fail-ID region to reject fake contributions from gluon-initiated jets. This ensures that the quark-gluon fraction of jet fakes is similar between the SR and WFR, reducing the extrapolation uncertainty. To evaluate Equation 4.3, both the MC simulation and multi-jet contributions derived in the WFR are subtracted from the data. The MC simulation is truth matched to genuine events in this case since the multi-jet contribution is available. The multi-jet contribution for this region is derived by applying the multi-jet fake factor to the corresponding application region in the WFR (fail-ISO). The fake factor is evaluated using the Medium BDT identification requirement described in Section 3.3.3.

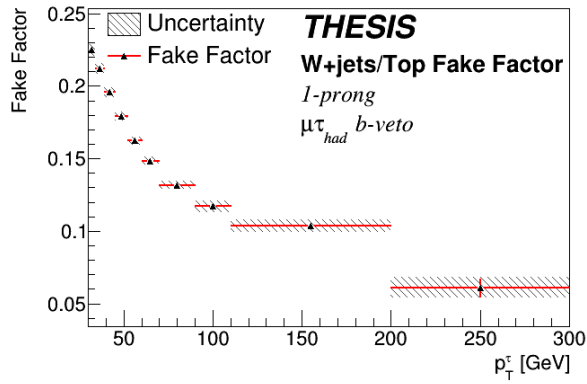
The W +jets/top fake factors are parameterised as a function of p_T^τ and the number of tau prongs. The b -tag WFR receives a significant contribution from real tau t -quark events, leading to the fake factor shape being dominated by statistical uncertainty. To address this issue, the b -veto fake factors were used instead of the b -tag, while normalising the b -veto fake factors to the integral of the b -tag fake factors. To validate this approach, a top control region (TCR), detailed in Section 4.5.2, was used to inspect the discrepancy in the real t -quark modelling, and to confirm that the shapes of the b -veto and b -tag fake factors were consistent within their uncertainties after a b -tag top correction. The b -veto fake factors are displayed in Figure 4.9, where the uncertainty bars and bands were calculated in the same way as the multi-jet fake factor, with a 10% MC variation applied for all regions, as the lepton is isolated. For the b -veto FF applied to b -tag fakes, the associated uncertainty in the normalisation was included as an additional systematic uncertainty.



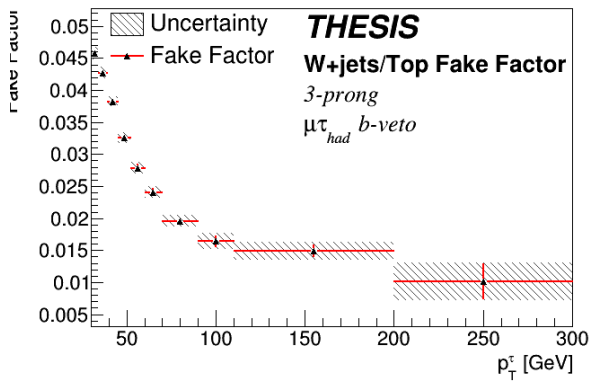
(a) $e\tau_{\text{had}}$ b -veto 1p



(b) $e\tau_{\text{had}}$ b -veto 3p



(c) $\mu\tau_{\text{had}}$ b -veto 1p



(d) $\mu\tau_{\text{had}}$ b -veto 3p

Figure 4.9: The W +jets/top fake factors for the $e\tau_{\text{had}}$ and $\mu\tau_{\text{had}}$ channels. Only the b -veto fake factor is used, the b -tag fake factor uses a normalised version of this. The uncertainty bar corresponds to the statistical uncertainty whilst the uncertainty band also considers the assigned systematic uncertainty.

Several variables in the b -veto category show a discrepancy after applying the W +jets/top fake factor. A correction to the b -veto WFF parameterised in p_T^ℓ and the number of tau prongs is derived as illustrated in Figure 4.10. Similar to the multi-jet case, the full correction is included as a systematic uncertainty, which is also applied to b -tag events, even though they are not subject to the correction. Validation plots representing the improved modelling of the WFR after the final fake factors are applied are presented in Figures 4.11, 4.12, 4.13 and 4.14.

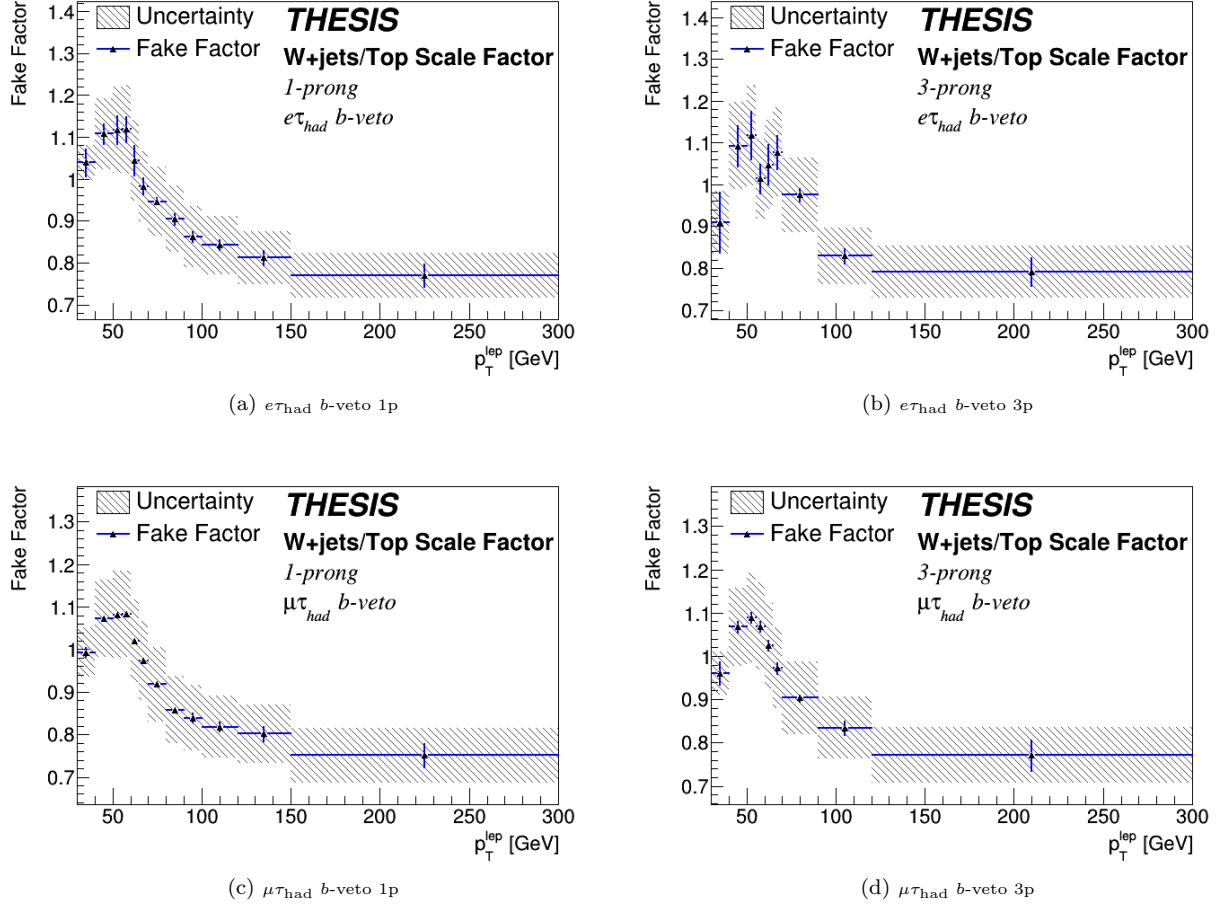
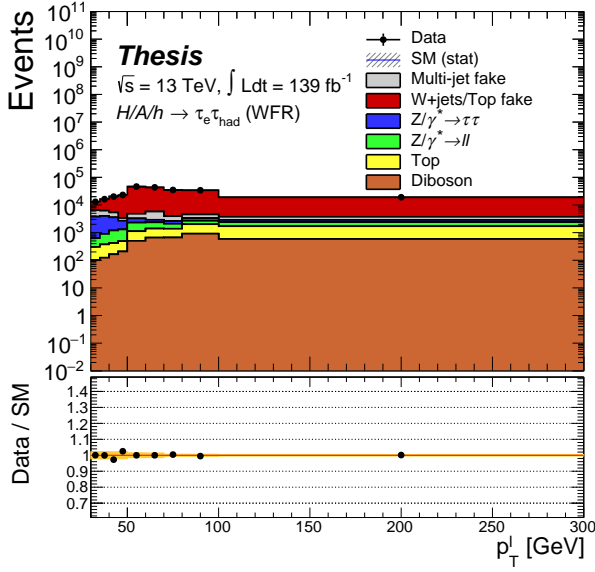
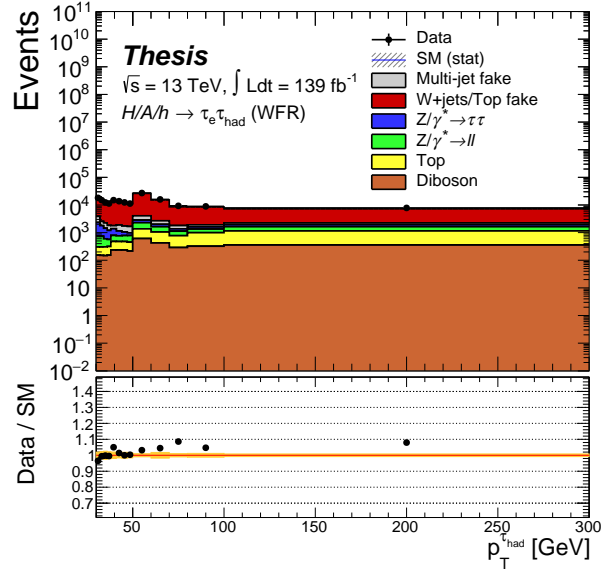


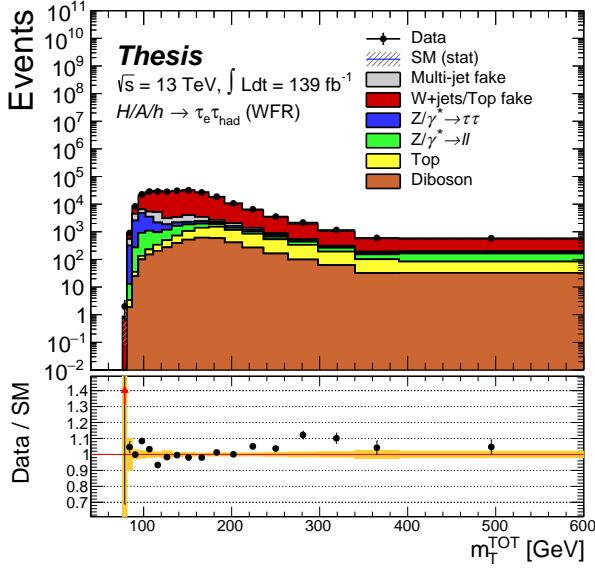
Figure 4.10: The correction to the b -veto W +jets/top fake factor for the $e\tau_{\text{had}}$ and $\mu\tau_{\text{had}}$ channels. The uncertainty bar corresponds to the statistical uncertainty whilst the uncertainty band also considers the assigned systematic uncertainty.



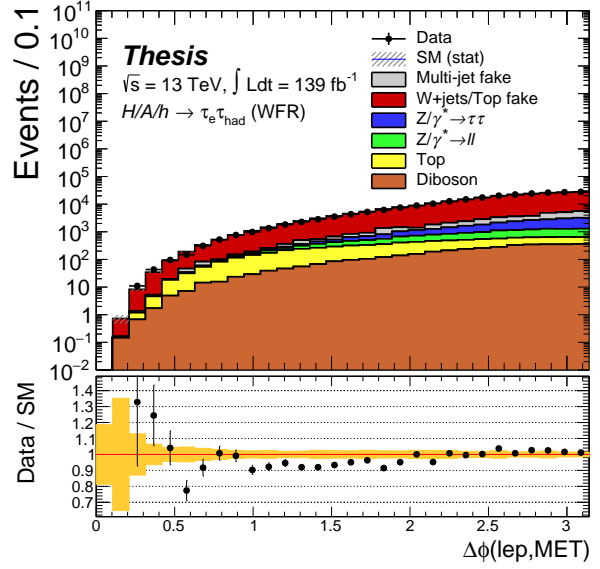
(a) $e\tau_{\text{had}} p_T^\ell$



(b) $e\tau_{\text{had}} p_T^{\tau_{\text{had}}}$

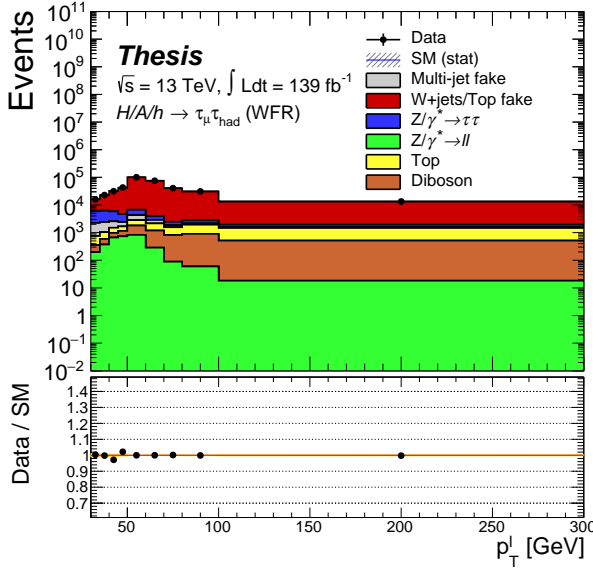


(c) $e\tau_{\text{had}} M_T^{\text{TOT}}$

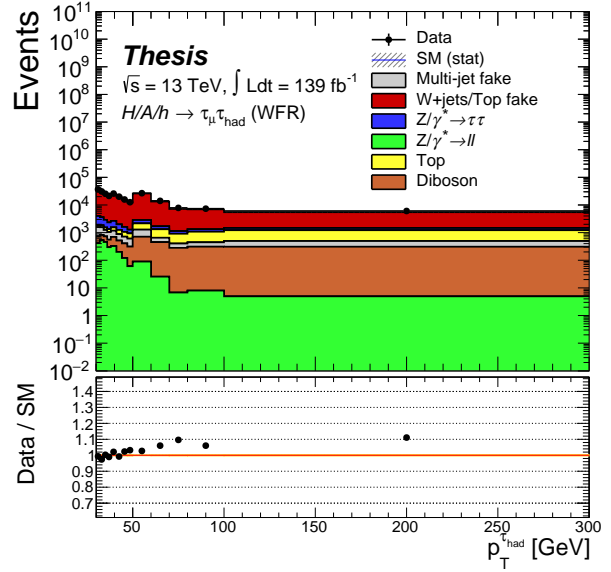


(d) $e\tau_{\text{had}} \Delta\phi(\ell, E_T^{\text{MISS}})$

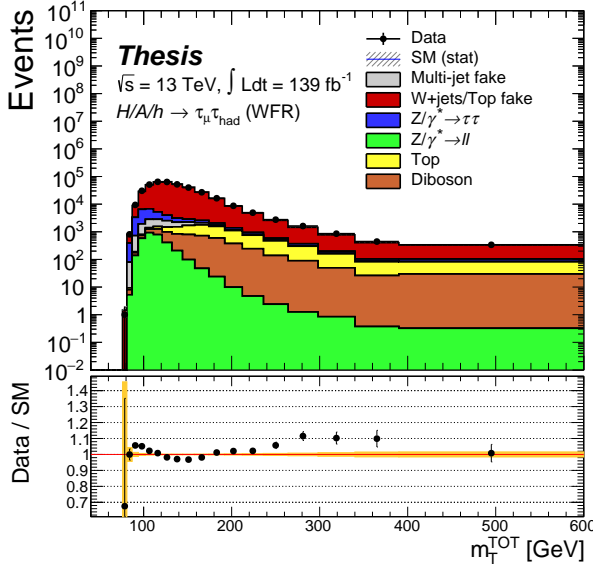
Figure 4.11: The W +jets/top fake region validation plots for the $e\tau_{\text{had}}$ channel in the b -veto category. The plots show the derived W +jets/top fake contribution from applying the fake factors. Distributions are shown for p_T^ℓ , $p_T^{\tau_{\text{had}}}$ and M_T^{TOT} . The ratio plot shows the ratio of the data and the total MC prediction. The uncertainty band considers only the statistical uncertainty on the background.



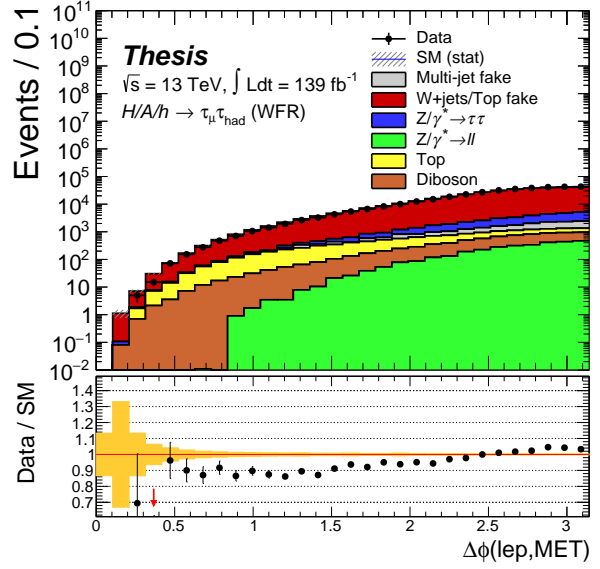
(a) $\mu\tau_{\text{had}} p_T^\ell$



(b) $\mu\tau_{\text{had}} p_T^{\tau_{\text{had}}}$

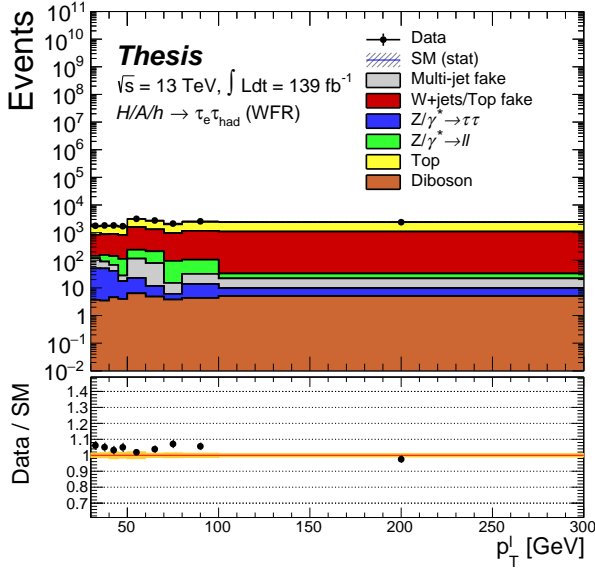


(c) $\mu\tau_{\text{had}} M_T^{\text{TOT}}$

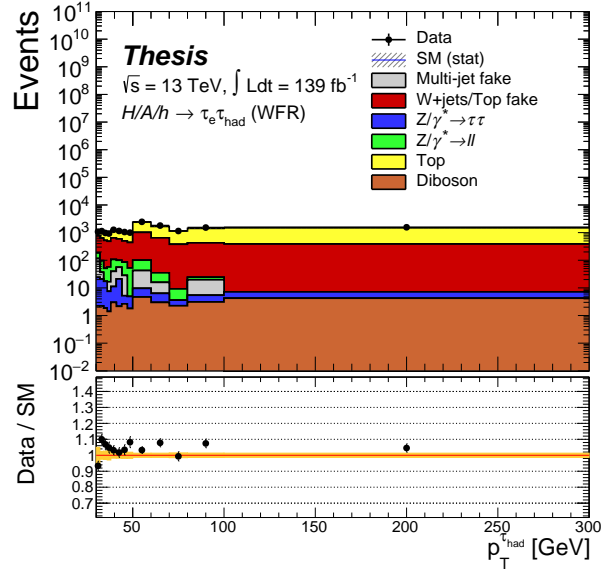


(d) $\mu\tau_{\text{had}} \Delta\phi(\ell, E_T^{\text{MISS}})$

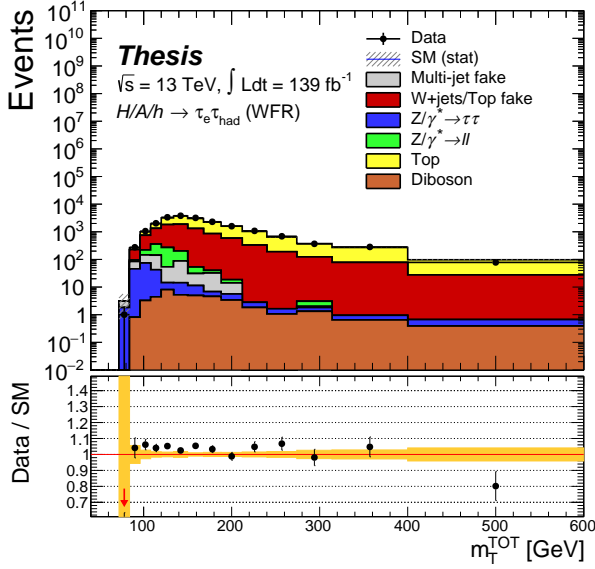
Figure 4.12: The W +jets/top fake region validation plots for the $\mu\tau_{\text{had}}$ channel in the b -veto category. The plots show the derived W +jets/top fake contribution from applying the fake factors. Distributions are shown for p_T^ℓ , $p_T^{\tau_{\text{had}}}$ and M_T^{TOT} . The ratio plot shows the ratio of the data and the total MC prediction. The uncertainty band considers only the statistical uncertainty on the background.



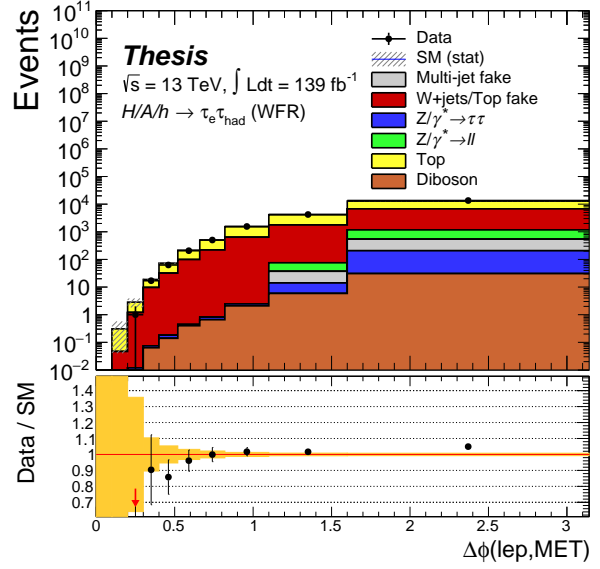
(a) $e\tau_{\text{had}} p_T^\ell$



(b) $e\tau_{\text{had}} p_T^{\tau_{\text{had}}}$

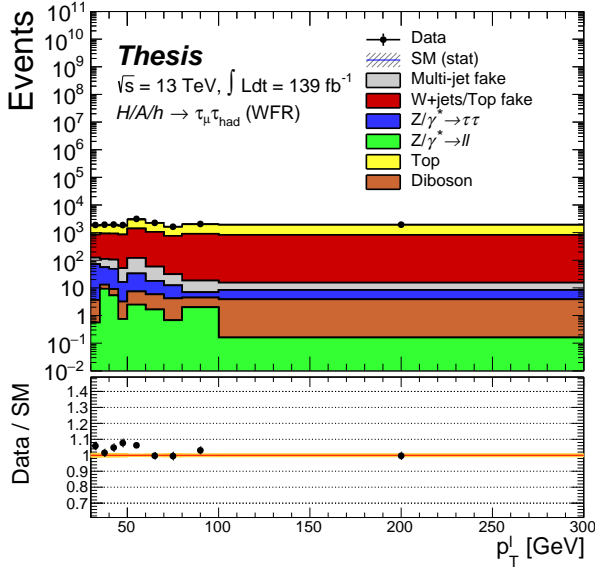


(c) $e\tau_{\text{had}} M_T^{\text{TOT}}$

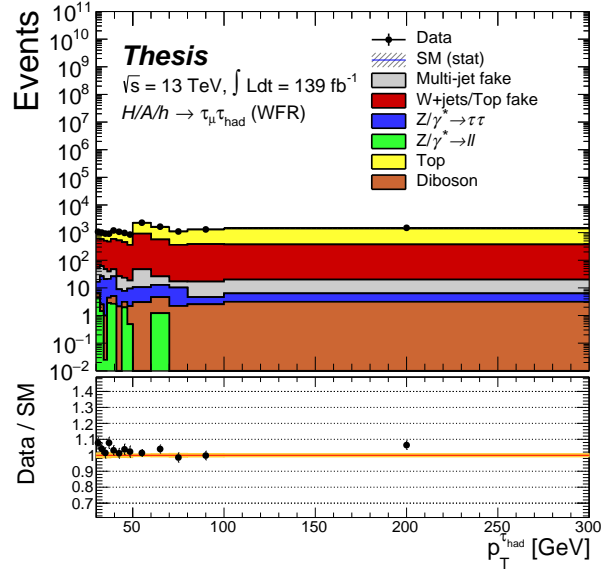


(d) $e\tau_{\text{had}} \Delta\phi(\ell, E_T^{\text{MISS}})$

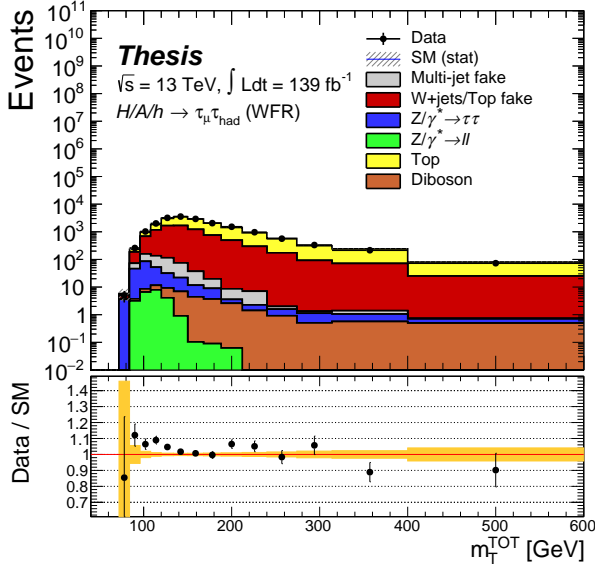
Figure 4.13: The W +jets/top fake region validation plots for the $e\tau_{\text{had}}$ channel in the b -tag category. The plots show the derived W +jets/top fake contribution from applying the fake factors. Distributions are shown for p_T^ℓ , $p_T^{\tau_{\text{had}}}$ and M_T^{TOT} . The ratio plot shows the ratio of the data and the total MC prediction. The uncertainty band considers only the statistical uncertainty on the background.



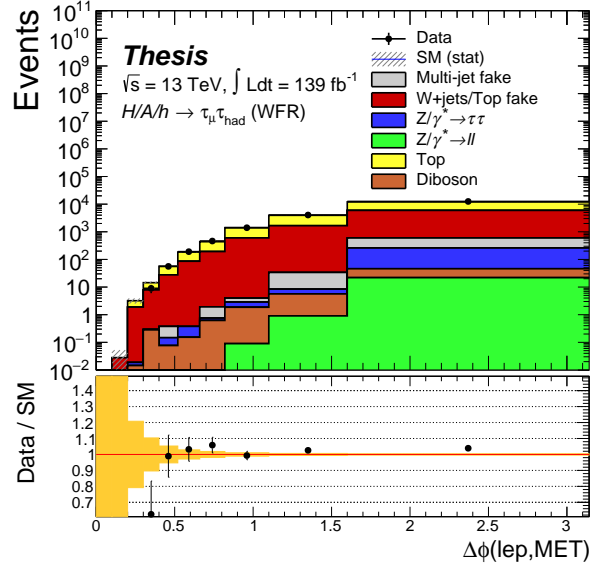
(a) $\mu\tau_{\text{had}} p_T^\ell$



(b) $\mu\tau_{\text{had}} p_T^{\tau_{\text{had}}}$



(c) $\mu\tau_{\text{had}} M_T^{\text{TOT}}$

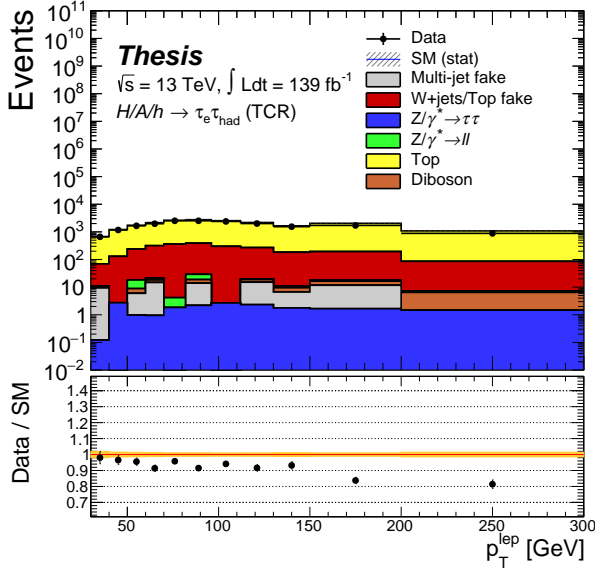


(d) $\mu\tau_{\text{had}} \Delta\phi(\ell, E_T^{\text{MISS}})$

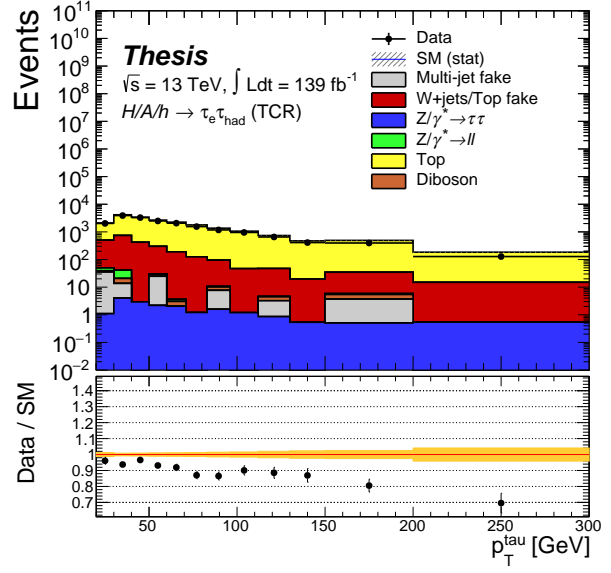
Figure 4.14: The W +jets/top fake region validation plots for the $\mu\tau_{\text{had}}$ channel in the b -tag category. The plots show the derived W +jets/top fake contribution from applying the fake factors. Distributions are shown for p_T^ℓ , $p_T^{\tau_{\text{had}}}$ and M_T^{TOT} . The ratio plot shows the ratio of the data and the total MC prediction. The uncertainty band considers only the statistical uncertainty on the background.

4.5.2 Constraining the t -quark Background

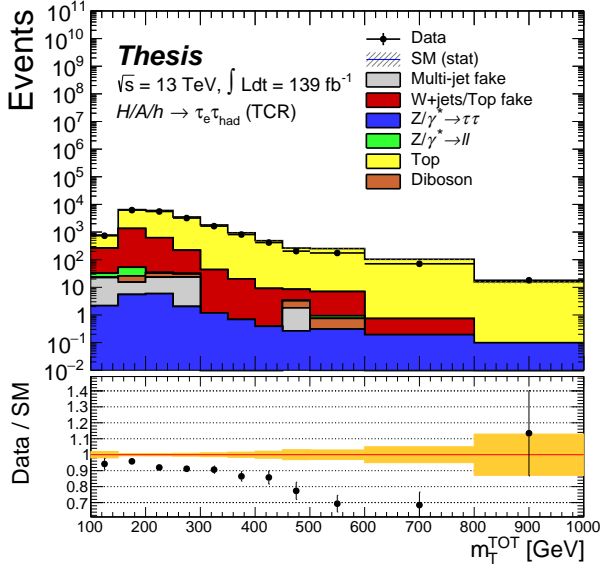
The TCR introduced in the previous section serves two purposes: it is included in the final fit described in Section 4.7, and it is used to validate the use of b -veto fake factors in the b -tag region. The TCR is defined to be close to the SR, but with the $m_T(\ell, E_T^{\text{MISS}})$ region above 110 GeV, which is rich in genuine $t\bar{t}$ events. Figures 4.15 and 4.16 present the TCR distributions for p_T^ℓ , p_T^τ , M_T^{TOT} and $\Delta\phi(\ell, E_T^{\text{MISS}})$.



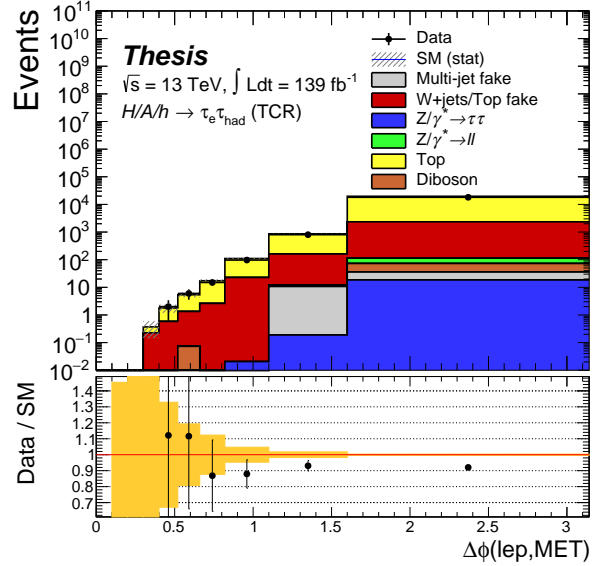
(a) $e\tau_{\text{had}} p_T^\ell$



(b) $e\tau_{\text{had}} p_T^{\tau_{\text{had}}}$

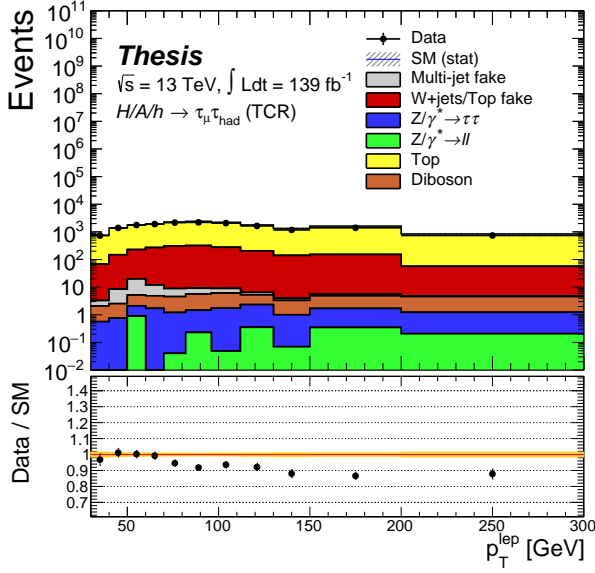


(c) $e\tau_{\text{had}} M_T^{\text{TOT}}$

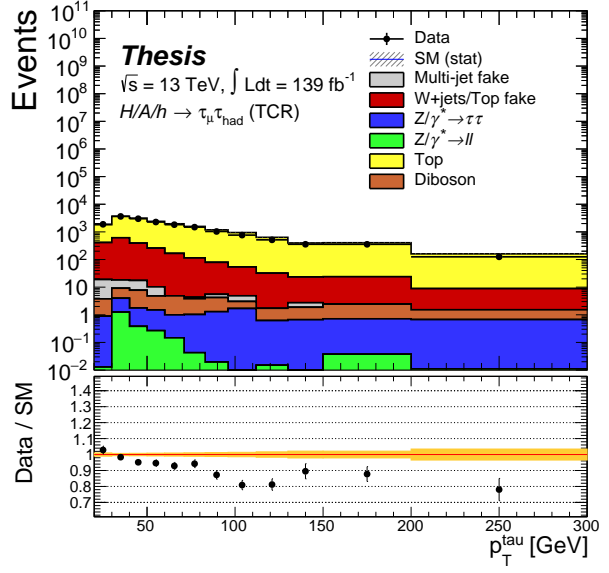


(d) $e\tau_{\text{had}} \Delta\phi(\ell, E_T^{\text{MISS}})$

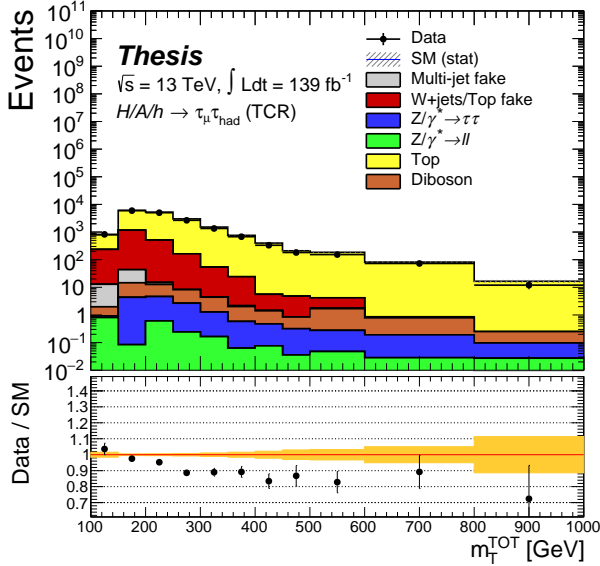
Figure 4.15: The p_T^ℓ , p_T^τ , M_T^{TOT} and $\Delta\phi(\ell, E_T^{\text{MISS}})$ distributions in the TCR for the b -tag $e\tau_{\text{had}}$ channel, the M_T^{TOT} distribution is used in the final fit. The ratio plots show the ratio of the data and the total MC prediction. The uncertainty bands consider only the statistical uncertainty on the background.



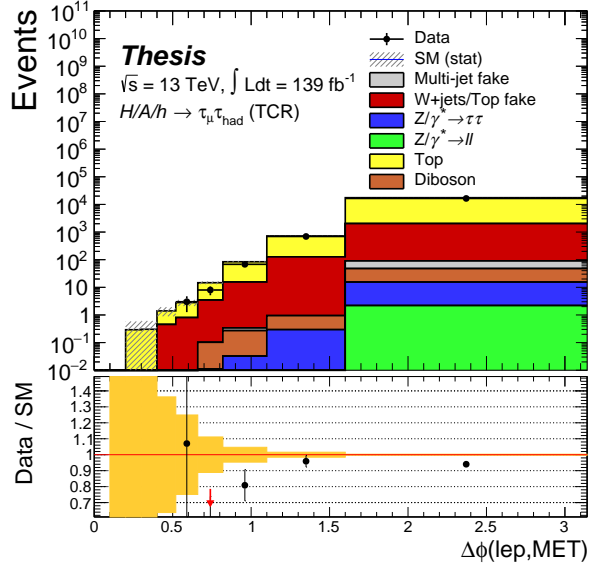
(a) $\mu\tau_{\text{had}} p_T^{\ell}$



(b) $\mu\tau_{\text{had}} p_T^{\tau_{\text{had}}}$



(c) $\mu\tau_{\text{had}} M_T^{\text{TOT}}$



(d) $\mu\tau_{\text{had}} \Delta\phi(\ell, E_T^{\text{MISS}})$

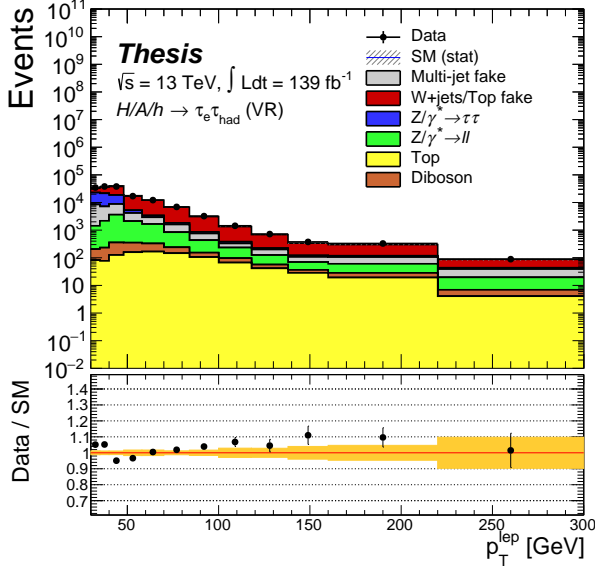
Figure 4.16: The p_T^{ℓ} , p_T^{τ} , M_T^{TOT} and $\Delta\phi(\ell, E_T^{\text{MISS}})$ distributions in the TCR for the b -tag $\mu\tau_{\text{had}}$ channel, the M_T^{TOT} distribution is used in the final fit. The ratio plots show the ratio of the data and the total MC prediction. The uncertainty bands consider only the statistical uncertainty on the background.

4.5.3 Fake Background Validation

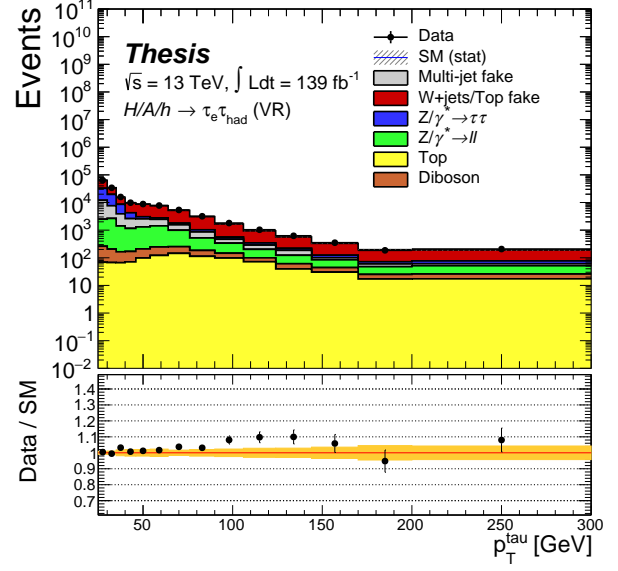
To ensure that the fake estimation is well modelled, a validation region is defined that is identical to the SR, except that the $m_T(\ell, E_T^{\text{MISS}})$ interval is required to be between 40 and 60 GeV. It is essential that the VR has minimal signal contamination to properly account for the background. After estimating the fakes, the modelling should be adequate in the WFR, so any mismodelling in the VR is attributed to extrapolation from the WFR to the VR.

To account for mismodelling in this region, a validation scale factor (VSF) is derived that is parameterised in p_T^τ , the number of tau prongs and an additional three bins of $\Delta\phi(\ell, E_T^{\text{MISS}})$ for the b -veto category, resulting in 16 scale factors. These factors are not directly applied to the nominal result but are assigned as additional systematic uncertainty. For reference, the 16 scale factors are represented in Appendix B.1.

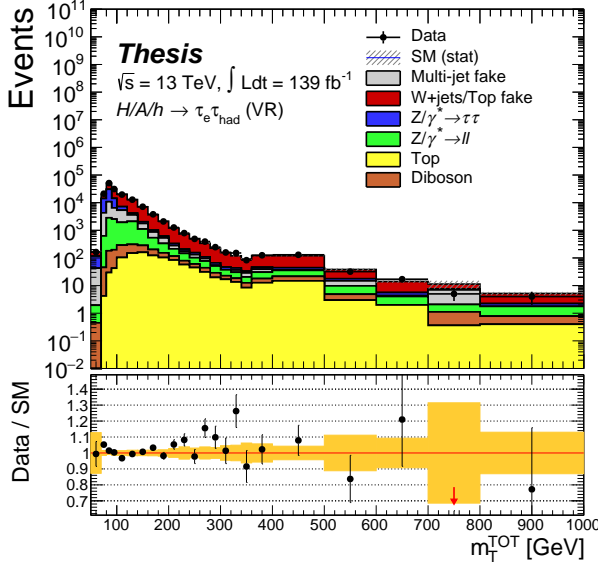
The final validation region modelling is shown in Figures 4.17, 4.18, 4.19 and 4.20 with only the statistical uncertainty considered at this point. In general, the modelling is satisfactory and any deviations from the expectation can be covered by the systematic uncertainty.



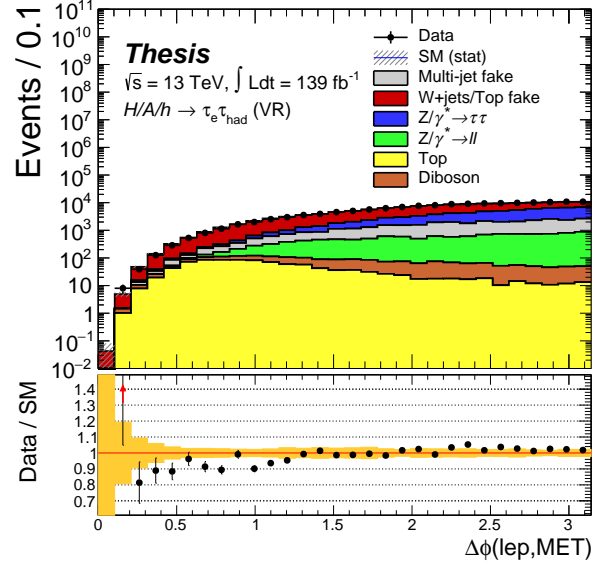
(a) $e\tau_{\text{had}} p_T^\ell$



(b) $e\tau_{\text{had}} p_T^{\text{had}}$

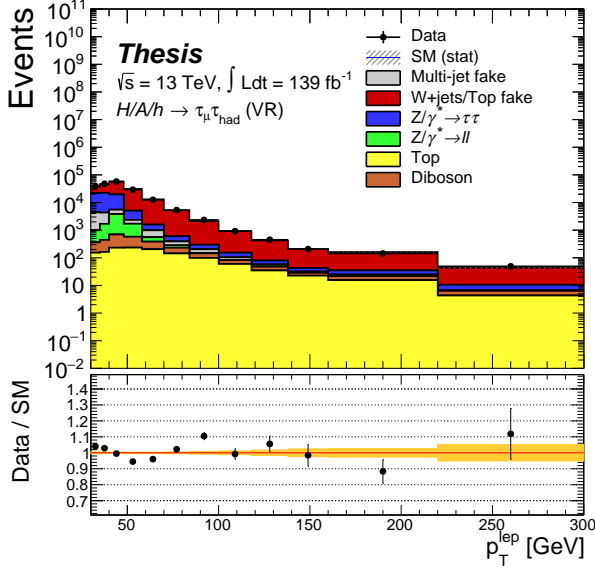


(c) $e\tau_{\text{had}} M_T^{\text{TOT}}$

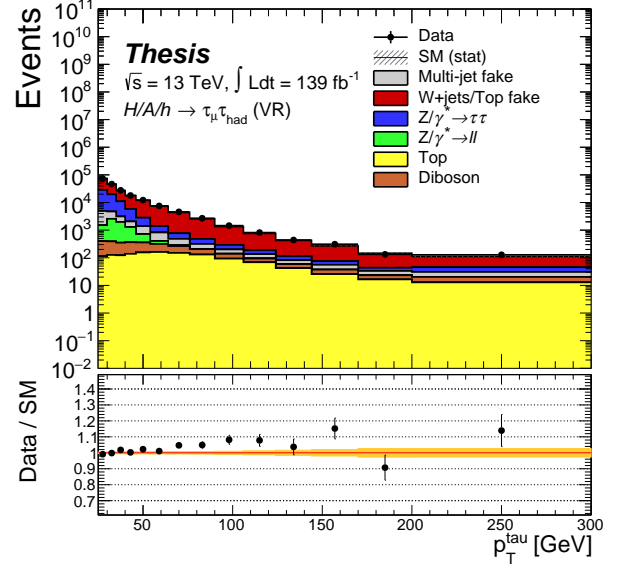


(d) $e\tau_{\text{had}} \Delta\phi(\ell, E_T^{\text{MISS}})$

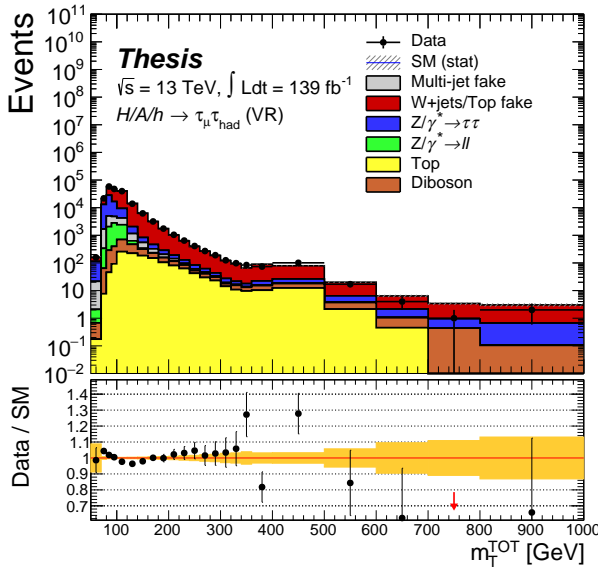
Figure 4.17: The p_T^ℓ , p_T^τ , M_T^{TOT} and $\Delta\phi(\ell, E_T^{\text{MISS}})$ distributions in the b -veto validation region for the $e\tau_{\text{had}}$ channel. The ratio plots show the ratio of the data and the total MC prediction. The uncertainty bands consider only the statistical uncertainty on the background.



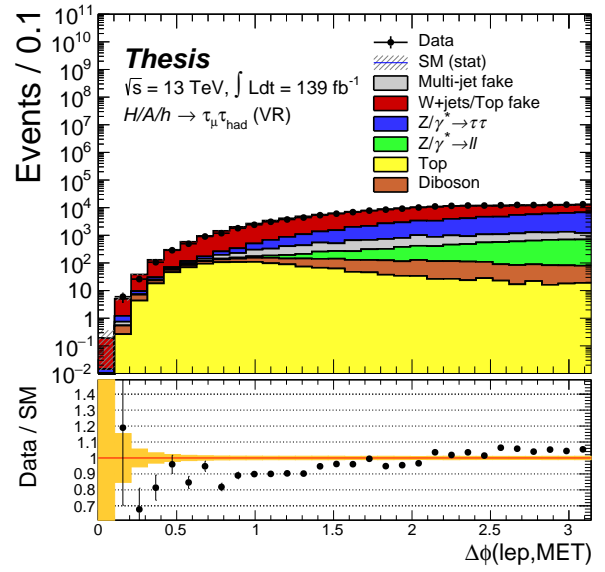
(a) $\mu\tau_{\text{had}} p_T^\ell$



(b) $\mu\tau_{\text{had}} p_T^{\tau_{\text{had}}}$

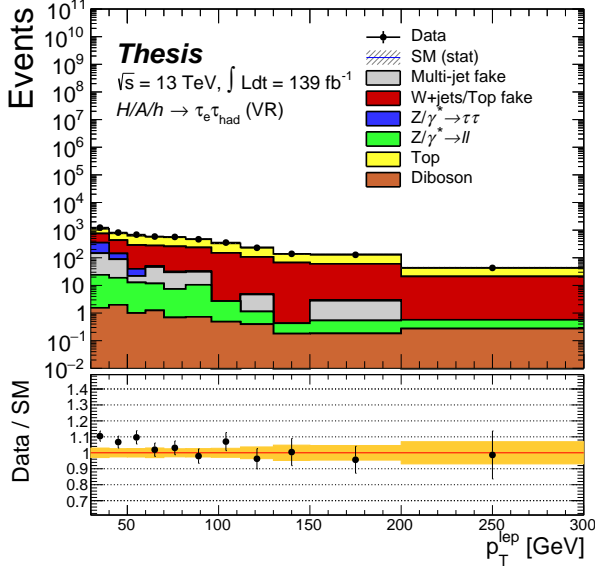


(c) $\mu\tau_{\text{had}} M_T^{\text{TOT}}$

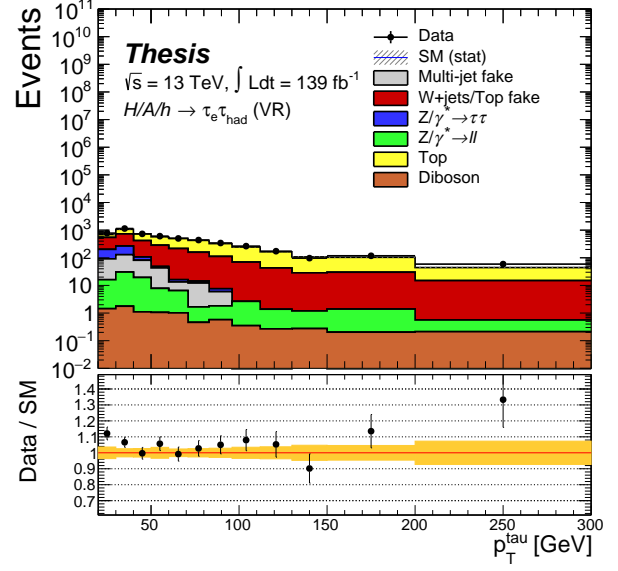


(d) $\mu\tau_{\text{had}} \Delta\phi(\ell, E_T^{\text{MISS}})$

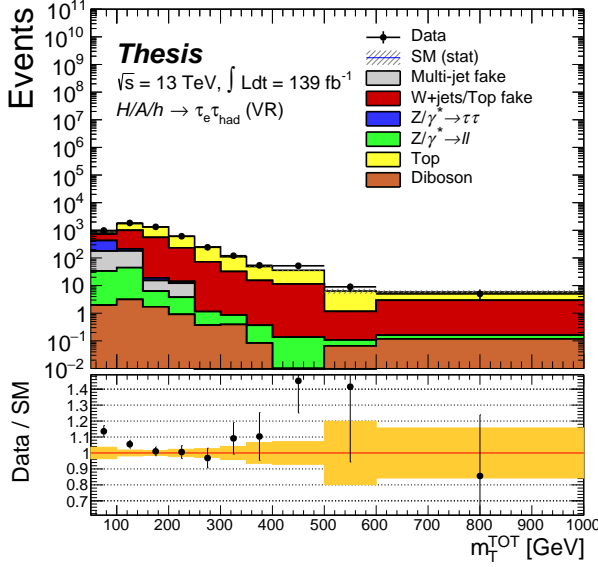
Figure 4.18: The p_T^ℓ , p_T^τ , M_T^{TOT} and $\Delta\phi(\ell, E_T^{\text{MISS}})$ distributions in the b -veto validation region for the $\mu\tau_{\text{had}}$ channel. The ratio plots show the ratio of the data and the total MC prediction. The uncertainty bands consider only the statistical uncertainty on the background.



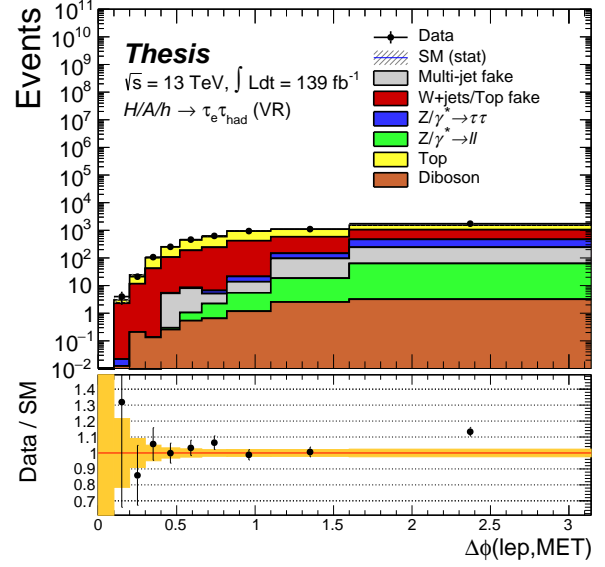
(a) $e\tau_{\text{had}} p_T^\ell$



(b) $e\tau_{\text{had}} p_T^{\tau_{\text{had}}}$

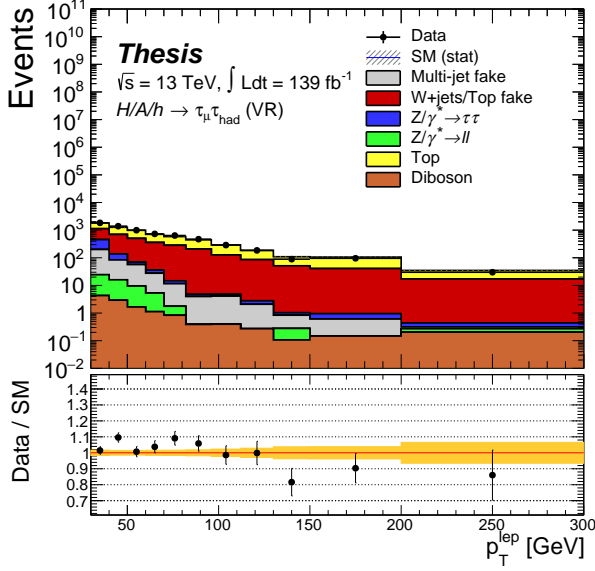


(c) $e\tau_{\text{had}} M_T^{\text{TOT}}$

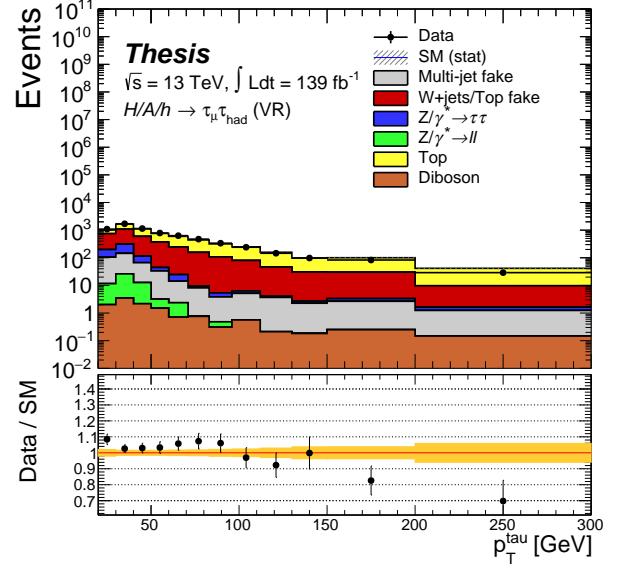


(d) $e\tau_{\text{had}} \Delta\phi(\ell, E_T^{\text{MISS}})$

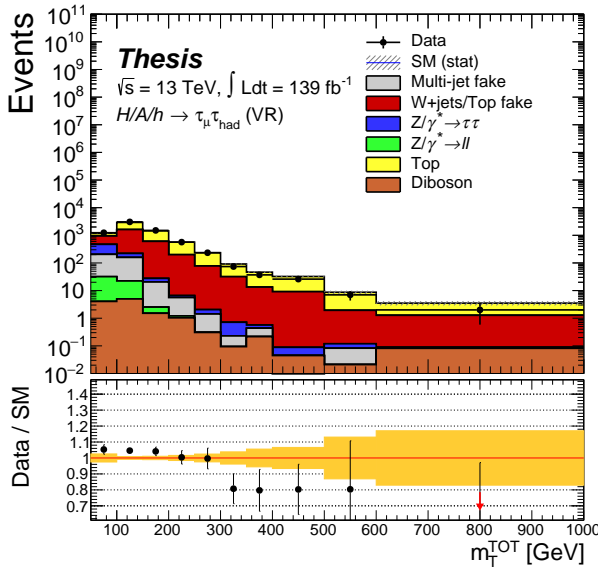
Figure 4.19: The p_T^ℓ , p_T^τ , M_T^{TOT} and $\Delta\phi(\ell, E_T^{\text{MISS}})$ distributions in the b -tag validation region for the $e\tau_{\text{had}}$ channel. The ratio plot shows the ratio of the data and the total MC prediction. The uncertainty bands consider only the statistical uncertainty on the background.



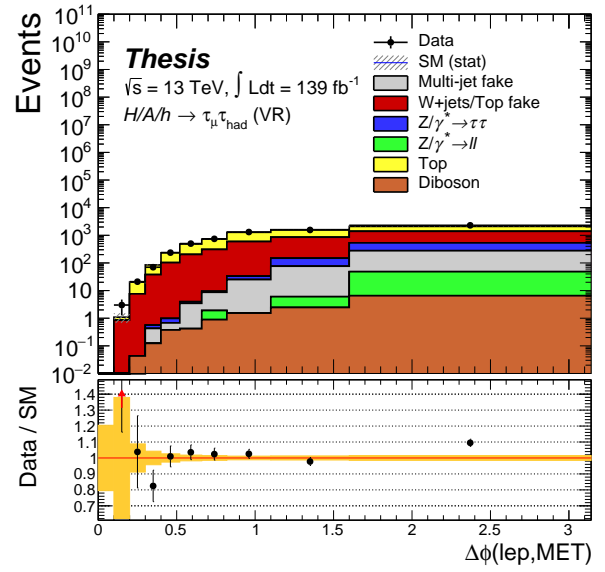
(a) $\mu\tau_{\text{had}} p_T^\ell$



(b) $\mu\tau_{\text{had}} p_T^{\tau_{\text{had}}}$



(c) $\mu\tau_{\text{had}} M_T^{\text{TOT}}$



(d) $\mu\tau_{\text{had}} \Delta\phi(\ell, E_T^{\text{MISS}})$

Figure 4.20: The p_T^ℓ , p_T^τ , M_T^{TOT} and $\Delta\phi(\ell, E_T^{\text{MISS}})$ distributions in the b -tag validation region for the $\mu\tau_{\text{had}}$ channel. The ratio plot shows the ratio of the data and the total MC prediction. The uncertainty bands consider only the statistical uncertainty on the background.

4.6 Systematic Uncertainties

To ensure the reliability of the analysis, systematic uncertainties are considered in a variety of ways. It is important to differentiate between experimental uncertainties and theoretical uncertainties. Experimental uncertainties are often calculated by ATLAS combined performance groups and their recommendations are then implemented at the analysis level. Experimental uncertainties can include different types such as data-driven fake estimation uncertainties discussed in Section 4.5.1, beam condition uncertainties (e.g., luminosity, pile-up), or uncertainties in the calibration of the physics objects used in the analysis (e.g., tau, electron, muon reconstruction). On the other hand, theoretical uncertainties arise from the calculation of the cross-section or signal acceptance due to PDF and strong coupling constant (α_s) variations. Uncertainties can affect either the shape of the distribution, the normalisation of the distribution, or both.

In some cases the analysis team must evaluate systematics themselves, particularly for some theoretical uncertainties. For example, centrally produced t -quark related MC samples which vary the PS model, matrix element generator, ISR/FSR and PDF are provided for the top theory uncertainties. To evaluate them, one must perform the analysis for each case and measure the difference in yield. For other samples such as the Z +jets background, the centrally provided LPXKFACTORTOOL uses the prescription in [162] to derive the variations for each analysis and apply them as weights to the n-tuple. The signal theory uncertainties are evaluated in a similar way to the top theory systematics. However, since signals are unique to each analysis, relatively small personal samples are generated and the truth level difference in the cross-section or SR acceptance per variation is evaluated. This prescription is followed for variations on the PDF, α_s , ISR and FSR. The MC generator parameters known as the renormalisation (μ_r) and factorisation (μ_f) scales are used for QCD calculations to cancel out the divergences incurred when calculating the matrix element. By varying each one relative to the other, the uncertainty from missing higher orders in the cross-section can be calculated.

For the analysis implementation of systematic uncertainties, there are typically two types of variation: weight and kinematic. The weight variation is simply taken from the nominal tree in the analysis n-tuple and the resulting event weight is used in the analysis chain to build an M_T^{TOT} template from the systematic variation. Kinematic variations typically result in a change to a physics object, they have their own TTree in the n-tuple. In this case, to build the variation template, the whole analysis chain is done separately for this TTree in the same way as the nominal case. In the end, the majority of the uncertainties have unique background or signal template distributions and these are added as nuisance parameters in the fitting procedure described in Section 4.7.

Table 4.5 provides a description of each uncertainty group and the number of template variations from the nominal M_T^{TOT} distribution that contribute to the final fit. These uncertainties are then combined in quadrature to obtain a pre-fit uncertainty band. In Figure 4.21, the four $\tau_{\text{lep}}\tau_{\text{had}}$ signal regions are shown, along with the pre-fit uncertainty band.

Overall, the uncertainty band accounts for any discrepancies between the observed data and the expected background from MC simulation. However, in the $\mu\tau_{\text{had}}$ channel at high M_T^{TOT} , there is some overestimation of the background, which is remedied in the subsequent fitting procedure discussed in the next section.

Table 4.5: A summary of each systematic set, showing the number of nuisance parameters (NPs) entering the fit and the number of variations there are.

Systematic Set (Label)	Variations	NPs	Description
Experimental Uncertainties			
Tau (TAUS)	18	9	Reconstruction, ID, e -veto and energy scale
Electron (EG/El)	24	12	Reconstruction, trigger, ID, ISO and energy scale
Muon (MUON)	30	15	Reconstruction, trigger, ID, ISO and energy scale
Jet (JER/JES/JVT)	26	17	Energy scale, resolution and vertex tagging
E_T^{MISS} (METsoft)	4	3	Soft terms in E_T^{MISS} calculation
Flavour tagging (b -tag)	28	14	Efficiencies from b -tagging software
Pile-up (prw)	2	1	Uncertainty on the pile-up profile
Luminosity (Lumi)	1	1	Uncertainty on the integrated luminosity measurement (3.2 %) [208, 209]
Theoretical Uncertainties			
Z +jets modelling (LPX)	24	12	PDF, α_s , QCD scale
Top modelling (TTBAR)	6	4	Matrix element generator, PS, ISR, FSR
Signal modelling (AU)	2	2	μ_r μ_f scale, PDF, α_s , ISR, FSR
Diboson & $t\bar{t}$ σ (xsec)	2	2	Uncertainty assigned to the Diboson (10 %) and $t\bar{t}$ (6%) cross-section [170, 177, 210]
Data-driven background (FakeFactor)	44	22	Data-driven background uncertainties detailed in Section 4.5.1
Total	211	114	

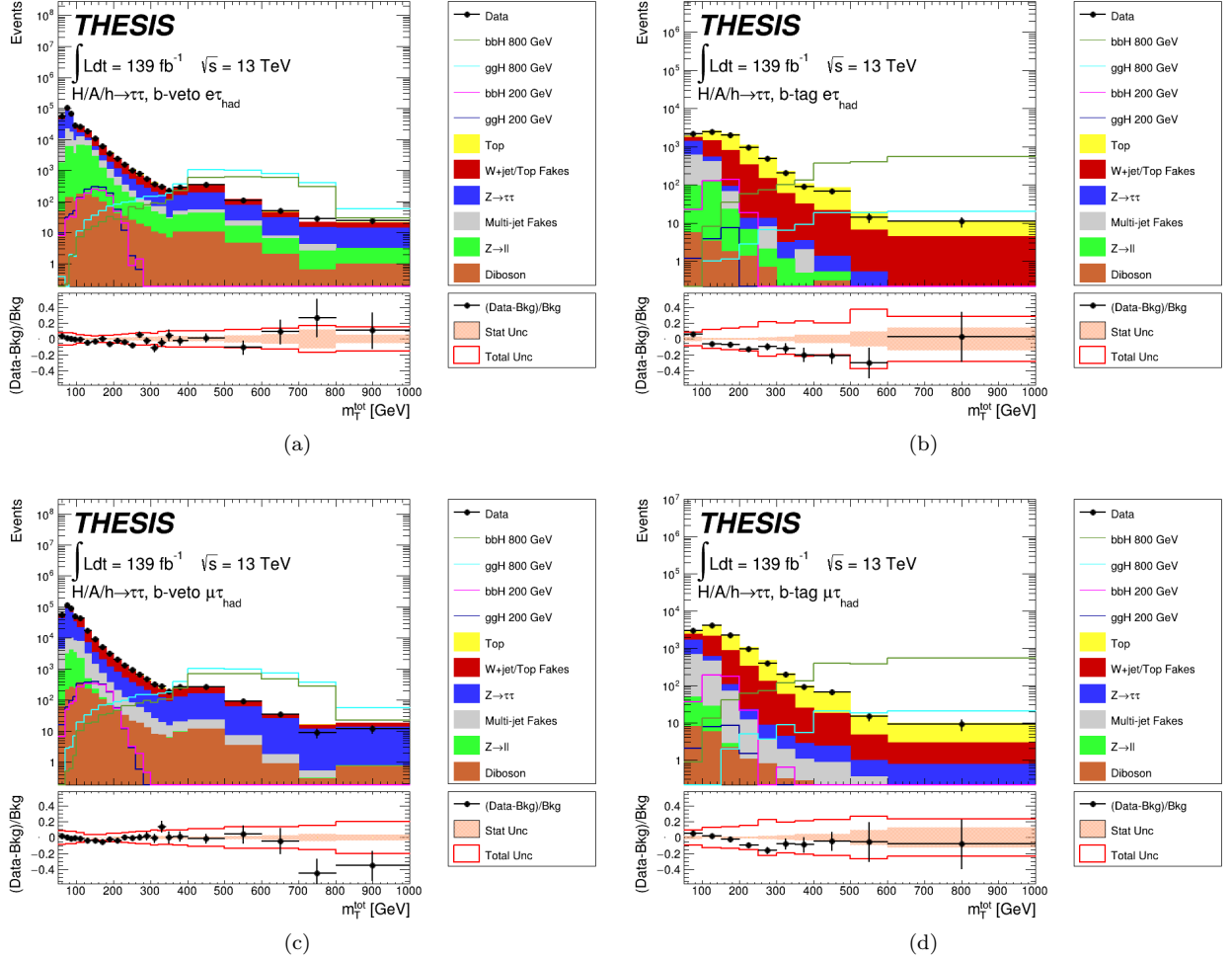


Figure 4.21: The pre-fit distributions for the (a) $e\tau_{\text{had}}$ b -veto (b) $e\tau_{\text{had}}$ b -tag (c) $\mu\tau_{\text{had}}$ b -veto and (d) $\mu\tau_{\text{had}}$ b -tag signal regions. The ggH and bbH signals are shown for the 200 GeV and 800 GeV mass points. Example bbH and ggH signals normalised to a cross section of 1 pb are superimposed for the 200 GeV and 800 GeV mass points. The ratio plot is defined as the ratio of the total background subtracted from the data and the total background. The filled uncertainty band represents the statistical uncertainty on the background and the red line indicates the total pre-fit uncertainty from all the variations added in quadrature.

4.7 Statistical Analysis

In statistical analysis, fitting techniques are commonly employed to estimate important parameters from a given distribution. The parameter of interest in this analysis is the signal strength (μ), defined as the ratio of the fitted signal cross-section \times branching ratio ($\sigma \times \mathcal{B}$) to the one predicted by the signal model. The signal strength is a crucial quantity as it indicates the presence or absence of the signal process in the data. Specifically, $\mu = 0$ corresponds to a scenario where no signal is observed (b-only hypothesis), while $\mu = 1$ corresponds to the scenario where the signal process is present in addition to the background (s+b hypothesis). However, estimating the signal strength is complicated by the presence of nuisance parameters ($\boldsymbol{\theta}$) that parameterise the systematic uncertainties in the measurement. They must be accounted for in the fitting procedure to obtain accurate estimates of the signal strength.

4.7.1 Profile Likelihood Fit

A fitting technique suitable for this analysis is a profile likelihood fit, which employs the maximum likelihood method, among other techniques [211]. Suppose one has N statistically independent bins with values $\mathbf{n} = (n_1, n_2, \dots, n_N)$, all following the same probability density function ($f(n_i; \mu, \boldsymbol{\theta})$). Here, the probability to observe a bin value n_i depends on the fit parameters μ and $\boldsymbol{\theta}$. A basic likelihood function such as:

$$L(\mu, \boldsymbol{\theta}) = \prod_{i=1}^N f(n_i; \mu, \boldsymbol{\theta}) \quad (4.7)$$

can be constructed and the fit parameters are estimated by maximising the likelihood function.

To construct the likelihood for this analysis, $f(n_i; \mu, \boldsymbol{\theta})$ is assumed to be a Poisson distribution with the expected number of events (E_i) as the mean. The fit parameter μ is introduced by E_i , which is defined as:

$$E_i = \mu s_i + b_i \quad (4.8)$$

where s_i and b_i are dependent on $\boldsymbol{\theta}$ and represent the predicted signal and background events in a given bin, respectively. The signal strength therefore acts as a normalisation factor to the signal prediction from the model under test, providing information on the level of agreement between the data and the s+b hypothesis. This forms the first term of the final likelihood which is represented by the equation:

$$L(n_i, \boldsymbol{\theta}^0; \mu, \boldsymbol{\theta}) = \prod_{i=1}^N \frac{(\mu s_i + b_i)^{n_i}}{n_i!} e^{-(\mu s_i + b_i)} \times \prod_{j=1}^M \frac{u_j^{m_j}}{m_j!} e^{-u_j} \times \prod_{k \in \text{systs}} G(\boldsymbol{\theta}_k^0 - \boldsymbol{\theta}_k) \quad (4.9)$$

where the second term represents extra information gathered from auxiliary measurements and the third term parameterises the nuisance parameters, both terms are detailed below.

For a profile likelihood fit in ATLAS analyses, the background normalisation parameter (μ_b) is typically treated as a free nuisance parameter [212]. If μ_b has no constraint, the value of μ

can be set arbitrarily, highlighting the importance of constraining the background normalisation. To perform the constraint, a measurement from a sideband control region is often added as an auxiliary measurement to profile the likelihood and provide information on the background. In this analysis, the TCR discussed in Section 4.5.2 serves this purpose and is included with the signal regions in the fit. A Poisson distribution can also be used to describe this action, as shown in the second term in Equation 4.9. This term in the likelihood represents a control region auxiliary measurement with a distribution of M bins with contents \mathbf{m} and background expectation u_j , which is also a function of $\boldsymbol{\theta}$.

Each systematic uncertainty can also be considered as an auxiliary measurement (forming a set of nuisance parameters with central values $\boldsymbol{\theta}^0$). The third term in Equation 4.9 represents this by introducing a set of unit-width Gaussian probability distribution functions (G) that provide information on each systematic uncertainty as a Gaussian constraint [212].

To extract physics results for this analysis, the methods above are implemented using the HISTFITTER software [212], which is built on the popular analysis packages HISTFACTORY and ROOSTATS [213, 214]. The four $\tau_{\text{lep}}\tau_{\text{had}}$ ($e\tau_{\text{had}}$ and $\mu\tau_{\text{had}}$ channels, b -veto and b -tag categories) and two $\tau_{\text{had}}\tau_{\text{had}}$ (b -veto and b -tag categories) signal regions are combined with the two $\tau_{\text{lep}}\tau_{\text{had}}$ top control regions ($e\tau_{\text{had}}$ and $\mu\tau_{\text{had}}$ channels, b -tag category) in a simultaneous fit. The final background-only (μ fixed to zero) post-fit plots are shown for the four $\tau_{\text{lep}}\tau_{\text{had}}$ and $\tau_{\text{had}}\tau_{\text{had}}$ regions ($e\tau_{\text{had}}$ and $\mu\tau_{\text{had}}$ merged) in Figure 4.22. The fit has the ability to change the background prediction compared to the pre-fit plots if the best fit $\boldsymbol{\theta}$ values differ to $\boldsymbol{\theta}^0$. The best fit values of the nuisance parameters and how much they are pulled from the central value can be visualised in pull plots, which are typically used to assess the quality of the fit, examples can be found in Appendix B.2. Improved knowledge entering the fit from auxiliary measurements and correlations between nuisance parameters are able to reduce the total uncertainty compared to the pre-fit uncertainties from Figure 4.21.

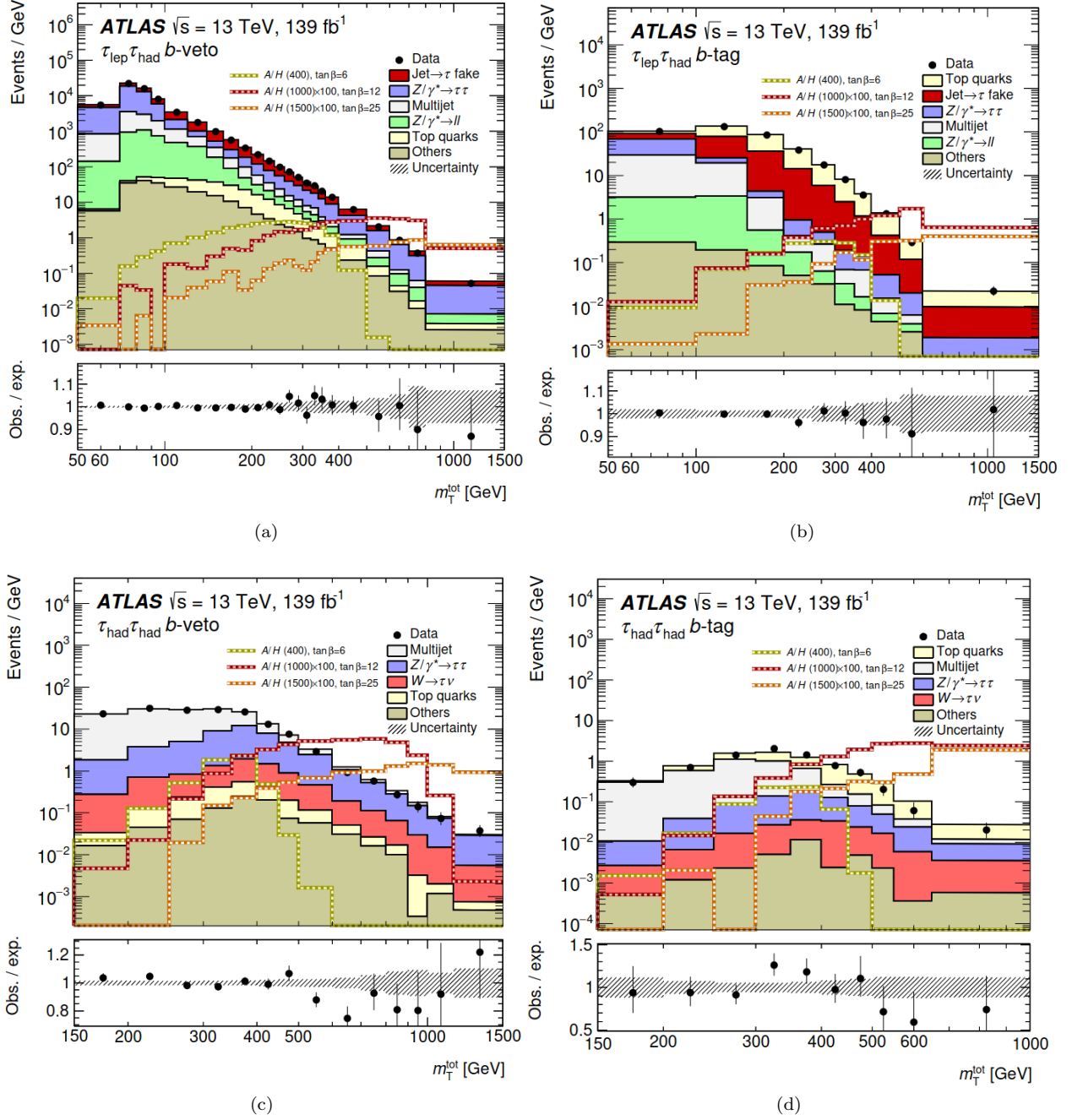


Figure 4.22: The background-only post-fit distributions for the (a) $\tau_{\text{lep}}\tau_{\text{had}}$ b -veto (b) $\tau_{\text{lep}}\tau_{\text{had}}$ b -tag (c) $\tau_{\text{had}}\tau_{\text{had}}$ b -veto (d) $\tau_{\text{had}}\tau_{\text{had}}$ b -tag signal regions [8]. Signals are superimposed for 400 GeV ($\tan\beta = 6$), 1000 GeV ($\tan\beta = 12$) and 1500 GeV ($\tan\beta = 25$). The ‘jet $\rightarrow \tau$ fake’ label represents the W + jets/top fakes. The ratio plot shows the ratio of the data and the total MC prediction. The uncertainty band represents the total post-fit uncertainty.

4.7.2 Hypothesis Testing and Exclusion Limits

With the likelihood function defined, conclusions can be drawn by testing hypothesised values of μ to either reject the b-only hypothesis or set limits on μ using the frequentist approach. The optimal way to separate the b-only from the $s + b$ hypothesis is via the profile likelihood ratio. A test statistic (t_μ) is therefore derived based on this, where t_μ has the ability to characterise a full dataset as a number. If $\mu \geq 0$ is required, the test statistic can be defined by the following relations for $\mu > 0$ and $\mu = 0$:

$$\tilde{t}_\mu = \begin{cases} -2 \ln \frac{L(\mu, \hat{\hat{\theta}})}{L(0, \hat{\hat{\theta}})} & \text{if } \hat{\mu} < 0, \\ -2 \ln \frac{L(\mu, \hat{\hat{\theta}})}{L(\hat{\mu}, \hat{\hat{\theta}})} & \text{if } 0 \leq \hat{\mu} \leq \mu, \\ 0 & \text{if } \hat{\mu} > 0 \end{cases} \quad (4.10)$$

$$t_0 = \begin{cases} -2 \ln \frac{L(0, \hat{\hat{\theta}})}{L(\hat{\mu}, \hat{\hat{\theta}})} & \text{if } \hat{\mu} \geq 0, \\ 0 & \text{if } \hat{\mu} < 0. \end{cases} \quad (4.11)$$

where $L(\hat{\mu}, \hat{\hat{\theta}})$ corresponds to the unconditionally maximised likelihood, whereas $L(\mu, \hat{\hat{\theta}})$ corresponds to the maximised likelihood for a given value of μ .

In order to derive the $\sigma \times \mathcal{B}$ upper limits shown in the subsequent chapters, p -values must be determined. The p -value is defined as the probability of finding the data as far away or more from the hypothesis as the observed data, should the experiment be repeated. The definitions for the p -values under different hypotheses are represented by:

$$p_0 = \int_{t_{0,\text{obs}}}^{\infty} g(t_0|0) dt_0 \quad (4.12)$$

$$p_\mu = \int_{t_{\mu,\text{obs}}}^{\infty} g(t_\mu|\mu) dt_\mu \quad (4.13)$$

where $g(t_0|0)$ and $g(t_\mu|\mu)$ are the probability density functions of the test statistics under the assumption of the b-only hypothesis and a hypothesised μ value (s+b hypothesis), respectively. The symbol $t_{0,\text{obs}}$ represents the observed test statistic calculated from the data. When quoting physics results, the significance is usually used, the p -value can easily be transformed to this using the relation:

$$Z = \Phi^{-1}(1 - p) \quad (4.14)$$

where Φ is the cumulative Gaussian function. A significance of 5σ is often the benchmark for discovery, which is a p -value of 2.87×10^{-7} .

The challenge is to determine the distribution of the test statistic for each hypothesis, this is essentially a visualisation of how $\hat{\mu}$ would change if the experiment was conducted many times should the s+b hypothesis be true. Therefore, each distribution follows a Gaussian

distribution. In general, the test statistic distribution can be retrieved by randomly sampling the test statistic using pseudo-datasets called toy MC. This is typically time consuming and computationally expensive. Thankfully, an approximation can be used for distributions with a large number of events (N), this is called the asymptotic approximation, detailed in [215]. The asymptotic approximation uses the work of Wilks [216] and Wald [217] to prove that $g(t|\mu)$ follows a non-central chi-square distribution for large N when considering one parameter of interest. One can then use the MC predicted b-only and s+b templates (so-called Asimov datasets for this case) to estimate the non-centrality parameter Λ of the chi-square distribution, resulting in an estimate for $g(t|\mu)$.

The distributions of the test statistic $g(t_0|0)$ and $g(t_\mu|\mu)$ can be visualised using the schematic in Figure 4.23. It shows the corresponding distribution of the test statistic for the s+b ($\mu=1$) and the b-only ($\mu=0$) hypotheses ($g(t; \text{b-only})$ and $g(t; \text{s+b})$ in this case). As $\mu \rightarrow 0$, $g(t; \text{s+b}) \rightarrow g(t; \text{b-only})$. The observed test statistic value (t_{obs} in this case) computed from the data is also shown. The relevant observed p -values can be obtained from the shaded areas. The expected p -values are obtained by placing a vertical line at the median value of the b-only distribution (the case where the data exactly matches the background) and then computing the corresponding CL_{s+b} for this case. If this derived p -value is lower than some pre-defined value the s+b hypothesis can be excluded. From this formulation, it is clear to see how upper limits on μ can be achieved by finding the μ and $g(t; \mu s + b)$ for which the CL_{s+b} is less than 0.05, for example.

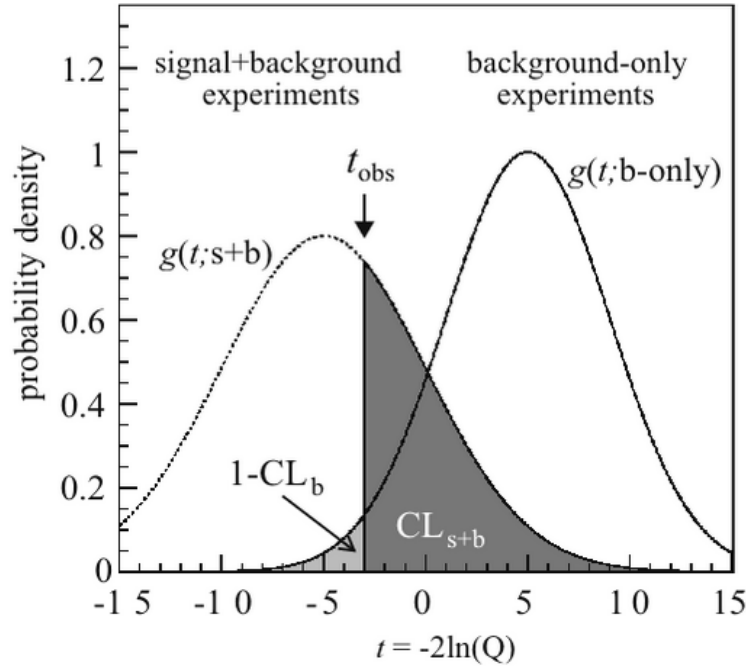


Figure 4.23: An illustrative example of the test statistic distribution for the background-only ($g(t; \text{b-only})$) and s+b ($g(t; \text{s+b})$) hypotheses, taken from [218]. The observed test statistic from the data t_{obs} is shown. The plot can be used to represent the compatibility of t_{obs} with each hypothesis.

In practice, the CL_s method described in [219] and is used to derive the upper limits for this analysis. The CL_s is determined using the equation:

$$CL_s = \frac{CL_{s+b}}{CL_b} \quad (4.15)$$

where the CL_{s+b} and CL_b fill areas shown in Figure 4.23 are the s+b and b-only confidence levels, equal to p_μ and $1 - p_0$, respectively. A given signal hypothesis can be excluded if $1 - CL_s < CL$, where CL is left for the user to decide, in this case it is 0.95 (95% confidence). The CL_s method is preferred over simply using the p -values as it has been found to be more conservative in its calculation [219].

The limit on μ can then be easily transformed to the limit on the cross-section \times branching fraction of a MSSM Higgs decaying to two taus ($\sigma \times \mathcal{B}(H/A/h \rightarrow \tau\tau)$) by using signals normalised to $\sigma = 1$ pb. The corresponding limit for the ggH and bbH signals are shown in Figure 4.24. The 95 % CL observed (expected) limits are 1.8 fb (3.8 fb) for ggH and 1.1 fb (2.2 fb) for bbH production at $m_{H/A/h} (m_\phi) = 1$ TeV. The lowest p_0 for ggH (bbH) is 2.2σ (2.7σ) at $m_\phi = 400$ GeV. Finally, by inspecting the predicted cross-sections from well-motivated MSSM models in [204], upper limits can be set on $\tan \beta$ against m_A for particular models, as shown in Figure 4.24(c) for the M_h^{125} scenario. The 95 % CL observed (expected) limits exclude $\tan \beta > 21$ (24) at $m_A = 1.5$ TeV for this particular model.

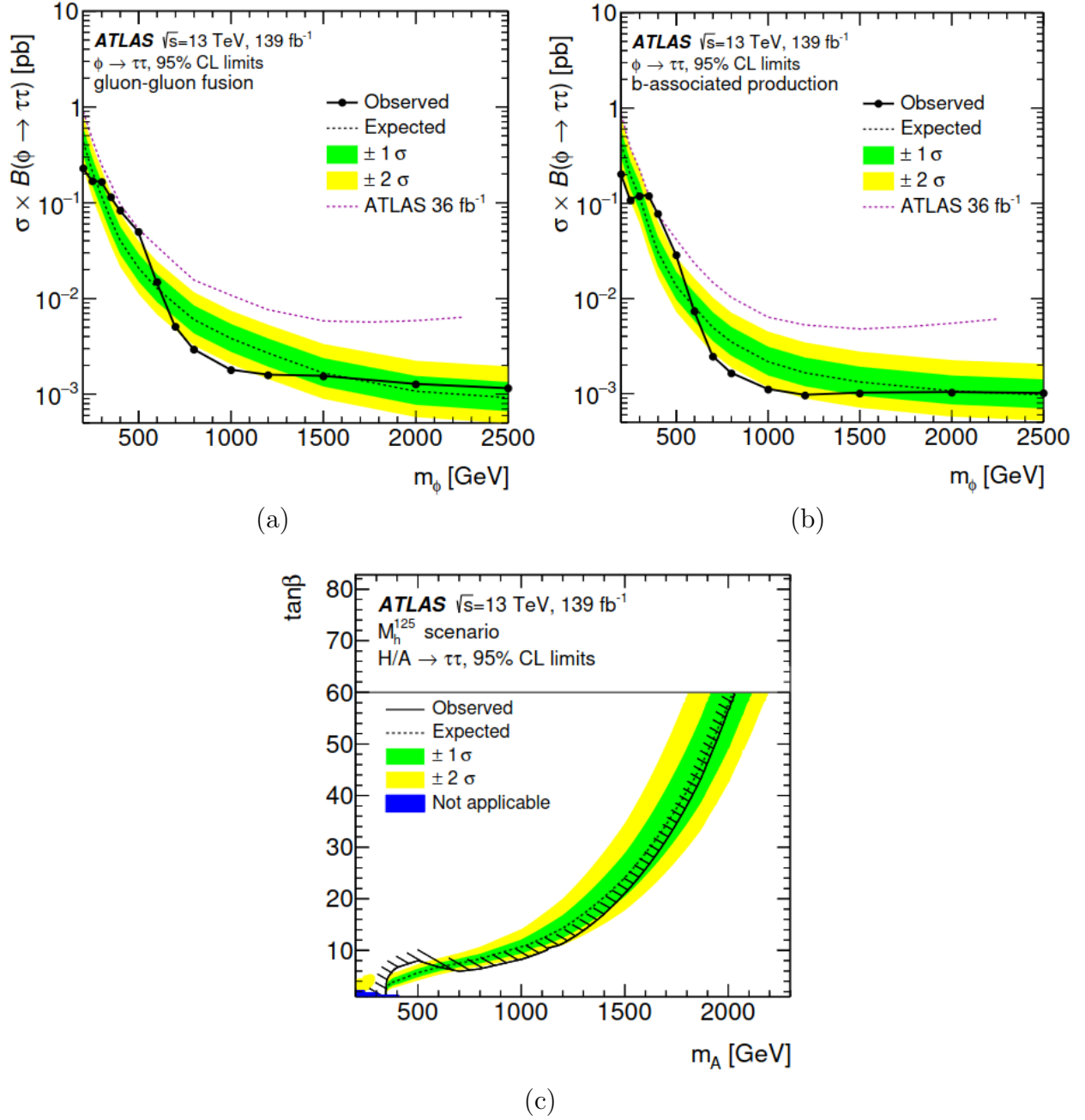


Figure 4.24: The 95% CL upper limits on the $\sigma \times \mathcal{B}(H/A/h \rightarrow \tau\tau)$ as a function of M_ϕ for the (a) ggH and (b) bbH production modes, and (c) the 95% CL upper limits on $\tan\beta$ for different values of m_A for the M_h^{125} benchmark scenario [8, 220]. The black solid (dashed) line indicates the observed (expected) limit. The green and yellow bands represent the $\pm 1\sigma$ and $\pm 2\sigma$ uncertainties on the expected limit. The limits are calculated using the 139 fb^{-1} full Run-II ATLAS dataset from a combined fit of the $\tau_{\text{lep}}\tau_{\text{had}}$, $\tau_{\text{had}}\tau_{\text{had}}$ signal regions and the $\tau_{\text{lep}}\tau_{\text{had}}$ top control regions. The red dashed lines in (a) and (b) show the result from the 36 fb^{-1} result [57]. The solid blue area in (c) indicates the regions in which the M_h^{125} scenario provides predictions that are incompatible with the observed $m_h = 125$ GeV measurement by more than 3σ [221].

Chapter 5

Search for Heavy Z' Bosons in the $\tau\tau$ Final State

5.1 Analysis Strategy

A compelling extension to the Standard Model could include the existence of a spin-1 Z' particle produced via quark-antiquark annihilation. The leading order Feynman diagram for the Drell-Yan (DY) production of a Z' boson is depicted in Figure 5.1, and the corresponding theory motivation is outlined in Chapter 2. In this chapter, a re-interpretation of the legacy full Run-II MSSM Higgs boson search [8] from Chapter 4 is performed for the detection of Z' signals predicted by the SSM. The search strategy is mostly identical to the legacy case, except for the event categorisation. The signal region categorisation treatment differs for Z' signals when compared to the legacy MSSM Higgs Boson search. In this case, there is minimal benefit in segregating events into b -veto and b -tag categories. Instead, a b -inclusive (b -inc) category is defined by merging the two. After validating the signal samples and determining the relevant systematics, a statistical analysis is performed to derive upper limits on the $\sigma \times \mathcal{B}(Z' \rightarrow \tau\tau)$. The chapter ends with presentation of preliminary results for the next iteration of the ATLAS Heavy Resonance Combination (HRC) search for HVT V' bosons, building on the results outlined in Section 2.3.2.

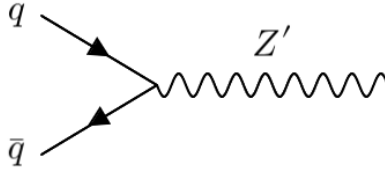


Figure 5.1: The leading order Feynman diagram for the Drell-Yan production of a Z' particle.

5.2 Monte Carlo Signal Samples

To generate the necessary Z' samples, DY $Z/\gamma^* \rightarrow \tau^+\tau^- + \text{jets}$ invariant mass sliced samples are simulated at LO starting from a mass of 120 GeV, with the last slice requiring an invariant mass above 5 TeV. The relevant generator information used to derive LO $Z/\gamma^* \rightarrow \tau\tau + \text{jets}$ samples is detailed in Table 5.1, more information on the samples can be found in Appendix C.2 showing the exact mass slices used and the number of events generated. The sliced samples are then reweighted using the TAU SPINNER TOOL to narrow width Z' resonances ranging in mass from 0.2 TeV to 6.0 TeV. The mass slicing is necessary to get reasonable statistics at high resonance mass for a moderate amount of total simulated events. Once the Z' samples are produced for each resonance mass, a final weighting is applied to take into account QCD NNLO corrections. These corrections are applied using the LPXKFACTORTOOL which employs the VRAP 0.9 software and the CT14NNLO PDF set to derive corrections for each resonance mass [162]. In this case, the analogous electroweak corrections are not applied since they are Z' model dependent. The background and data samples are shown in Table 4.1, they are the same as the ones used in the legacy analysis.

Table 5.1: Overview of the Z' signal samples for reweighted LO Drell-Yan $Z/\gamma^* \rightarrow \tau\tau + \text{jets}$ invariant mass slices, including information on the generator, PDF set, the underlying event, parton shower and hadronisation (UEPS) model, and the cross-section calculation order ($\mathcal{O}(\sigma)$).

Process	Generator	PDF	UEPS	$\mathcal{O}(\sigma)$
Z'	PYTHIA 8.243 [133]	NNPDF 2.3 LO	PYTHIA 8.243	NNLO [162]

5.2.1 The Reweighting of Drell-Yan $Z/\gamma^* \rightarrow \tau\tau + \text{jets}$ Sliced Samples to Z' Signals

The concept of spin, explained in Section 2.1, is integral in the TAU SPINNER TOOL reweighting. When a particle decays to its constituents, the spins of the resulting particles can become dependent on (correlated with) each other. The spin correlations then have implications on the directions of the tau decay products. Other useful quantities are the closely related helicity and polarisation vectors which are the projection of the particle spin along its direction of motion and the alignment of the spin along a particular axis, respectively. The TAU SPINNER TOOL [222, 223] is capable of reconstructing and modifying tau spin correlations and calculating polarisation vectors using the tau kinematics and decay products from the event record.

The possible helicity states of a spin-1 Z/γ^* decaying to $\tau^+\tau^-$ are represented in Figure 5.2. The possible longitudinal (component along the direction of motion) polarisations for the two taus are $(P_{\tau+}, P_{\tau-}) = (+1, +1)$ or $(-1, -1)$ with probabilities equal to p_{τ}^Z and $1-p_{\tau}^Z$, respectively [224]. The p_{τ}^Z state probability is dependent on the scattering angle of the tau and \sqrt{s} , and is determined by averaging over all possible initial state quark configurations. The

initial quark states are stochastically inferred from an approximation of the effective Born level cross-section, the kinematics of the tau and Z boson and the usage of the NNPDF2.3LO PDF set. The recipe for calculating the Born level cross-section is detailed in [225]. In the $\tau\tau$ final state, the weight per event is given by:

$$wt_{SM}^{spin} = R_{ij} h^i h^j \quad (5.1)$$

where R_{ij} is the full spin correlation and spin states, and $h^{i/j}$ are the time and space components of the polarimetric vectors for the two taus [222].

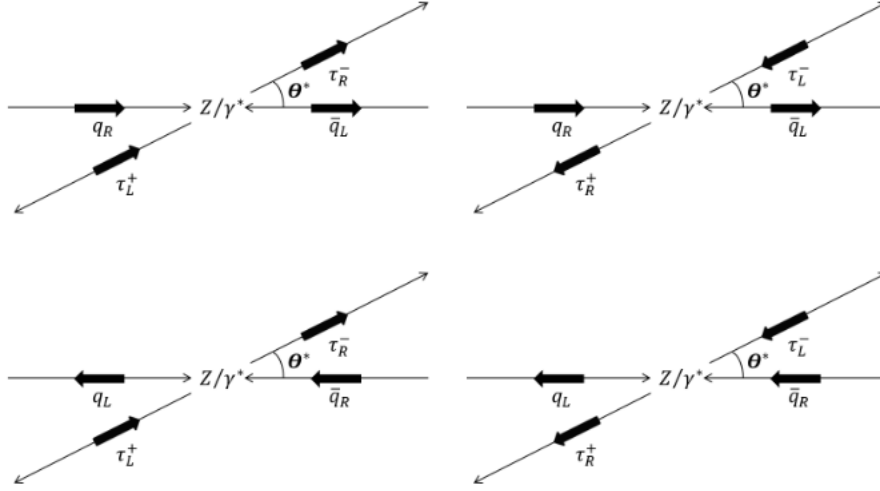


Figure 5.2: The possible tau helicity states for the $q\bar{q} \rightarrow Z/\gamma^* \rightarrow \tau^+\tau^-$ decay, taken from [226]. The handedness of the particle is also shown.

Usually, only longitudinal spin correlations are accounted for, the transverse direction correlations do not lead to measurable effects. By disregarding the transverse direction and assuming the ultra-relativistic limit, the spin weight can be expressed as:

$$wt_{SM}^{spin} = 1 + h_z^+ h_z^- + P_\tau h_z^+ + P_\tau h_z^- \quad (5.2)$$

for the $Z/\gamma^* \rightarrow \tau\tau$ case. Here, P_τ denotes the polarisation of the tau in a mixed quantum state, and h_z is the z -direction component of the polarimetric vector. The polarimetric vector is computed differently by the TAUSPINNERTOOL, depending on the tau decay mode and event topology. Lastly, the aforementioned approximations require that the polarisation is described as follows:

$$P_\tau = 2p_\tau^Z - 1 \quad (5.3)$$

which is a linear function of the probability of the tau polarisation states. By applying these approximations, the wt_{BSM}^{spin} can be determined from the deduced p_τ^Z and polarimetric vectors.

Another TAUSPINNERTOOL feature is the capability to account for BSM contributions to the amplitude of $q\bar{q} \rightarrow Z/\gamma^* \rightarrow \tau\tau$ and account for the relevant interference effects from SM contributions. The new contribution is assumed to modify the spin correlations between

the outgoing two taus only through the inclusion of additional angular dependence. Consequently, the existing algorithm for determining the spin weight per event for the SM case (wt_{SM}^{spin}) can be adapted to obtain a BSM spin weight (wt_{BSM}^{spin}) [225]. The weight can be decomposed into a normalisation and spin part, which are independent of each other, as shown by the equation:

$$wt_{BSM} = \frac{wt_{BSM}^{spin}}{wt_{SM}^{spin}} \times wt_{SM \rightarrow BSM}^{norm} \quad (5.4)$$

where wt_{BSM} is the computed BSM spin weight. A normalisation weight ($wt_{SM \rightarrow BSM}^{norm}$) must be applied to extrapolate from the calculated SM to BSM cross-section, and this is computed in the same way as the SM Born cross-sections.

The Born level cross-sections for the Z' search depend on several factors, such as \sqrt{s} , the scattering angle of the tau in the di-tau rest frame, and the Z' model assumptions, including its resonance mass, signal width, and couplings. The couplings are determined by the SSM Z' model, and the width is obtained by generating SSM Z' events in PYTHIA 8.2. The resulting width is then passed to the TAUSPINNERTOOL. The width for SSM signals is typically about 3% of the resonance mass.

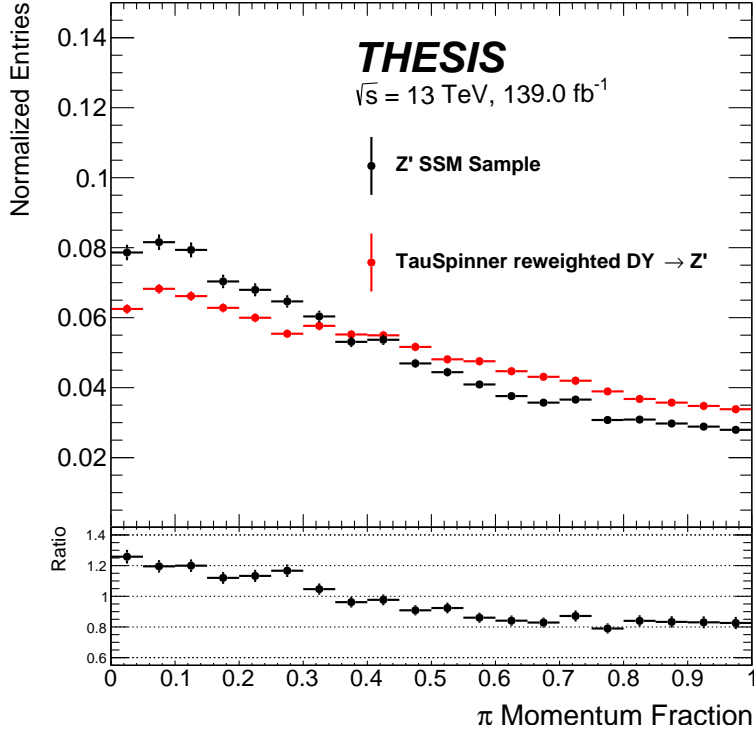
5.2.2 The Z' Sample Validation

The TAUSPINNERTOOL has been effectively utilised in numerous analyses for both SM and BSM use cases, its use has been extensively validated by both the corresponding analysis teams and the TAUSPINNERTOOL authors [225]. In the 2018 ATLAS $H/A/Z' \rightarrow \tau\tau$ analysis, which was conducted on a dataset with an integrated luminosity of 36 fb^{-1} . The TAUSPINNERTOOL was employed in a similar manner to this analysis and the validation was closely followed [57, 227].

To evaluate the TAUSPINNERTOOL implementation in this analysis, a comparison is conducted between the invariant mass slices of the DY $Z/\gamma^* \rightarrow \tau\tau + \text{jets}$ samples reweighted to a Z' resonance and a dedicated Z' validation sample. The resonance mass of both Z' samples are set at 3 TeV. The Z' sample is produced at LO under the SSM model using the same generator information provided in Table 5.1. For consistency, the Z' validation sample is generated without spin weights, and the TAUSPINNERTOOL is then used to add them. In this comparison, the LPXKFACTORTOOL is not applied to incorporate the LO \rightarrow NNLO correction.

One method to ensure that the spin weighting is applied properly is to examine the momentum fraction of pions in cases where $\tau^\pm \rightarrow \pi^\pm \nu$. The inclusion of spin effects results in suppressed and enhanced tau decay topologies due to the requirements on the handedness of the outgoing tau and neutrino. As shown in Figure 5.3, the fraction of momentum taken up by the pion exhibits a non-uniform shape, with a peak at low pion momentum fraction. Although there is some disagreement between the two distributions of up to 25%, the crucial observation is that the shape is similar in both samples, indicating that the spin weights have been applied in both samples. Furthermore, the shape aligns with that presented in

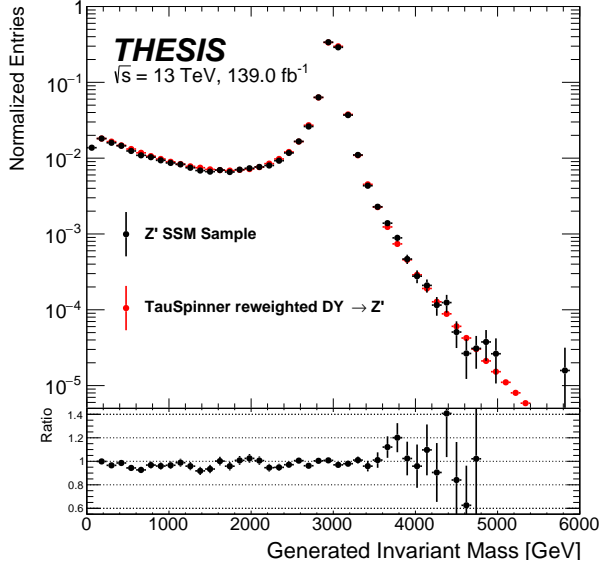
the relevant literature, providing further evidence that the weights have been incorporated correctly [224].



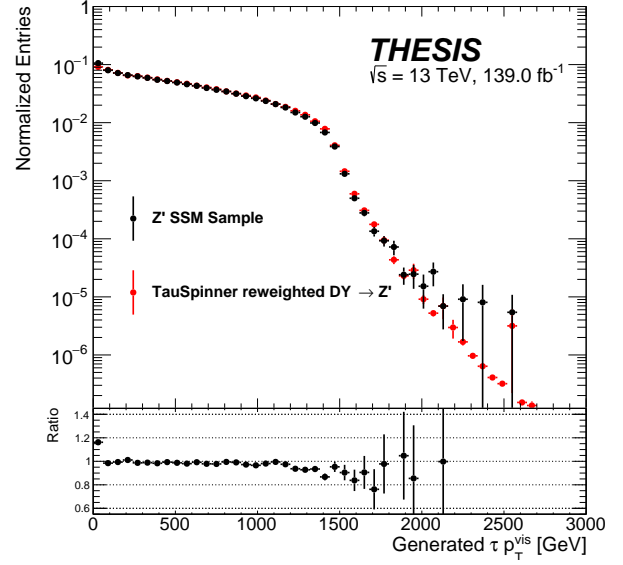
(a)

Figure 5.3: Comparison of the fraction of the τ momentum taken up by the π in $\tau^\pm \rightarrow \pi^\pm \nu$ events between a dedicated Z' validation sample (black points) and the TAUSPINNERTOOL reweighted DY slices (red points) both with an invariant mass of 3 TeV. The lower plot shows the ratio of the two distributions with the statistical uncertainty considered.

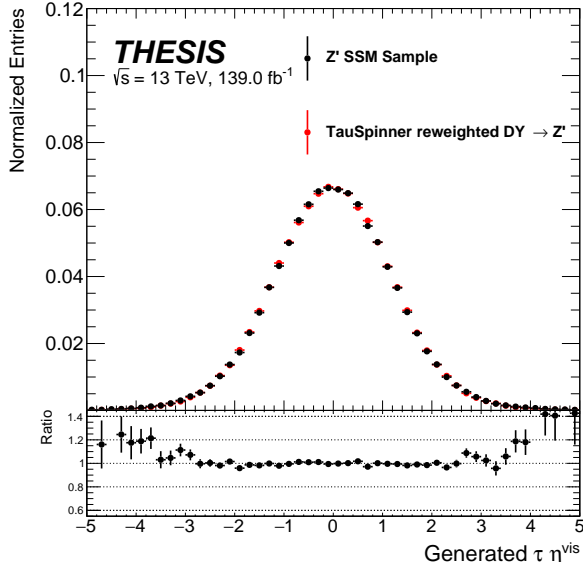
The performance of the TAUSPINNERTOOL is evaluated further by comparing the truth resonance mass (M_{inv}), p_T^τ , $|\eta^\tau|$, and M_T^{TOT} variables for the two samples. The M_T^{TOT} variable is shown after applying SR cuts to ensure that the modelling is sufficient, while the other variables are shown without any selection cuts. The comparison is presented in Figure 5.4, where reasonable modelling is observed with only minor deviations visible, mostly in regions with low coverage from the validation sample.



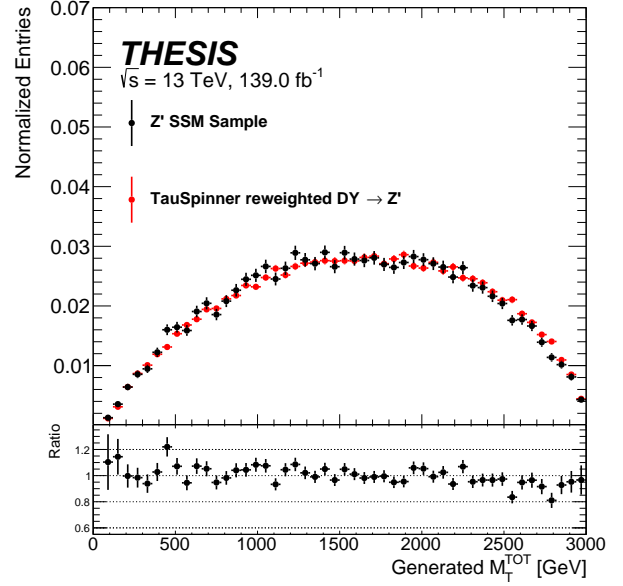
(a) M_{inv}



(b) p_T^τ



(c) $|\eta^\tau|$



(d) M_T^{TOT}

Figure 5.4: Comparison of SSM Z' distributions with an invariant mass of 3 TeV. One sample (red) originates from TAUSPINNERTOOL reweighted DY $Z/\gamma^* \rightarrow \tau\tau + \text{jets}$ samples and the other (black) is a dedicated SSM $Z' \rightarrow \tau\tau$ validation sample. Distributions of M_{inv} , p_T and $|\eta|$ variables are shown before any selection, while the M_T^{TOT} distribution is shown after SR cuts. Reasonable agreement is observed between the two samples, with minor deviations visible in regions where the validation sample has low statistics.

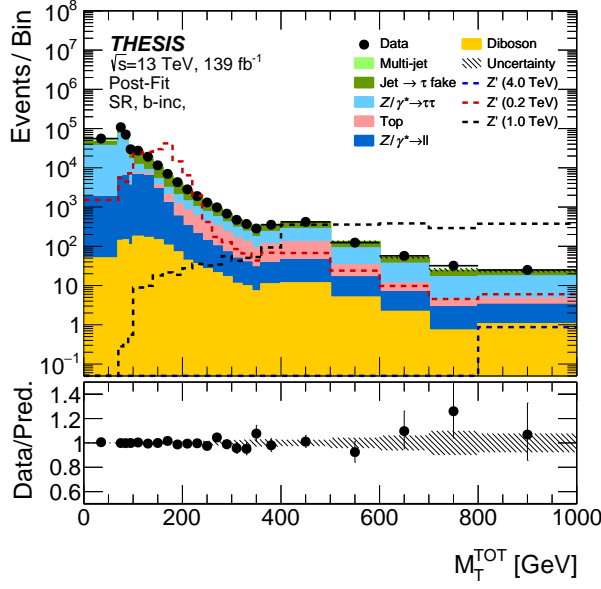
5.3 Systematic Uncertainties

The systematic uncertainties for the TAU SPINNER TOOL reweighted Z' signal samples include experimental uncertainties associated with hadronic taus, leptons, E_T^{MISS} , flavour tagging, pile-up reconstruction, and other sources. These uncertainties are provided by the combined performance groups in the usual way, as described in more detail in Section 4.6. The main difference from the MSSM signal systematics described in the legacy analysis is in the treatment of the signal theory uncertainties. Since the LPXKFACTOR TOOL is used for LO \rightarrow NNLO reweighting, it can also be used to retrieve PDF, beam energy, α_s , and other theory systematics, similar to the $Z \rightarrow \tau\tau + \text{jets}$ SM background systematics described in Section 4.6. Thus, the uncertainties provided by the LPXKFACTOR TOOL serve the purpose of the signal acceptance uncertainty. For the Z' cross-section uncertainty, the upper range is taken of the event yield from each LPXKfactor theory uncertainty.

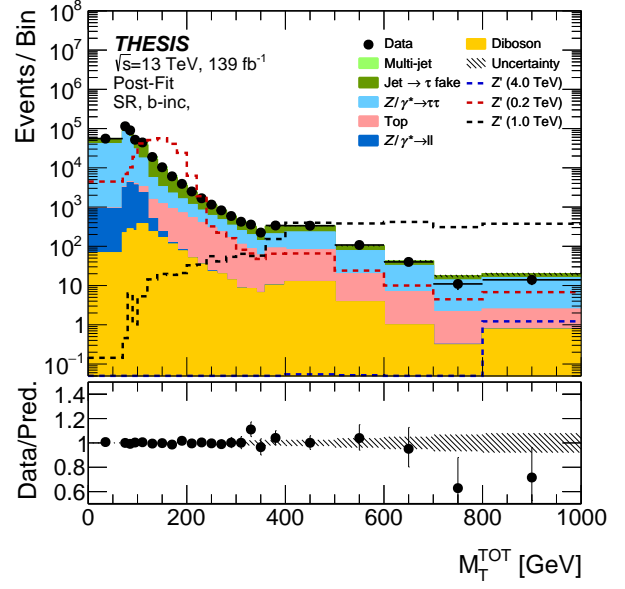
5.4 Results

5.4.1 Post-fit Results

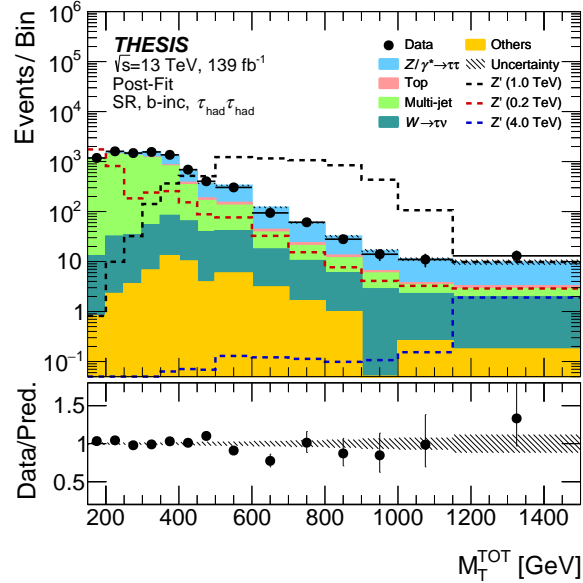
A background-only fit (μ fixed to zero) is executed using the techniques described in Section 4.7. The results of the fit for the $e\tau_{\text{had}}$, $\mu\tau_{\text{had}}$, and $\tau_{\text{had}}\tau_{\text{had}}$ channels are displayed in Figure 5.5. Since the b -tag and b -veto categories are combined in this analysis, the TCR is not integrated into the fit as it contains only b -tag histograms. The signal templates are superimposed for 0.2, 1.0, and 4.0 TeV Z' SSM signals scaled to their predicted cross-sections. The binning is selected to match the b -veto SR binning used in the previous section, adding the b -tag contribution has a minor effect on the bin contents. The data and standard model backgrounds are the same as those in the previous section, so any variation from the previous section is attributable to the merging of regions.



(a) $e\tau_{\text{had}}$



(b) $\mu\tau_{\text{had}}$



(c) $\tau_{\text{had}}\tau_{\text{had}}$

Figure 5.5: Post-fit distributions for the $e\tau_{\text{had}}$, $\mu\tau_{\text{had}}$ and $\tau_{\text{had}}\tau_{\text{had}}$ signal regions. Signals are overlaid for a 0.2 TeV, 1.0 TeV and 4.0 TeV SSM Z' particle, they are scaled to their predicted cross sections of 139 pb, 4×10^{-1} pb and 3×10^{-4} pb, respectively. The ratio plot represents the ratio of the data and background prediction. The post-fit uncertainty is represented by the uncertainty band.

5.4.2 Exclusion Limits

Figure 5.5 demonstrates that the data is adequately modelled by the SM background, thus allowing for the setting of upper limits on the product of the cross-section and branching ratio of $Z' \rightarrow \tau\tau$ at a 95% confidence level, using the techniques outlined in Section 4.7.2. The resulting upper limit for the SSM model is shown in Figure 5.6, which depicts an improvement over the 36 fb⁻¹ result from [57], represented by the shaded grey area. Although the last mass-sliced sample requires events with an invariant mass above 5 TeV, the limit is extended to 6.0 TeV to facilitate the HRC analysis described in the next section. Since this elongated mass range has no significant negative effect on the upper limit, it is kept for comparison against the past results. The magenta line shows the predicted SSM cross-section for the $Z' \rightarrow \tau\tau$ process, and the intersection between this line and the limit indicates the mass at which the SSM Z' is excluded. Notably, this analysis improves upon the previous result by excluding SSM Z' masses below 3.06 TeV (3.14 TeV), compared to the previous exclusion of masses below 2.33 TeV (2.40 TeV) when using the observed (expected) limit. It is worth noting that the exclusion for the 36 fb⁻¹ is slightly different to the 2.42 TeV quoted in Section 2.3.2 and in [58]. The cross-section depends on the method used for the calculation. However, in this analysis the SSM cross-section is taken from the HRC analysis and the values were used in [62].

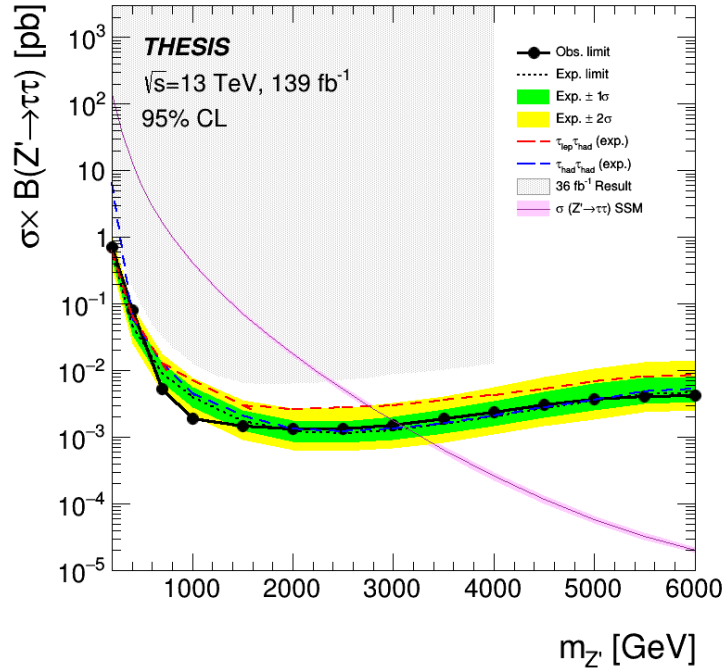


Figure 5.6: The 95% CL upper limits on the $\sigma \times \mathcal{B}(Z' \rightarrow \tau\tau)$. The black solid (dashed) line indicates the observed (expected) limit. The green and yellow bands represent the $\pm 1\sigma$ and $\pm 2\sigma$ uncertainties on the expected limit. The expected limit from the $\tau_{\text{lep}}\tau_{\text{had}}$ and $\tau_{\text{had}}\tau_{\text{had}}$ channels are represented by the red and blue dashed lines, respectively. The previous result [57] with an integrated luminosity of 36 fb⁻¹ is represented by the grey filled area.

An explanation for the behaviour of the limit shape can be obtained by examining the acceptance \times efficiency ($A \times \epsilon$) plots shown in Figure 5.7 for each signal region. The $\tau_{\text{lep}}\tau_{\text{had}}$ limit is initially better than the $\tau_{\text{had}}\tau_{\text{had}}$ limit due to the larger signal acceptance at low signal masses. The reduced signal acceptance in the $\tau_{\text{had}}\tau_{\text{had}}$ channel for lower mass points is due to the higher trigger thresholds relative to the $\tau_{\text{lep}}\tau_{\text{had}}$ channel. The $\tau_{\text{lep}}\tau_{\text{had}}$ limit increases at high mass due to the lower signal efficiency for high mass signals mixed with the higher background in the final bin of the M_T^{TOT} distribution compared to the $\tau_{\text{had}}\tau_{\text{had}}$ channel. In contrast, the $\tau_{\text{had}}\tau_{\text{had}}$ limit stays relatively constant at high mass points due to the low background yield at high M_T^{TOT} values. Additionally, higher signal masses produce boosted taus with kinematics that have larger reconstruction inefficiencies in the detector, which explains the reduction in $A \times \epsilon$ for these points.

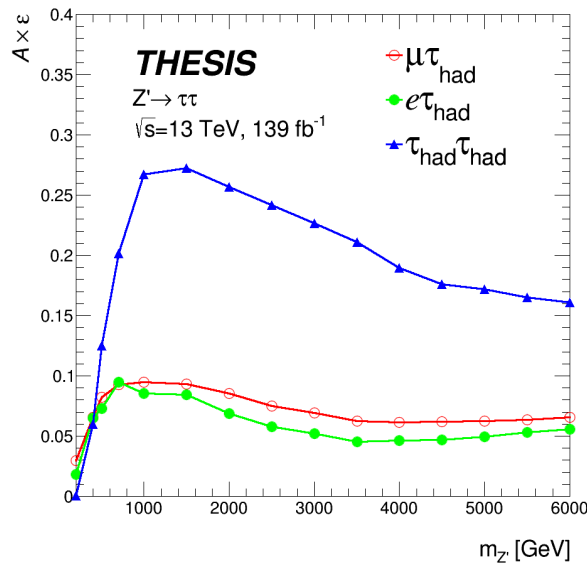


Figure 5.7: The signal acceptance \times efficiency ($A \times \epsilon$) for the $e\tau_{\text{had}}$ (green), $\mu\tau_{\text{had}}$ (red) and $\tau_{\text{had}}\tau_{\text{had}}$ (blue) signal regions. They are calculated by examining the signal yield in each signal region compared to the number of events before any selections.

5.5 The ATLAS Heavy Resonance Combination

The Z' search results reported in this chapter are involved in the comprehensive ATLAS HRC effort [62]. Numerous independent searches within ATLAS have been conducted simultaneously, targeting comparable narrow-width resonances but in diverse final states. By amalgamating these distinct searches, even more stringent limitations on the production of BSM particles can be established, when compared to simply overlaying the individual search results.

The incorporation of the SSM $Z' \rightarrow \tau\tau$ search into the HRC further strengthens the derived exclusion limits and adds a further search channel to either discount or strengthen any po-

tential excesses observed in other channels. By combining the results of various searches, the HRC can leverage the strengths of each analysis, effectively increasing the statistical significance and reducing the uncertainties associated with the presence of potential new particles.

This section details the 2022 HRC analysis [62] which was briefly described in Section 2.3.2. This analysis didn't involve the $\tau\tau$ final state. Therefore, the addition of this channel for the next iteration of the combination is also discussed.

5.5.1 The Combination Setup

The HVT model is discussed in Section 2.3.2, along with the relevant HVT benchmark (Model A: $g_H = -0.56$, $g_f = -0.55$, $g_f = g_q = g_\ell$) for this thesis and some HRC results from the 2022 combination. Figure 5.8 displays Feynman diagrams that illustrate the relevant qqA production of a V' , followed by its subsequent decay into VV/VH or $\ell\ell/\ell\nu/q\bar{q}/q\bar{q}'$.

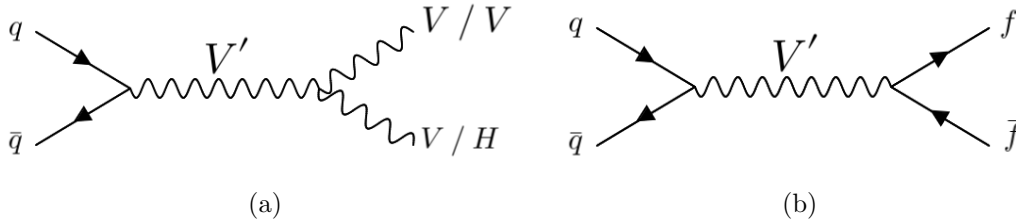


Figure 5.8: Feynman diagrams for the HVT V' production via quark-antiquark annihilation qqA . A V' decay to VV or VH is shown in (a) and (b) represents the decay to $\ell\bar{\ell}$, $\ell\nu$, $q\bar{q}$ or $q\bar{q}'$, where q' indicates a different flavour quark.

The individual analyses contributing to these exclusion planes are categorised as either leptonic or bosonic, as presented in Table 5.2. The 2D exclusion planes that are relevant to the analysis are explained in Section 2.3.2 and the leptonic + bosonic combination is depicted in Figure 2.5 for the $\{g_H, g_f\}$ and $\{g_q, g_\ell\}$ planes. These exclusion planes, specific to the 2022 HRC analysis, provide valuable insights into the parameter space exclusion for the HVT model. The bosonic category is primarily sensitive to the coupling parameter g_H due to the application of the equivalence theorem. However, there is also some sensitivity to g_f and g_q stemming from the qqA production mechanism. On the other hand, the leptonic analyses are solely sensitive to g_f and g_q . These characteristics largely account for the specific shape observed in the 2D planes for each subgroup. However, the sensitivity of the leptonic subgroup decreases as $|g_H|$ increases. This occurs because as $|g_H|$ rises, the decays to bosonic final states become more prominent, consequently diminishing the sensitivity of the leptonic analyses.

Table 5.2: The individual analyses used in the 2022 HRC combination [62] and the next iteration discussed in this chapter. Each analysis belongs to a sub-combination which is also shown. The analyses in bold are the ones which are newly introduced for this next iteration.

Group	Process	Signal	Sub-process
Bosonic	VV, VH	HVT Z'	$ZH \rightarrow qqbb, ZH \rightarrow \nu\nu bb, ZH \rightarrow \ell\ell bb$ $WW \rightarrow qqqq, \mathbf{WW} \rightarrow \ell\nu qq, \mathbf{WW} \rightarrow \ell\nu\ell\nu$
		HVT W'	$WZ \rightarrow qqqq, WZ \rightarrow \ell\nu qq, WZ \rightarrow \ell\nu\ell\ell$ $WZ \rightarrow \ell\ell qq, WH \rightarrow qqbb, WH \rightarrow \ell\nu bb$
Leptonic	$\ell\ell, \tau\tau$	HVT Z'	$\ell\ell, \mathbf{\tau\tau}$
		HVT W'	$\ell\nu, \tau\nu$
Quarkonic	qq	HVT Z'	qq (light quark), $bb, tt \rightarrow qqqqbb, tt \rightarrow qq\ell\nu bb,$ $tt \rightarrow \ell\nu\ell\nu bb$
		HVT W'	$qq', tb \rightarrow qqbb, tb \rightarrow \ell\nu bb$

The combination process encompasses several crucial steps. Firstly, each individual analysis generates ROOSTATS workspaces that contain templates for both the background and signal components. These workspaces serve as the foundation for conducting statistical analysis during the combination process. To ensure consistency, the signal templates are scaled to the relevant LO cross-section using the HVT calculator tool [52]. The specific cross-section employed depends on the particular region of parameter space from which the exclusion limit is being derived. Since different analyses may utilise distinct signal models, such as the SSM Z' signal mentioned in this chapter, a validation procedure is undertaken. This validation process aims to confirm that each analysis can effectively function as a suitable HVT template. The techniques outlined in [52] are employed for this validation.

To guarantee the independence of the analyses and prevent the duplication of events, an orthogonality check is conducted. This check evaluates the extent of overlap among the selected events in each analysis by running each analysis using a common set of MC samples. If any overlap is identified, necessary actions are taken to exclude those events from the final combination. For instance, in the case of the $Z' \rightarrow \tau\tau$ analysis for the next iteration, a thorough examination revealed minimal overlap with other analyses. This finding indicates that the $Z' \rightarrow \tau\tau$ analysis can be included safely in the combination process.

Once a list of orthogonal analyses is established, the results are extracted for three combinations: a leptonic sub-combination, a bosonic sub-combination, and a combined leptonic + bosonic combination. To achieve this, a simultaneous fit is performed across all individual channels, carefully considering the common and unique nuisance parameters from each analysis. Similar to standard analyses, a search phase is conducted to examine the data for

any potential excess compared to the background prediction. In this step, a p -value scan is extracted for each resonance mass to evaluate whether there are any significant deviations from the predictions of the SM. However, no substantial deviations are observed. Following the search phase, the next step involves calculating the 95% CL $\sigma \times \mathcal{B}$ exclusion limit. The calculation is carried out using the methods outlined in Section 4.7.

To construct the 2D exclusion planes, a slightly modified approach is utilised. In this case, the test statistic depicted in Equation 4.10 is adjusted by replacing μ with the set of coupling parameters (\vec{g}) of interest. This modification enables the relative proportions of each signal to vary independently. The underlying assumption is that all production takes place via the qqA mechanism, and the probabilities of V' production and decays are proportionate to g_q^2 and the square of the corresponding decay coupling, respectively.

The next upcoming iteration of the HRC will introduce several improvements and additional analyses aimed at enhancing the constraints on the couplings. To broaden the scope, the full combination will include a quarkonic sub-combination in addition to other added channels. This inclusion will provide an additional constraint on the couplings, specifically targeting the parameter g_q . Furthermore, the full combination 2D plane will incorporate Vector Boson Fusion (VBF) production, albeit not directly combined with the qqA results. Instead, the results from a new benchmark model based on VBF will be overlaid. This approach is adopted due to the lower sensitivity of the VBF mode relative to the qqA . By incorporating VBF production, additional constraints on the coupling parameter g_H will be obtained, particularly for lower mass values. Additionally, a new 2D plane $\{g_{q_3}, g_{\ell_3}\}$ will be introduced, which is similar to the $\{g_q, g_\ell\}$ plane but specifically pertains third-generation final states such as the $Z' \rightarrow \tau\tau$ decay mode.

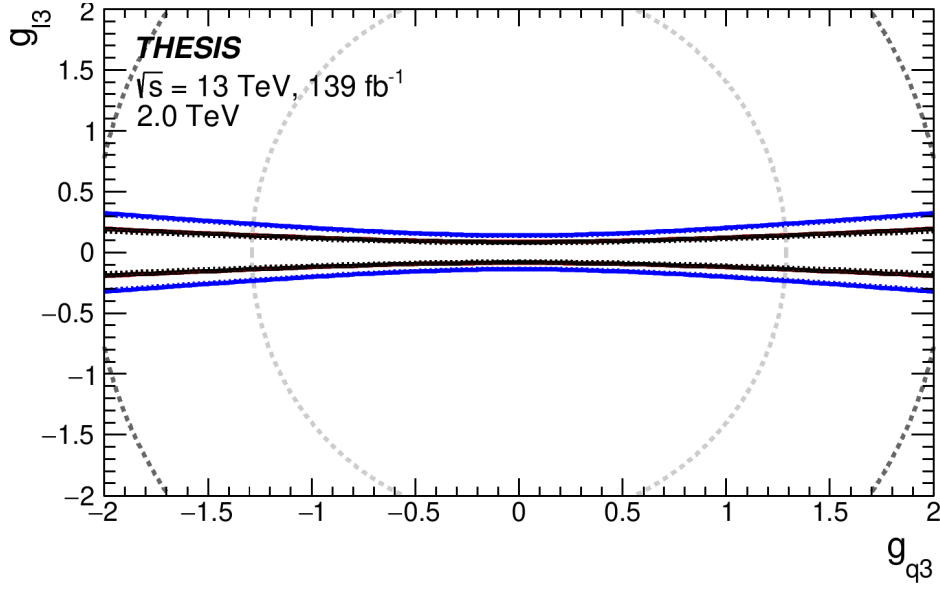
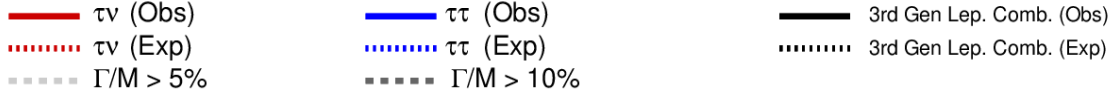
5.5.2 Preliminary Results for the Combination

This section outlines the relevant preliminary $\{g_H, g_f\}$, $\{g_q, g_\ell\}$ and $\{g_{q_3}, g_{\ell_3}\}$ exclusion planes for the next iteration of the HRC after the introduction of the new channels and quarkonic sub-group. The focus is specifically on the planes related to the $Z' \rightarrow \tau\tau$ decay mode. Hence, only the leptonic sub-combination is shown along with the full combination (leptonic + bosonic + quarkonic).

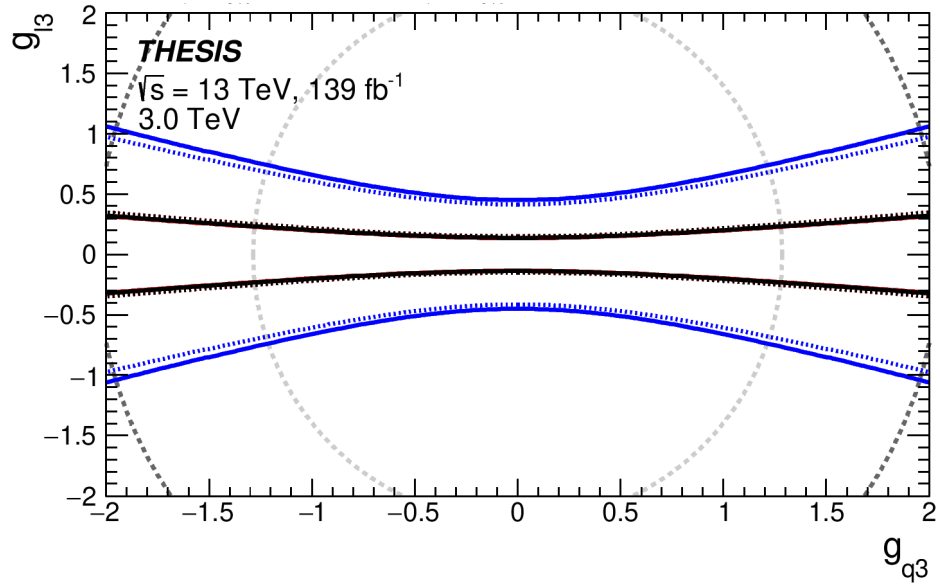
For the leptonic sub-combination, plots are shown for the 2 TeV and 3 TeV resonance mass points since for 4 TeV signals and above the $\tau\tau$ contribution is no longer visible. For the full combination, the $\tau\tau$ result is combined with the other leptonic modes enabling higher mass plots to be shown. Therefore, for the full combination, the 3 TeV and 4 TeV mass points are shown, below 3 TeV the constraints are so tight that the non-excluded region is barely visible.

Leptonic Sub-combination

The results from the leptonic sub-combination are presented in the $\{g_{q_3}, g_{\ell_3}\}$, $\{g_q, g_\ell\}$ and $\{g_H, g_f\}$ planes shown in Figures 5.9, 5.10 and 5.11, respectively. The $\tau\tau$ planes extracted from the results in this chapter are shown in blue.

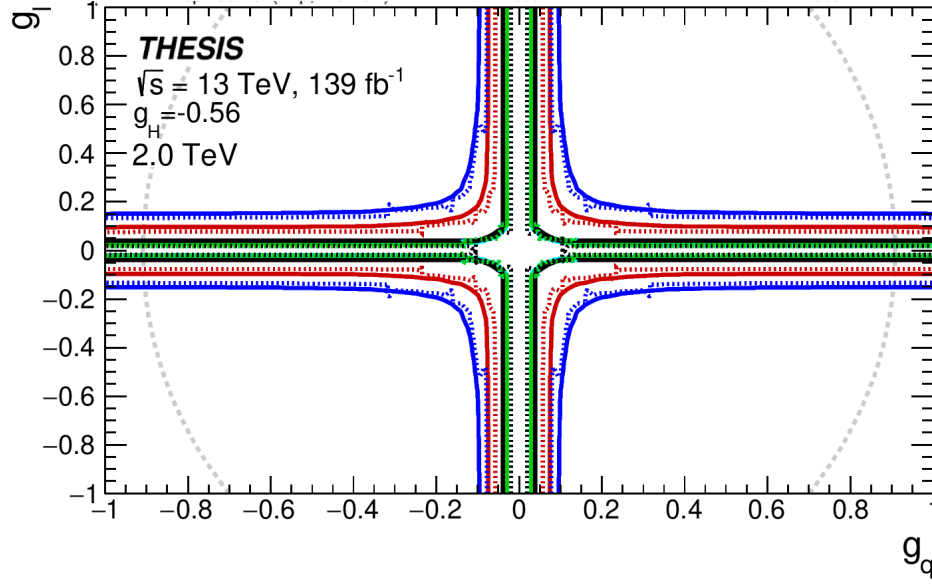
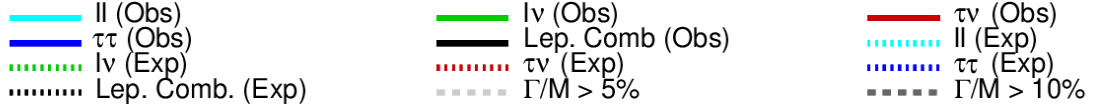


(a) 2 TeV

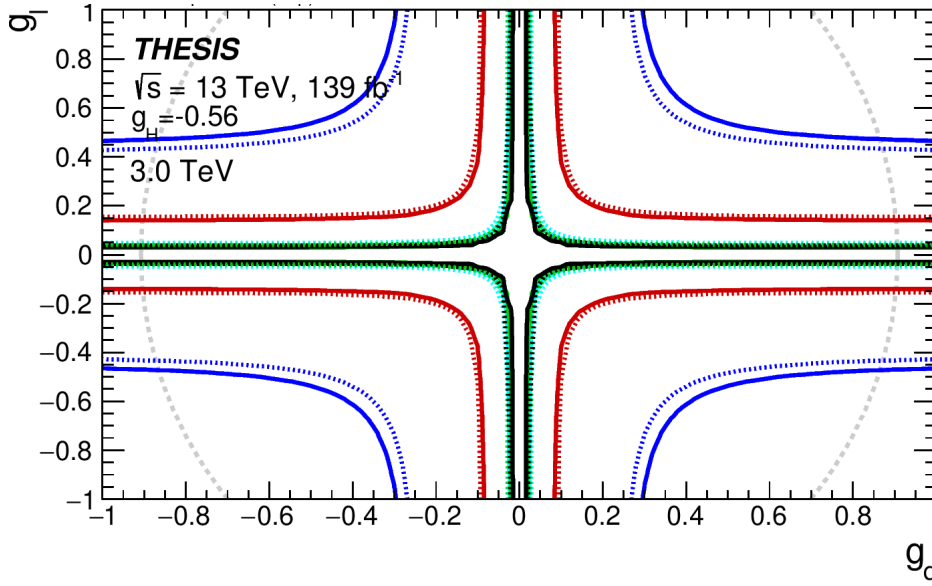


(b) 3 TeV

Figure 5.9: The 95% CL observed (solid line) and expected (dashed line) exclusion limit contours for the third-generation leptonic sub-combination and its constituent final states ($\tau\tau$ (blue) and $\tau\nu$ (red)) in the $\{g_{q3}, g_{l3}\}$ plane for a (a) 2 TeV and (b) 3 TeV resonance mass. The results assume that $g_H = -0.56$ as is predicted by the HVT Model A. The dashed grey ovals represent the regions of the parameter space where the width of the V' resonance is either 5% or 10% of the resonance mass. The inner region of the black contour excluded for the HVT model.



(a) 2 TeV



(b) 3 TeV

Figure 5.10: The 95% CL observed (solid line) and expected (dashed line) exclusion limit contours for the leptonic sub-combination and its constituent final states ($\tau\tau$ (blue), $\tau\nu$ (red), $\ell\ell$ (cyan) and $\ell\nu$ (green)) in the $\{g_q, g_\ell\}$ plane for a (a) 2 TeV and (b) 3 TeV resonance mass. The results assume that $g_H = -0.56$ as is predicted by the HVT Model A. The dashed grey ovals represent the regions of the parameter space where the width of the V' resonance is either 5% or 10% of the resonance mass. The inner region of the black contour excluded for the HVT model.

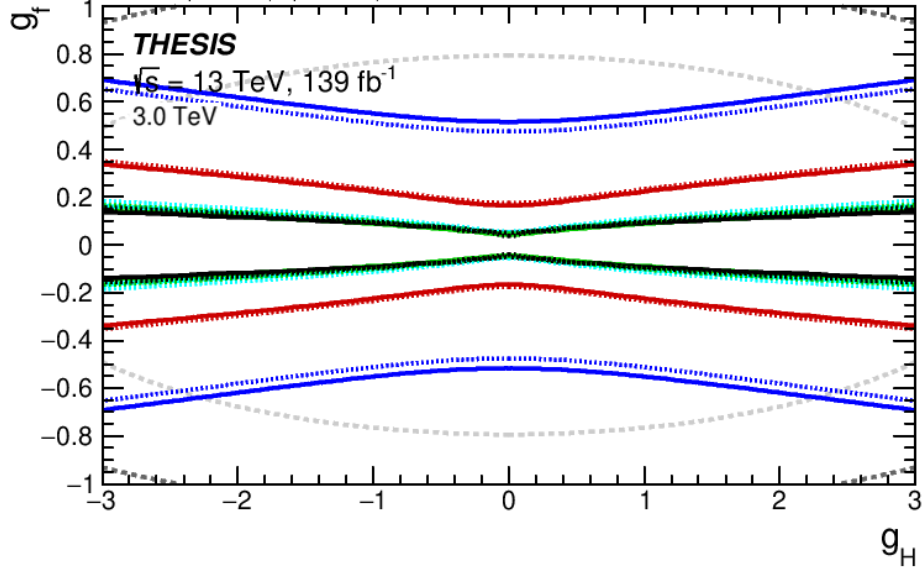
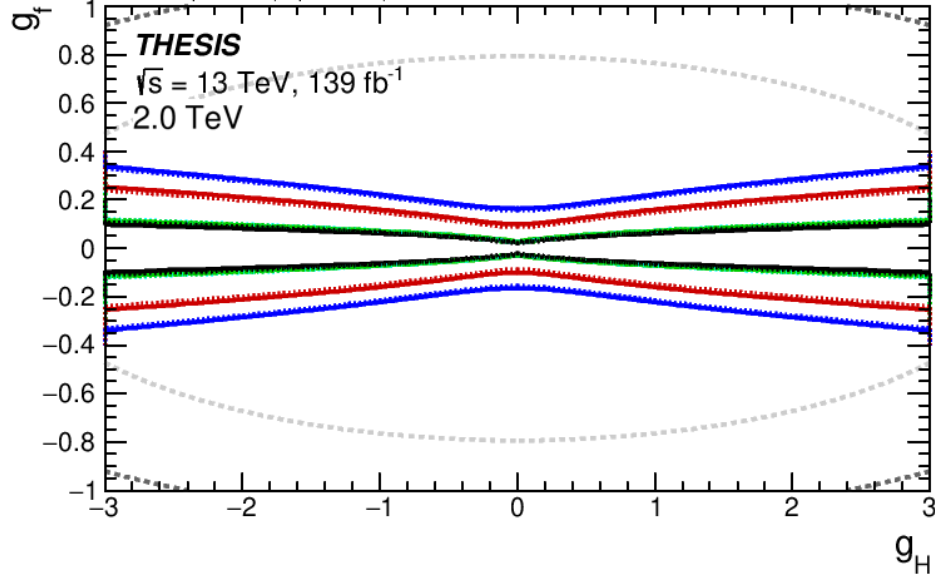
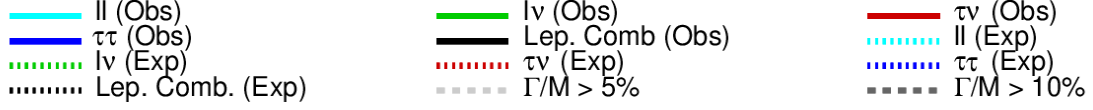


Figure 5.11: The 95% CL observed (solid line) and expected (dashed line) exclusion limit contours for the leptonic sub-combination and its constituent final states ($\tau\tau$ (blue), $\tau\nu$ (red), $\ell\ell$ (cyan) and $\ell\nu$ (green)) in the $\{g_H, g_q\}$ plane for a (a) 2 TeV and (b) 3 TeV resonance mass. The results assume common fermionic couplings ($g_f = g_q = g_\ell$). The dashed grey ovals represent the regions of the parameter space where the width of the V' resonance is either 5% or 10% of the resonance mass. The inner region of the black contour excluded for the HVT model.

The impact of the $Z' \rightarrow \tau\tau$ decay mode on the leptonic sub-combination is limited. This is especially evident when focusing on the third-generation final states in the $\{g_{q_3}, g_{\ell_3}\}$ plane shown in Figure 5.9. In this plane, the contributions originate from $\tau\nu$ and $\tau\tau$ decays for the leptonic case. There is no sensitivity to g_{q_3} due to the production being overwhelmingly dominated by the lightest quarks. The sensitivity of the leptonic sub-combination is mainly driven by the $\tau\nu$ decay channel. In fact, the exclusion line for $\tau\nu$ is obscured by the combination line. However, the exclusion line for $\tau\tau$ tends to approach the $\tau\nu$ exclusion line as the mass point decreases. The expected limit yields slightly tighter constraints compared to the observed limit. This suggests a minor excess in the data, which becomes more apparent at the 3 TeV mass point.

Similarly, in the generation inclusive $\{g_q, g_\ell\}$ and $\{g_H, g_f\}$ planes shown in Figures 5.10 and Figure 5.11, the $\tau\tau$ decay mode exhibits the weakest constraint compared to the other planes. The $\ell\nu$ channel has the most significant impact and the combined exclusion limit closely follows the exclusion plane of this channel. The combined limit provides a tight constraint but there is limited improvement compared to the 2022 HRC analysis [62]. The reduced impact of the $\tau\tau$ channel can be attributed to the lower $\sigma \times \mathcal{B}$ exclusion limit observed for this channel compared to the other channels. This difference is likely due to the challenges involved in reconstructing hadronic taus due to the presence of neutrinos. A similar effect is observed for the $\tau\nu$ channel, as indicated by the black lines in Figure 5.9 and red lines in Figures 5.10 and 5.11. In all the presented plots, the light grey exclusion regions indicate cases where the resonance width amounts to 5% or 10% of the pole mass. In this region, the assumptions made in the analysis begin to break down.

Full Combination (Leptonic + Bosonic + Quarkonic)

The results from the full combination (leptonic + bosonic + quarkonic) for the $\{g_{q_3}, g_{\ell_3}\}$, $\{g_q, g_\ell\}$, and $\{g_H, g_f\}$ planes are presented in Figures 5.12, 5.13, and 5.14, respectively. The $\tau\tau$ planes are included in the leptonic sub-combination contribution. The full combination yields remarkably stringent constraints on each coupling parameter, reflecting the collective power of the combined analyses.

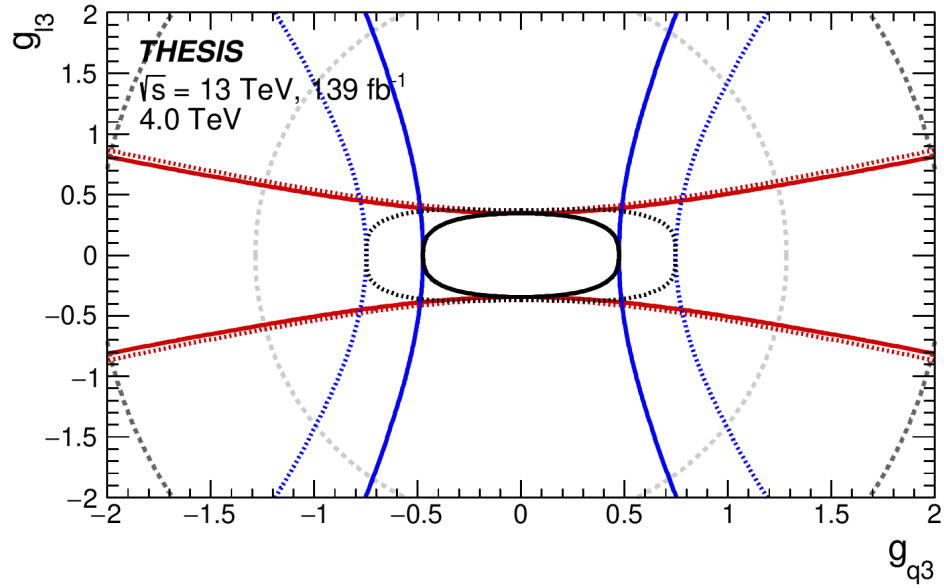
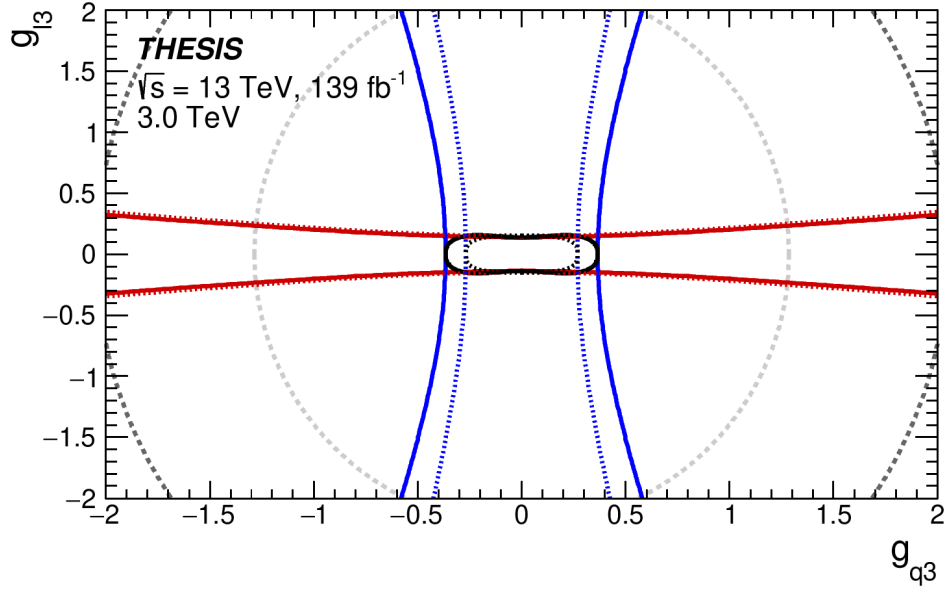
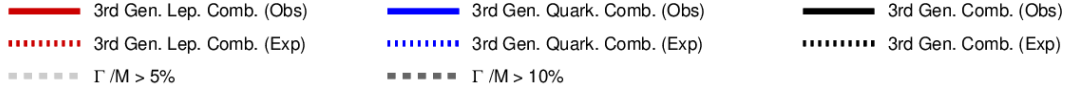
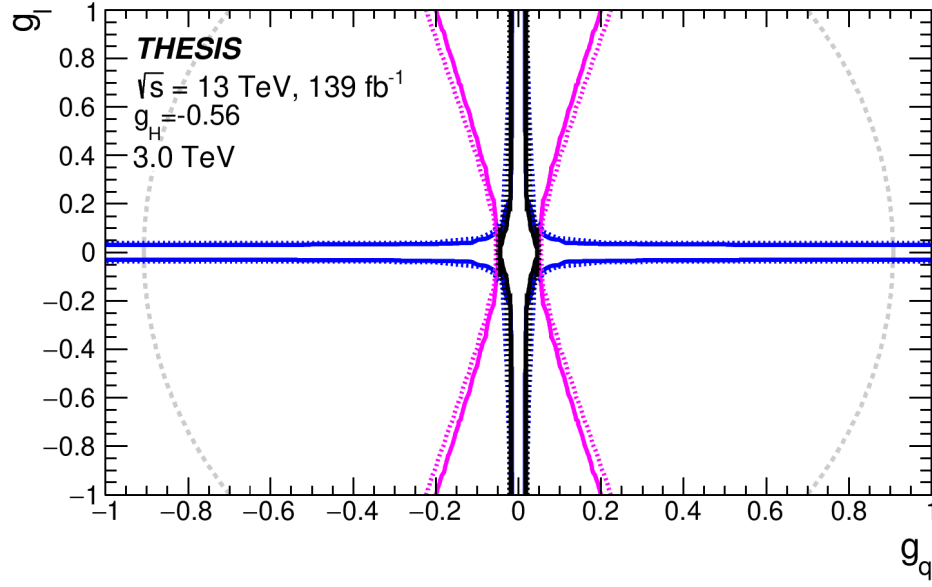
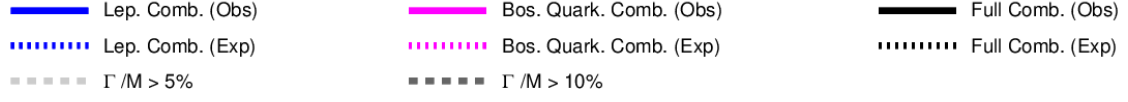
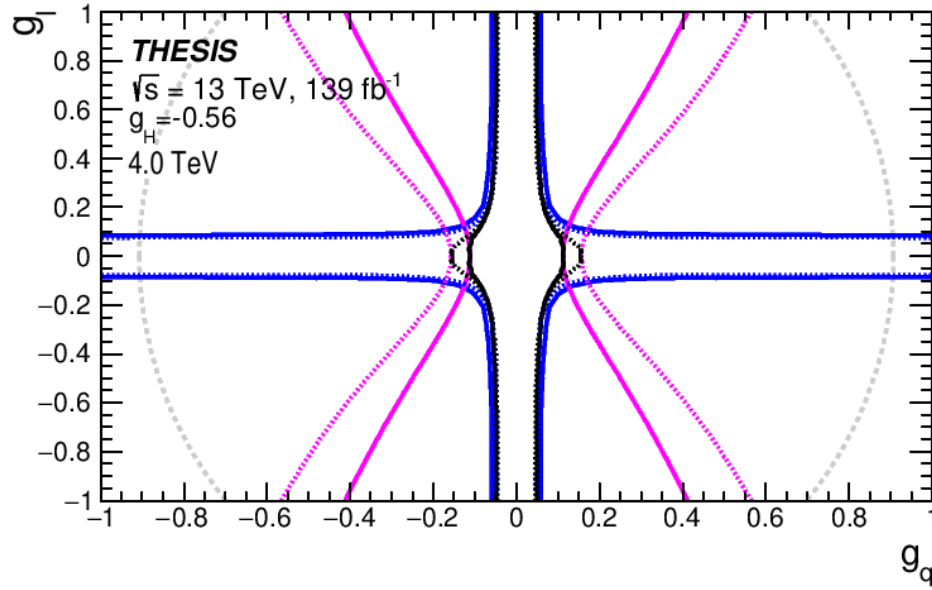


Figure 5.12: The 95% CL observed (solid line) and expected (dashed line) exclusion limit contours for the third-generation combination and the relevant sub-combinations (third-generation leptonic (red) and quarkonic (blue)) in the $\{g_{q3}, g_{l3}\}$ plane for a (a) 3 TeV and (b) 4 TeV resonance mass. The results assume that $g_H = -0.56$ as is predicted by the HVT Model A. The dashed grey ovals represent the regions of the parameter space where the width of the V' resonance is either 5% or 10% of the resonance mass. The inner region of the black contour excluded for the HVT model.

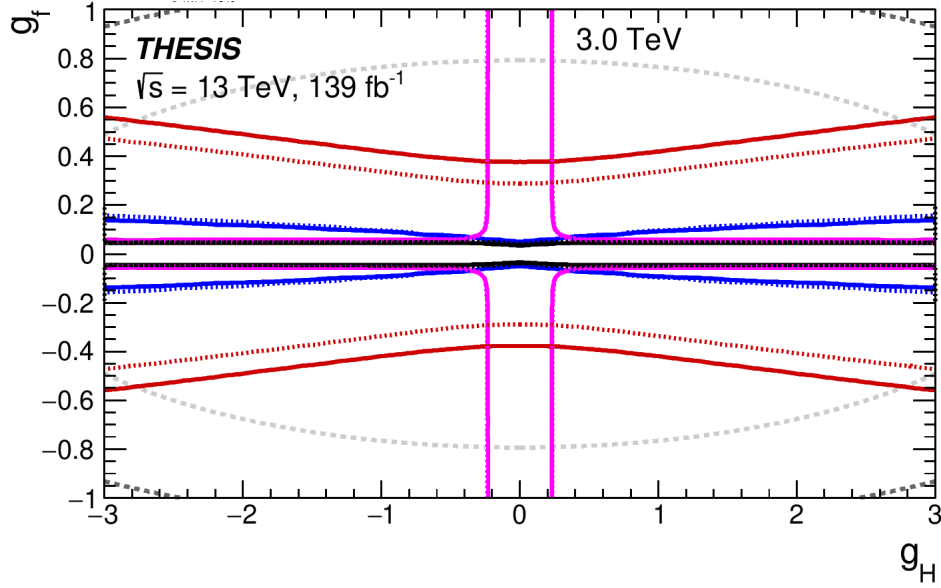
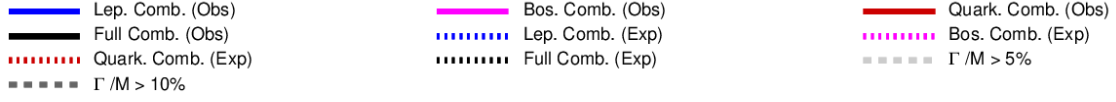


(a) 3 TeV

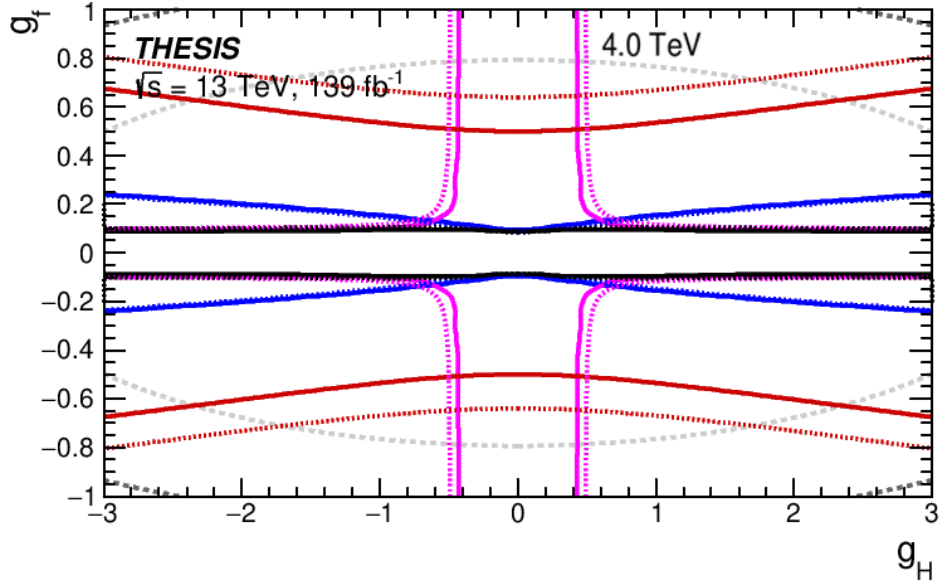


(b) 4 TeV

Figure 5.13: The 95% CL observed (solid line) and expected (dashed line) exclusion limit contours for the full combination (black) and the sub-combinations (leptonic (blue) and quarkonic + bosonic (pink)) in the $\{g_q, g_\ell\}$ plane for a (a) 3 TeV and (b) 4 TeV resonance mass. The results assume that $g_H = -0.56$ as is predicted by the HVT Model A. The dashed grey ovals represent the regions of the parameter space where the width of the V' resonance is either 5% or 10% of the resonance mass. The inner region of the black contour excluded for the HVT model.



(a) 3 TeV



(b) 4 TeV

Figure 5.14: The 95% CL observed (solid line) and expected (dashed line) exclusion limit contours for the full combination (black) and sub-combinations (leptonic (blue), bosonic (pink) and quarkonic (red)) in the $\{g_H, g_q\}$ plane for a (a) 3 TeV and (b) 4 TeV resonance mass. the results assume common fermionic couplings ($g_f = g_q = g_\ell$). The dashed grey ovals represent the regions of the parameter space where the width of the V' resonance is either 5% or 10% of the resonance mass. The inner region of the black contour excluded for the HVT model.

For the $\{g_{q_3}, g_{\ell_3}\}$, the quarkonic sub-group offers a very beneficial localisation of the allowed third-generation couplings as shown by the black ovals. For the $\{g_q, g_\ell\}$, minor improvement is observed when compared to the 2022 HRC result [62] as the leptonic combination dominates the exclusion and the $\ell\nu$ channel was already included. As $g_H = -0.56$ is set for the $\{g_q, g_\ell\}$ plots, the bosonic contribution quickly dies out as the mass point increases. This is expected as bosonic contributions reduce under Model A as mass increases, as mentioned in Section 2.3.2. Finally for the $\{g_H, g_f\}$ planes, at lower mass points, the bosonic contribution and the leptonic contribution offer a similar exclusion except at low values of $|g_H|$. The quarkonic contribution is comparatively less influential than the other sub-combinations. Therefore, the addition of the new channels again have negligible impact when compared to the 2022 HRC $\{g_H, g_f\}$ plane. Nevertheless, the inclusion of additional analyses such as the $\tau\tau$ channel enhances the ability to localise any potential excess or deviation from the SM.

5.6 Conclusion

Using the techniques employed in the 2020 MSSM $H/A/h \rightarrow \tau\tau$ [8] described in Chapter 4, a search for Sequential Standard Model Z' bosons decaying to two tau leptons was conducted. A set of Drell-Yan $Z/\gamma^* \rightarrow \tau\tau + \text{jets}$ invariant mass sliced samples are reweighted to yield SSM Z' resonances. As shown in Figure 5.5, no significant deviation from the SM was observed. Therefore, 95% CL upper limits on the $\sigma \times \mathcal{B}(Z' \rightarrow \tau\tau)$ are derived. Using the theoretical cross-section of the $Z' \rightarrow \tau\tau$ process predicted by the SSM, Z' masses below 3.06 TeV are excluded, as shown in Figure 5.6. This is a significant improvement when compared to the 2.33 TeV (or 2.42 TeV reported in [58]) exclusion derived from the previous SSM $Z' \rightarrow \tau\tau$ result using an integrated luminosity of 36 fb^{-1} [57]. The results are to be used in the next iteration of the ATLAS combined search for V' bosons under the Heavy Vector Triplet model [62]. The SSM Z' results constrain the 95% CL upper limits on the relevant HVT coupling constants, preliminary constraints on the $\{g_{q_3}, g_{\ell_3}\}$, $\{g_q, g_\ell\}$ and $\{g_H, g_f\}$ 2D planes are shown in Figures 5.9, 5.10 and 5.11 for the leptonic sub-combination and Figures 5.12, 5.13 and 5.14 for the full leptonic + bosonic + quarkonic combination.

Chapter 6

Search for Third-Generation Leptoquarks in the $b\tau\tau$ Final State

The techniques used in the 2020 full Run-II (legacy) MSSM Higgs search in the di-tau final state [8], as described in Chapter 4, along with the theoretical motivation for LQ s outlined in Section 2.3.3, can be applied to search for third-generation scalar and vector LQ . In this chapter, a search for singly produced and singly plus pair produced scalar (vector) LQ is conducted in the $b\tau\tau$ final state, where the LQ is studied under the assumption of the \tilde{S}_1 [70] (U_1 [72]) model. As is the case for all searches in this thesis, the full Run-II ATLAS dataset ($L_{\text{int}} = 139 \text{ fb}^{-1}$, $\sqrt{s} = 13 \text{ TeV}$) is employed for the search. The background modelling techniques outlined in this section concern the $\tau_{\text{lep}}\tau_{\text{had}}$ channel. However, results from the $\tau_{\text{had}}\tau_{\text{had}}$ channel are included in the discussion of the final results.

6.1 Building an Analysis Strategy

To simplify and unify the behaviour of the scalar and vector LQ , the production cross-section equation can be arranged to depend on the LQ mass (m_{LQ}), branching fraction of the decay to charged leptons, and the Yukawa LQ - τ - b coupling (λ). For this analysis, the branching fraction to $b\tau$ is set to 1. Referring to the relevant parts of the Lagrangian for the \tilde{S}_1 and U_1 models described in Section 2.3.3, this means that for the \tilde{S}_1 model, if $\mathcal{B}(LQ \rightarrow b\tau) = 1$, then $\lambda^{ij} = \lambda^{33} = \lambda$. For the U_1 model, it implies that $\beta_R^{ij} = 0$, $\beta_L^{33} = 1$, and all other $\beta_L^{ij} = 0$, so the Yukawa coupling can be expressed as $\lambda = \frac{g_U}{\sqrt{2}} \times \beta_L^{33}$. To generate a set of vector LQ MC signals with a common set of λ values relative to the scalar case, the g_U value can be scanned across. The number of vector LQ MC signals is doubled as both the YM ($\kappa = 0$) and MIN ($\kappa = 1$) coupling scenarios are considered.

The contribution from non-resonant diagrams increases with either m_{LQ} or λ when the other is fixed. Figures 6.1(a) and 6.1(b) show the leading order $pp \rightarrow \tau LQ$, $LQ \rightarrow b\tau$ process in which the LQ is produced resonantly via quark-gluon fusion and scattering. The non-resonant LQ quark-gluon scattering production is shown in Figure 6.1(c). However, the non-resonant contributions can interfere with the Z + jets SM background, which can be prob-

lematic [228]. Fortunately, the impact from non-resonant diagrams is small for $p_T^{b\text{-jet}} > 200$ GeV and the interference effect can be avoided by removing this region from the SR [229]. The related publications detailed in Section 2.3.3 typically keep the low $p_T^{b\text{-jet}}$ region and disregard the interference. Therefore, as a compensation, the low $p_T^{b\text{-jet}}$ region is not excluded for the model-independent interpretations discussed in Section 6.7.2.

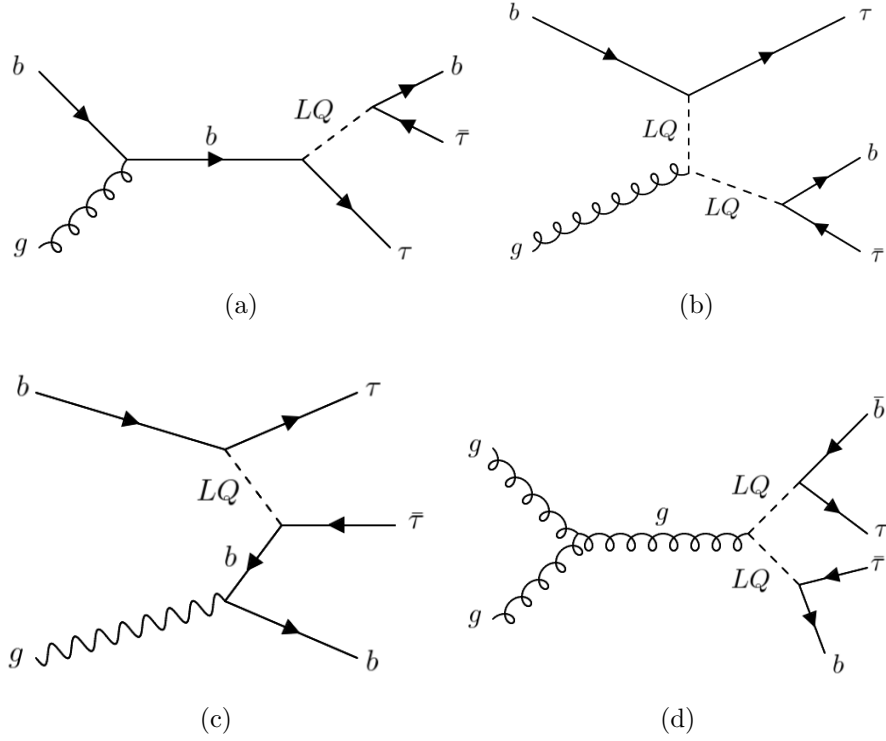


Figure 6.1: Feynman diagrams for (a-c) single leptoquark production (d) leptoquark pair production, where each leptoquark decays to a $b\tau$ final state. Resonant single leptoquark production is depicted in (a) and (b) whilst non-resonant single leptoquark production is shown in (c).

The splitting of the SR into the two $p_T^{b\text{-jet}}$ categories is summarised by the $A \times \epsilon$ for singly produced scalar LQ signals shown in Figure 6.2. In the high $p_T^{b\text{-jet}}$ category, when m_{LQ} is high and λ is fixed, the proportion of non-resonant diagrams increases, leading to a reduction in $A \times \epsilon$. Similarly, for fixed m_{LQ} and increasing λ , the same effect is observed.

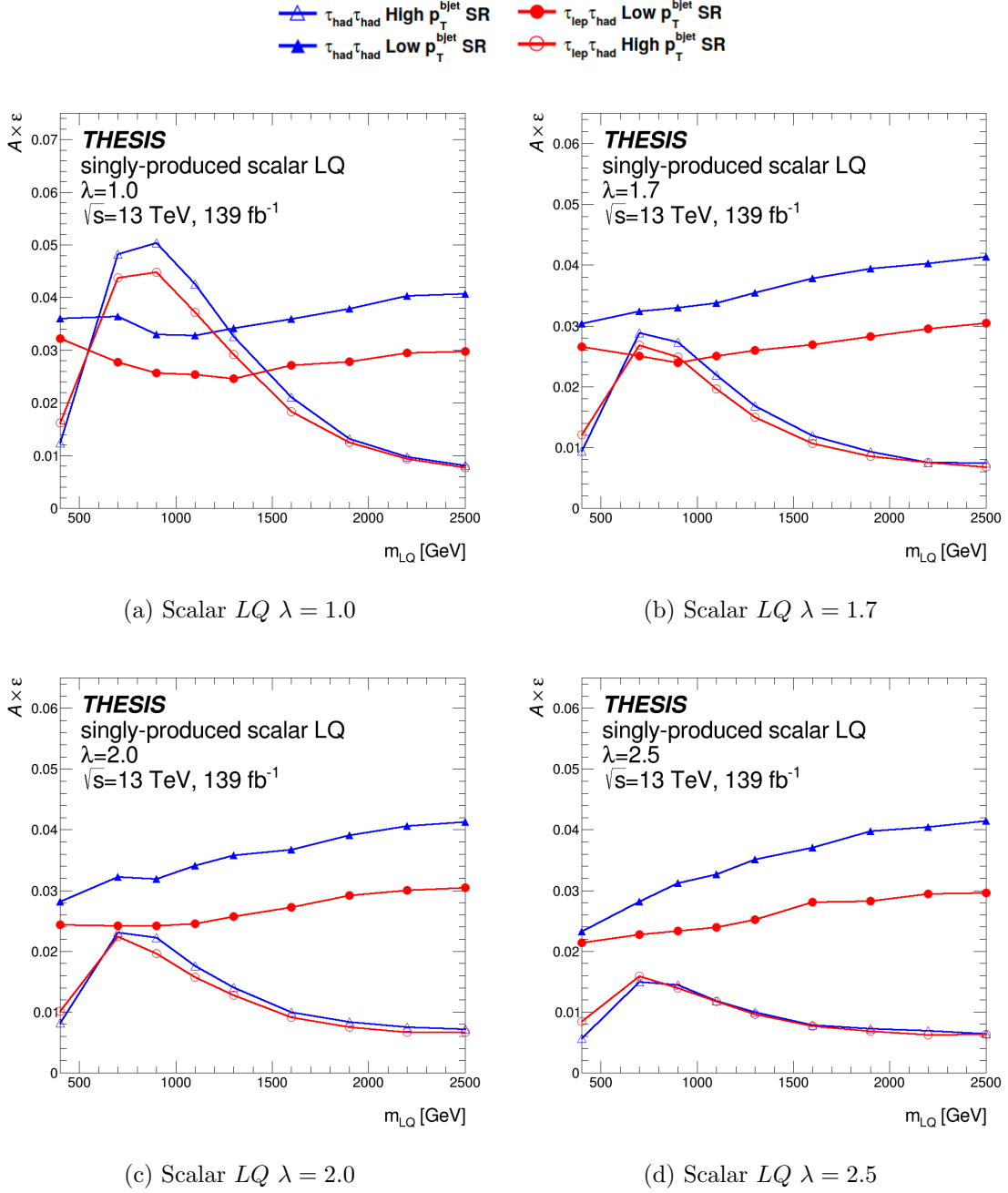


Figure 6.2: Acceptance \times efficiency ($A \times \epsilon$) for singly produced scalar leptoquark across the available mass points for $\lambda \in 1.0, 1.7, 2.0, 2.5$.

Figure 6.1(d) shows an example Feynman diagram for LQ pair production ($LQLQ$) through gluon-gluon fusion, this mode can produce a $b\bar{b}\tau\tau$ final state which can enter the signal region as a b -jet is present. Therefore, pair produced (vector) scalar (v) LQ signals are also included for (v) $LQLQ$ plus (v) LQ interpretations. For the (v) $LQLQ$ plus (v) LQ case which was introduced in Section 2.3.3, the relative fraction of pair produced LQ compared to singly produced LQ depends on their predicted cross-section for each mass point. The production of LQ pairs occurs typically via the strong interaction, making their cross-section mostly insensitive to λ [230].

While many techniques used in this analysis are inherited from the legacy analysis, the selection criteria in this chapter are specifically tailored to search for singly produced scalar LQ with relatively high masses, starting from a benchmark of 900 GeV. As a result, there are several background modelling optimisations that differ from those in the legacy analysis. These optimisations are described in detail in the following sections.

6.2 Monte Carlo Signal Samples

For detailed information on the generator, PDF, hadronisation, underlying event, and the order of the cross-section calculation for each signal process, one can refer to Table 6.1.

The simulation of singly produced scalar and vector LQ events is done in the same way, using the signal model described in [231]. Nine mass points ranging from 0.4 TeV to 2.5 TeV and six coupling points, $\lambda \in (0.5, 1.0, 1.5, 1.7, 2.0, 2.5)$, are used. The coupling is set such that each LQ decays into a b -quark and a tau lepton. Samples are produced for vector LQ with $\kappa = 0$ and $\kappa = 1$. The width of the singly produced (v) LQ samples depends on the mass and coupling. Across the entire mass range, the width is 16% of the (v) LQ mass or less. No higher-order cross-sections are available for the (v) LQ and $vLQLQ$ models, so the LO cross-sections calculated by MG5_AMC@NLO are used.

For pair produced scalar and vector LQ , the signal events are generated using the LQ models specified in [72, 232]. Pair produced scalar samples are originally generated to benefit another ATLAS analysis with different assumptions, explaining any version difference from the single LQ in Table 6.1. The scalar $LQLQ$ samples are available for the same mass points as the single LQ case up to 1900 GeV. They make use of $\lambda = 0.3$ and $\mathcal{B}(LQ \rightarrow \tau b) = \mathcal{B}(LQ \rightarrow t\nu_\tau) = 0.5$. A rescaling is performed such that $\mathcal{B}(LQ \rightarrow \tau b) = 1.0$. The cross-section for scalar $LQLQ$ are calculated at approximate NNLO in QCD with resummation of NNLL soft gluon terms [232–236]. Lepton t -channel contributions are not taken into account, as is the case in scalar $LQLQ$ model literature [232], possibly leading to percent level corrections [237].

Table 6.1: The scalar and vector leptoquark samples for the singly and pair produced production modes. The table shows the MC generator, the PDF set, the underlying event, parton shower and hadronisation (UEPS) model, and the order at which the cross-section was calculated.

Process	Generator	PDF	UEPS	$\mathcal{O}(\sigma)$
BSM Signals				
$(\nu)LQ$	MG5_aMC@NLO 2.8.1 [132]	NNPDF 3.0 NNLO [134, 163]	PYTHIA 8.244 [133]	LO [132]
$LQLQ$	MG5_aMC@NLO 2.6.0	NNPDF 3.0 NLO	PYTHIA 8.230	NNLO + NNLL [232–236]
$\nu LQLQ$	MG5_aMC@NLO 2.6.0	NNPDF 3.0 NLO	PYTHIA 8.244	LO

The data and MC background samples are the same as those shown in Table 4.1. Extra information on all samples used can be found in Appendix C.2.

6.3 Event Selection

Since a b -jet is required in the targeted final state, the analysis employs many of the selections from the legacy analysis b -tag SR mentioned in Section 4.3. While the trigger strategy is exactly the same as the legacy analysis, the OLR recipe is modified due to the adoption of the ATLAS standard OLR recommended by the ATLAS software group (ASG). The OLR is summarised in Table 6.2. The change in OLR results in a small improvement in signal acceptance, as discussed in Section 7.2.5 for bbH and ggH signals.

Table 6.2: The ASG standard OLR used for the $LQ \rightarrow b\tau\tau$ analysis.

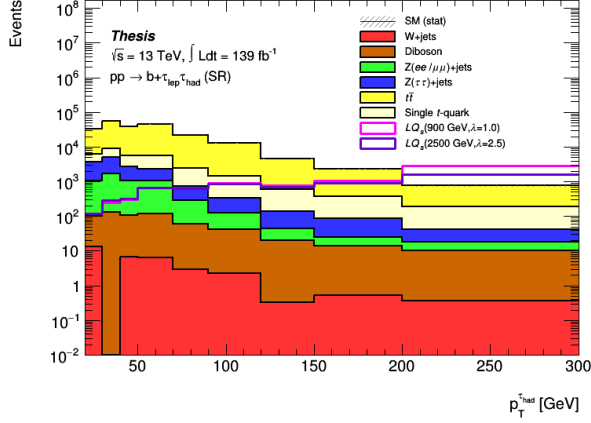
Reject	Keep	ASG Standard OLR Criteria
τ_{had}	e	$\Delta R_{\text{OLR}} < 0.2$
τ_{had}	μ	$\Delta R_{\text{OLR}} < 0.2$
e	μ	If they share a track, remove e if μ has signature in MS, Otherwise remove μ
j	e	$\Delta R_{\text{OLR}} < 0.2$
j	μ	$\Delta R_{\text{OLR}} < 0.2$ and $N_{\text{tracks}}^{\text{jet}} < 3$
e	j	$\Delta R_{\text{OLR}} < 0.4$
μ	j	$\Delta R_{\text{OLR}} < 0.4$
j	τ_{had}	$\Delta R_{\text{OLR}} < 0.2$

Examination of the signal and background compositions in a preselection region shown in Figure 6.3 recommend the changes to the legacy b -tag SR summarised in Table 6.3. This analysis incorporates many improvements and changes to ATLAS performance since the legacy analysis publication. Notably, updates have been made to the tau identification algorithm, b -tagging software, and jet definition. For this analysis, the RNN Medium working point is used for the tau ID, replacing the legacy analysis’s BDT. The b -tagging software now

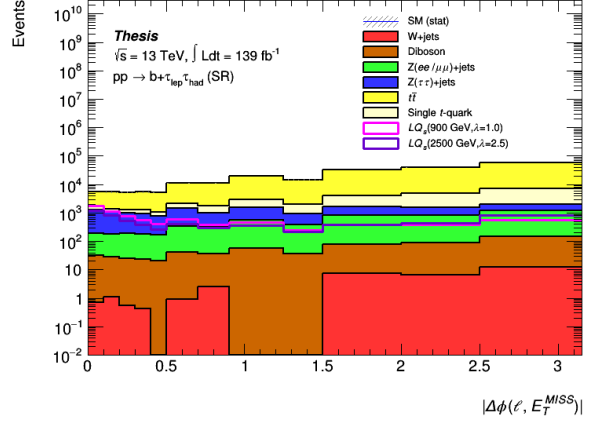
utilises the DL1r algorithm with 70% efficiency instead of the previous MV2c10 algorithm. Additionally, the jet definition now employs the p -flow algorithm (EMPflow jets) instead of EMTopo jets. The electron (muon) isolation uses the FCTight (PflowTightFixedRad) working point. The definitions for these objects and algorithms are included in Section 3.3. To determine the optimal working points for each algorithm, this analysis leverages the optimisation studies from the improved MSSM $H/A/h \rightarrow \tau\tau$ analysis, which are described in Section 7.2.2. The discriminating variable was changed from M_T^{TOT} to $S_T = p_T^{\tau_{\text{had}}} + p_T^{\tau_{\text{lep}}} + p_T^{b\text{-jet}}$ as it gave better separation between signal and background.

Table 6.3: A description of the signal regions used in this analysis with the necessary changes to the legacy b -tag SR outlined in Section 4.3 and the corresponding reasons for the change.

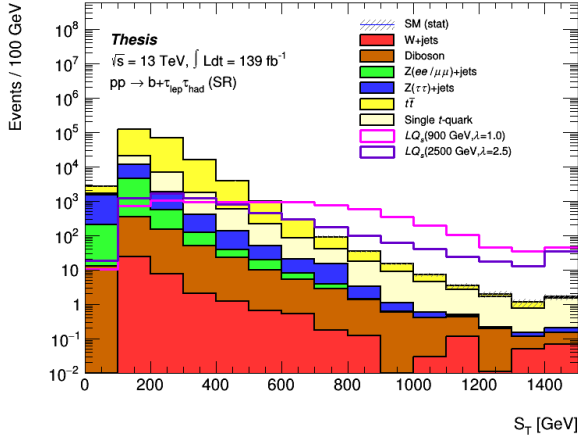
Region	Selection
Common between LQ SRs	$\ell(\text{trigger, isolated}), \tau_{\text{had}}(\text{Medium RNN}), p_T^{\tau} > 50 \text{ GeV}, q(\ell) \times q(\tau_{\text{had}}) < 0,$ $\Delta\phi(\ell, E_T^{\text{MISS}}) < 1.5, m_{\text{vis}}(\ell, \tau_{\text{had}}) > 100 \text{ GeV}, S_T > 300 \text{ GeV}, N_{b\text{-jets}} > 0$
High $p_T^{b\text{-jet}}$ SR	$p_T^{b\text{-jet}} > 200 \text{ GeV}$
Low $p_T^{b\text{-jet}}$ SR	$25 \text{ GeV} < p_T^{b\text{-jet}} \leq 200 \text{ GeV}$
Change to legacy b -tag SR	Reason
New cut: $p_T^{b\text{-jet}} > 200 \text{ GeV}$	To reduce the effects of interference from SM backgrounds
New cut: $m_{\text{vis}}(\ell, \tau) > 100 \text{ GeV}$	To suppress Z + jets events, shown in Figure 6.3(d)
New cut: $\Delta\phi(\ell, E_T^{\text{MISS}}) > 1.5$	To suppress some top background, shown in Figure 6.3(b)
New cut: $S_T = p_T^{\tau_{\text{had}}} + p_T^{\tau_{\text{lep}}} + p_T^{b\text{-jet}} > 300 \text{ GeV}$	To suppress most backgrounds, shown in Figure 6.3(c)
Shift threshold: $p_T^{\tau_{\text{had}}} > 50 \text{ GeV}$	To suppress most backgrounds, shown in Figure 6.3(a)
Discriminant change: Use S_T instead of M_T^{TOT}	Better signal to background separation observed



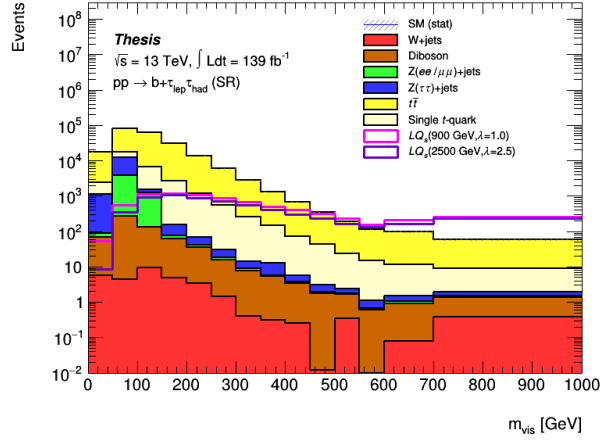
(a) p_T^τ



(b) $\Delta\phi(\ell, E_T^{\text{MISS}})$



(c) S_T



(d) m_{vis}

Figure 6.3: The distributions of key variables in a preselection region featuring only truth matched MC, including the p_T^τ , $\Delta\phi(\ell, E_T^{\text{MISS}})$, S_T , and m_{vis} . The magenta and purple histograms represent the signals for a scalar 900 GeV ($\lambda = 1.0$) and 2500 GeV ($\lambda = 2.0$) LQ , respectively. These plots provide insight into the phase space and motivate the need for specific cuts to enhance the signal to background ratio in the signal region. The uncertainty band reflects the statistical uncertainty.

6.4 Background Estimation in the $\tau_{\text{lep}}\tau_{\text{had}}$ Channel

In this analysis, there has been a significant change in the SR compared to the legacy SR. This change has resulted in a different background composition, with the main background now coming from real $t\bar{t}$ and single t -quark events, along with some contribution from fake top events (real lepton, fake tau). Therefore, it is crucial to accurately model the real top background.

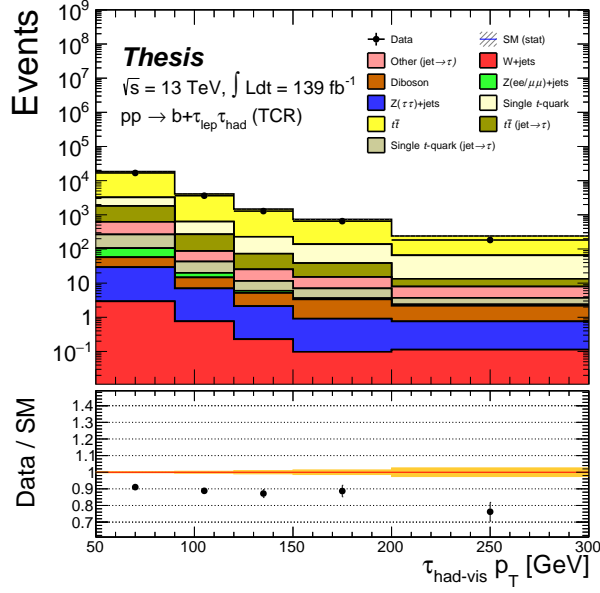
To constrain the background in this new SR, it is necessary to make changes to the control and fake regions. The regions are summarised in Table 6.4 and are mainly partitioned by the variable $\Delta\phi(\ell, E_T^{\text{MISS}})$, unlike the legacy analysis, which used the variable $m_T(\ell, E_T^{\text{MISS}})$. In the LQ analysis, a different data-driven technique is used for the top fake background estimation whereas the multi-jet background estimation is similar to the legacy analysis, this is explained in Section 4.5.1.

Table 6.4: The partitioning of the control, fake and validation regions for the $LQ \rightarrow b\tau\tau$ analysis.

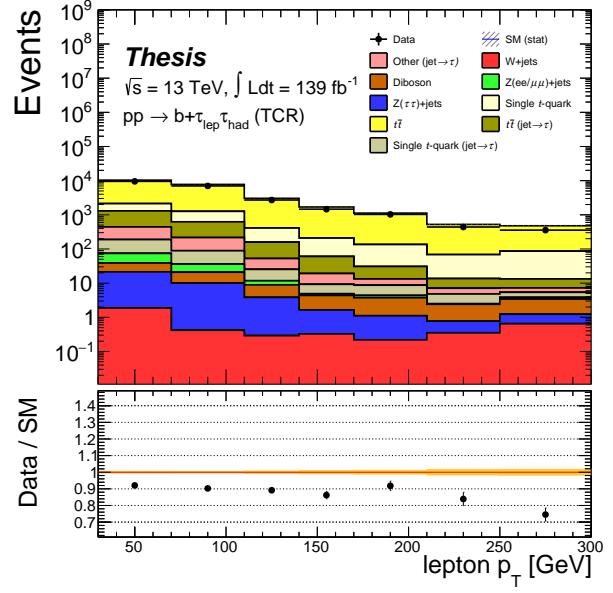
Region	Usage	Selection
MFR	Calculate the multi-jet fake factors	$\ell(\text{trigger}), \tau_{\text{had}}(\text{RNN score} < 0.01), N_\ell = 1, m_T(\ell, E_T^{\text{MISS}}) < 30 \text{ GeV}$ $E_T^{\text{MISS}} < 50 \text{ GeV } N_{b\text{-jets}} = 1$. Pass or fail isolation requirement
SS-CR	Correct the real lepton, fake tau cases	Pass SR except: Remove $\Delta\phi(\ell, E_T^{\text{MISS}})$ and S_T selection, $q(\ell) \times q(\tau_{\text{had}}) > 0$ Pass or fail ID requirement (RNN score > 0.01)
TCR	Used to correct the real top background in each region	Pass SR except: Remove S_T and $p_T^{b\text{-jet}}$ requirement, $\Delta\phi(\ell, E_T^{\text{MISS}}) > 2.5$
VR	Validating the background model	Pass SR except: $1.5 < \Delta\phi(\ell, E_T^{\text{MISS}}) > 2.5$
MF-AR1	The region to apply the multi-jet fake factor to get the SR multi-jet contribution	Pass SR except: $\ell(\text{trigger, fail lepton isolation})$

6.4.1 Constraining the t -quark Background

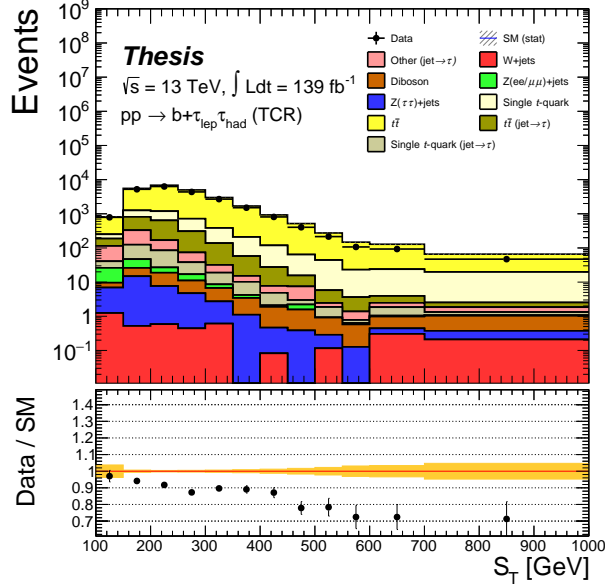
The distributions of some key variables in the TCR are shown in Figure 6.4, an overestimation of the top background is clearly visible. To address this mismodelling, a scale factor is derived and applied to every fake, validation, and signal region using a corresponding TCR. The TCR is orthogonal to the SR, having the same requirements, except for $\Delta\phi(\ell, E_T^{\text{MISS}}) \geq 2.5$ and no S_T requirement or condition on the leading b -jet. The TCR has negligible contamination from signal and 97% purity of top processes with 93% of these events originating from a truth tau. The distributions of some key variables in the TCR are shown in Figure 6.4, an overestimation of the top background is clearly visible.



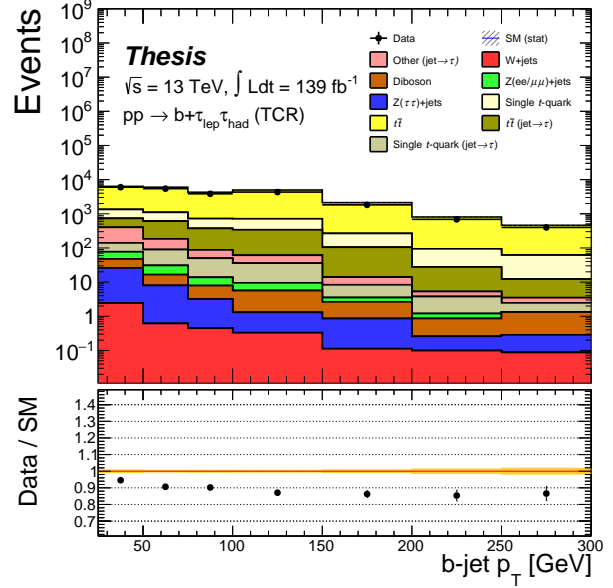
(a) p_T^τ



(b) p_T^ℓ



(c) S_T



(d) $p_T^{b\text{-jet}}$

Figure 6.4: The distributions of crucial variables (p_T^τ , p_T^ℓ , S_T and $p_T^{b\text{-jet}}$) in the TCR. The distributions are split into two truth categories: the scenario where the hadronic tau is genuine (truth matched) and the one where it is not truth matched, labelled as ‘jet $\rightarrow \tau$ ’ which is the majority of the cases. The uncertainty band represents the statistical uncertainty.

The top correction factor (SF_{top}) is defined by the equation:

$$SF_{Top}(S_T) = \frac{N_{\text{data}} - N_{\text{other MC}}}{N_{\text{top MC}}} \quad (6.1)$$

where N_{data} represents the data in the TCR, N_{other} represents the non-top MC background, and N_{top} represents the real and fake $t\bar{t}$ and single t -quark background. The inclusion of both real and fake top events in N_{top} has negligible effect on the scale factor. The derived top scale factor as a function of S_T is visualised in Figure 6.5, along with a linear fit calculated at 68% confidence, and the corresponding line for a logarithmic fit. These fits serve the purpose of interpolation and deriving systematics. Validation plots derived from reapplying the top scale factor back into the TCR are shown in Figure 6.6, where adequate modelling is now observed in the region.

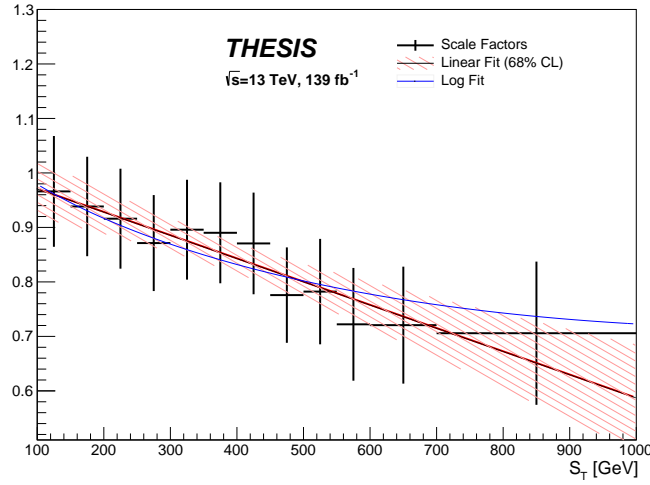
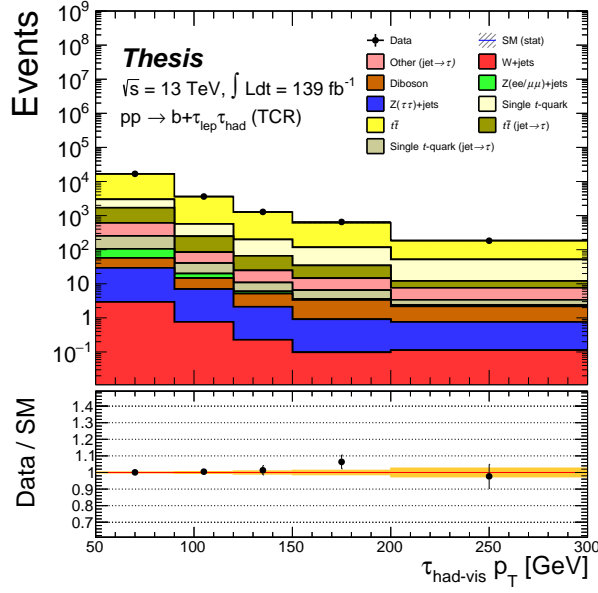
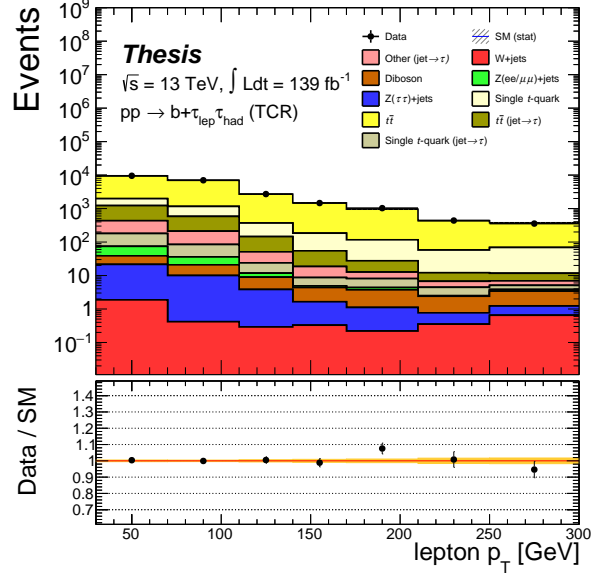


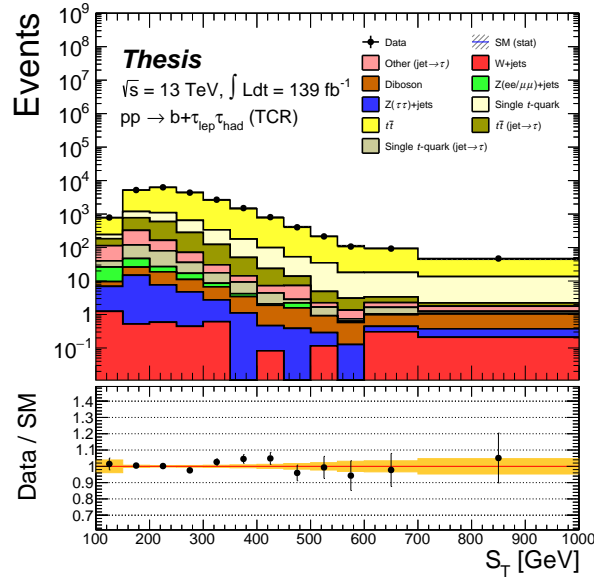
Figure 6.5: The top scale factor obtained from evaluating Equation 6.1. A linear fit to the scale factor is shown, along with its 68% confidence limit. Additionally, the figure includes the fit resulting from following a log function.



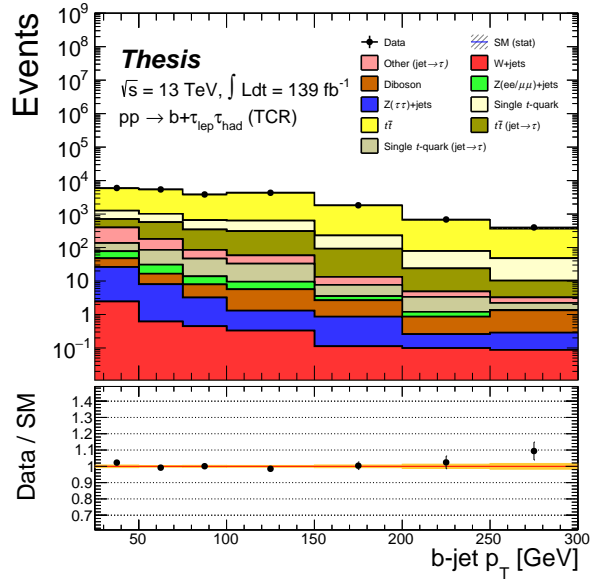
(a) p_T^τ



(b) p_T^ℓ



(c) S_T



(d) $p_T^{b\text{-jet}}$

Figure 6.6: The validation plots of important variables (p_T^τ , p_T^ℓ , S_T and $p_T^{b\text{-jet}}$) in the TCR, with the top correction applied. The distributions are split into two truth categories: the scenario where the hadronic tau is genuine (truth matched) and the one where it is not truth matched ‘jet $\rightarrow \tau$ ’. The uncertainty band represents the statistical uncertainty.

When considering the systematic uncertainty of the top correction, the statistical uncertainty, and the 10% modelling uncertainty on the real tau MC are evaluated in the same way as the legacy analysis fake factor systematic uncertainty, which was mentioned in Section 4.5.1.

Additional systematic uncertainties must be derived to account for the combination of $t\bar{t}$ and single t -quark processes in the calculation of the scale factor. In principle, a scale factor should be derived for each process. However, it is difficult to do so due to the interference between the $t\bar{t}$ and tW diagrams [238]. Therefore, in this analysis, a combined top correction is used, and an extrapolation systematic is derived to account for the different fraction of single t -quark events compared to $t\bar{t}$ in the SR.

In the TCR, almost all of the single t -quark contribution (97%) comes from the tW process, this is similar in the SR. Therefore, the effect of having a different fraction of single t -quark subprocesses in each region is not taken into account for the extrapolation systematic. Figure 6.7(a) shows a large difference in the $\frac{\text{single } t\text{-quark}}{\text{total top}}$ ratio between the SR and TCR. Although there exists a dedicated tW interference combined performance derived systematic uncertainty provided by the ATLAS top working group, which is considered in Section 6.6 and is equivalent to the extrapolation uncertainty, a separate systematic to address this effect was derived and included in this analysis. The extrapolation uncertainty is calculated by applying the top correction using only $t\bar{t}$ events and assigning the difference between this and the combined correction as the uncertainty. The derived uncertainty as a function of S_T is shown in Figure 6.7(b).

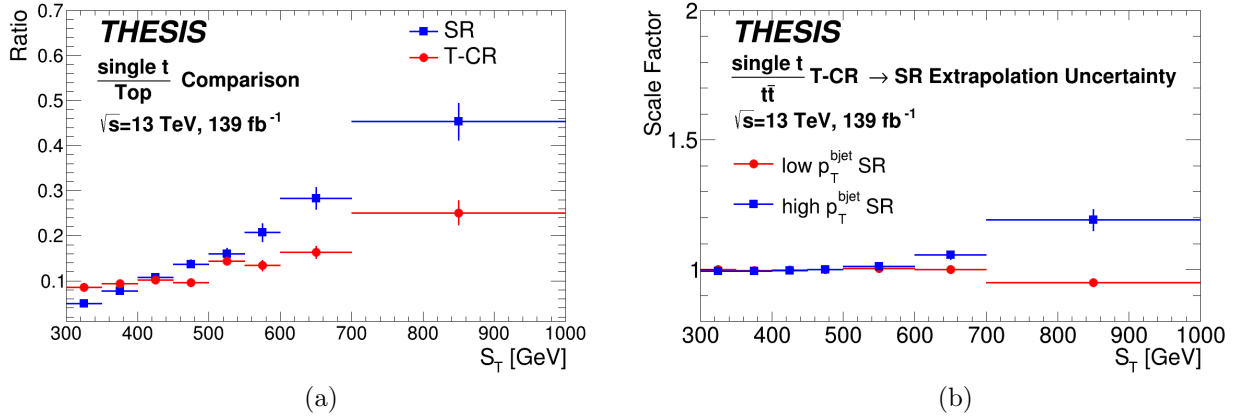


Figure 6.7: a) A comparison of the $\frac{\text{single } t\text{-quark}}{\text{total top}}$ in the SR and TCR. b) The resulting extrapolation uncertainty derived to cover the difference between $\frac{\text{single } t\text{-quark}}{\text{total top}}$ in the SR and TCR.

As the scale factor is determined by an interpolation from a linear fit, an uncertainty is derived to account for a non-linear function being a better choice. A logarithmic fit with the function $SF_{top} = a \ln(S_T) + b$ is used as an alternative to the linear fit. The difference between the logarithmic fit and the nominal linear fit is taken as a systematic uncertainty.

6.5 Estimation of the Fake Background

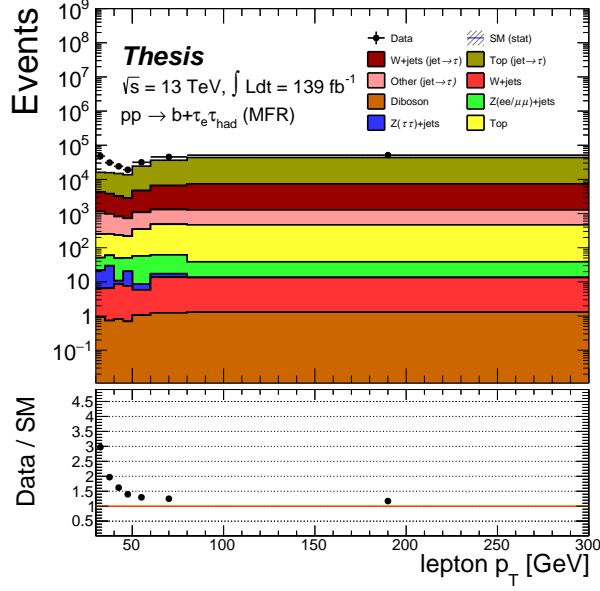
In this analysis, a significant portion of the background comes from jet fakes. In the multi-jet case, where both the lepton and the tau are fake, the contribution in the SR is negligible ($< 1\%$). Nevertheless, the multi-jet contribution is estimated using the same methods as the legacy analysis, as described in Section 4.5.1.

For the other case, where the lepton is real but the tau is a jet fake (referred to as top fakes for this analysis, they are typically $t\bar{t}$ or single t -quark fakes), the recipe is considerably different to the legacy analysis W +jets/top fake estimation from Section 4.5.1.

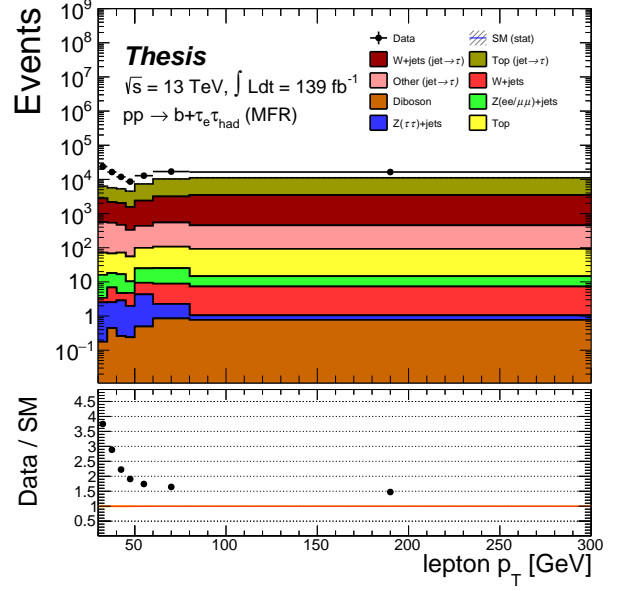
Multi-jet Fake Estimation

The MFR has the same selection criteria as in the legacy analysis, which is shown in Table 4.4. However, two additional requirements are added: $E_T^{\text{MISS}} < 50$ GeV and $N_{b\text{-jets}} = 1$. These criteria and their motivation are recommended from the improved analysis optimisation studies mentioned in Section 7.2.6, in order to enhance the purity of multi-jet fakes in the MFR.

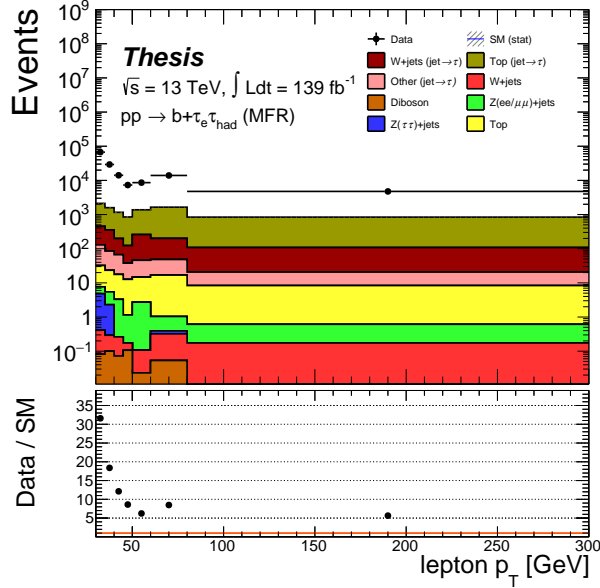
The fake factors are evaluated in the usual way by evaluating Equation 4.3 using the pass and fail isolation regions. However, the isolation working points used in this analysis are FCTight (PflowTight_FixedRad) for electrons (muons), which are defined in Table 3.2. The multi-jet fake factors are now parameterised in $(p_T^\ell, |\eta(\ell)|)$ for the barrel ($|\eta(\ell)| < 1.52$) and end-cap ($|\eta(\ell)| \geq 1.52$), for simplicity and harmonisation with other ATLAS analyses. The poor modelling of the pass-ISO p_T^ℓ distribution in the MFR is shown in Figures 6.8 and 6.9 for the two $|\eta|$ intervals in the $e\tau_{\text{had}}$ and $\mu\tau_{\text{had}}$ channels, before the fake factors are applied. The resulting fake factors in intervals of $|\eta(\ell)|$ are presented for the $e\tau_{\text{had}}$ and $\mu\tau_{\text{had}}$ channels in Figure 6.10. The behaviour of the fake factors is similar to that of the legacy analysis, with the discontinuities due to the activation of different triggers. In the $\mu\tau_{\text{had}}$ channel, the fake factor uncertainty bar is large due to the low purity of multi-jet events in the final bin of the pass-ISO region. Since the multi-jet fake yield is negligible in the SR, the uncertainty bars have no effect as the corresponding nuisance parameters are pruned away during the fitting procedure. Validation plots in Figure 6.11 demonstrate that the pass-ISO part of the multi-jet fake region is adequately modelled for p_T^ℓ , p_T^τ , S_T , and $p_T^{b\text{-jet}}$ once the fake factors are applied into the MFR application (fail-ISO) region.



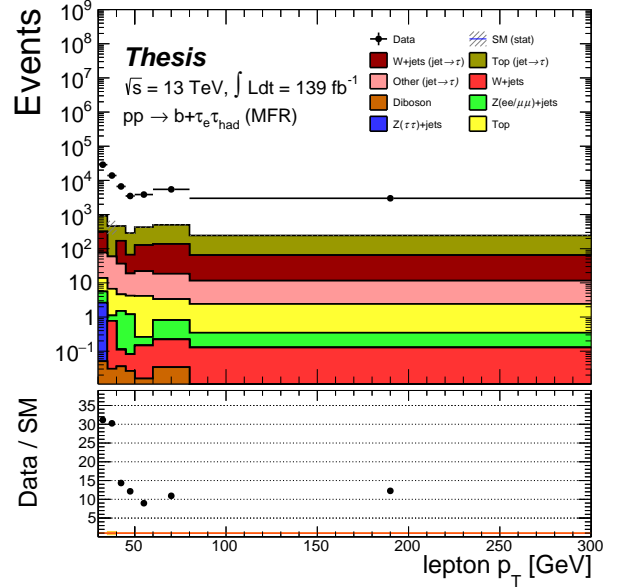
(a) p_T^ℓ , $|\eta| < 1.52$, $e\tau_{\text{had}}$, pass-ISO



(b) p_T^ℓ , $|\eta| \geq 1.52$, $e\tau_{\text{had}}$, pass-ISO

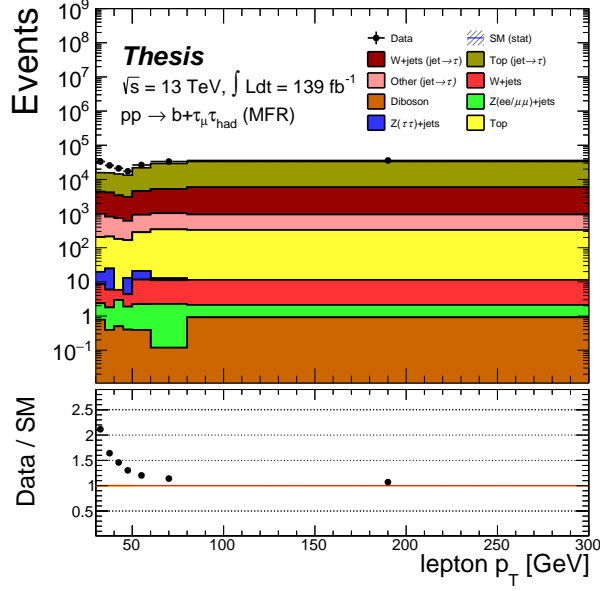


(c) p_T^ℓ , $|\eta| < 1.52$, $e\tau_{\text{had}}$, fail-ISO

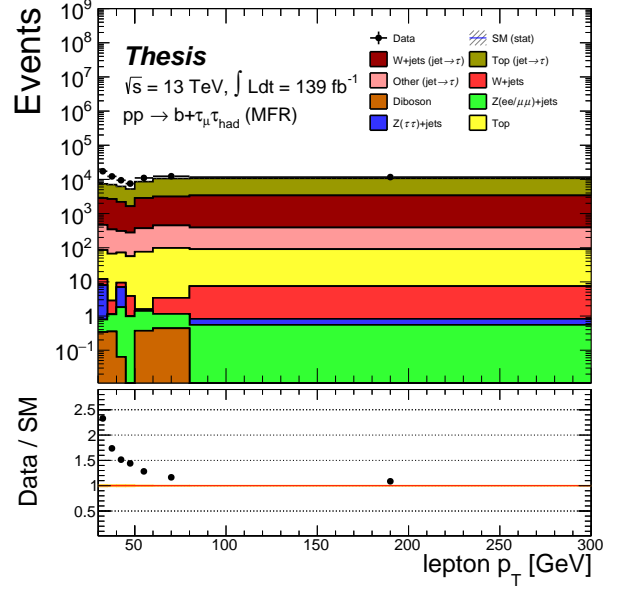


(d) p_T^ℓ , $|\eta| \geq 1.52$, $e\tau_{\text{had}}$, fail-ISO

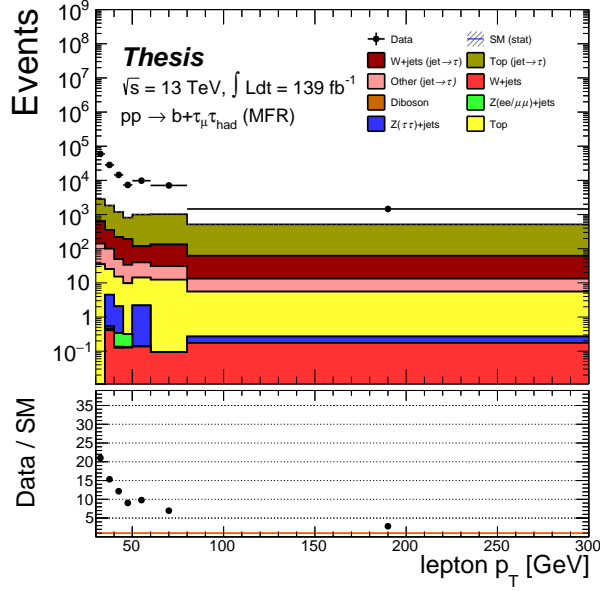
Figure 6.8: The distributions used to evaluate Equation 4.3 in the $e\tau_{\text{had}}$ multi-jet fake region, shown before applying the multi-jet fake factor. The distributions are split into two truth categories: the scenario where the hadronic tau is genuine (truth matched) and the one where it is not truth matched ‘jet $\rightarrow \tau$ ’. The uncertainty band represents the statistical uncertainty.



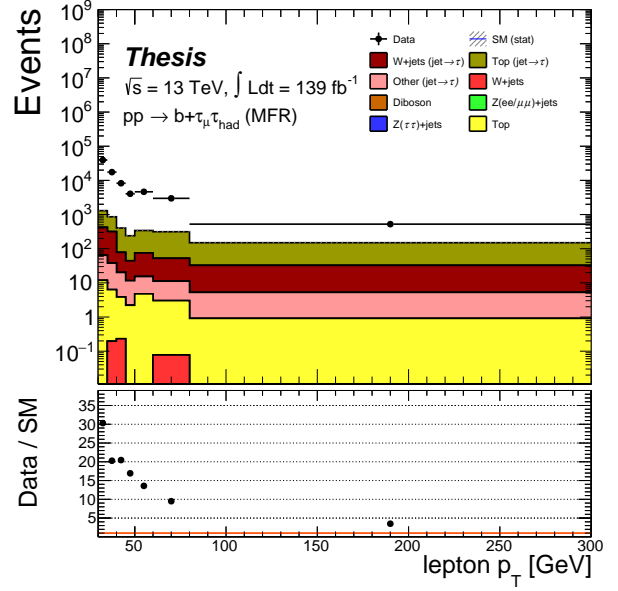
(a) p_T^ℓ , $|\eta| < 1.52$, $\mu\tau_{\text{had}}$, pass-ISO



(b) p_T^ℓ , $|\eta| \geq 1.52$, $\mu\tau_{\text{had}}$, pass-ISO

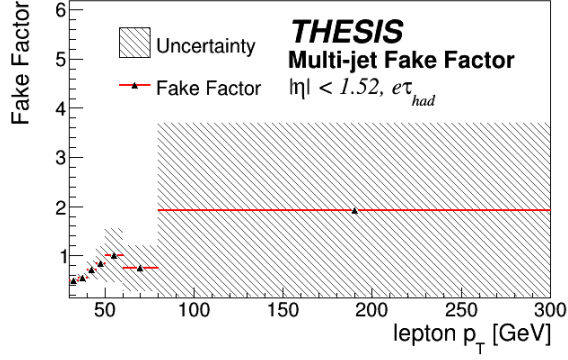


(c) p_T^ℓ , $|\eta| < 1.52$, $\mu\tau_{\text{had}}$, fail-ISO

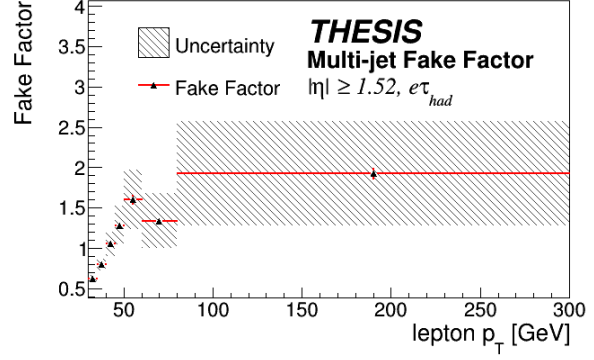


(d) p_T^ℓ , $|\eta| \geq 1.52$, $\mu\tau_{\text{had}}$, fail-ISO

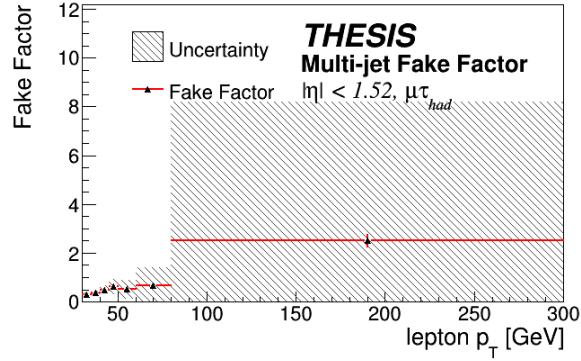
Figure 6.9: The distributions used to evaluate Equation 4.3 in the $\mu\tau_{\text{had}}$ multi-jet fake region, shown before applying the multi-jet fake factor. The distributions are split into two truth categories: the scenario where the hadronic tau is genuine (truth matched) and the one where it is not truth matched ‘jet $\rightarrow \tau$ ’. The uncertainty band represents the statistical uncertainty.



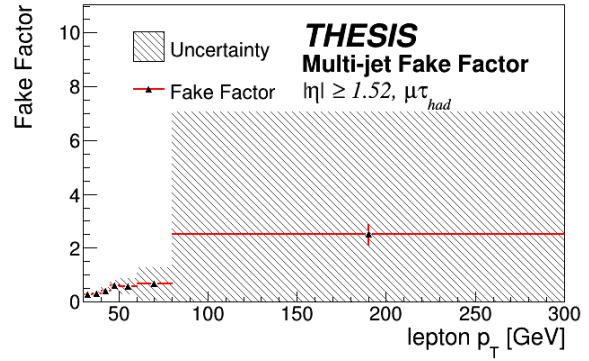
(a) $|\eta| < 1.52, e\tau_{had}$



(b) $|\eta| \geq 1.52, e\tau_{had}$

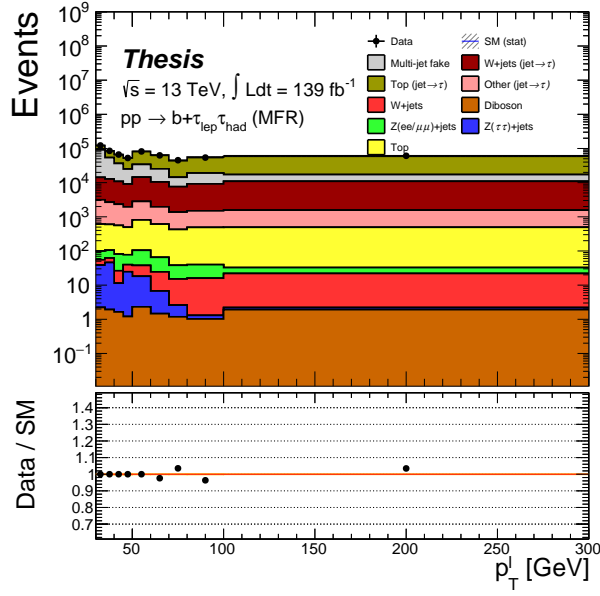


(c) $|\eta| < 1.52, \mu\tau_{had}$

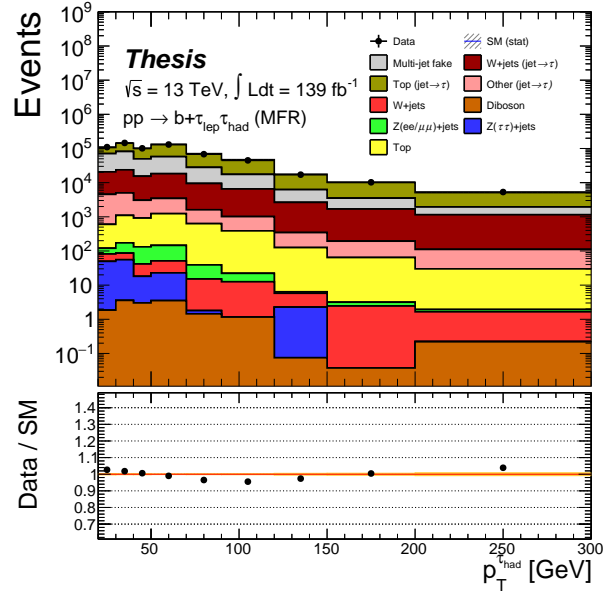


(d) $|\eta| \geq 1.52, \mu\tau_{had}$

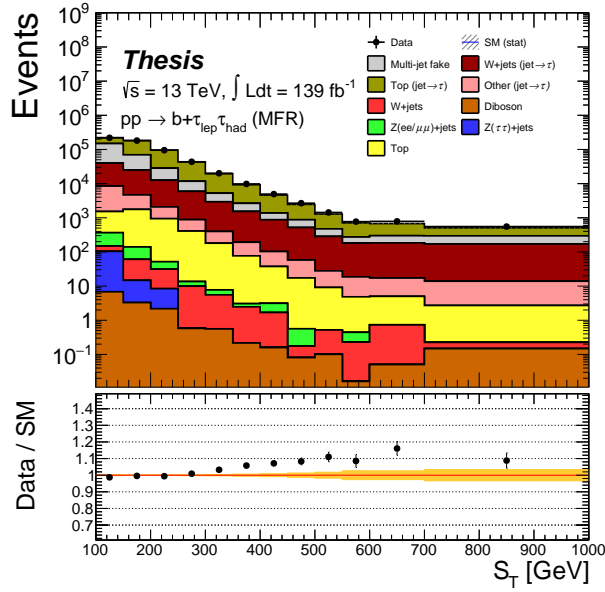
Figure 6.10: The evaluated multi-jet fake factors for the $e\tau_{had}$ and $\mu\tau_{had}$ channels used to derive the SR multi-jet contribution. The uncertainty bar represents the statistical uncertainty, whereas the uncertainty band visualises both the statistical and systematic uncertainty.



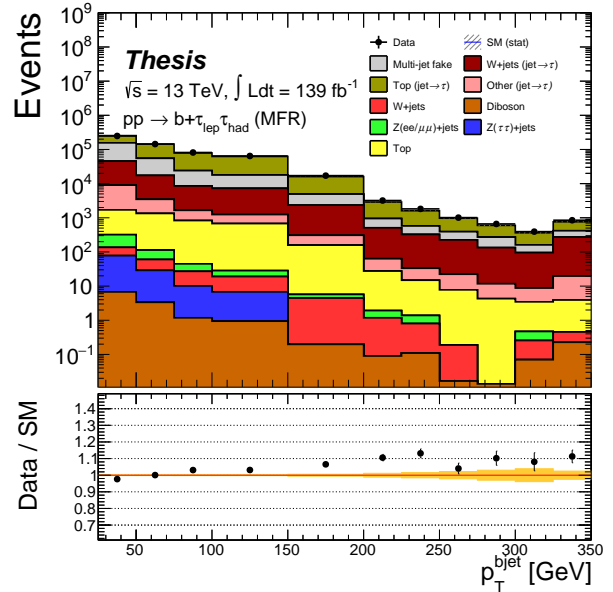
(a) $p_T^\ell, \tau_{\text{lep}}\tau_{\text{had}}$



(b) $p_T^\tau, \tau_{\text{lep}}\tau_{\text{had}}$



(c) $S_T, \tau_{\text{lep}}\tau_{\text{had}}$



(d) $p_T^{b\text{-jet}}, \tau_{\text{lep}}\tau_{\text{had}}$

Figure 6.11: The validation plots of important variables (p_T^ℓ , p_T^τ , S_T and $p_T^{b\text{-jet}}$) in the MFR, with the top correction multi-jet fake factors applied. The distributions are split into two truth categories: the scenario where the hadronic tau is genuine (truth matched) and the one where it is not truth matched ‘jet $\rightarrow \tau$ ’. The uncertainty band represents the statistical uncertainty.

For the statistical and modelling uncertainty, these are kept mostly the same as in Section 4.5.1, with the 20% uncertainty applied for the non-isolated lepton in the denominator of Equation 4.3. As a validation, the fake factors were applied to a separate MFR application region, with the only difference being that the $m_T(\ell, E_T^{\text{MISS}}) < 30$ GeV cut was changed to $m_T(\ell, E_T^{\text{MISS}}) > 60$ GeV, and the tau ID score < 0.01 cut was removed, allowing the pass-ISO part of the region to mimic the SR. The MC in this region was underestimated by approximately 15%, possibly due to mismodelling of top fakes, which is addressed in the following section. To be conservative, the normal 10% variation on the numerator of the fake factor in Equation 4.3 was increased to 15% to account for this discrepancy if it were due to real tau mismodelling.

W+jet/top Fake Estimation

Due to the changes required to implement the LQ analysis, the b -tag WFR from Section 4.5.1 is no longer a viable option to estimate the top fake contribution. This is because the control regions orthogonal to the signal region are no longer partitioned based on $m_T(\ell, E_T^{\text{MISS}})$. Despite an exhaustive search, no orthogonal region with enough top fake purity was found to use the fake factor method without encountering high statistical uncertainty. To compensate, a region with reasonable purity was found and an alternative fake estimation technique was employed.

The SS-SR fake region, defined in Table 6.4, is used to estimate the top fake contribution. The region is close to the SR apart from a few selections. Firstly, $q(\ell) \times q(\tau_{\text{had}})$ is flipped to target same-sign taus. To increase the number of events, the requirements on $\Delta\phi(\ell, E_T^{\text{MISS}})$ and S_T are removed. Approximately 60% of the events in this region involve a fake tau with a real lepton, while the rest are mainly true top backgrounds. However, a portion of the events in the $e\tau_{\text{had}}$ channel contain a real tau and a fake lepton, which is a different source of fake and not explicitly corrected for in this region. To address this issue, the $\mu\tau_{\text{had}}$ channel is used to derive the fake factors for both the $e\tau_{\text{had}}$ and $\mu\tau_{\text{had}}$ channels.

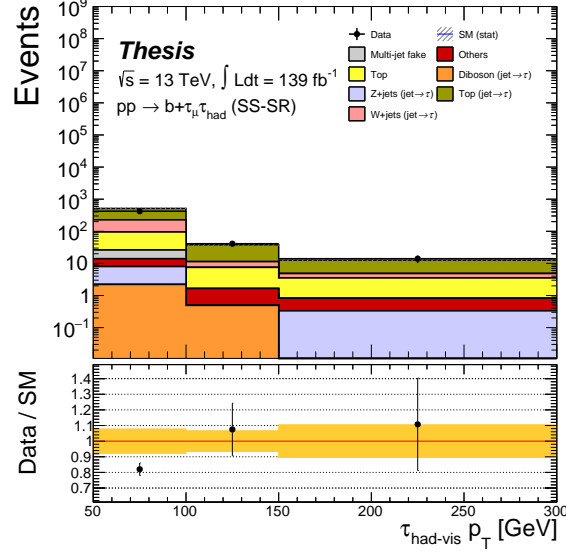
To estimate the number of events involving fake taus and real leptons, the MC prediction of the fakes is corrected using the equation:

$$SF_{\text{SS-SR}} = \frac{N_{\text{data}} - N_{\text{true tau}}}{N_{\text{fake tau}}} \quad (6.2)$$

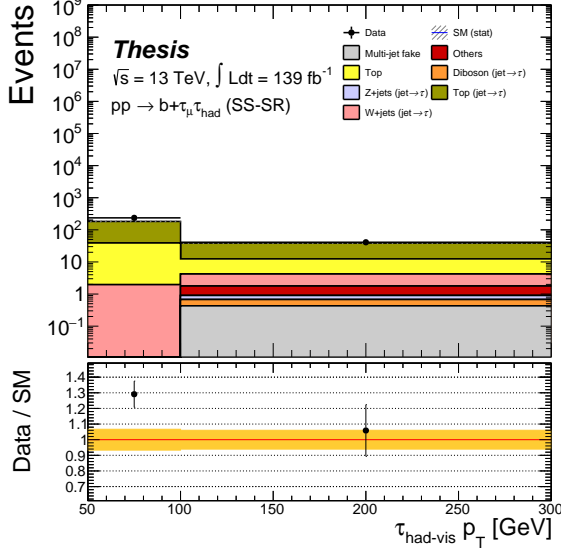
where the quantity $N_{\text{true tau}}$ represents the reconstructed MC prediction which can be truth matched to real particles, whereas $N_{\text{fake tau}}$ is the MC prediction where the reconstructed tau is not truth matched. The set of non-truth matched events will typically be dominated by truth jets faking taus.

Figures 6.12 and 6.13 display the distribution of p_T^τ in the SS-SR for different intervals of $p_T^{b\text{-jet}}$ in the $\mu\tau_{\text{had}}$ channel for 1-prong and 3-prong hadronic taus, respectively. From these plots, a scale factor is derived for each interval. The resulting scale factors are presented in Figure 6.14. By applying these scale factors back to the SS-SR, the modelling for p_T^τ and S_T is improved, as shown in Figures 6.15 and 6.16, which display the validation plots in the

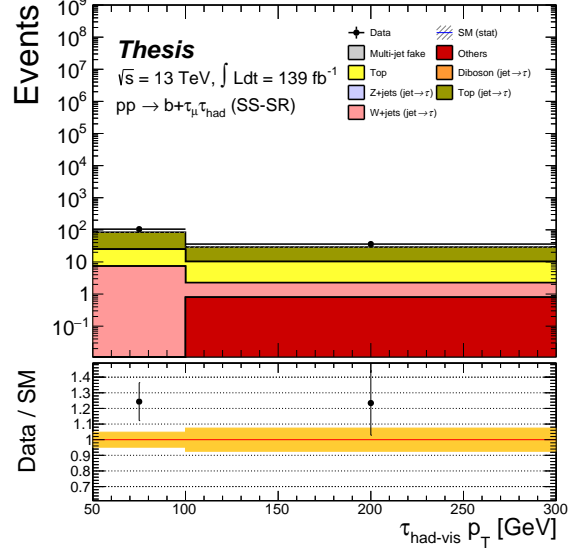
1-prong and 3-prong $\tau_{\text{lep}}\tau_{\text{had}}$ channels, respectively. Note that an overestimation in the final bin of p_T^ℓ is observed for the 3-prong case, which is addressed in the fake modelling validation discussed in Section 6.5.1.



(a) $25 \text{ GeV} \leq p_T^{b\text{-jet}} < 75 \text{ GeV}$
 1-prong $\mu\tau_{\text{had}}$

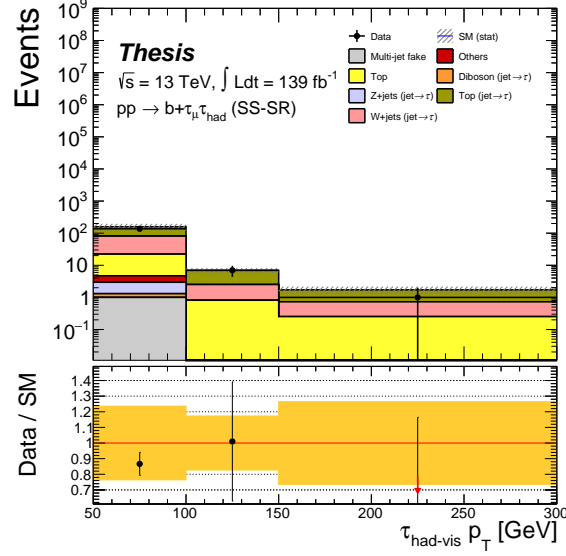


(b) $75 \text{ GeV} \leq p_T^{b\text{-jet}} < 125 \text{ GeV}$
 1-prong $\mu\tau_{\text{had}}$

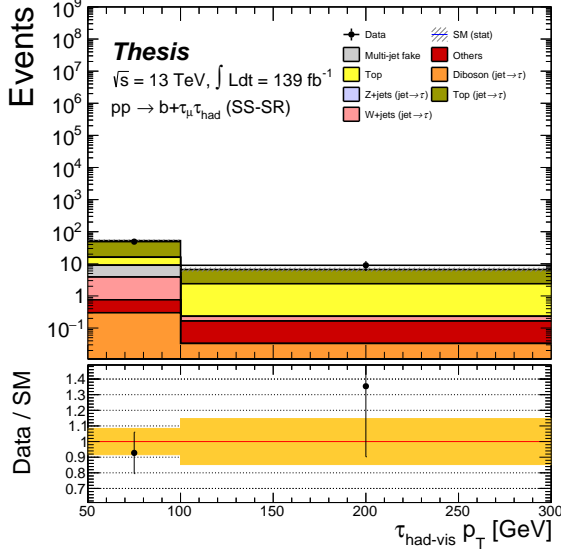


(c) $p_T^{b\text{-jet}} \geq 125 \text{ GeV}$
 1-prong $\mu\tau_{\text{had}}$

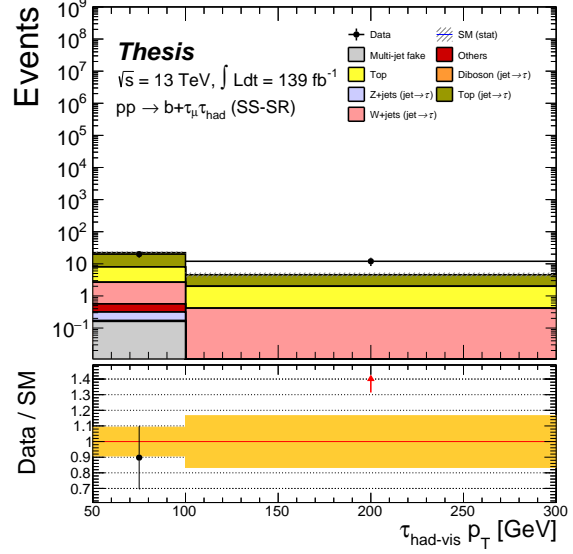
Figure 6.12: The distributions used in the calculation of the correction to the MC fake prediction for the 1-prong $\mu\tau_{\text{had}}$ channel in the SS-SR control region. The distributions are split into two truth categories: the scenario where the hadronic tau is genuine (truth matched) and the one where it is not truth matched ‘jet $\rightarrow \tau$ ’. The uncertainty band represents the statistical uncertainty.



(a) $25 \text{ GeV} \leq p_T^{b\text{-jet}} < 75 \text{ GeV}$
3-prong $\mu\tau_{\text{had}}$

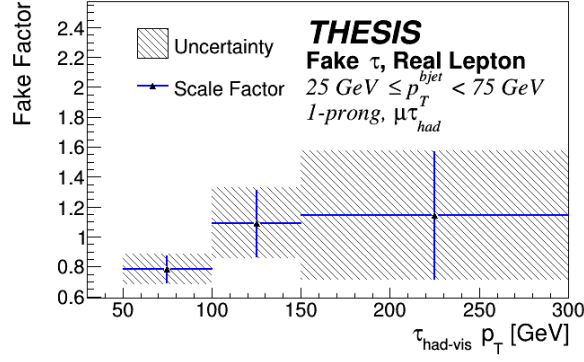


(b) $75 \text{ GeV} \leq p_T^{b\text{-jet}} < 125 \text{ GeV}$
3-prong $\mu\tau_{\text{had}}$

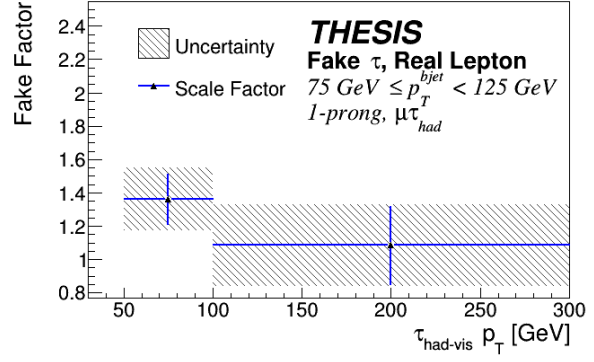


(c) $p_T^{b\text{-jet}} \geq 125 \text{ GeV}$
3-prong $\mu\tau_{\text{had}}$

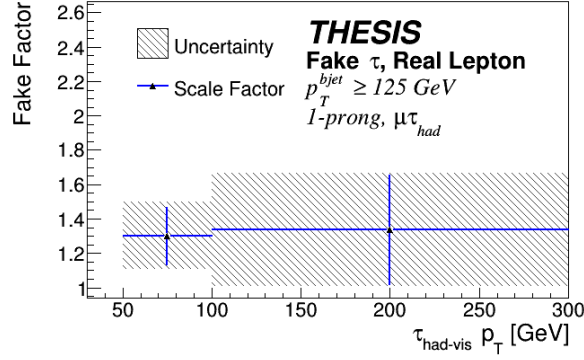
Figure 6.13: The distributions used in the calculation of the correction to the MC fake prediction for the 3-prong $\mu\tau_{\text{had}}$ channel in the SS-SR control region. The distributions are split into two truth categories: the scenario where the hadronic tau is genuine (truth matched) and the one where it is not truth matched ‘jet $\rightarrow \tau$ ’. The uncertainty band represents the statistical uncertainty.



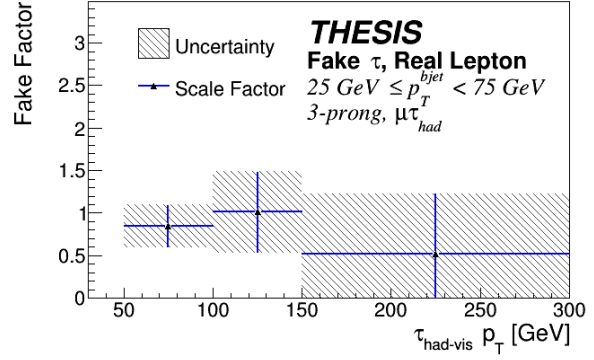
(a) $25 \text{ GeV} \leq p_T^{b\text{-jet}} < 75 \text{ GeV}$
 $\mu\tau_{\text{had}}$ 1-Prong



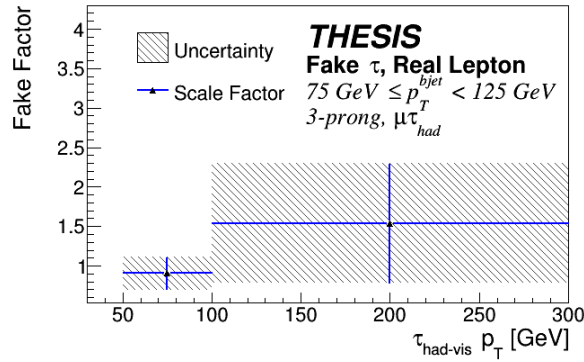
(b) $75 \text{ GeV} \leq p_T^{b\text{-jet}} < 125 \text{ GeV}$
 $\mu\tau_{\text{had}}$ 1-Prong



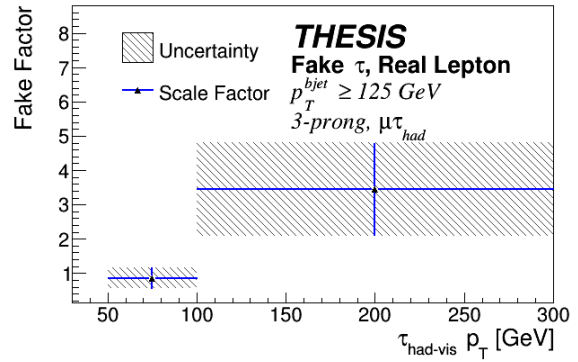
(c) $p_T^{b\text{-jet}} \geq 125 \text{ GeV}$
 $\mu\tau_{\text{had}}$ 1-Prong



(d) $25 \text{ GeV} \leq p_T^{b\text{-jet}} < 75 \text{ GeV}$
 $\mu\tau_{\text{had}}$ 3-Prong

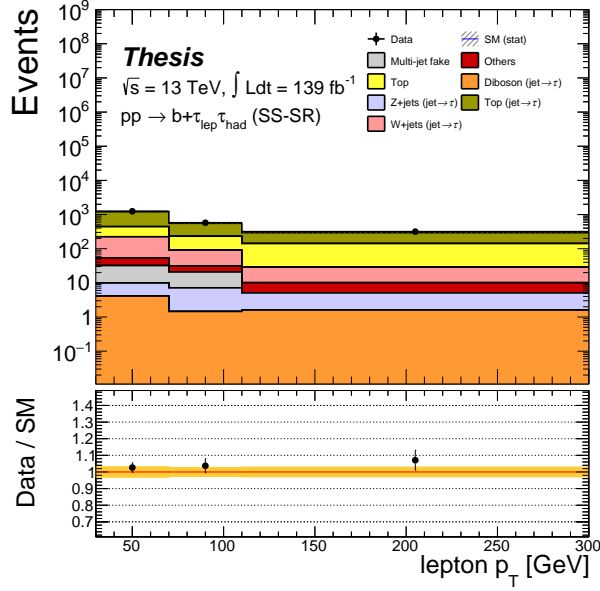


(e) $75 \text{ GeV} \leq p_T^{b\text{-jet}} < 125 \text{ GeV}$
 $\mu\tau_{\text{had}}$ 3-Prong

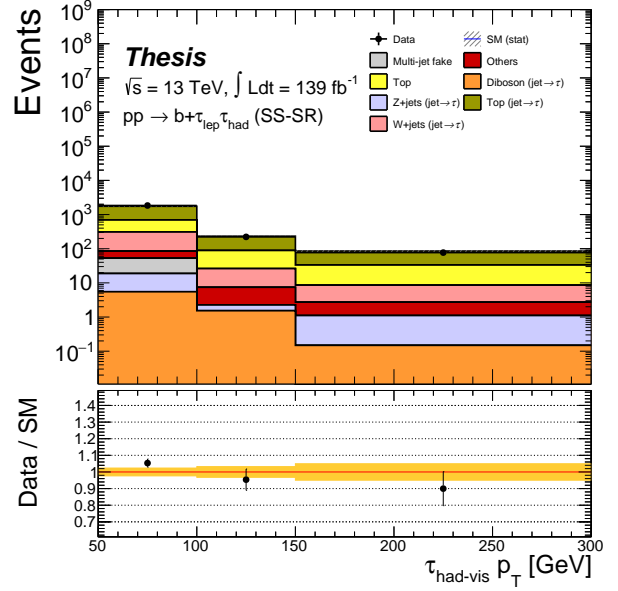


(f) $p_T^{b\text{-jet}} \geq 125 \text{ GeV}$
 $\mu\tau_{\text{had}}$ 3-Prong

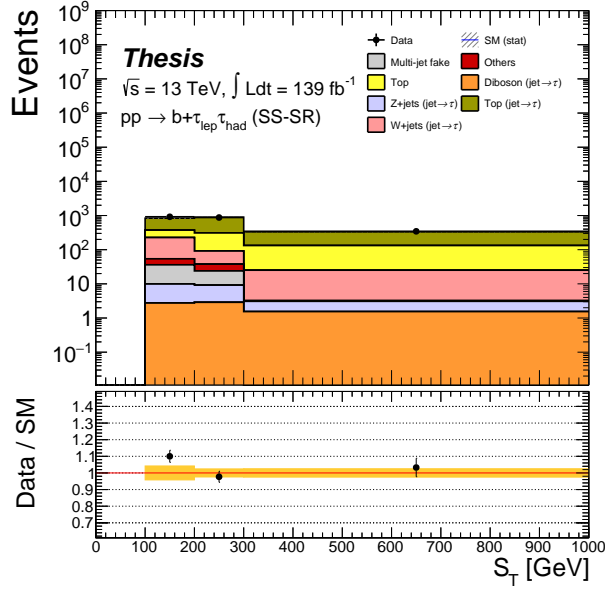
Figure 6.14: The derived scale factors in the $\mu\tau_{\text{had}}$ channel used to correct the events containing a fake hadronic tau and real lepton. The uncertainty bar represents the statistical uncertainty, whereas the uncertainty band visualises the statistical and systematic uncertainty.



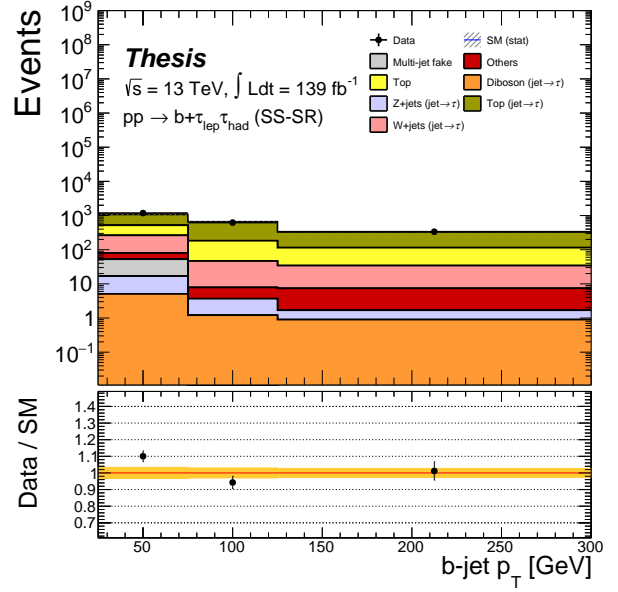
(a) 1-prong p_T^ℓ



(b) 1-prong p_T^τ

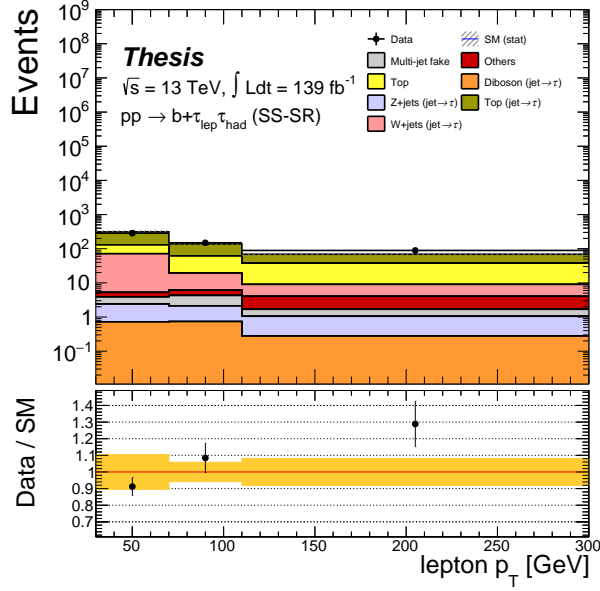


(c) 1-prong S_T

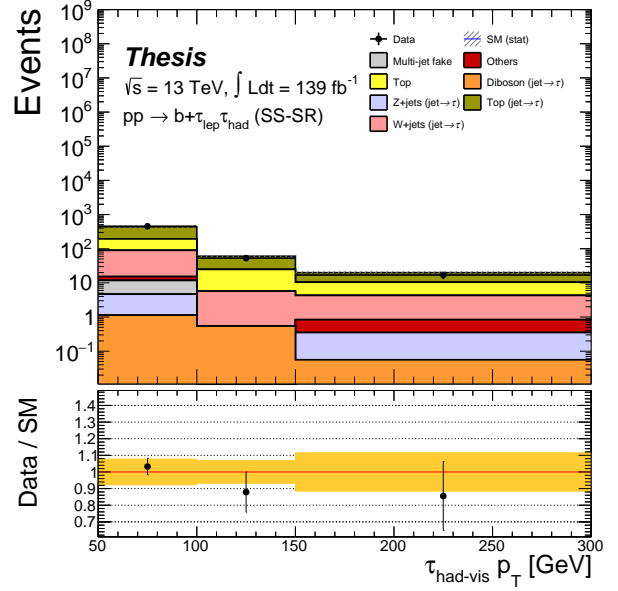


(d) 1-prong $p_T^{b\text{-jet}}$

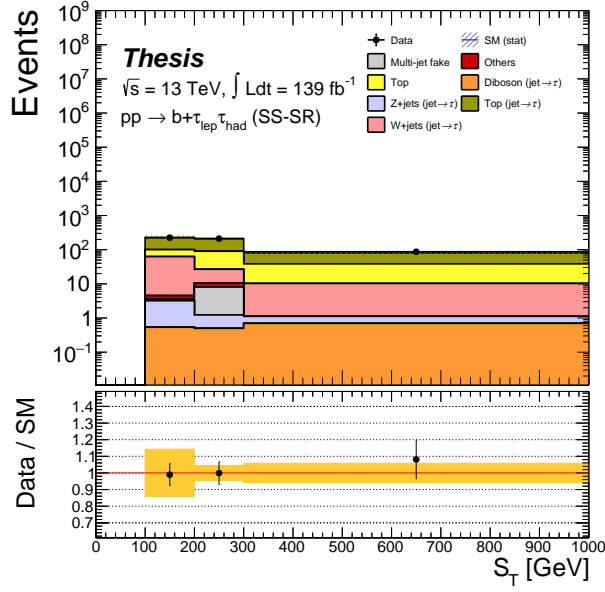
Figure 6.15: The distribution of key variables (p_T^ℓ , p_T^τ , S_T and $p_T^{b\text{-jet}}$) in the $\tau_{\text{lep}}\tau_{\text{had}}$ channel after the correction factors have been applied for the 1-prong cases. The distributions are split into two truth categories: the scenario where the hadronic tau is genuine (truth matched) and the one where it is not truth matched ‘jet $\rightarrow \tau$ ’. The uncertainty band represents the statistical uncertainty.



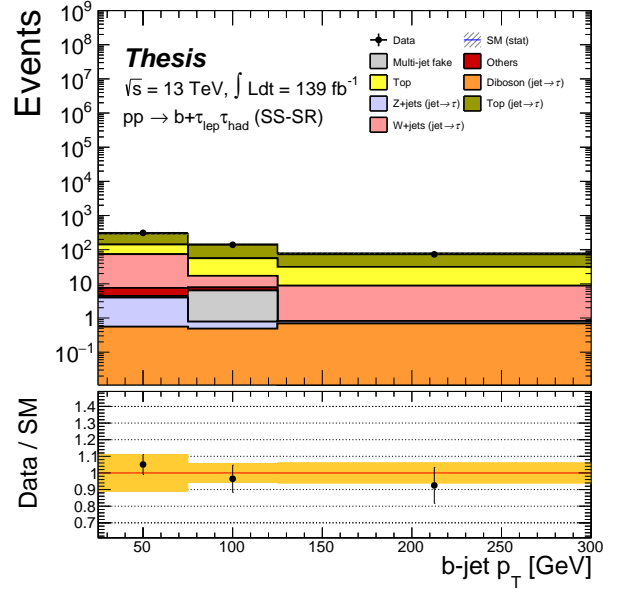
(a) 3-prong p_T^ℓ



(b) 3-prong p_T^τ



(c) 3-prong S_T



(d) 3-prong $p_T^{b\text{-jet}}$

Figure 6.16: The distribution of key variables (p_T^ℓ , p_T^τ , S_T and $p_T^{b\text{-jet}}$) in the $\tau_{\text{lep}}\tau_{\text{had}}$ channel after the correction factors have been applied for the 3-prong cases. The distributions are split into two truth categories: the scenario where the hadronic tau is genuine (truth matched) and the one where it is not truth matched ‘jet $\rightarrow \tau$ ’. The uncertainty band represents the statistical uncertainty.

The systematic uncertainties related to the estimation of top fake events are similar to those discussed for the uncertainties in the legacy analysis WFR, as mentioned in Section 4.5.1. Statistical uncertainty is handled in the usual way, while a modelling uncertainty applies to the numerator of Equation 6.2. In the $\mu\tau_{\text{had}}$ channel, the contribution of charge misidentified true taus to the overall true tau composition is significant. As a result, a 4% prior added as a nuisance parameter in the ATLAS $H \rightarrow \tau\tau$ coupling analysis [239] to account for this charge misidentification is used for this analysis. Therefore, a variation of 12% is assigned to the numerator, which is calculated from the quadratic sum of the original 10% variation (for a pass-ID region) applied in the legacy analysis and the 4% maximum uncertainty arising from the charge misidentification.

6.5.1 Fake Background Validation

To ensure adequate background modelling, a VR is defined with a selection that is identical to the SR, except that $1.5 \leq \Delta\phi(\ell, E_T^{\text{MISS}}) < 2.5$. The signal to background ratio is lower than 5% in the range $300 \text{ GeV} \leq S_T < 600 \text{ GeV}$, and this part of the VR is used to inspect the modelling. Figures 6.17 and 6.18 show the fake estimation modelling for the high and low $p_T^{b\text{-jet}}$ VRs, respectively. In general, the background is modelled well, even with a possible slope in the p_T^ℓ distribution. No further action is taken, and the fake estimation is deemed acceptable since the post-fit distributions in Section 6.7 show adequate modelling.

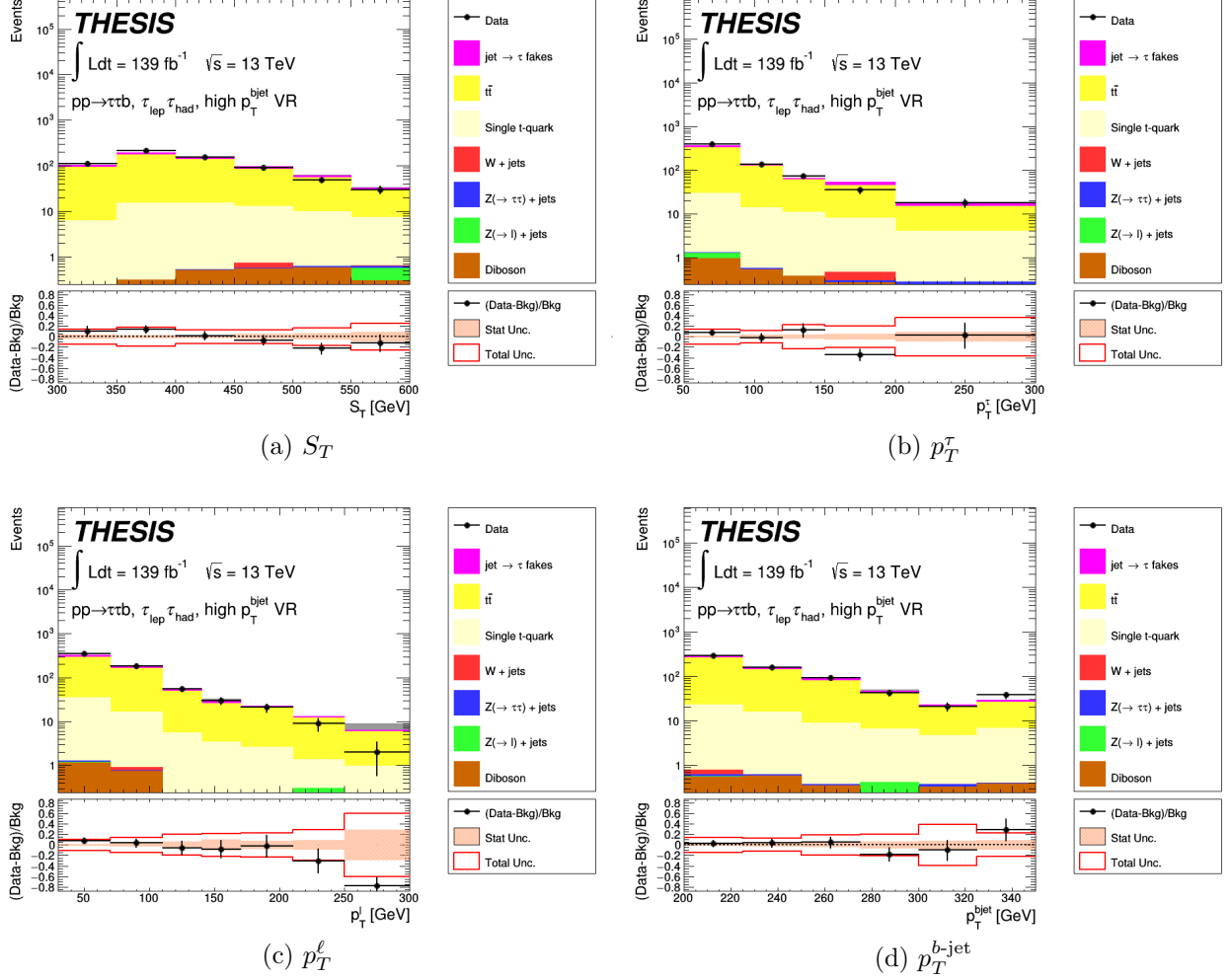


Figure 6.17: The distribution of key variables (S_T , p_T^τ , p_T^ℓ and $p_T^{b\text{-jet}}$) in the high $p_T^{b\text{-jet}}$ VR. The label ‘jet $\rightarrow \tau$ fakes’ corresponds to the contribution from events that involve a fake hadronic tau and a genuine lepton. The filled uncertainty band represents the statistical uncertainty and the red line indicates the total pre-fit uncertainty from all the variations added in quadrature.

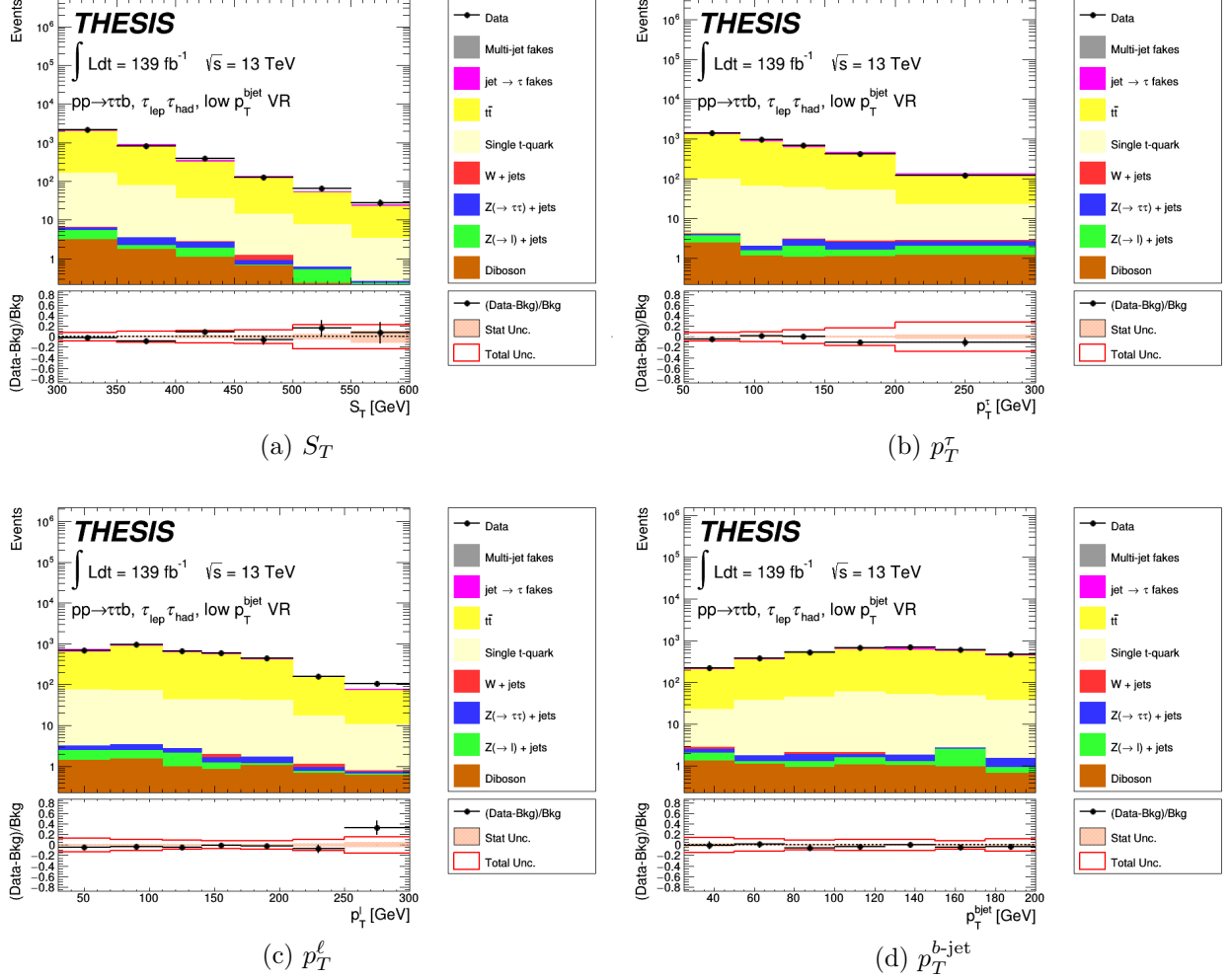


Figure 6.18: The distribution of key variables (S_T , p_T^τ , p_T^ℓ and $p_T^{b\text{-jet}}$) in the low $p_T^{b\text{-jet}}$ VR. The label ‘jet $\rightarrow \tau$ fakes’ corresponds to the contribution from events that involve a fake hadronic tau and a genuine lepton. The filled uncertainty band represents the statistical uncertainty and the red line indicates the total pre-fit uncertainty from all the variations added in quadrature.

6.6 Systematic Uncertainties

The experimental and signal modelling uncertainties used in the legacy analysis described in Section 4.6 are mostly retained in this analysis, with minor changes to the NP names to reflect updated recommendations from the combined performance groups. However, the treatment of the top theory systematics is different. Since single t -quark events make a non-negligible contribution to this analysis, an additional set of nuisance parameters is evaluated. Alternative samples with variations on the ISR, FSR, matrix element and PS are again used for $t\bar{t}$ processes, and the variation from the nominal for this analysis is assessed by recalculating the top scale factor for each variation.

Since a data-driven correction is used to derive top scale factors, any uncertainty in the cross-section of top backgrounds can be neglected as it is covered by the scale factor. In order to be extra conservative in the uncertainty estimation, the modelling uncertainty is still considered when evaluating the extrapolation uncertainty from the TCR to the SR even though the SF_{top} normalisation to data deems it unnecessary. The variation from each alternative sample is given by the equation:

$$\sigma_{ex} = \frac{N_{\text{Var, Corrected}} - N_{\text{Nom, Corrected}}}{N_{\text{Nom, Corrected}}} \quad (6.3)$$

where $N_{\text{Corrected}}$ represents the corrected yield for either the nominal sample or the variation sample. The same procedure is performed for the single top samples, which also undergo the same variations. An additional sample is included to account for the interference between the tW and $t\bar{t}$ processes, which uses the diagram subtraction scheme rather than the diagram removal scheme utilised in nominal samples [238]. The impact of using the alternative samples to derive the top correction factor for single t -quark and $t\bar{t}$ backgrounds are shown in Figures 6.19(a) and 6.19(b), respectively.

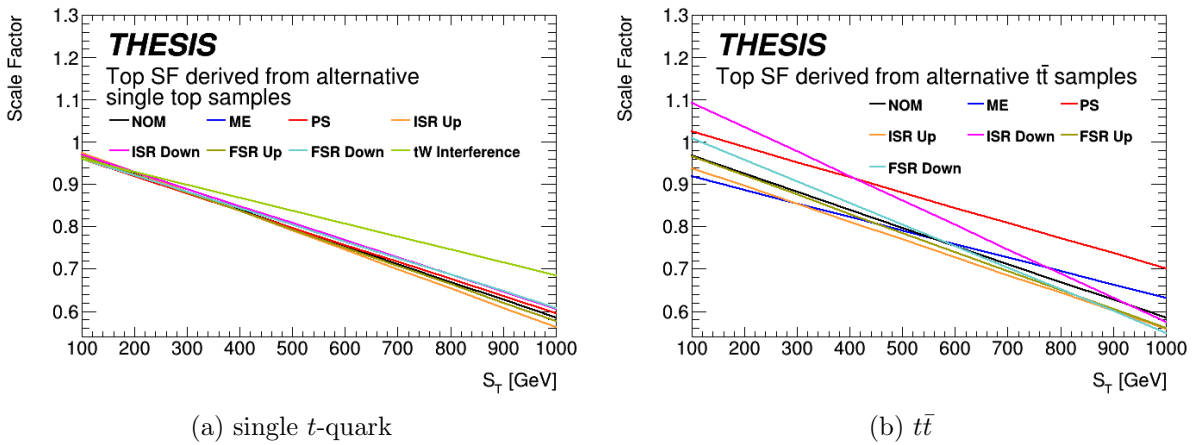
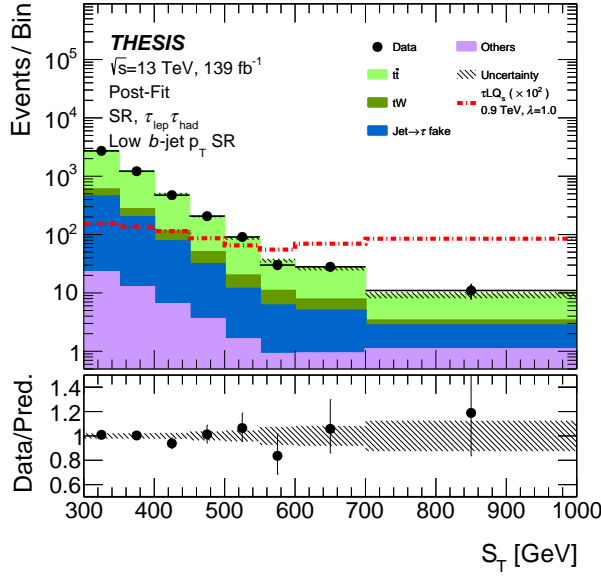


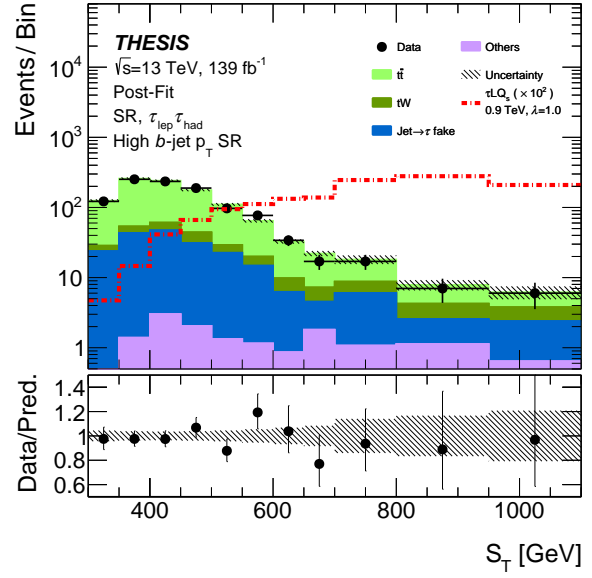
Figure 6.19: A comparison of the top scale factors derived from varied single t -quark and $t\bar{t}$ samples which take into account modelling uncertainties.

6.7 Results

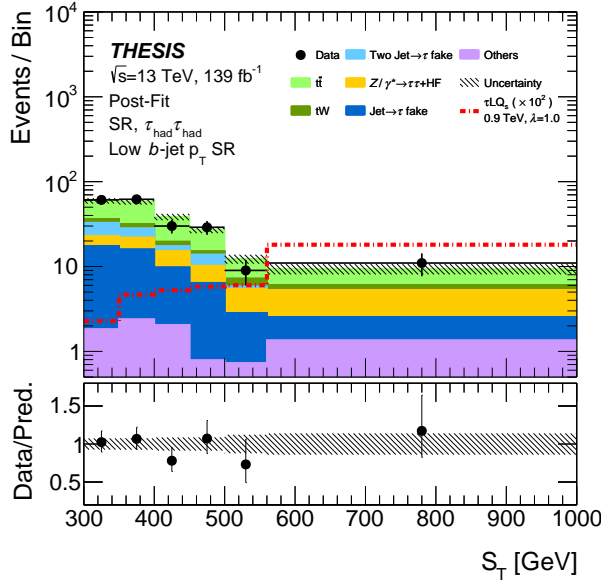
Results from both the $\tau_{\text{had}}\tau_{\text{had}}$ and $\tau_{\text{lep}}\tau_{\text{had}}$ channels are combined and retrieved. The fitting procedures described in Section 4.7 are utilised to obtain a simultaneous background-only fit to assess the modelling in the unblinded SR. Each bin must have a minimum of 10 background events to ensure the asymptotic approximation is valid. The resulting post-fit outcomes are presented in Figure 6.20 for both $\tau_{\text{had}}\tau_{\text{had}}$ and $\tau_{\text{lep}}\tau_{\text{had}}$ channels in both high and low $p_T^{b\text{-jet}}$ regions. In general, the data are found to be in good agreement with the background-only predictions.



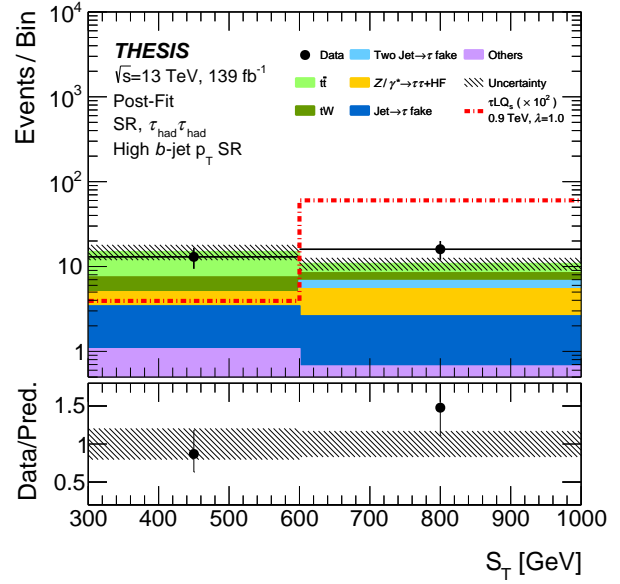
(a) $\tau_{\text{lep}}\tau_{\text{had}}$ Low $p_T^{b\text{-jet}}$ SR



(b) $\tau_{\text{lep}}\tau_{\text{had}}$ High $p_T^{b\text{-jet}}$ SR



(c) $\tau_{\text{had}}\tau_{\text{had}}$ Low $p_T^{b\text{-jet}}$ SR



(d) $\tau_{\text{had}}\tau_{\text{had}}$ High $p_T^{b\text{-jet}}$ SR

Figure 6.20: The post-fit distributions of the S_T discriminant in the high and low $p_T^{b\text{-jet}}$ signal regions. The combined $\tau_{\text{lep}}\tau_{\text{had}}$ and $\tau_{\text{had}}\tau_{\text{had}}$ fit is conducted under the background-only hypothesis. The label ‘jet $\rightarrow \tau$ fakes’ corresponds to events involving a fake hadronic tau and a genuine lepton. Additionally, an example signal of a 900 GeV singly produced scalar LQ with $\lambda = 1.0$ is included with its cross section of 4.7×10^{-3} pb multiplied by 100. In the $\tau_{\text{had}}\tau_{\text{had}}$ channel, ‘ $Z/\gamma^* \rightarrow \tau\tau + \text{HF}$ ’ represents Z/γ^* production along with a heavy flavour jet. The uncertainty band represents the post-fit uncertainty, and the binning displayed is the same as the one used in the fit.

6.7.1 Exclusion Limits

The combined $\tau_{\text{had}}\tau_{\text{had}}$ and $\tau_{\text{lep}}\tau_{\text{had}}$ channels undergo a simultaneous signal + background fit to establish upper limits on the $pp \rightarrow \tau LQ$ and $pp \rightarrow \tau LQ + pp \rightarrow LQ\overline{LQ}$ cross-section. The branching fraction is neglected since $\mathcal{B}(LQ \rightarrow b\tau)$ is set to 1. The frequentist CL_s method is utilised, in the same way as the legacy analysis outlined in Section 4.7.2.

The 95% CL upper limits on the cross-section for scalar LQ , YM vector LQ , and MIN vector LQ are depicted in Figures 6.21, 6.22, and 6.23, respectively. The observed limit consistently exceeds the expected limit in all three cases, as shown by the plots. This can be attributed to the slight excess observed in the final bin of the high $p_T^{b\text{-jet}} \tau_{\text{had}}\tau_{\text{had}}$ channel (Figure 6.20). Since all signals predict an excess in this bin, the observed limit is shifted for all mass points. Additionally, the $\tau_{\text{had}}\tau_{\text{had}}$ channel exhibits the highest sensitivity due to a better signal to background separation in this final bin coupled with the higher $A \times \epsilon$ for $\tau_{\text{had}}\tau_{\text{had}}$ shown in Figure 6.2.

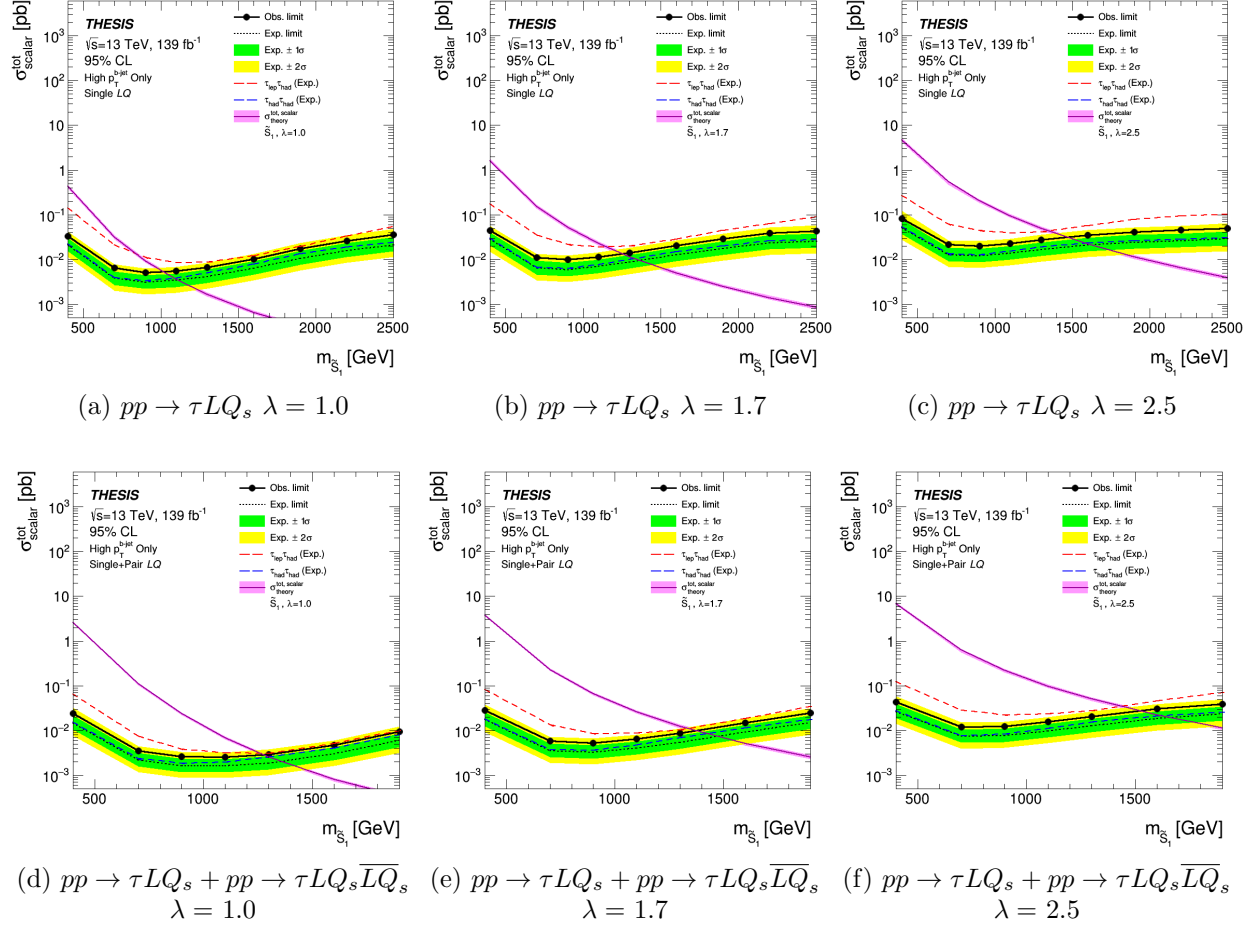


Figure 6.21: The 95% CL upper limits on the cross-section for singly (a-c) and singly plus pair (d-f) produced LQ under the \tilde{S}_1 model. Limits are shown for $\lambda = 1.0, 1.7$ and 2.5 and contain only the contribution from the high $p_T^{b\text{-jet}}$ signal regions. The area above the curve is the excluded region. The black observed and expected lines are formed from the combination of the $\tau_{\text{lep}}\tau_{\text{had}}$ and $\tau_{\text{had}}\tau_{\text{had}}$ channels. However, separate limits from the $\tau_{\text{lep}}\tau_{\text{had}}$ and $\tau_{\text{had}}\tau_{\text{had}}$ channels are included in red and blue, respectively. The predicted LO cross-section under the \tilde{S}_1 model is superimposed in magenta. The green and yellow bands represent the $\pm 1\sigma$ and $\pm 2\sigma$ uncertainty on the upper limit, respectively.

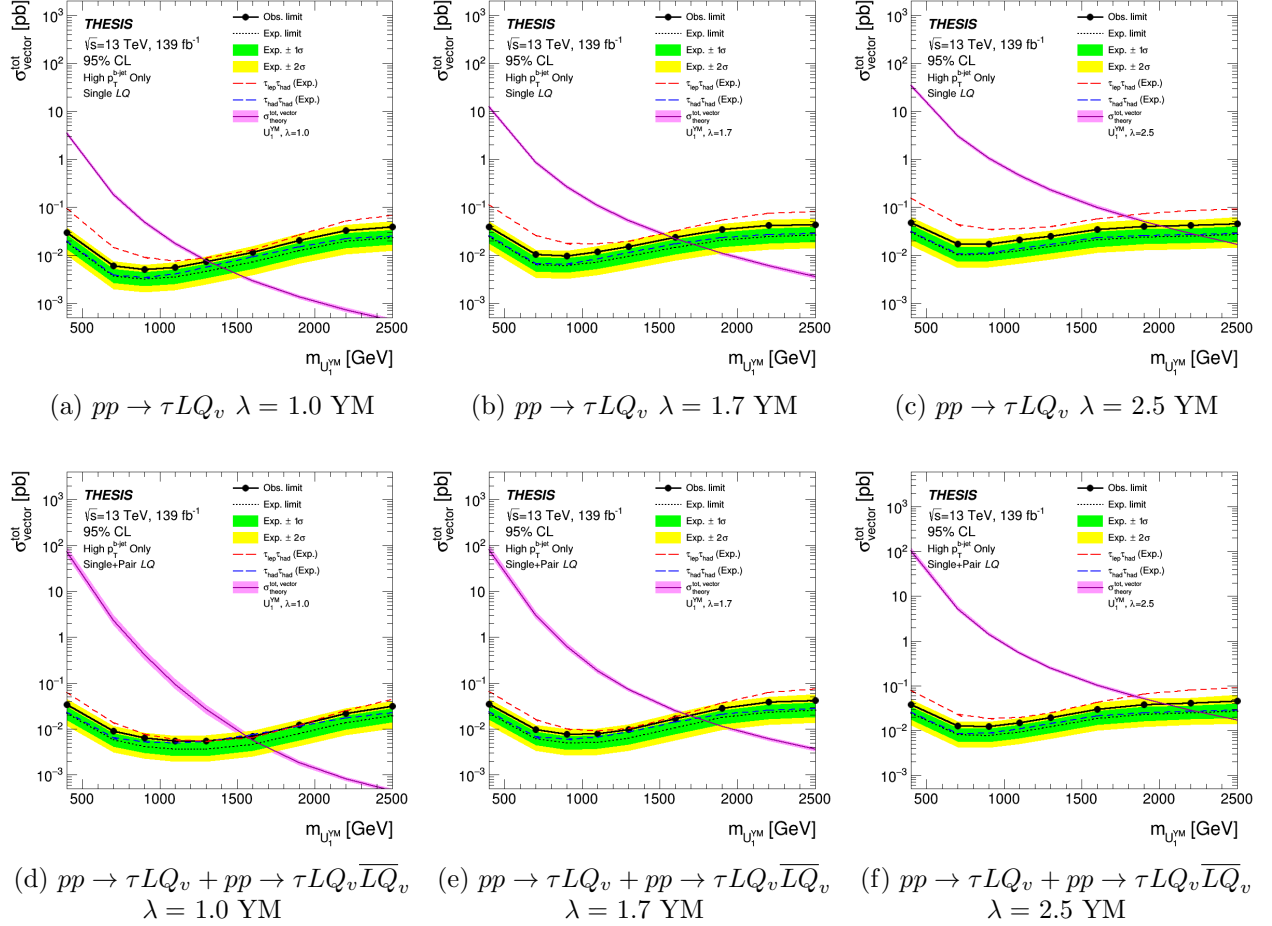


Figure 6.22: The 95% CL upper limits on the cross-section for singly (a-c) and singly plus pair (d-f) produced LQ under the $U_1^{\text{YM}}(\kappa=0)$ model. Limits are shown for $\lambda = 1.0, 1.7$ and 2.5 and contain only the contribution from the high $p_T^{b\text{-jet}}$ signal regions. The area above the curve is the excluded region. The black observed and expected lines are formed from the combination of the $\tau_{\text{lep}}\tau_{\text{had}}$ and $\tau_{\text{had}}\tau_{\text{had}}$ channels. However, separate limits from the $\tau_{\text{lep}}\tau_{\text{had}}$ and $\tau_{\text{had}}\tau_{\text{had}}$ channels are included in red and blue, respectively. The predicted LO cross-section under the $U_1^{\text{YM}}(\kappa=0)$ model is superimposed in magenta. The green and yellow bands represent the $\pm 1\sigma$ and $\pm 2\sigma$ uncertainty on the upper limit, respectively.

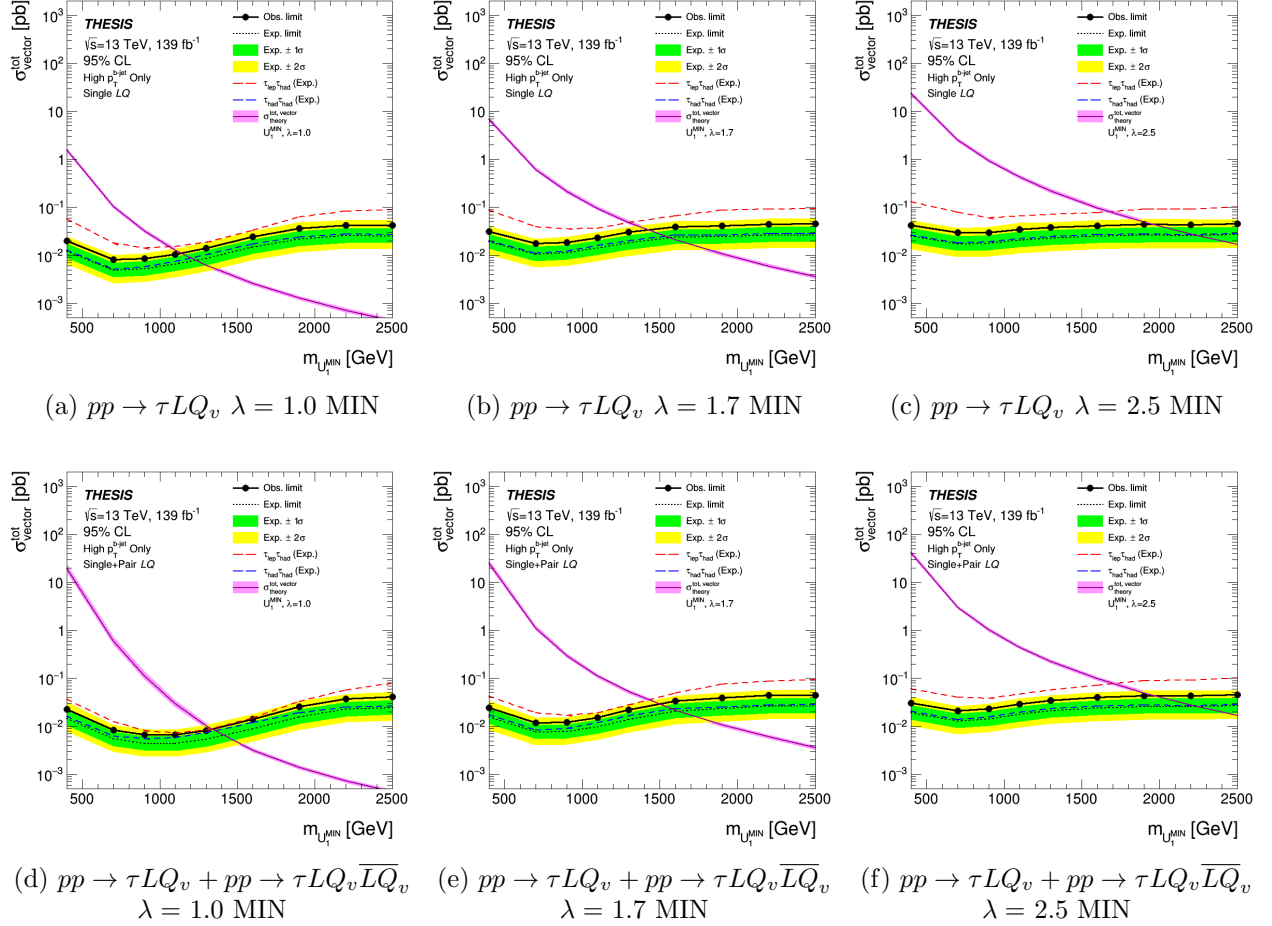


Figure 6.23: The 95% CL upper limits on the cross-section for singly (a-c) and singly plus pair (d-f) produced LQ under the $U_1^{\text{MIN}}(\kappa = 1)$ model. Limits are shown for $\lambda = 1.0, 1.7$ and 2.5 and contain only the contribution from the high $p_T^{b\text{-jet}}$ signal regions. The area above the curve is the excluded region. The black observed and expected lines are formed from the combination of the $\tau_{\text{lep}}\tau_{\text{had}}$ and $\tau_{\text{had}}\tau_{\text{had}}$ channels. However, separate limits from the $\tau_{\text{lep}}\tau_{\text{had}}$ and $\tau_{\text{had}}\tau_{\text{had}}$ channels are included in red and blue, respectively. The predicted LO cross-section under the $U_1^{\text{MIN}}(\kappa = 1)$ model is superimposed in magenta. The green and yellow bands represent the $\pm 1\sigma$ and $\pm 2\sigma$ uncertainty on the upper limit, respectively.

The intersection of the limit with the predicted cross-section from the model enables the construction of a limit in the $m_{LQ} - \lambda$ plane, as shown in Figures 6.24(a), 6.24(b), and 6.24(c) for scalar, YM vector, and MIN vector cases, respectively. Table 6.5 summarises the upper limits on m_{LQ} for various λ values obtained from the $m_{LQ} - \lambda$ plot.

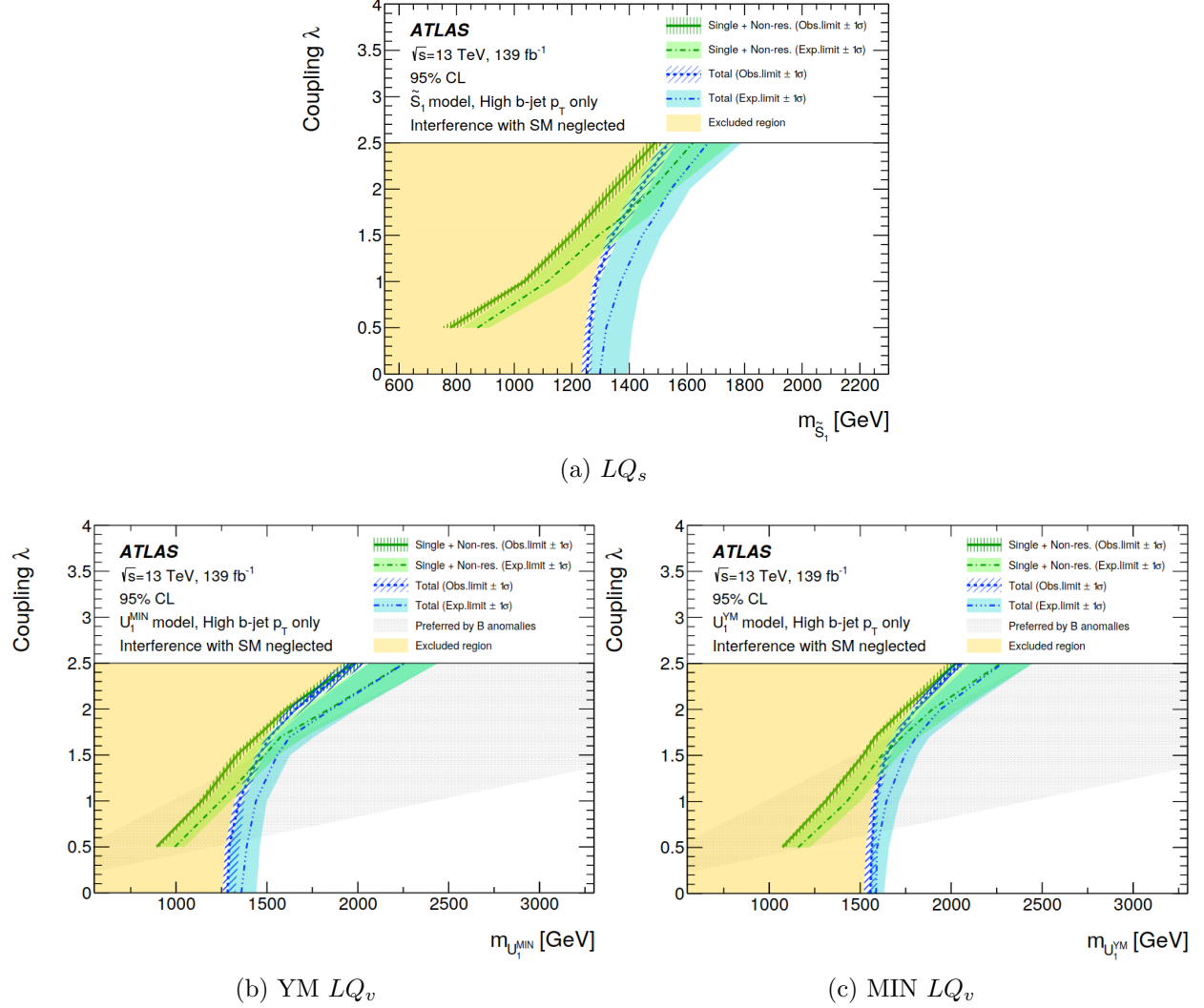


Figure 6.24: The 2D exclusion limits in the $m_{LQ} - \lambda$ plane for (a) scalar (\tilde{S}_1 model) and vector ((b) U_1^{YM} and (c) U_1^{MIN} models) LQ . The green lines indicate the limit for singly produced LQ , while the blue lines correspond to the limit for singly plus pair produced LQ . The label ‘Single + Non-res’ is used to maintain consistency with the relevant literature and implies the involvement of all singly produced diagrams in Figure 6.1. The orange filled area is the excluded region, while the filled grey area for the vector LQ case represents the favoured region where the U_1 model could explain the observed B anomalies [69, 240].

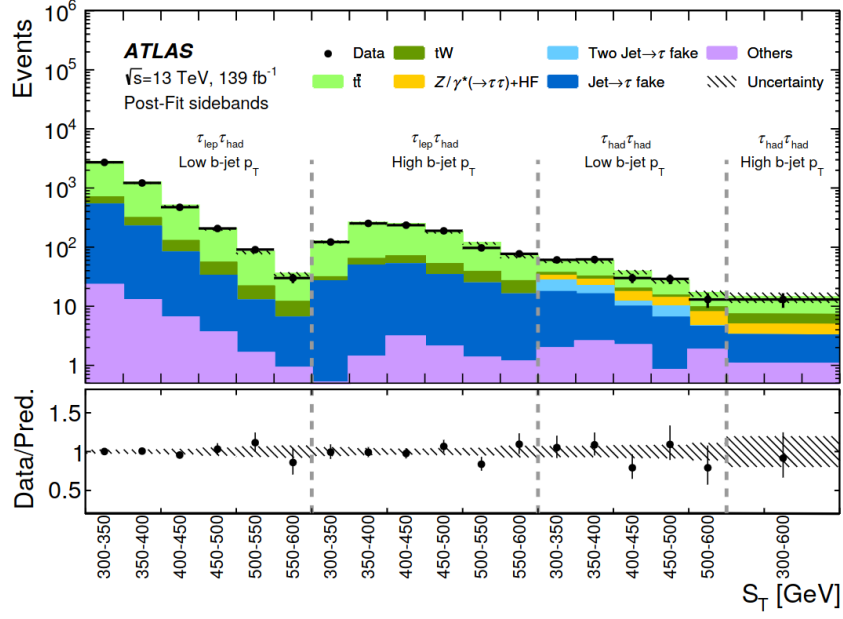
Table 6.5: Observed (expected) limits on m_{LQ} for different values of λ extracted from the $m_{LQ} - \lambda$ plots. Limits are quoted in units of TeV.

Model	$\lambda = 1.0$	$\lambda = 1.7$	$\lambda = 2.5$
LQ_s	1.04 (1.11)	1.26 (1.38)	1.49 (1.62)
$LQ_s + LQ_s \overline{LQ}_s$	1.28 (1.37)	1.38 (1.49)	1.53 (1.67)
LQ_v YM	1.31 (1.43)	1.59 (1.73)	2.03 (2.27)
LQ_v MIN	1.15 (1.24)	1.45 (1.58)	1.98 (2.26)
$LQ_v + LQ_v \overline{LQ}_v$ YM	1.58 (1.64)	1.70 (1.81)	2.05 (2.28)
$LQ_v + LQ_v \overline{LQ}_v$ MIN	1.35 (1.44)	1.52 (1.63)	1.99 (2.26)

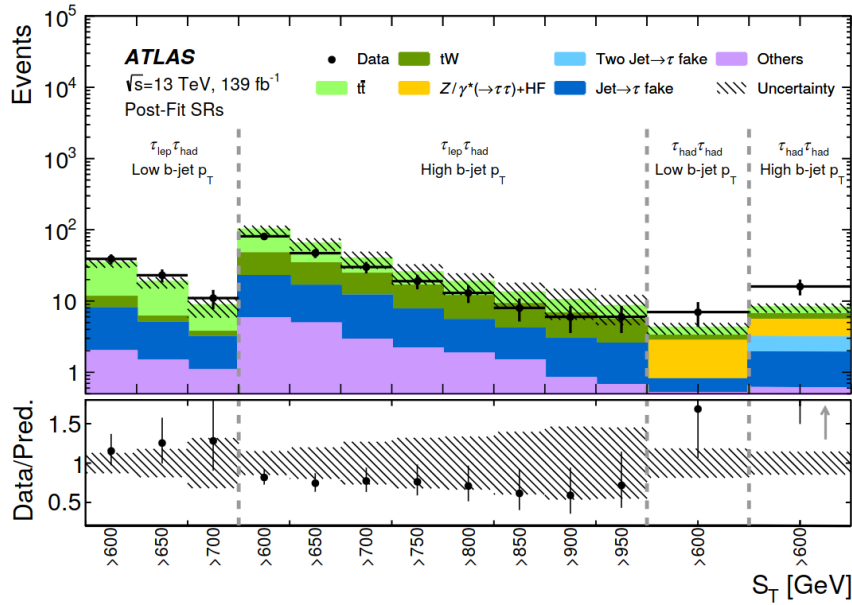
6.7.2 Model-independent Interpretation in the Low and High $p_T^{b\text{-jet}}$ Regions

The non-resonant LQ signal is predicted to interfere with SM backgrounds such as Z +jets in the low $p_T^{b\text{-jet}}$ SR. This interference effect is model dependent, which led to the exclusion of this region from the statistical analysis in previous studies. To compensate for this, a model-independent search is constructed to include potentially interesting results.

To perform the model-independent search, SR events with $S_T < 600$ GeV are selected to form a sideband region. For events that do not satisfy this requirement, a set of new signal regions are defined by varying the S_T threshold at which the SR starts. The sidebands are visualised in Figure 6.25(a), displaying each sideband post-fit distribution. A simultaneous background-only fit is performed on the sidebands using the fitting procedures described in Section 4.7. The results of this fit are projected onto each SR threshold bin and used to predict the background contribution. The post-fit distributions for the signal regions with varying S_T thresholds are shown in Figure 6.25(b), with each S_T lower bound threshold signal region displayed. An excess against the background-only hypothesis is present in the $\tau_{\text{had}}\tau_{\text{had}}$ high $p_T^{b\text{-jet}}$ $S_T > 600$ GeV bin which corresponds to a significance of 2.1σ .



(a)



(b)

Figure 6.25: (a) The post-fit distributions of S_T in the sideband regions, where each distribution is included in a simultaneous background-only fit. (b) The signal region distribution, where each bin corresponds to a separate signal region obtained by shifting the lower threshold of S_T at which the region is defined. The results from the background-only fit in (a) are projected onto these signal regions in (b) to compare the predicted background to the data. In each case, results are shown for the low and high $p_T^{b\text{-jet}}$ regions in both the $\tau_{\text{lep}}\tau_{\text{had}}$ and $\tau_{\text{had}}\tau_{\text{had}}$ channels. The contribution from events involving a fake hadronic tau and a genuine lepton is labelled as ‘jet $\rightarrow \tau$ fakes’, while Z/γ^* production along with a heavy flavour jet in $\tau_{\text{had}}\tau_{\text{had}}$ is labelled as ‘ $Z/\gamma^* \rightarrow \tau\tau + \text{HF}$ ’. The uncertainty band represents the post-fit uncertainty derived from the fit. The ratio plot shows the ratio of the data to the MC post-fit prediction.

A simultaneous signal + background fit is performed involving the four sidebands and one signal region (inclusive bin of S_T) at a time. The model independence is achieved by including a generic signal which is normalised to 1 pb at $L_{\text{int}} = 139 \text{ fb}^{-1}$. The goal of this fit is to determine the upper limit on the visible cross-section (σ_{vis}) using the CL_s method defined in Section 4.7.2. The resulting upper limits are shown in Figure 6.26. The upper limit on μ can easily be transformed to the limit on the number of observed signal events by multiplying by the generic signal pre-fit yield. Dividing this by the integrated luminosity yields the visible cross-section. These upper limits on σ_{vis} are valuable since they can be easily translated into upper limits on the cross-section for a specific physics model by dividing the σ_{vis} limit by the $A \times \epsilon$ of the model under the corresponding SR definition.

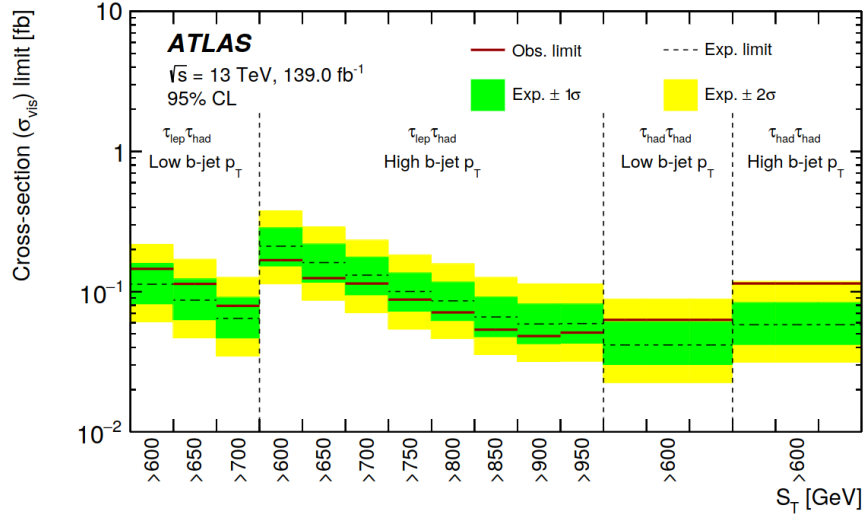


Figure 6.26: The 95% CL upper limit on the visible cross-section (σ_{vis}) derived by combining the low and high $p_T^{b\text{-jet}}$ regions and the $\tau_{\text{lep}}\tau_{\text{had}}$ and $\tau_{\text{had}}\tau_{\text{had}}$ channels in a simultaneous signal + background fit. The fit includes the four sidebands shown in Figure 6.25(a) and one signal region bin from Figure 6.25(b). These limits can be used to obtain an upper limit on the cross-section for any model, provided that the acceptance and efficiency in the signal region bin of interest are known.

6.8 Conclusion

Using the techniques developed for the legacy analysis described in Chapter 4 and detailed in [8], a search was conducted for scalar and vector leptoquarks in the $b\tau\tau$ final state. The full ATLAS Run-II $\sqrt{s} = 13$ TeV pp collision dataset was used corresponding to an integrated luminosity of 139 fb^{-1} . For the signals, the benchmark models chosen were \tilde{S}_1 for the scalar case and U_1 for the vector case under either the Yang-Mills or minimal coupling scenarios. Each search was conducted with a signal mass (Yukawa coupling) grid ranging from 400 GeV (0.5) to 2.5 TeV (2.5).

A background-only fit is shown for the high and low $p_T^{b\text{-jet}}$ signal regions in Figure 6.20, representing good agreement between data and the Standard Model backgrounds. Upper limits for each model at 95% CL on the $\sigma \times \mathcal{B}$ are provided in Figures 6.21, 6.22 and 6.23 for the singly produced and singly plus pair produced cases in the high $p_T^{b\text{-jet}}$ region. Excluded leptoquark masses for each model can be obtained by consulting Figure 6.24 and Table 6.5. For the singly plus pair production mode, the lower observed (expected) limit on the \tilde{S}_1 leptoquark mass is 1.28 (1.37) TeV for $\lambda = 1.0$. For the vector case under the U_1 model, the limit is 1.58 (1.64) TeV for the Yang-Mills coupling scenario and 1.35 (1.44) TeV for the minimal coupling scenario, for $\lambda = 1.0$.

Due to the interference between the LQ diagrams and some SM diagrams at low $p_T^{b\text{-jet}}$, a model-independent interpretation is performed. This produced a set of 95% CL upper limits on the visible cross-section as a function of the S_T threshold in each of the high and low $p_T^{b\text{-jet}}$ SRs, as shown in Figure 6.25. Depending on the SR, the visible cross-section limit shown in Figure 6.26 varies from 0.17 fb to 4.8×10^{-2} fb as the S_T threshold is varied from $S_T > 600$ GeV to $S_T > 950$ GeV.

Chapter 7

Efforts to Improve the Full Run-II Search for MSSM Higgs Bosons in the $\tau\tau$ Final State

The traditional techniques mentioned in Chapter 4 for the legacy full Run-II result [8], in which a resonance peak is searched for in some mass distribution (M_T^{TOT} in this case) can often be improved upon by instead employing a machine learning (ML) discriminant. By employing ML classification models such as neural networks, for instance, one can improve the search for a peak by using a signal likelihood score distribution as a discriminant. In this chapter, the use of neural networks to enhance the sensitivity of the legacy result is explored. The acceptance to interesting events is improved by lowering the trigger thresholds and optimising the object selection. The reduction of high impact systematics and improved background modelling is also explored. This remit resulted in the formation of a new MSSM $H/A/h \rightarrow \tau\tau$ ATLAS analysis team referred to as the improved analysis. The exploratory work conducted by the author for this analysis is discussed in this chapter along with the expected improvement to the upper limits.

7.1 Proposed Improvements to the Legacy Analysis

The proposed improvements to the legacy analysis are expected to significantly enhance sensitivity, primarily due to the incorporation of a neural network. Additionally, a significant improvement should come from the increase in signal acceptance in the $\tau_{\text{had}}\tau_{\text{had}}$ channel from including a hadronic di-tau trigger. The lowest threshold of this trigger is reduced to $(\tau_{\text{had}}^1, \tau_{\text{had}}^2, \text{pass ID}) = (35 \text{ GeV}, 25 \text{ GeV}, \text{both Loose})$, compared to the single tau trigger's $(\tau_{\text{had}}^1, \text{pass ID})$ threshold of $(80 \text{ GeV}, \text{Medium})$ [206]. The thresholds are lowered for all data taking campaigns with the highest threshold being $(\tau_{\text{had}}^1, \tau_{\text{had}}^2, \text{pass ID}) = (80 \text{ GeV}, 60 \text{ GeV}, \text{both Medium})$ for the di-tau trigger compared to $(\tau_{\text{had}}^1, \text{pass ID}) = (160 \text{ GeV}, \text{Medium})$ for the single tau trigger [207]. This increase in signal acceptance to low p_T hadronic taus is expected to improve the $\sigma \times \mathcal{B}(H/A/h \rightarrow \tau\tau)$ limit sensitivity for low signal masses. Addi-

tionally, updated combined performance recommendations in tau identification and b -tagging techniques are expected to minimise fake contributions and further enhance sensitivity.

7.2 Efforts Towards $\tau_{\text{lep}}\tau_{\text{had}}$ Analysis Optimisation

Optimising analysis regions and techniques is a challenging task, as numerous ideas have been explored in the many previous $H/A/h \rightarrow \tau\tau$ analyses. For instance, the usage of M_T^{TOT} as the discriminant has been queried many times, while attempts to reconstruct the di-tau invariant mass using various algorithms have shown little gain. A scan of the many working points of each combined performance algorithm was conducted where possible. In some cases, changing a working point would require a new n-tuple production, which is a time-consuming task. The changes to the legacy $\tau_{\text{lep}}\tau_{\text{had}}$ channel summarised in Table 4.4 are shown in Table 7.1 where appropriate. The reasons for each change are explained throughout this section.

Table 7.1: The changes to the legacy $H/A/h \rightarrow \tau\tau$ strategy detailed in Table 4.4 for the proposed improved analysis.

Region	Selection
TCR	Pass b -tag SR except: $120 \text{ GeV} \geq m_T(\ell, E_T^{\text{MISS}}) < 220 \text{ GeV}$
MFR	$\ell(\text{trigger}), \tau_{\text{had}}(\text{RNN score} < 0.01), N_\ell = 1, m_T(\ell, E_T^{\text{MISS}}) < 30 \text{ GeV},$ $q(\ell) \times q(\tau_{\text{had}}) > 0, E_T^{\text{MISS}} \leq 50 \text{ GeV}, N_{b\text{-jets}} = 1$ (b -tag) Pass or fail lepton isolation
WFR	Pass SR except: $60 \text{ GeV} < m_T(\ell, E_T^{\text{MISS}}) < 150$ (110) GeV (b -tag), Pass or fail τ_{had} ID (RNN score > 0.01)

7.2.1 Updating and Simplifying Analysis Inputs (n-tuples)

To facilitate the improved analysis, new n-tuple production campaigns were carried out several times to update combined performance recommendations or add interesting variables that could serve as input features for the neural networks mentioned in Section 7.3. The sample list for data and MC is unchanged from the legacy analysis list presented in Table 4.1. The computational requirement to produce n-tuples is a problem for this analysis and will be further exacerbated for the Run-III analysis with increased integrated luminosity. A streamlined and analysis specific channel was developed in the xTAUFRAMEWORK software to help remedy this. The new channel significantly reduced the n-tuple generation time from one month for the legacy analysis to a few weeks, while also decreasing the number of grid jobs that entered the exhausted state due to too much memory consumption.

7.2.2 Updating Combined Performance Recommendations

Before updating the combined performance recommendations, a working point scan was conducted. The chosen working point depends on the rules given by the combined performance groups, the modelling in each region and the SR signal to background ratio. The optimisation of the working point choice essentially involved switching the working point where possible and in most cases the difference in the expected $\sigma \times \mathcal{B}$ upper limit was measured.

In some cases a mini batch of n-tuples were made with the varied working point for the main backgrounds and a few LQ , bbH and ggH signal points were tested (since the LQ and improved analyses were conducted in parallel). The change in $\frac{\text{signal yield}}{\sqrt{\text{bkg yield}}}$ was measured to inform the correct choice of working point. The most effective working points for the LQ and ggH/bbH signals were the same. Therefore, the working points are the same between the LQ and improved analysis and they can be found listed in Section 6.3, their definitions are discussed in Section 3.3.

7.2.3 Analysis Simplification

This section outlines the steps taken to streamline the analysis process, either by removing unnecessary steps or enhancing the analysis software.

Multi-jet Fake Estimation

To ensure consistency with other similar ATLAS analyses and the LQ analysis in Section 6.5, the multi-jet fake factor parameterisation was modified to define two intervals based on p_T^ℓ and $|\eta|$ for events in the barrel ($|\eta| \leq 1.52$) and end-cap ($|\eta| > 1.52$) regions. Despite this simplification, there was no significant impact on the limit.

The multi-jet scale factor used in the legacy analysis was identified as a candidate for removal, as it was found to have minimal impact on the final limit. The reason why the scale factor can be removed with minimal impact can be attributed to the anti-correlation of the fakes, which was previously discussed in Section 4.5.1, and which makes such changes to the multi-jet fake factor have little influence on the overall yield of fake events.

Analysis Software Updates

Maintaining up to date software is crucial to ensure compatibility with release 22 of ATHENA, which will be used during early Run-III analysis. As mentioned in Section 7.2.1, to run the analysis is a large computational effort, making it essential to reduce the analysis disk usage and memory requirements, especially for Run-III. For the $\tau_{\text{lep}}\tau_{\text{had}}$ analysis, systematic processing poses a challenge, the job sizes often exceed the processing capacity of batch nodes. Additionally, the merging of ROOT files at the end of a batch job can also present difficulties. Typically, a dedicated worker node with high amounts of Random Access Memory (RAM) is often needed to merge sample folders built from the BSMTAUTAUCAF software. To address these issues, several measures have been implemented, such as using nominal templates instead of systematic templates where possible, partitioning events carefully, and

processing datasets in smaller but numerous chunks. After careful tuning of the analysis code, systematics can now be evaluated easily using any available batch nodes.

7.2.4 The t -quark Background Correction

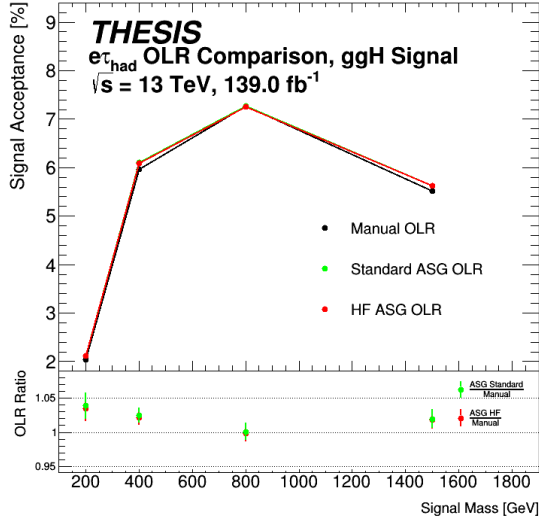
The pull plots from the legacy analysis show many of the top control region related NPs are pulled by up to 2σ , as shown in Appendix B.2. Therefore, a top correction parameterised in S_T is derived and applied to every region in an almost identical way to the one used in Section 6.4.1 for the LQ analysis. The TCR enriched with real $t\bar{t}$ events, as defined in Table 7.1, is similar to the TCR in Table 4.3 from the legacy analysis, except selection is now $120 \text{ GeV} \geq m_T(\ell, E_T^{\text{MISS}}) < 220 \text{ GeV}$. This modification is made so that the top scale factor can be validated using the side bands. The top scale factor in this analysis is mostly identical in shape to the one shown in Figure 6.5, implying that the mismodelling is due to top theory uncertainties as is the case in the LQ analysis.

7.2.5 Overlap Removal Optimisation

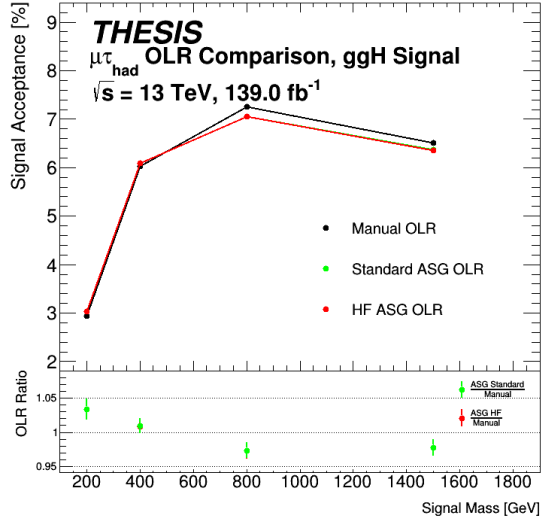
Optimisation of the OLR can be used to increase the acceptance to interesting events. In the legacy analysis, a basic manual overlap removal was used, the definition of which is shown in Table 4.3.1, this simple OLR can lead to signal events being wrongly rejected, such as when an electron is mistakenly classified as a jet.

The first optimisation strategy to consider requires the conversion to the ASG recommended standard OLR working point, shown in Table 6.2. The standard ASG OLR has been optimised for general analyses and has added complexity when compared to the manual method. Another relevant working point for this analysis is the heavy flavour (HF) ASG OLR, which is optimised for heavy flavour jets and prompt leptons in the final state that are not heavily boosted. This is implemented by simply changing the j - e and j - μ criteria in Table 6.2 such that jets are only rejected if they are not b -tagged. This could potentially improve the signal efficiency for the b -tag analysis.

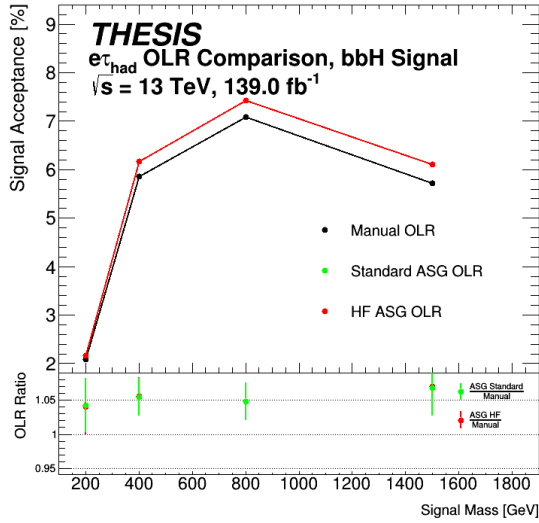
Figure 7.1 shows the change in signal yield for bbH and ggH signals in the $e\tau_{\text{had}}$ and $\mu\tau_{\text{had}}$ channels when moving from the manual OLR to either the ASG standard or HF OLR. The ASG standard OLR (green line) results in up to 4% (7%) improvement over the manual OLR (black line) for the ggH (bbH) production mode, the bbH signals showing the most improvement. While the HF working point (red line) provides negligible (less than 1%) improvement over the standard working point, small acceptance gains of around 1% are visible for bbH signals in the $\mu\tau_{\text{had}}$ channel, likely due to the increased acceptance to b -jets.



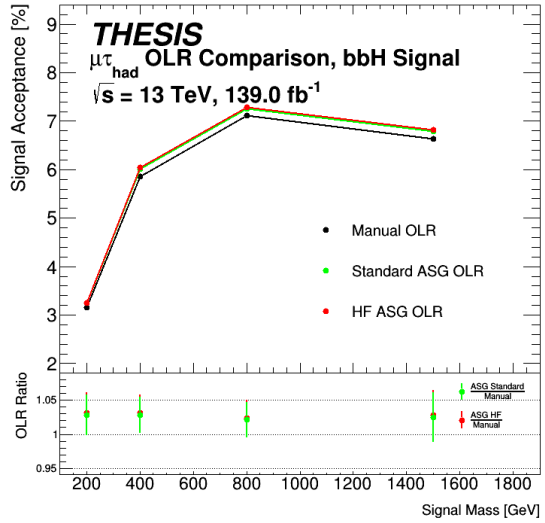
(a) $e\tau_{\text{had}} ggH$



(b) $\mu\tau_{\text{had}} ggH$



(c) $e\tau_{\text{had}} bbH$



(d) $\mu\tau_{\text{had}} bbH$

Figure 7.1: The ggH and bbH signal yield should the manual (black), ASG standard (green) or ASG HF (red) OLR working points be used for this analysis. The uncertainty bar considers the statistical uncertainty.

For high mass ggH signals in the $\mu\tau_{\text{had}}$ channel, the ASG OLR show a reduction in signal yield compared to the manual OLR due to the $j\text{-}\mu$ criteria in Table 6.2, which recommends rejecting jets over muons when $N_{\text{tracks}}^{\text{jet}} < 3$. For boosted topologies, this reduces the acceptance due to final state radiation leading to larger tracks multiplicities, resulting in muons being wrongly rejected. Removing this requirement was shown to increase the yield for the $\mu\tau_{\text{had}}$ channel. Alternatively, a p_T dependent sliding cone technique could be used to better account for muons in the boosted regime. Similar to the variable radius isolation cone discussed in Section 3.3.1, the lepton rejection cone is reduced as a function of the p_T^ℓ . The cone size can be varied but the default configuration follows the function $\Delta R = \min(0.4, 0.04 + \frac{10 [\text{GeV}]}{p_T})$. However, since removing the $N_{\text{tracks}}^{\text{jet}}$ requirement recovered sensitivity, this was not pursued further.

In addition to its impact on signal efficiency, the use of ASG OLR has implications on the acceptance of background events. Overall, the use of ASG OLR improves the limit by up to 5% when compared to the manual OLR. However, for the HF working point, the difference in the limit is negligible compared to the standard working point. For the remaining studies in this chapter, the ASG standard OLR with no modifications is adopted as it resulted in an appreciable improvement in the limit, was validated in the LQ analysis and saved time by avoiding the need for a new n-tuple campaign to incorporate the boosted topology considerations.

7.2.6 Multi-jet Fake Region Purity

The use of the RNN tau ID significantly improves background rejection, thereby reducing the acceptance of multi-jet and W +jets/top fakes in the SR. As mentioned in Section 4.5.1 a low tau ID score cut is applied to populate the MFR with multi-jet fakes. Therefore, an improved tau ID algorithm could increase the purity of multi-jets in the MFR as gluon jets are typically easier to reject. On the other hand, since the MC predicted jet fakes (mainly quark-initiated fakes) are included in the calculation of the MFF, as detailed in Section 4.5.1, the MFR purity could be reduced if the algorithm is effective at rejecting these. The MFR with the RNN tau ID is observed to have a reduced multi-jet purity compared to the legacy analysis. Specifically, the legacy analysis reported purities of 72% (74%) and 76% (85%) for the $e\tau_{\text{had}}$ and $\mu\tau_{\text{had}}$ b -veto (b -tag) channels, respectively. It is important though to enrich the MFR with multi-jet fakes such as to give a representative multi-jet fake factor.

To increase the MFR purity, selections are added based on the observed multi-jet distribution for certain kinematic variables. Table 7.2 shows the selections, with the biggest improvement in purity obtained by using same-sign taus ($q(\ell) \times q(\tau_{\text{had}}) > 0$). This approach can be implemented since multi-jets are not expected to fake any particular sign of taus. Several configurations are chosen for further analysis, and inspection of the corresponding fake factors reveals that as the purity increases, so does the value of each fake factor bin due to the increased number of fakes in the pass-ISO region. The change in the $\sigma \times \mathcal{B}$ limit for each chosen configuration relative to the limit calculated with the same-sign requirement is shown in Table 7.3. In this limit the multi-jet fake factor systematics are the only NPs in the fit.

As shown, increasing the purity leads to a reduction in the limit, likely due to the reduced uncertainties and a more accurate estimation of the fake contribution. It is important to note, however, that due to the fake anti-correlation effect, described in Section 4.5.1, the impact on the final limit is minimal. For this analysis, the third configuration is chosen to maintain consistency with the LQ analysis, which uses the same multi-jet fake region.

Table 7.2: The selection of cuts applied to the MFR to improve the multi-jet purity. Values are quoted before any isolation requirement is applied.

MFR Cuts	Purity of MFR [%]			
	$e\tau_{\text{had}}$		$\mu\tau_{\text{had}}$	
	b -veto	b -tag	b -veto	b -tag
Full Run-II Legacy MFR (L-MFR) Selection	68	45	59	45
1) L-MFR & Same-sign taus only (SS)	75	55	66	55
2) L-MFR & SS & $N_{b\text{-jets}} = 1$ (for b -tag)	75	60	66	61
3) L-MFR & SS & $N_{b\text{-jets}} = 1$ & $E_T^{\text{MISS}} < 50$ GeV	78	72	68	70
4) L-MFR & SS & $N_{b\text{-jets}} = 1$ & $E_T^{\text{MISS}} + m_T(\ell, E_T^{\text{MISS}}) < 30$ GeV	83	79	73	75
5) L-MFR & SS & $N_{b\text{-jets}} = 1$ & $E_T^{\text{MISS}} + m_T(\ell, E_T^{\text{MISS}}) < 30$ GeV & $\frac{p_T^\tau}{p_T^\ell} > 0.6$	85	83	75	79

Table 7.3: The change to the $\tau_{\text{lep}}\tau_{\text{had}} \sigma \times \mathcal{B}$ limit for different MFR purity configurations. The first row of values shows the limit values for each mass point, whilst the rest of the rows show the percentage change to the limit for each signal mass relative to the limit in case (1). The limit is calculated by including only the multi-jet fake factor systematics as nuisance parameters in the fit.

Purity Configuration Comparison		Signal Mass [GeV]							
		200	400	600	800	1200	1500	2000	2500
1) SS Expected Limit	ggH	0.4523	0.0509	0.0204	0.0115	0.0062	0.0044	0.0039	0.0039
	bbH	0.4369	0.0482	0.0147	0.0068	0.0041	0.0035	0.0035	0.0036
3) SS, $N_{b\text{-jets}} = 1$, $E_T^{\text{MISS}} \leq 50$ GeV Expected Limit Reduction	ggH	9.15	4.52	1.47	0.00	-1.61	-2.27	0.00	0.00
	bbH	8.72	-0.62	0.00	0.00	0.00	0.00	0.00	-2.78
5) SS, $N_{b\text{-jet}} = 1$, $m_T(\ell, E_T^{\text{MISS}}) + E_T^{\text{MISS}} < 30$ GeV, $\frac{p_T^\tau}{p_T^\ell} > 0.6$ Expected Limit Reduction	ggH	11.45	8.25	2.94	-0.87	-3.23	-2.27	-2.56	0.00
	bbH	10.80	7.88	2.04	0.00	0.00	-2.86	0.00	-2.78

7.2.7 Reconsidering the Lower τ Identification Cut

Figures 7.2 and 7.3 depict the composition of the jets which fake taus in the WFR and SR for $t\bar{t}$ and W +jets samples in the b -tag and b -veto regions, respectively. The plots show that the majority of gluon-initiated fakes are concentrated at low RNN tau ID score values as expected. As mentioned in Section 4.5.1, a lower tau ID score selection (BDT score < 0.01) is applied to the WFR and SR to ensure a similar quark-gluon ratio. The ratio heavily

impacts the WFF, if a region contains more gluon fakes, the fake factors tend to have lower values since more events will enter the fail-ID region.

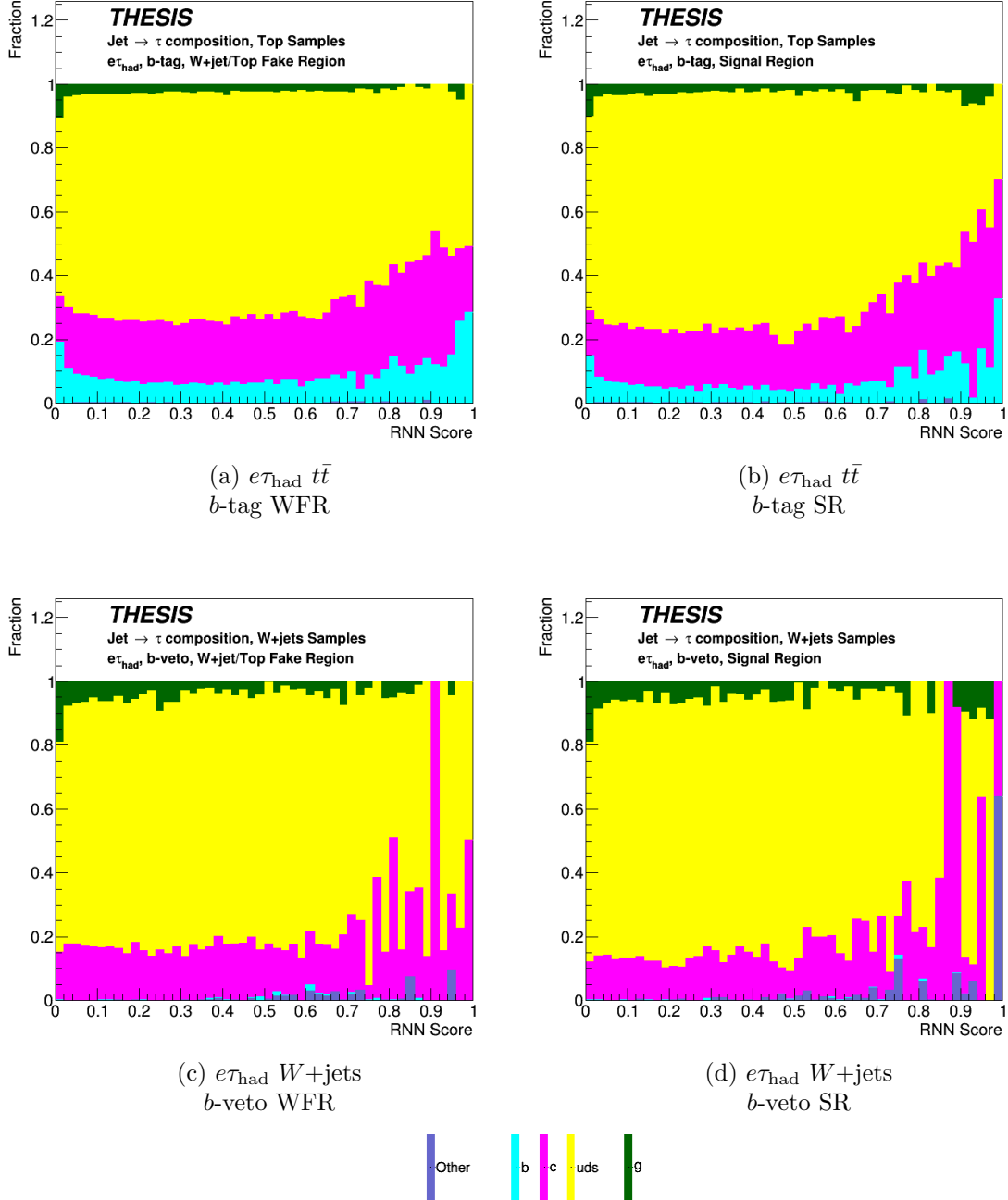


Figure 7.2: A comparison of the jet $\rightarrow \tau$ fake composition for the $e\tau_{\text{had}}$ WFR and SR for $t\bar{t}$ and W +jets samples in the b -tag and b -veto channels, respectively. The legend at the bottom shows the available classifications: gluon jet, b -jet, c -jet, light quark jet (uds) and other sources such as lepton fakes.

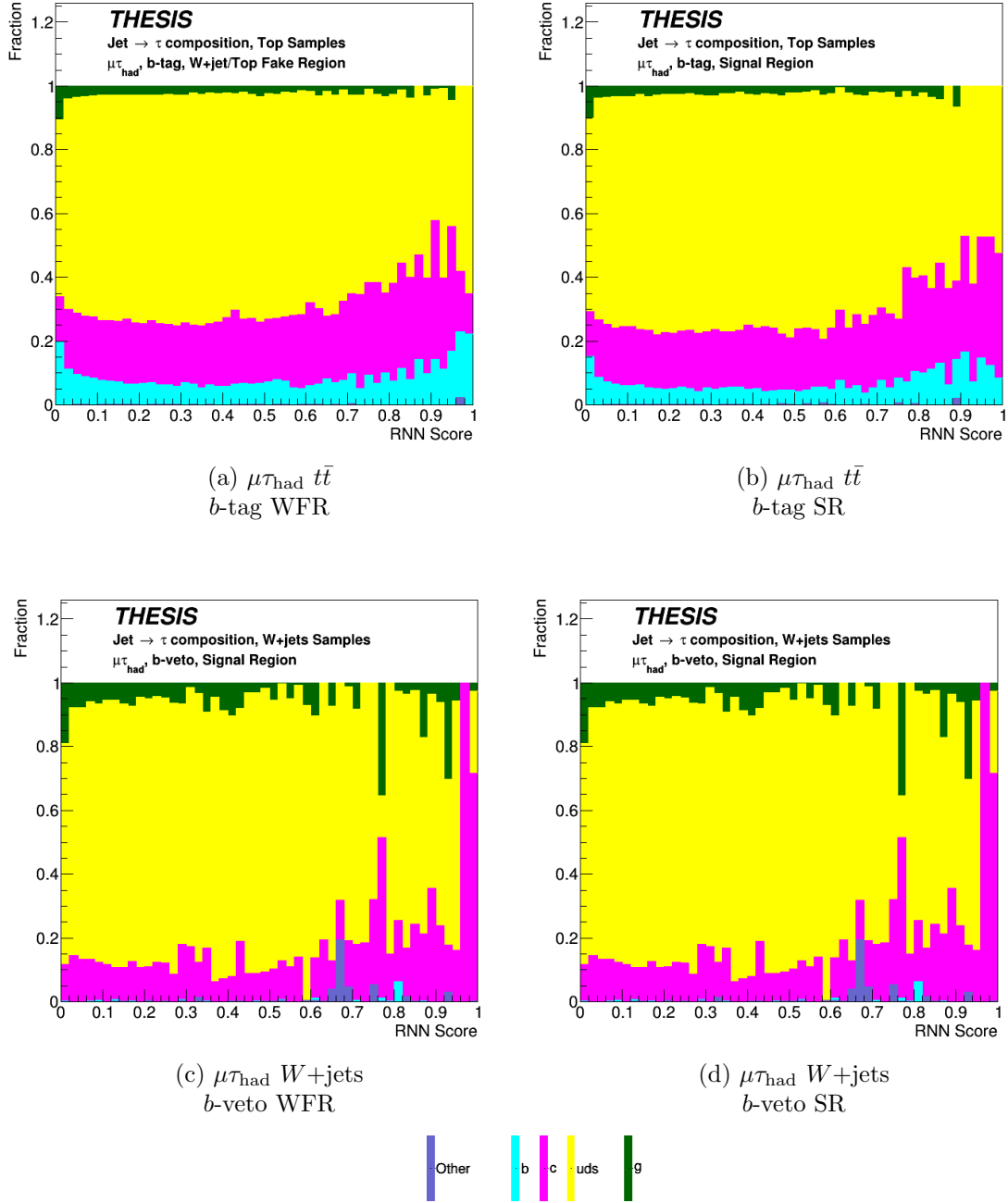


Figure 7.3: A comparison of the jet $\rightarrow \tau$ fake composition for the $\mu\tau_{\text{had}}$ WFR and SR for $t\bar{t}$ and W +jets samples in the b -tag and b -veto channels, respectively. The legend at the bottom shows the available classifications: gluon jet, b -jet, c -jet, light quark jet (uds) and other sources such as lepton fakes.

To determine the appropriate point for the RNN tau ID score cut, it is necessary to examine the distribution of the RNN tau ID score for both the WFR and the SR. When the ratio between the two distributions becomes flat, it indicates that the majority of non-tau like gluon jets have been removed. A flat ratio also implies that a similar number of events are rejected per step in RNN tau ID score between the two regions, indicating that the quark-gluon fake fraction is similar. Upon inspection of the RNN distributions, it was observed that the ratio becomes constant at RNN score < 0.01 for both b -veto and b -tag, the same value as used for the legacy analysis lower tau ID cut. Therefore, it was left unchanged. After inspecting the jet fake composition plots in Figures 7.2 and 7.3, the shape of the distributions look similar between the WFR and SR. The change in c -jet fakes could potentially represent mismodelling as these fakes would in theory give different fake factors. However, since the fake estimation is validated in the VR, this is not considered further.

7.2.8 The Updated Analysis Strategy

After implementing the optimisations discussed in this section, the resulting analysis is used as input for the machine learning techniques discussed in the following section. The fake factors and scale factors associated with the improved analysis behave similarly to those used in the legacy and LQ analyses discussed in earlier chapters.

To get a preliminary approximation of the level of improvement achieved by the optimisations in this section before the ML is considered, one can compare the $\tau_{\text{lep}}\tau_{\text{had}}$ expected limit for the improved analysis to that of the legacy analysis with only statistical uncertainty considered. This comparison is shown in the final results in Figure 7.16 and 7.17. An improvement of between 10% (16%) and 22% (21%) across all mass points for the ggH (bbH) production mode is observed. Since many of the systematic uncertainties are the same as those in the legacy case or have also been updated as part of the combined performance recommendations, it is reasonable to expect that this improvement will persist when they are taken into account.

7.3 Machine Learning Techniques for the Improved Run-II $H/A/h \rightarrow \tau\tau$ Analysis

Machine learning is a rapidly growing discipline focusing on the development of algorithms capable of learning patterns in a given dataset, in order to solve complex problems. For the case of the improved analysis, the accurate classification of events between signal and background is the challenge. To accomplish this, a feed-forward artificial neural network that utilises supervised machine learning is chosen. In the case of supervised learning, the solution (e.g., 1 for signal or 0 for background) is provided to the network along with the input features, enabling it to learn the relationship between the features and the solution. A generalised predictive model is created which is then able to evaluate unseen events and output a signal probability [218, 241, 242].

The following sections describe the basic principles of machine learning discriminators and how neural networks can use these ideas to determine signal from background for this analysis.

7.3.1 Estimating Class Probability

When building machine learning models for classification tasks, logistic regression is often the method of choice. Logistic regression is an extension of linear regression and is represented by the equation

$$\hat{y} = \theta_0 + \theta_1 x_1 + \theta_2 x_2 + \dots + \theta_n x_n \quad (7.1)$$

which involves using a linear combination of weights (θ_n) and a bias term (θ_0) to predict an output value (\hat{y}). To determine the model parameters, the equation $\sum_i (\hat{y}_i - y_i)^2$ is minimised, where y_i is the observed output value, this equation can be called the loss function.

Logistic regression has the capability to estimate the probability that a given instance belongs to a particular class. In a similar manner to linear regression, a weighted sum of input features with a bias term is generated, the sum is then passed through a logistic (otherwise known as sigmoid) function. This function is defined as:

$$y' = \frac{1}{1 + e^{-\hat{y}}} \quad (7.2)$$

and has the ability to map \hat{y} into the range $\{0, 1\}$ such that it can be compared with a binary class label.

For logistic regression, the loss function used in linear regression is replaced by the binary cross-entropy loss represented by the equation:

$$L(\mathbf{w}) = \sum_i^{Events} [y_i \ln(y'(\mathbf{x}_i, \mathbf{w})) + (1 - y_i) \ln(1 - y'(\mathbf{x}_i, \mathbf{w}))] \quad (7.3)$$

where y' is the output of the ML algorithm which depends on the set of features \mathbf{x} and weights \mathbf{w} , while y_i represents the true class label [241]. The sigmoid function ensures a high loss if an instance with a signal (class 1) label is given a low probability of belonging to that class, and negligible loss if it is given a high probability value. Since the objective is to minimise the loss function, achieving the correct labels is favoured. The weights that minimise this equation can be computed using a minimisation algorithm, typically the gradient descent algorithm is used [243].

Figure 7.4 provides a visual representation of how gradient descent algorithms work. The weights are randomly initialised and iteratively updated based on the negative gradient of the loss function, following the equation:

$$\mathbf{w}^{n+1} = \mathbf{w}^n - \eta \nabla_{\mathbf{w}} L \quad (7.4)$$

where the learning rate, denoted by η , is a hyperparameter set by the user that controls the step size taken by the algorithm during each iteration. The algorithm continues to update the weights until it converges to a minimum. Optimisation of the learning rate is essential because a low value will result in many iterations for convergence, whereas a high value may cause convergence to a local minimum or miss any minimum entirely.

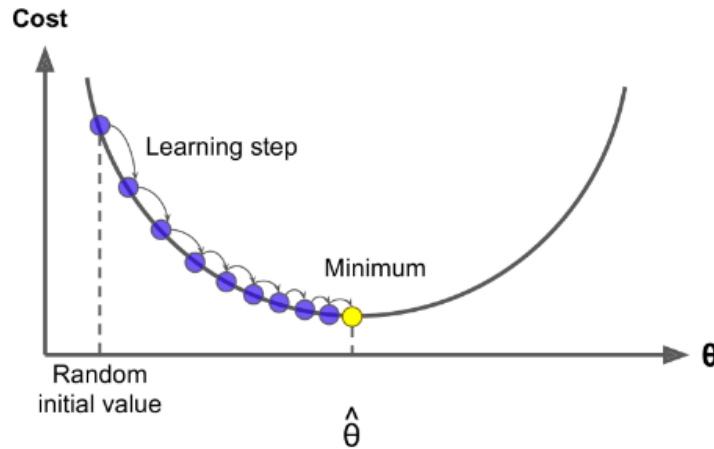


Figure 7.4: This schematic taken from [241] illustrates how the gradient descent algorithm finds the minimum of the loss function by varying some weight θ until the minimum value $\hat{\theta}$ is found. The initial value is randomly assigned and the step size depends on the learning rate η .

7.3.2 Neural Networks

Neural networks are a powerful tool that leverage the principles of the previous section to build ML models. An example of a feed-forward artificial NN is shown in Figure 7.5. A NN has an input layer, one or more hidden layers, and an output layer. Each layer has a number of nodes, where each input layer node corresponds to an input feature and the number of nodes in the hidden layers is tuned by the user. A bias node is present in all layers except for the final layer. Each node is connected to the nodes in the previous and next layer by a weight carrying neuron. An output value is produced by each node from the linear combination of each connecting node's value multiplied by its weight.

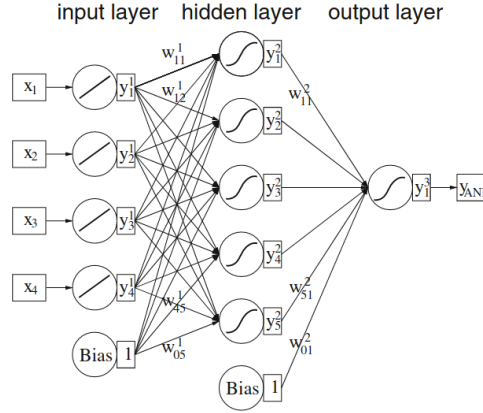


Figure 7.5: A schematic of a neural network provided by [218]. There are 4 input features, a hidden layer with 5 nodes and an output node. A given node forms a combination of each connecting node's value (y) multiplied by its weight (w) and passes it through an activation function (the graph in the node) to form its own value.

The graph inside the nodes in Figure 7.5 corresponds to the activation function, each node's preliminary value is passed through one. The activation function has the same purpose as the logistic function described in Section 7.3.1. For neural networks, there are a range of activation functions to choose from, the most popular being sigmoid, tanh, ReLu (rectified linear unit) [244], leaky ReLu [244] and softmax [242]. The tanh function is useful because it maps to the domain $\{-1, 1\}$, thereby normalising the output of each node to be centred at 0, which can aid the minimisation. The ReLu function is computationally efficient and has no maximum value, which can be beneficial for gradient descent. Leaky ReLu can also be employed to help revive nodes which continually produce zero values. The softmax function is similar to sigmoid as it maps to the $\{0, 1\}$ domain but is typically used when there is more than one output node as it ensures that each class probability adds up to 1. Figure 7.6 shows some of these activation functions, including the step function for comparison.

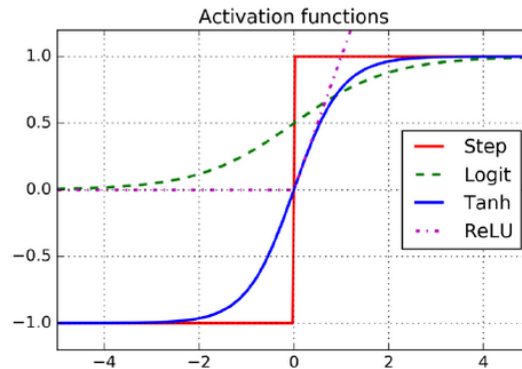


Figure 7.6: A representation of some common activation functions taken from [241]. The tanh, logit (sigmoid) and ReLu functions are shown in blue, green and purple respectively. The step function is shown in red for reference.

To train the network, a modified version of gradient descent is used, which employs the back-propagation training algorithm [242]. Firstly, a forward pass is done through the network and the difference between the desired output and the network output is evaluated. Next, the error contribution of each node in the last hidden layer is computed, and this process is repeated for all preceding layers, continuing until the input layer is reached. This backward pass enables the measurement of the error gradient across all neurons in the network, which corresponds to $\nabla_{\mathbf{w}}$ from Equation 7.4. The weights are then adjusted to minimise loss.

To find the minimum, the training process typically requires many passes through the dataset, where each pass is called an epoch. Updating weights once per epoch can be slow, so batches can be used to improve the process by updating the weights after each batch has been processed. The model is evaluated after each iteration by measuring the loss of a validation set not used in the training. The training process typically stops automatically when the loss of the validation dataset becomes constant.

7.3.3 Implementation and Evaluation of a Neural Network

This analysis was conducted using the KERAS software package, which supports the back-propagation based feed-forward neural network described earlier [245]. The standard gradient descent method, discussed previously, was replaced with stochastic gradient descent using the Adam optimiser as recommended by KERAS. In stochastic gradient descent, the actual error gradient is replaced by an estimate calculated from a random subset of the data [243]. The Adam optimiser applies adaptive learning rates to the training process [246]. In traditional stochastic gradient descent, a single learning rate is applied to all weights, which does not change during training. Adam supports maintaining a learning rate for each weight and optimises it as learning progresses. These changes serve the same purpose of minimising the loss function whilst easing the computational burden.

Organising Inputs and K-Fold Cross Validation

The input dataset is typically split into two subsets, the first subset is further split to make up the training and validation set, usually in the ratio 80:20. The other subset is isolated from the training as an extra validation set to avoid bias, the network is evaluated on this subset to test for overtraining and adequate performance.

To further mitigate bias, k-fold cross-validation is employed on the first subset of data [241]. This involves splitting the subset into k equal parts (k-folds) and training k models. The training and validation sets are still divided in the ratio 80:20, but the validation set consists of a unique set of events after each fold. The validation set from the previous fold is then incorporated into the training set of the current fold. To account for the k different models, one can take the mean average of the output of each model, with some precautions in place if the models produce significantly different output probabilities.

Preventing Overfitting

A common issue with machine learning is overfitting, where the model can learn unintended features of the training dataset such as statistical fluctuations. The accuracy of the model is reduced if it learns the features which are only present in the training dataset. Figure 7.7 shows overfitting in practice by representing how a model may try to classify a set of events based on two variables x_1 and x_2 . A good model would be close to the minimal misclassification rate shown by the solid black line. To remedy overfitting, one can either decrease the complexity of the model architecture, reduce the duplication of information in the input features, or stop the training at an earlier epoch. Adding dropout layers to the network, where nodes are randomly disabled during training, also helps reduce the learning of statistical properties of the dataset [247]. To check for overfitting, one can manually observe the modelling of the training dataset compared to the isolated validation dataset.

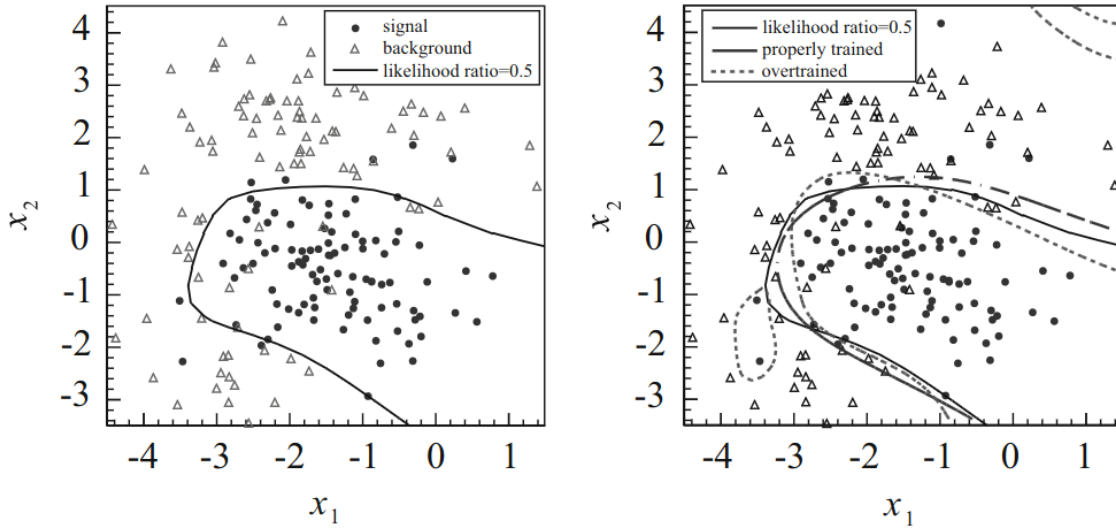


Figure 7.7: A 2D representation of a basic machine learning model overfitting the data as illustrated in [218]. The likelihood ratio line (solid black) represents the minimal misclassification rate and the properly trained line is as close as possible to this. The overtrained model has learned some statistical features of the training dataset.

Evaluating a Models Performance

The Receiver Operating Characteristic (ROC) curve is a valuable tool for assessing the performance of a machine learning model on a validation set. It provides insight into the balance between signal efficiency and accuracy, revealing the rate at which signal events are correctly identified. Typically, the ROC curve is plotted as signal efficiency (or probability of true positives) against background rejection (or probability of false positives). At high values of signal efficiency, the probability of misclassifying a background event as signal is high for an imperfect model (type I error). When the opposite is true, the probability of failing to correctly classify a signal event is high (type II error) [218].

A neural network output might for example be shown on the left plot of Figure 7.8, with the corresponding ROC plot shown on the right. One could pick a value for the neural network score (y) to maximise the background rejection and the signal efficiency. A cut of $y = 0.1$ is represented by the vertical line on the left plot of Figure 7.8 and the star on the right plot. If the vertical line is shifted to the right, both the signal and background efficiency will be reduced. Therefore, the star will shift towards the top left of the right plot of Figure 7.8. The ROC curves are constructed by scanning the background rejection and signal efficiency as the NN score is varied.

The left plot of Figure 7.8 will be similar to the distribution that enters the fit, the sensitivity of the result depends on the background and signal separation. Therefore, an effective model will result from a ROC curve which takes up as much area (AUC) as possible. An AUC of 1 indicates a perfect model, while a lower value indicates there is room for improvement. Although accuracy is a commonly used metric in machine learning, it is not always suitable, especially when dealing with unbalanced datasets. For instance, if the majority of the validation set consists of background events, the model could predict everything as background and still achieve a high accuracy score. This is a misleading result that does not reflect the model's true performance on signal events. Therefore, it is disregarded in this analysis.

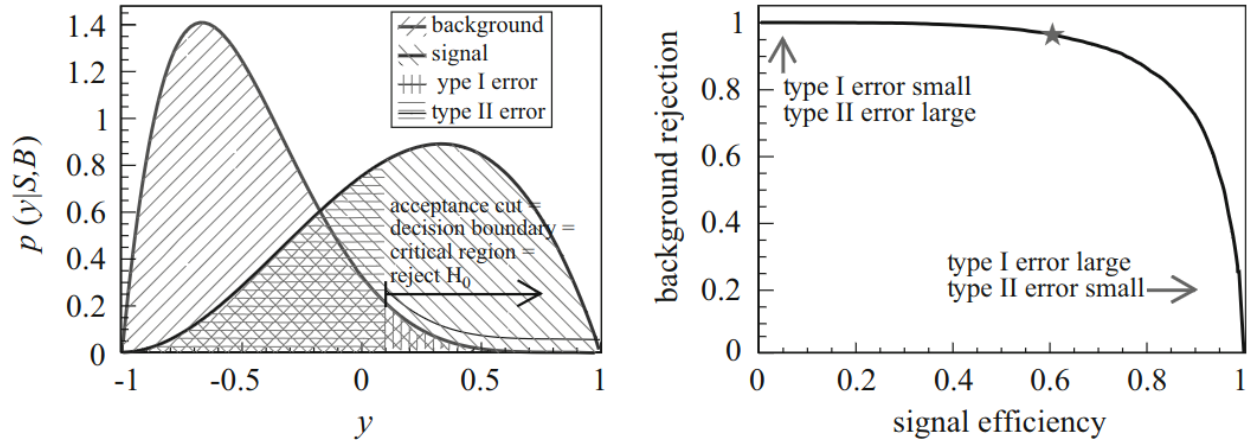


Figure 7.8: A schematic of how a ROC curve is constructed provided by [218]. The plot in (a) shows the signal and background distributions as a function of the NN score (y). The cut at $y = 0.1$, corresponds to the star in the plot in (b). Therefore it shows how choosing different cuts would build a ROC curve. Type I errors occur when a background is misclassified as signal and type II errors are where a signal event is not categorised as such.

7.3.4 Creating a Parameterised Neural Network

For this analysis, one would expect to train against many backgrounds including both real and fake processes. The challenge however is that there are many types of signal which differ by their mass, training a model for each mass point, SR and production mode would be an arduous process but necessary to reconstruct the upper limit on the $\sigma \times \mathcal{B}$.

Fortunately, a workaround was developed in [248] called a parameterised neural network (PNN), which enables the merging of all signal masses into a single training process. The signal mass is added as an input feature, allowing the model to learn how it impacts the result. For background, a common approach would be to assign a random signal mass.

To obtain the $\sigma \times \mathcal{B}$ upper limit for a particular signal mass, the desired mass is passed to the PNN at evaluation time, which outputs scores for signal and background at that mass.

7.4 Neural Network Application in the Improved Run-II $H/A/h \rightarrow \tau\tau$ Analysis

To use a feed-forward neural network for classification in a physics analysis, several aspects need to be considered, including the network’s architecture, input features and tuning. In the following sections, the decisions made when constructing a mass-parameterised neural network for each of the four improved $H/A/h \rightarrow \tau\tau$ signal regions is discussed.

7.4.1 Input Features

The input features are obtained by running the analysis frameworks for both channels and transforming the output to small n-tuples. The n-tuples are then transformed to CSV files which serve as inputs to the model. In the training process, the bbH and ggH signals are merged. An attempt was made to train the b -tag network on bbH signals and b -veto on ggH signals, but models generated using this configuration did not perform as well as the ones described in the following sections.

Feature labelling

For this analysis, the only interesting classification is whether the event is expected to be signal or background. Therefore, no other labels are defined to try and distinguish specific backgrounds. A naive attempt at applying specific background labels seemed to reduce the performance considerably.

Feature Scaling and Normalisation

When considering the scaling of input features, there are a few types of scaling to take into account. These are as follows:

- Scaling to equalise background samples.

No attempt is made to balance the number of events in each background type by scaling. Instead, the standard weight applied to the event in the SR, including all scale factors and fake factors, is used for the model. An alternative approach of weighting all backgrounds equally was attempted but resulted in reduced performance.

- Scaling of feature values.

In some cases, it can be beneficial to scale input feature values to ensure that all values fall within the range $\{0, 1\}$. This can be achieved using the StandardScaler from the SCIKIT-LEARN package [249]. This scaling method is applied only to the $\tau_{\text{had}}\tau_{\text{had}}$ channel as it was observed to provide up to five times better performance depending on the mass point, with at least 100% improvement for any given ggH or bbH mass point.

- Scaling such that each signal mass has the same total weight.

To train a PNN, leaving the signal mass feature unfilled for backgrounds will bias the model, a random signal mass can be applied to each background event to remedy this. For a set of signals with an unequal weight between each mass, it is important to guard against bias by correcting for the probability distribution of each signal mass when applying the random numbers. In practice, a better technique is to make a copy of the background distribution for each signal mass point, assign that signal mass to the background events and then merge all the copies together. This ensures that each signal type has the same background distribution. Each set of events with a particular signal mass feature is then scaled to the same value to ensure consistency across all mass points. This method makes it necessary to filter out events associated with signal masses which differ to the evaluation mass when analysing the performance of the network on the training and testing datasets. The neural network is trained on all available signals and backgrounds but one is only ever interested in one signal mass at a time. For example, if one evaluates the PNN at a mass point of 1000 GeV, the neural network score for a 200 GeV signal or background event should not be included in the performance metrics.

Feature Choice

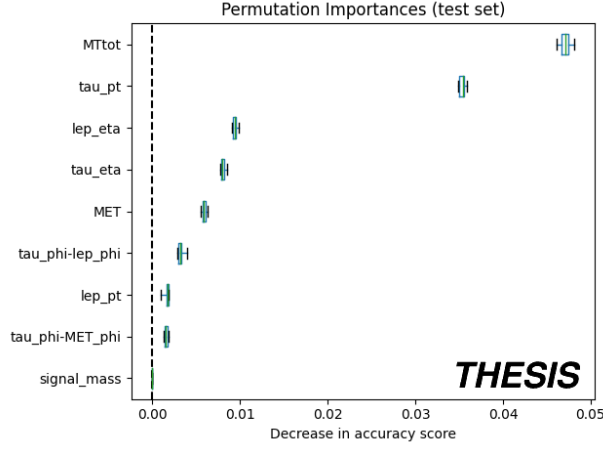
The features in which one would expect the most signal to background separation are generally the most efficient choice. Since there are many backgrounds and many signal masses for a PNN, this is not a trivial procedure.

For the irreducible $Z/\gamma^* \rightarrow \tau\tau$ background, separating it from Higgs like signals can be challenging. Mass variables or variables sensitive to the spin of the Higgs can be used to achieve this separation. Mass variables are essentially invariant mass alternatives that attempt to consider the information lost via the escaping neutrinos. Several mass variables have been proposed, but this analysis considers m_{vis} , M_T^{TOT} , and the MMC_{mlm} variable derived in [250]. The MMC_{mlm} algorithm attempts to fully reconstruct the di-tau mass by using the tau kinematics and known probability distributions. The distribution of $\Delta R(\tau_{\text{vis}}, \nu)$ parameterised in p_T^τ and the number of tau prongs is included to build and minimise a likelihood function. This method provides a better estimation of the di-tau mass than, for example, the collinear approximation, which assumes that the neutrinos from each tau decay are nearly collinear

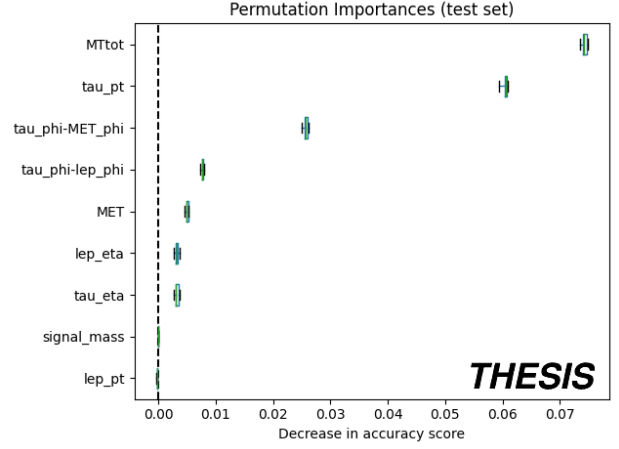
with the visible tau decay products, this is accurate for extremely boosted taus. Two variations of the MMC calculation exist: MMC_{mlm} and MMC_{maxw} . The former was chosen since it is a more comprehensive version of the algorithm and was found to give better results. Mass variables such as M_T^{TOT} have large width and intersect with other backgrounds, especially for high signal masses. Therefore, a combination of MMC_{mlm} , m_{vis} , and M_T^{TOT} could provide new information to the model whilst avoiding overfitting.

For all backgrounds, the PNN can benefit from having basic event kinematics as features. For example, E_T^{MISS} , p_T and angular variables can help give information on what is likely to be signal and what could be a jet or lepton fake. To further boost the performance, either the tau ID score or its inputs (e.g., jet substructure variables) could be considered as features. For this analysis, it was decided to remove tau ID related variables to avoid potential bias introduced by the fake estimation strategy. Since fail-ID events are given a fake factor weight and allowed to enter the SR, the MC events and the equivalent fakes in data are not comparable.

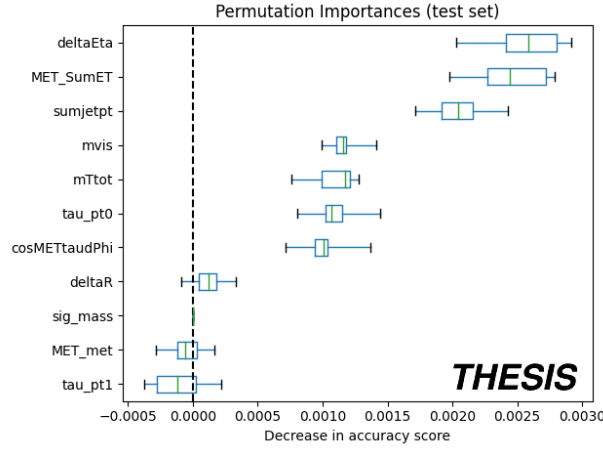
The permutation feature importance package from SCIKIT-LEARN can be used to rank the features that contribute the most to the models [249]. This technique measures the decrease in model score when an input features column of values is randomly shuffled. To emulate the ranking results for a PNN evaluated at a particular mass, a model must be trained on one mass point. The ranking is performed 10 times and the mean is taken. The mean rankings are shown for each of the models with the final list of input features in Figures 7.9 and 7.10. Rankings corresponding to models evaluated at 200 GeV and 2.5 TeV are shown to illustrate how the importance changes depending on the mass. As expected, M_T^{TOT} ranks highly whilst angular variables generally have low impact. The signal mass is consistently the lowest since each mass feature value is the same for this test. The larger uncertainty in the $\tau_{\text{had}}\tau_{\text{had}}$ 200 GeV plots is due to the lower signal yield in the $\tau_{\text{had}}\tau_{\text{had}}$ channel for this mass point.



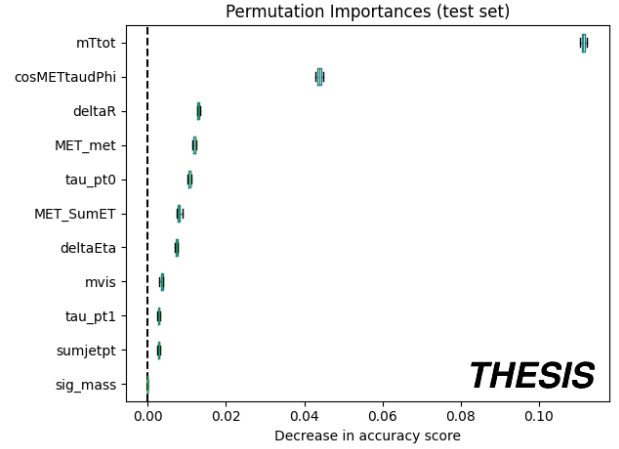
(a) $\tau_{\text{lep}}\tau_{\text{had}}$ b -veto 200 GeV



(b) $\tau_{\text{lep}}\tau_{\text{had}}$ b -veto 2500 GeV

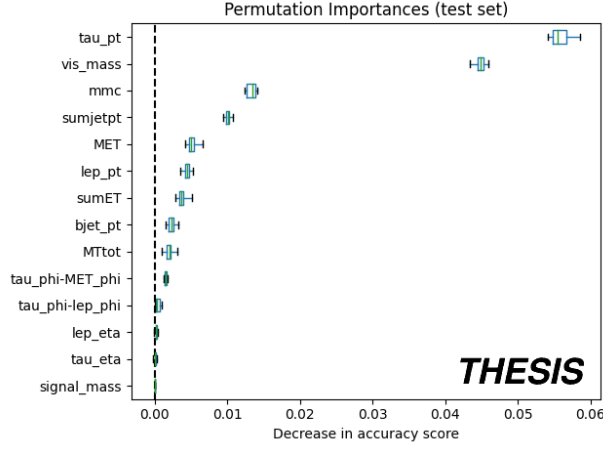


(c) $\tau_{\text{had}}\tau_{\text{had}}$ b -veto 200 GeV

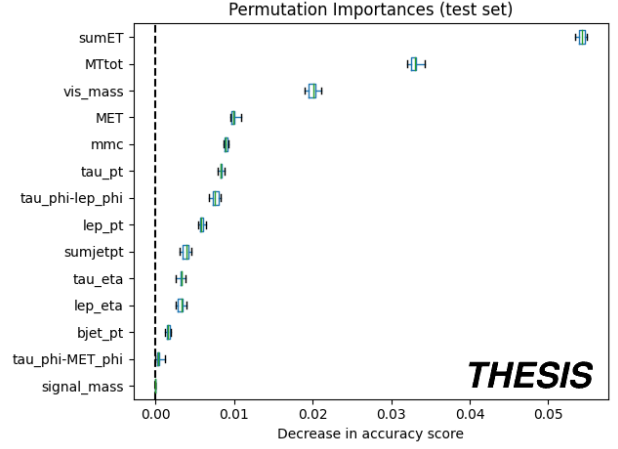


(d) $\tau_{\text{had}}\tau_{\text{had}}$ b -veto 2500 GeV

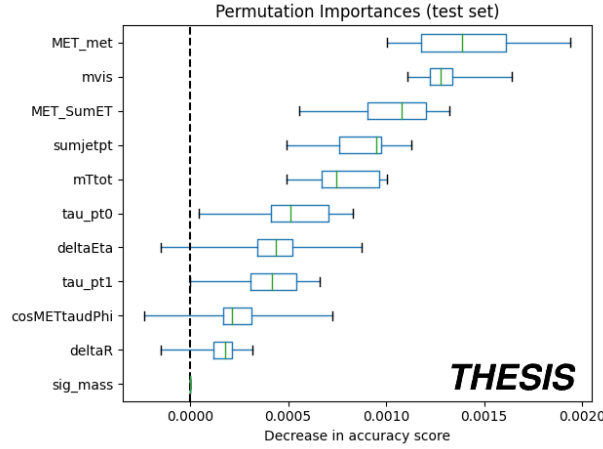
Figure 7.9: The mean feature ranking over 10 iterations as calculated by the permutation feature importance from SCIKIT-LEARN [249]. The feature ranking is shown for each b -veto PNN model evaluated at 200 GeV and 2500 GeV. The labels can be inferred from the input features in Table 7.4. The uncertainty bar represents the mean squared error.



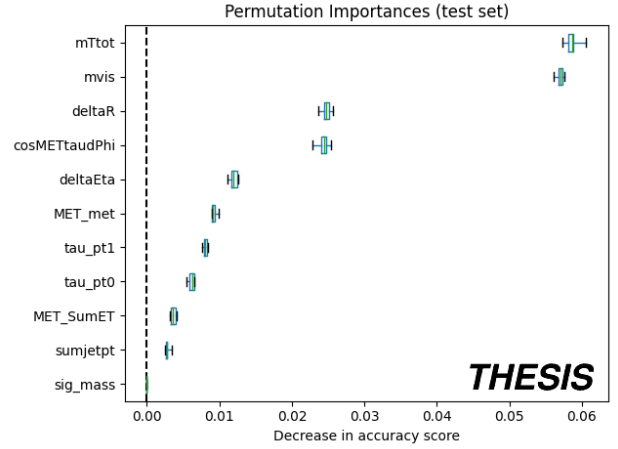
(a) $\tau_{\text{lep}}\tau_{\text{had}}$ b -tag 200 GeV



(b) $\tau_{\text{lep}}\tau_{\text{had}}$ b -tag 2500 GeV



(c) $\tau_{\text{had}}\tau_{\text{had}}$ b -tag 200 GeV



(d) $\tau_{\text{had}}\tau_{\text{had}}$ b -tag 2500 GeV

Figure 7.10: The mean feature ranking over 10 iterations as calculated by the permutation feature importance from SCIKIT-LEARN [249]. The feature ranking is shown for each b -tag PNN model evaluated at 200 GeV and 2500 GeV. The labels can be inferred from the input features in Table 7.4. The uncertainty bar represents the mean squared error.

The optimisation of input features was conducted using a combination of ranking information with trial and error. It was found that whilst various feature combinations improved the AUC for some mass points, it did not necessarily improve the $\sigma \times \mathcal{B}$ limit. The sensitivity doesn't always align with which model had the highest AUC per mass point because of the limits dependence on effective binning, the resulting distribution and the goodness of the signal + background fit. In some cases, the AUC may even increase for some mass points but decrease for others. Thus, selecting the input features is not a trivial task, and a trial and error approach is only feasible for a limited set of configurations, given that transforming a trained model to a limit, even with only statistical uncertainty considered, is time-consuming.

Based on these considerations, a final list of input features was selected and is presented in Table 7.4. Note that the b -veto and b -tag share the same features unless otherwise stated.

Table 7.4: Table showing the feature selection for the four trained PNN models, if the b -tag selection is different to the b -veto it is stated. The variables are stated in the order in which they are given to the model.

PNN	Features
$\tau_{\text{lep}}\tau_{\text{had}}$	$M_T^{\text{TOT}}, p_T^\tau, p_T^\ell, E_T^{\text{MISS}}, \Delta\phi(\tau, \ell),$ $\Delta\phi(\tau, E_T^{\text{MISS}}), \eta_\tau , \eta_\ell , p_T^{b\text{-jet}}$ (for b -tag), $M_\phi, \Delta\phi(H/A/h, b\text{-jet})$ (for b -tag)
$\tau_{\text{had}}\tau_{\text{had}}$	$M_T^{\text{TOT}}, p_T^{\tau_1}, p_T^{\tau_2}, E_T^{\text{MISS}}, \Sigma E_T,$ $m_{\text{vis}}, \Delta\eta(\tau_1, \tau_2) , \Delta R(\tau_1, \tau_2), \cos(\Delta\phi(E_T^{\text{MISS}}, \tau_0)) + \cos(\Delta\phi(E_T^{\text{MISS}}, \tau_1)), \Sigma p_T^{\text{jets}}, M_\phi$

7.4.2 Model Architecture and Hyperparameters

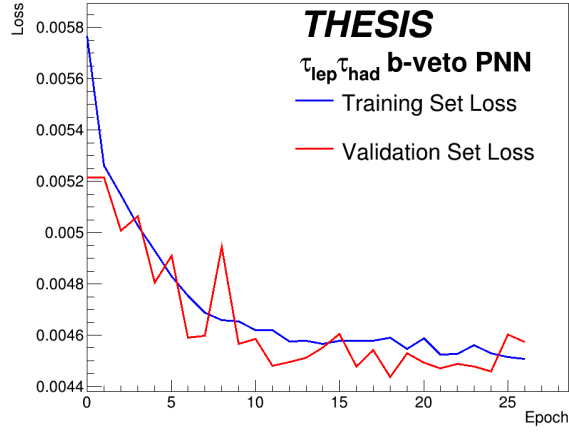
Improving machine learning models often involves tuning the model hyperparameters and architecture to promote deeper learning and avoid overfitting. The SCIKIT-LEARN provided grid search is a common technique used to iterate through available parameter permutations to enhance model performance [249]. Due to the time taken to train the four required models, only a coarse scan of hyperparameters and model architectures was conducted. For the same reasons as stated in the feature optimisation, improving AUC doesn't necessarily mean a lower value limit so checking the actual impact of each changed hyperparameter is an extremely intensive and time-consuming task. After experimentation, the final hyperparameters and layer configurations were chosen based on performance and lack of visible overfitting, as shown in Table 7.5.

Table 7.5: The chosen hyperparameters for the four trained PNNs in the improved $H/A/h \rightarrow \tau\tau$ analysis. The activation function and number of nodes is N/A for dropout layers.

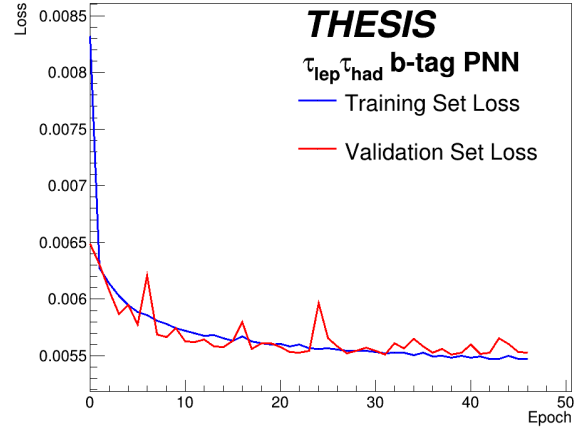
Hyperparameter/Property	Value/Description
Network Layers and Setup	Layers (Total: 7): Dense, Dense, Dropout, Dense, Dense, Dropout, Dense Activation: ReLu, ReLu, N/A, ReLu, ReLu, NA, Sigmoid Nodes: N_{Features} , 256, N/A, 256, 256, N/A, 1 Dropout: 0.05
Optimiser	Adam, η : 0.0001
Epochs and Batch Size	Early stopping, 128
K-folds	5

7.4.3 Model Training

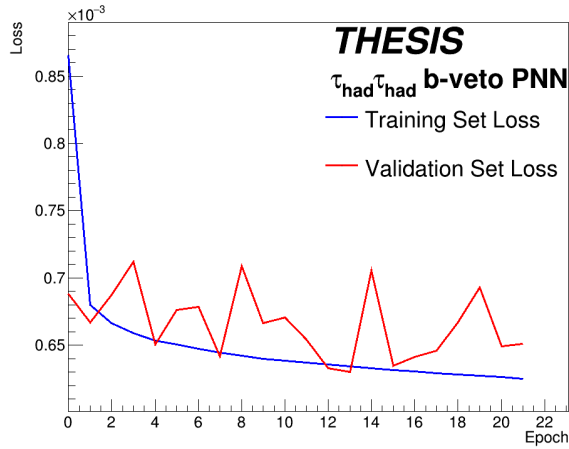
The evolution of the first fold loss against epoch for each model is shown in Figure 7.11 for the four PNN models. Early stopping functionality was used, and training was stopped at epoch 26 (46) for $\tau_{\text{lep}}\tau_{\text{had}}$ b -veto (b -tag) and epoch 22 (36) for $\tau_{\text{had}}\tau_{\text{had}}$ b -veto (b -tag). In general, the learning rate appears to be well optimised, with a minimum reached in each case after a reasonable number of epochs, indicating that underfitting is not an issue. For $\tau_{\text{lep}}\tau_{\text{had}}$ b -tag, it appears that a local minimum was reached before another minimum was found. The training loss plateaus in all cases, and the validation loss mostly matches the training loss without rising towards the end, indicating no overfitting. Although there is some fluctuation in the $\tau_{\text{lep}}\tau_{\text{had}}$ b -veto model, the difference between the validation and training loss is still small by the end of training.



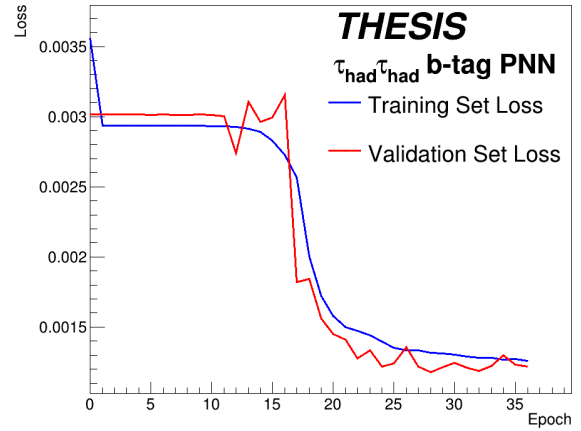
(a) $\tau_{lep}\tau_{had}$ b -veto



(b) $\tau_{lep}\tau_{had}$ b -tag



(c) $\tau_{had}\tau_{had}$ b -veto



(d) $\tau_{had}\tau_{had}$ b -tag

Figure 7.11: The loss against epoch for the four machine learning models. The blue line represents the training datasets loss, while the red line corresponds to the validation set's loss.

The ROC curves for the four signal regions are shown in Figure 7.12 for the networks evaluated at 200 GeV, 1000 GeV and 2500 GeV signal mass. The resulting evolution of the AUC when evaluating the network for all available mass points is shown in Figure 7.13. As expected, the AUC rises and almost complete separation ($AUC = 1$) between signal and background is achieved at high mass. However, an inflection point is observed in the $\tau_{\text{had}}\tau_{\text{had}}$ AUC plots, which can be attributed to the signal overlap with the background in many of the input feature distributions.

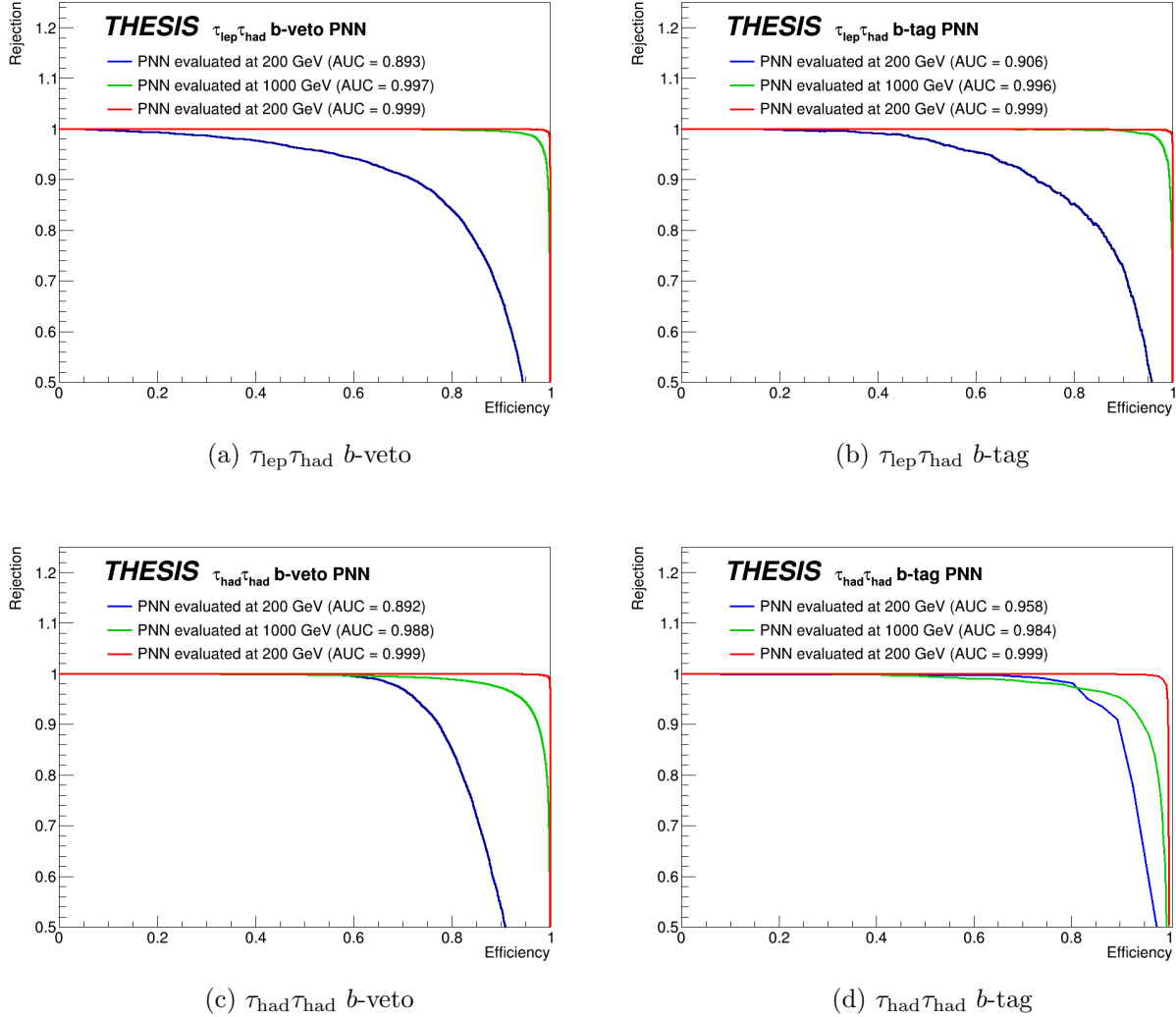
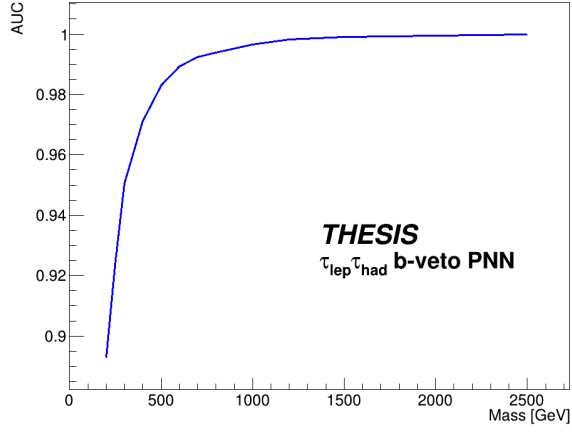
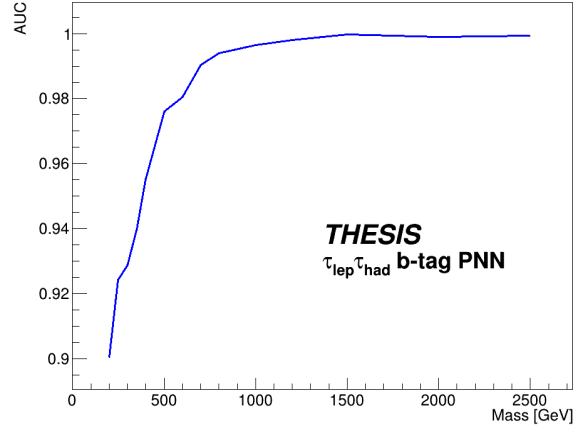


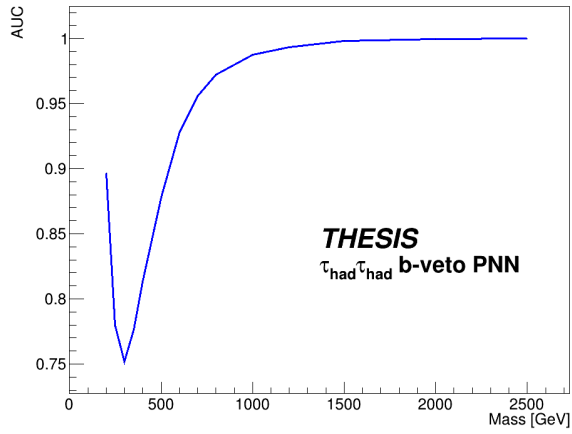
Figure 7.12: The ROC curves for each PNN model. The blue, green, and red curves represent the PNN evaluated at the mass points 200 GeV, 1000 GeV, and 2500 GeV, respectively.



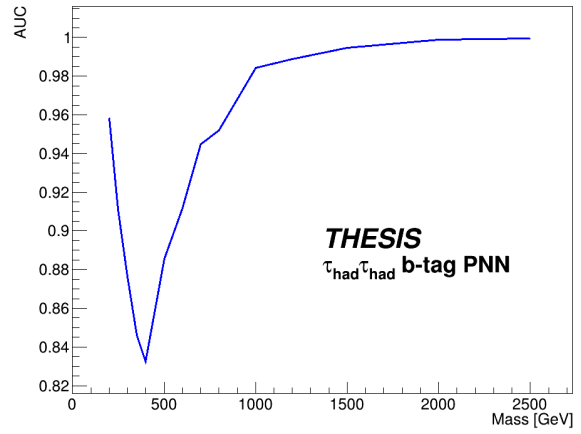
(a) $\tau_{\text{lep}}\tau_{\text{had}}$ *b*-veto



(b) $\tau_{\text{lep}}\tau_{\text{had}}$ *b*-tag



(c) $\tau_{\text{had}}\tau_{\text{had}}$ *b*-veto



(d) $\tau_{\text{had}}\tau_{\text{had}}$ *b*-tag

Figure 7.13: The AUC for each PNN model evaluated at every used mass point.

A crucial aspect of evaluating each model is checking for overfitting by comparing its performance on the training and isolated validation datasets at each evaluation mass. This is achieved by simply overlaying the training and validation set signal and background score distributions for the PNN evaluated at a mass point. Figures 7.14 and 7.15 display the corresponding overfitting plots for the four PNN models evaluated at the masses of 200 GeV, 1000 GeV, and 2500 GeV. Where all signals with masses different to the evaluation mass are filtered out. In general, the scores obtained for the validation sample closely match those of the training sample, except for some small regions where the statistics are low.

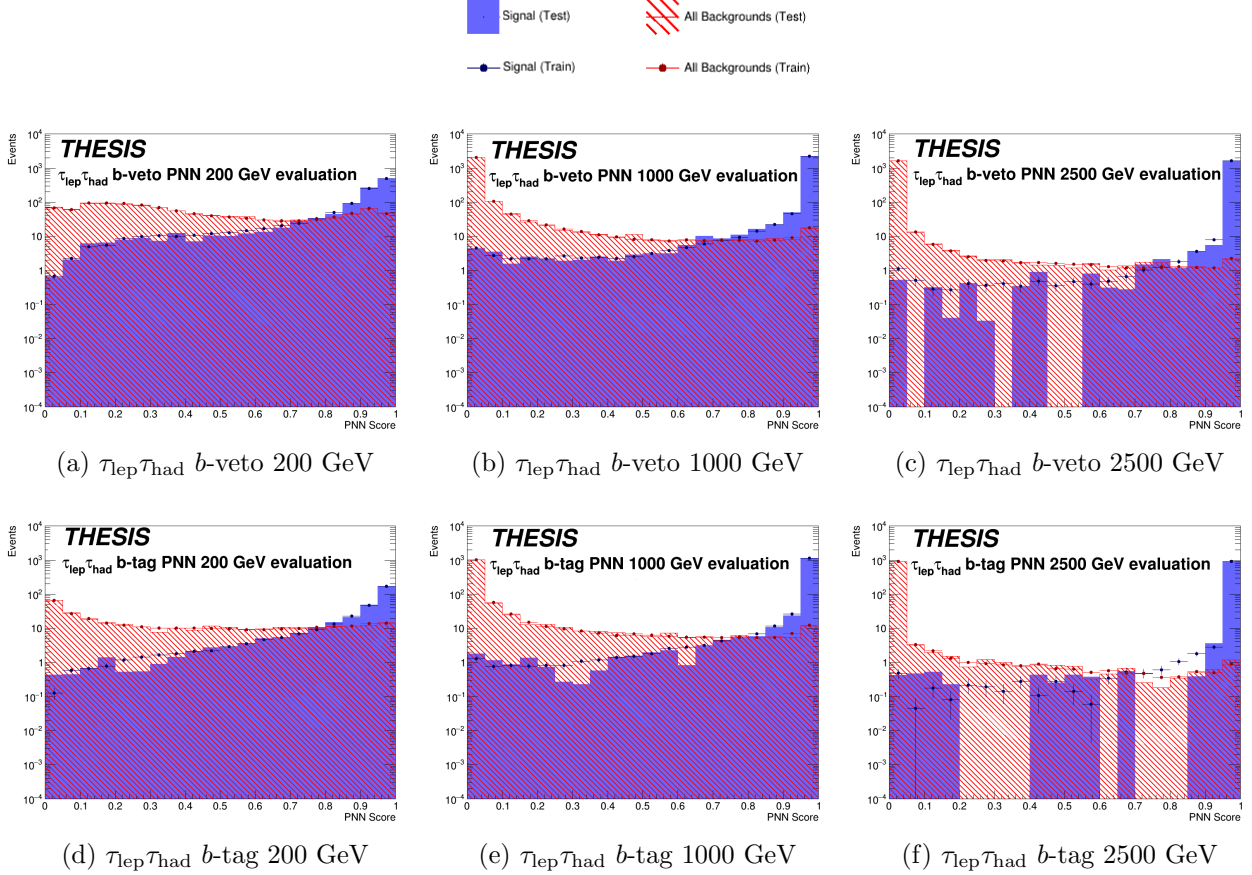


Figure 7.14: The training and validation set signal and background score distributions for the two $\tau_{\text{lep}}\tau_{\text{had}}$ PNN models evaluated at 200 GeV, 1000 GeV and 2500 GeV. As shown by the legend, the solid blue histogram represents the signal from the validation set, the blue markers indicate the signal from the training set. The dashed red histogram represents the background from the validation set and the red markers indicate the background from the training set. Signals which don't match the evaluation mass are filtered out.

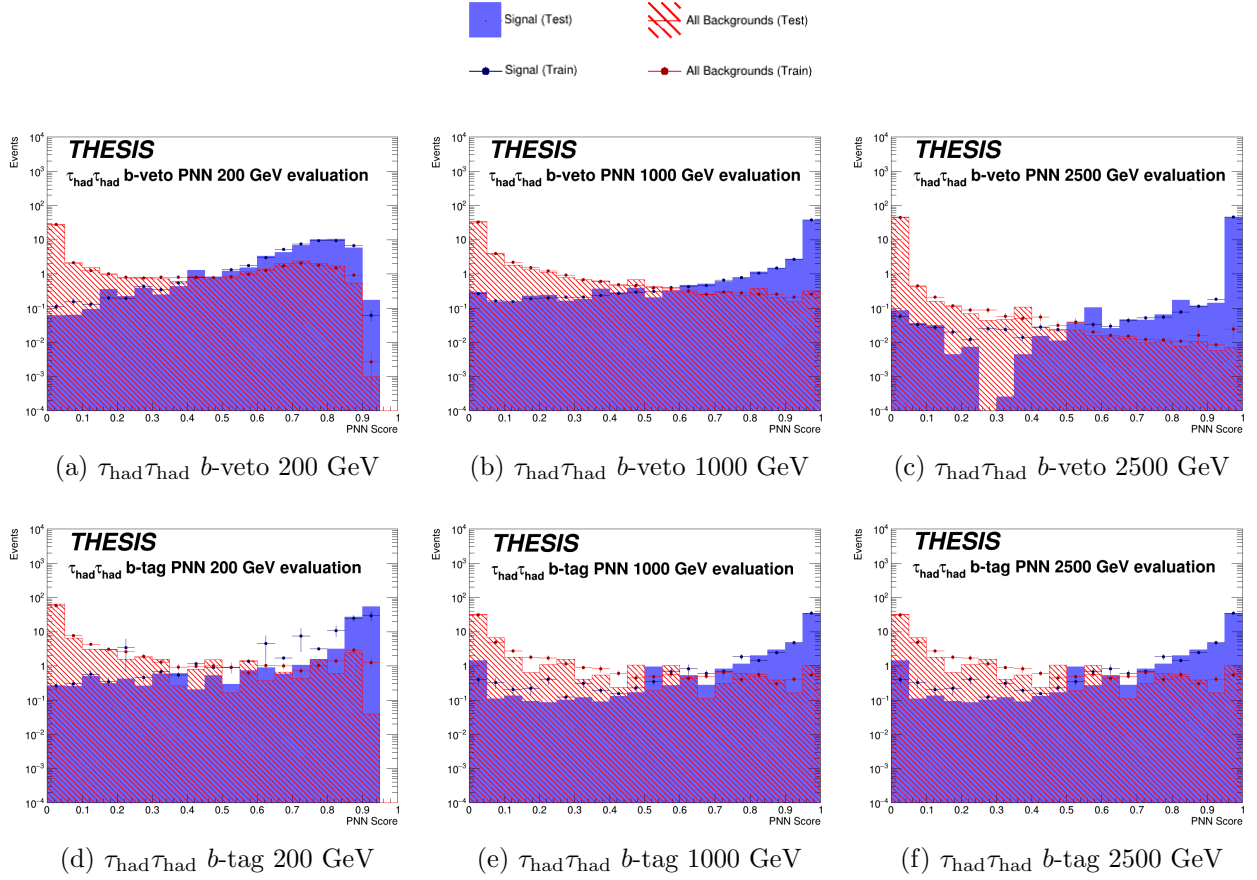


Figure 7.15: The training and validation set signal and background score distributions for the two $\tau_{\text{had}}\tau_{\text{had}}$ PNN models evaluated at 200 GeV, 1000 GeV and 2500 GeV. As shown by the legend, the solid blue histogram represents the signal from the validation set, the blue markers indicate the signal from the training set. The dashed red histogram represents the background from the validation set and the red markers indicate the background from the training set. Signals which don't match the evaluation mass are filtered out.

7.4.4 Statistical Fit and Binning Studies

An upper limit on the $\sigma \times \mathcal{B}(H/A/h \rightarrow \tau\tau)$ is constructed using the methods outlined in Section 4.7, with the four signal regions used in a s+b simultaneous fit. However, the implementation of this fit is different to the legacy case, as the background templates vary for each mass point. Moreover, the binning used in the previous iteration of the analysis was no longer usable. To save time and avoid the need to optimise the binning for each mass point and every region, a binning algorithm from the ATLAS TRANSFORMTOOL software package was used, which generates a set of bins for any input histogram. The TRANSFORMTOOL includes various simple binning algorithms, such as enforcing a lower threshold on the bin uncertainty, as well as more advanced algorithms adopted from [251]. To determine the most suitable algorithm, a scan across all the options was performed, finding minimal differences between algorithms across all mass points, the maximum gain in sensitivity was approximately 1%. The choice of algorithm depended on several factors, including the sensitivity, stability of the fit, and the minimum background events in each bin. A threshold of at least 10 events per bin was required to use the asymptotic approximation discussed in Section 4.7.

The transform D optimisation was chosen, this is represented by the equation:

$$Z = \frac{z_s n_s}{N_s} + \frac{z_b n_b}{N_b} \quad (7.5)$$

where $z_{s/b}$ are free parameters, $N_{s/b}$ are the total number of signal or background events, and $n_{s/b}$ are the number of signal or background events in some interval. This binning algorithm transforms a finely binned histogram into an optimised coarsely binned one. Starting from the rightmost bin of the finely binned histogram, the Z function is evaluated. If $Z < 1$, the bin contents are added to the next bin and the evaluation is repeated. If $Z \geq 1$, a bin boundary for the new histogram has been found, and the process begins again for the next bin boundary. One can set additional requirements, such as a maximum uncertainty on the background events in each bin or a minimum number of background events. Finally, all the fine bins between the coarse bin boundaries are merged. Although transform D is somewhat simpler, it does have some advantages over the other choices. If one sets z_s to zero and varies z_b , the background will be equally distributed among the bins, and vice versa for when z_b is zero with z_s varied. To keep the number of bins constant one can fix $z_s + z_b$. For this analysis, the z_s and z_b were set to 10 as it gave the most performant upper limit, although the difference between parameter choices was generally less than 1%.

For large signal masses, the signal and background distribution is highly concentrated in the final and first bin of the PNN score, respectively, as shown in Figures 7.14 and 7.15. This presents a challenge in obtaining an effective binning of the signal that can improve the fit and achieve a lower limit. A packing function can help remedy this, the chosen function is defined as follows:

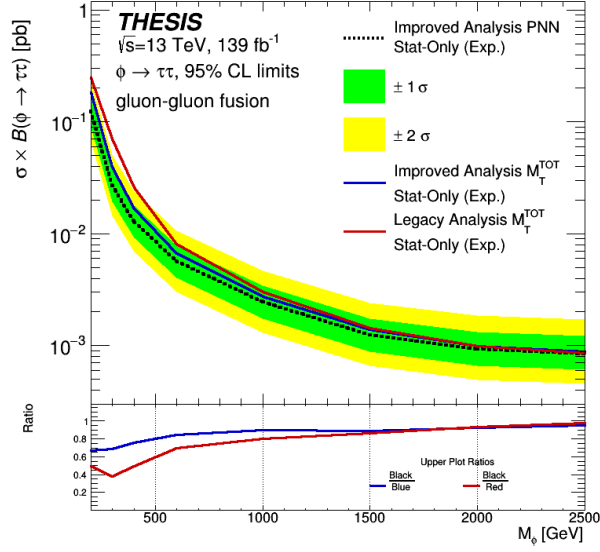
$$S_{pack} = \frac{(1 - \alpha)}{2 \ln(\delta)} \left(\ln(1 - (1 - \delta)S) - \ln(S + \delta) \right) + \frac{\alpha(S - \frac{1}{2})}{2} \quad (7.6)$$

where S is the PNN score, δ and α are constants set to 1×10^{-6} and 0.5 respectively. The function spreads out values close to a score of 1 or 0, such that a PNN score of 0.999 is

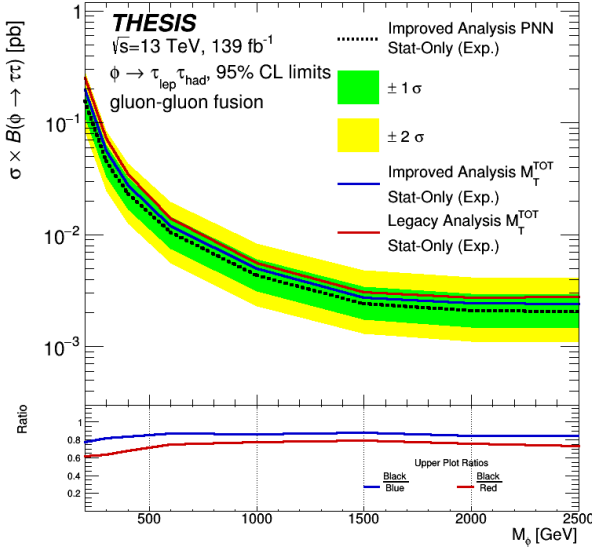
transformed to 0.828, for example. The values for the δ and α parameter choices were the product of a tuning study used to optimise the spread across the $\{0, 1\}$ range. Implementation of this function results in significant improvement, particularly at higher mass points, with improvements in the limit of up to 35% observed across all signal masses.

7.4.5 Resulting Exclusion Limits

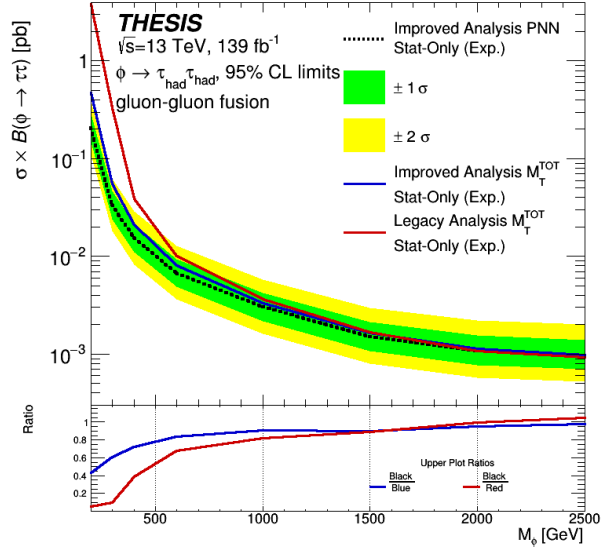
The improved analysis is at an early stage of the analysis timeline. As a consequence, the systematic uncertainties have not been fully implemented. Therefore, the upper limit on the $\sigma \times \mathcal{B}$ is only shown with statistical uncertainty taken into account in the fit (stat-only). For the ggH and bbH production modes, Figures 7.16 and 7.17 present a comparison between the improved analysis using the PNN and M_T^{TOT} as discriminants, and the legacy analysis result.



(a) $\tau_{\text{lep}}\tau_{\text{had}} + \tau_{\text{had}}\tau_{\text{had}}$

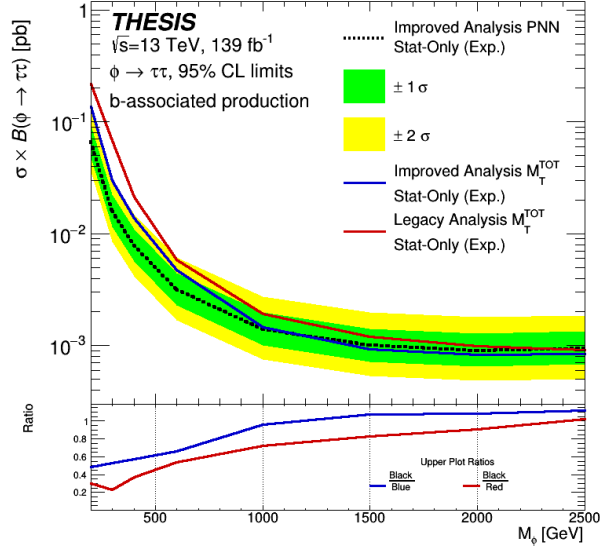


(b) $\tau_{\text{lep}}\tau_{\text{had}}$

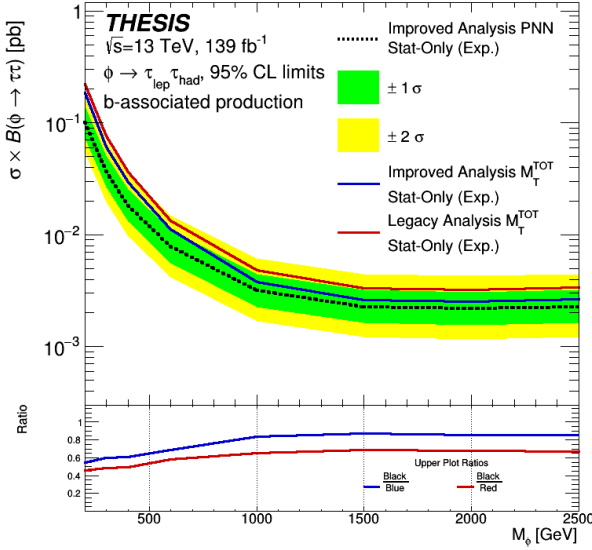


(c) $\tau_{\text{had}}\tau_{\text{had}}$

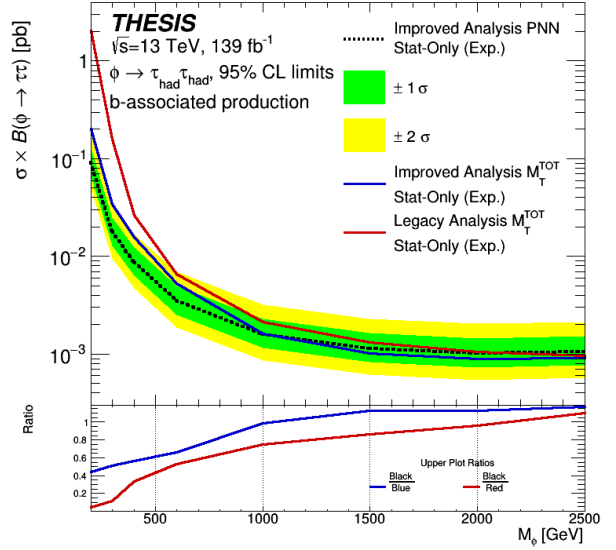
Figure 7.16: The 95% CL expected upper limit on the $\sigma \times \mathcal{B}(H/A/h \rightarrow \tau\tau)$ in the combined, $\tau_{\text{lep}}\tau_{\text{had}}$ and $\tau_{\text{had}}\tau_{\text{had}}$ channels for the ggH production mode. The limits consider only the statistical uncertainty. The limits from the improved analysis using the PNN and M_T^{TOT} discriminants are represented by the black and blue lines, respectively. The limit from the 2020 $H/A/h \rightarrow \tau\tau$ (legacy) [8] analysis is shown in red. The green and yellow bands represent the $\pm 1\sigma$ and $\pm 2\sigma$ uncertainty on the expected PNN upper limit respectively. The ratio of the improved M_T^{TOT} and legacy M_T^{TOT} to the improved PNN is shown in the ratio plot.



(a) $\tau_{\text{lep}}\tau_{\text{had}} + \tau_{\text{had}}\tau_{\text{had}}$



(b) $\tau_{\text{lep}}\tau_{\text{had}}$



(c) $\tau_{\text{had}}\tau_{\text{had}}$

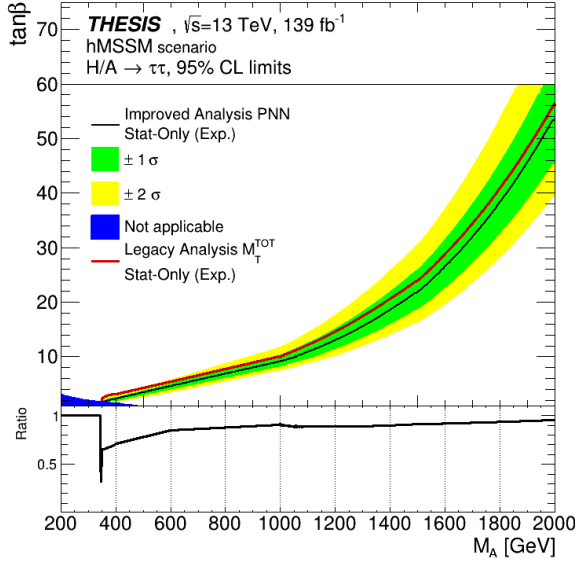
Figure 7.17: The 95% CL expected upper limit on the $\sigma \times \mathcal{B}(H/A/h \rightarrow \tau\tau)$ in the combined, $\tau_{\text{lep}}\tau_{\text{had}}$ and $\tau_{\text{had}}\tau_{\text{had}}$ channels for the bbH production mode. The limits consider only the statistical uncertainty. The limits from the improved analysis using the PNN and M_T^{TOT} discriminants are represented by the black and blue lines, respectively. The limit from the 2020 $H/A/h \rightarrow \tau\tau$ (legacy) [8] analysis is shown in red. The green and yellow bands represent the $\pm 1\sigma$ and $\pm 2\sigma$ uncertainty on the expected PNN upper limit respectively. The ratio of the improved M_T^{TOT} and legacy M_T^{TOT} to the improved PNN is shown in the ratio plot.

When comparing the percentage difference from the legacy result for each mass point, the improved analysis using M_T^{TOT} as the discriminant shows a significant improvement of up to 22% (21%) in the $\tau_{\text{lep}}\tau_{\text{had}}$ channel for the ggH (bbH) mode, as previously mentioned in Section 7.2.6. Furthermore, the $\tau_{\text{had}}\tau_{\text{had}}$ channel shows an exceptionally large improvement due to the addition of the di-tau trigger discussed at the beginning of this chapter. The combined channel displays an overall improvement of up to 44% (55%) for the ggH (bbH) mode, indicating a substantial enhancement in the analysis.

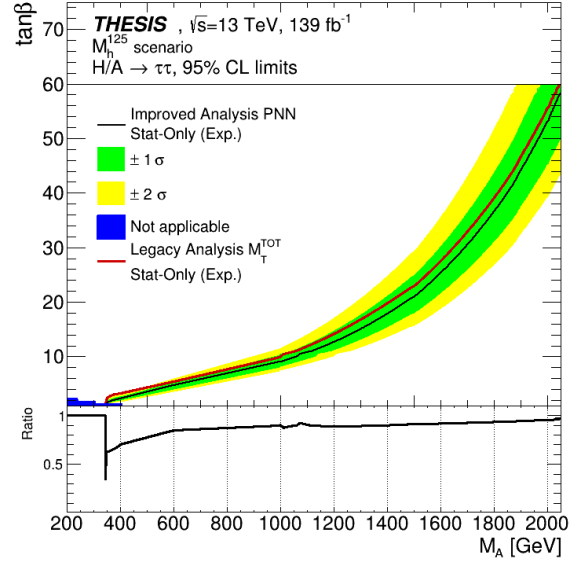
Comparing the PNN to M_T^{TOT} for the improved analysis, significant improvements of up to 40% (45%) in the $\tau_{\text{lep}}\tau_{\text{had}}$ channel, 57% (55%) in the $\tau_{\text{had}}\tau_{\text{had}}$ channel, and 33% (51%) in the combined channel for the ggH (bbH) modes across all mass points can be observed. However, there is no significant improvement at high mass as the M_T^{TOT} variable already provides high separation between the signal and background, resulting in an AUC of ~ 0.99 if only this variable is included in the training. Nevertheless, the $\tau_{\text{lep}}\tau_{\text{had}}$ channel still outperforms the M_T^{TOT} variable at high mass, indicating that the PNN is well optimised for this channel.

The comparisons mentioned above show improvements across all mass points, except for the high mass range in the $\tau_{\text{had}}\tau_{\text{had}}$ channel for the bbH mode. In principle, if M_T^{TOT} is included in the training and the binning is optimised accordingly, the model should not perform worse than just using the M_T^{TOT} discriminant. However, the limit was found to be worse at these high mass points because the training employs the absolute value of the event weight. This issue causes a small inefficiency associated with the PNN when training on samples that contain a considerable amount of negative weights. When constructing the limit using the absolute value of all event weights, the M_T^{TOT} bbH $\tau_{\text{had}}\tau_{\text{had}}$ limit and the corresponding PNN limit converge to a similar value, as expected.

The performance gain for the improved analysis using the PNN when compared to the legacy analysis is also shown in the $\{m_A, \tan\beta\}$ plane for the hMSSM and M_h^{125} benchmark scenarios in Figure 7.18. The improvement is similar in both scenarios, with over 3 times improvement at $m_A = 350$ GeV, the transition point where the benchmarks become valid. The improvement then reduces with increasing m_A , as suggested by the ggH and bbH limits.



(a) $\tau_{\text{lep}}\tau_{\text{had}} + \tau_{\text{had}}\tau_{\text{had}}$



(b) $\tau_{\text{lep}}\tau_{\text{had}} + \tau_{\text{had}}\tau_{\text{had}}$

Figure 7.18: The $\{m_A, \tan \beta\}$ exclusion plane for the (a) hMSSM and (b) M_h^{125} benchmark scenarios with the improved result using the PNN. The 2020 $H/A/h \rightarrow \tau\tau$ (legacy) [8] analysis is shown in red. The regions of parameter space in which the benchmark scenarios are invalid are shown in blue. All limits are calculated using only the statistical uncertainty. The ratio of the improved PNN and legacy limits are shown in the ratio plot.

7.4.6 Conclusions

Using machine learning techniques, analysis optimisation, and the latest advancements in ATLAS object reconstruction, exploratory studies were conducted with a view towards enhancing the 2020 $H/A/h \rightarrow \tau\tau$ (legacy) analysis [8]. A mass-parameterised neural network was selected as the discriminant to distinguish between signal and background, as it provided a straightforward solution to the problem of having to train many models. Numerous efforts were made to improve the acceptance of signal events in the legacy analysis, including optimising overlap removal, refining the definition of fake regions, and adjusting the object working points recommended by the combined performance groups. The upper limit on the $\sigma \times \mathcal{B}(H/A/h \rightarrow \tau\tau)$ with only statistical uncertainty considered is compared between the improved analysis incorporating the PNN and the legacy analysis in Figures 7.16 and 7.17. Up to 4.2 (2.6) times improvement is observed with the improved analysis for the bbH (ggH) limit when considering all decay modes combined ($\tau_{\text{lep}}\tau_{\text{had}} + \tau_{\text{had}}\tau_{\text{had}}$ mode). Results are also shown for two popular benchmark scenarios in Figure 7.18, showing up to 3.1 (2.9) times improvement with the improved analysis in the context of the hMSSM (M_h^{125}) benchmark. The improvement is almost entirely at lower mass points, where the PNN demonstrates higher performance. At higher mass points, the limits of both the legacy and improved analysis converge to approximately the same value, as the PNN performs comparably to the M_T^{TOT} discriminant used in the legacy analysis. This exploratory work, alongside the analysis simplification procedures outlined in this section, can be utilised to enhance the performance during the Run-III iteration of this analysis.

Chapter 8

The ATLAS Inner Tracker as part of the High Luminosity - LHC Upgrade

This chapter provides an overview of the ATLAS Phase-II upgrade, which is scheduled for installation during Long Shutdown 3 of the LHC (December 2025 - February 2029) and will be operational for Run-IV (February 2029 - December 2032) in conjunction with the High Luminosity - LHC (HL-LHC) upgrade to the current LHC. The need for the HL-LHC is discussed, as well as the importance of the ATLAS Phase-II upgrade, with particular attention paid to the new ATLAS Inner Tracker upgrade, which will replace the current Inner Detector.

The University of Sheffield, where the author is based, is identified as a key site for building the silicon strip barrel modules that make up part of the ITk upgrade. As a result, the latter part of this chapter focuses on the mass production of these modules, using an example module built by the author. The production process, from the reception of module parts to construction, quality assurance, databasing, and shipping, is detailed in full, providing a comprehensive overview of the production chain relevant to a module building site.

8.1 The High Luminosity - LHC and the ATLAS Phase-II Upgrade

After collecting approximately 300 fb^{-1} of data at $\sqrt{s} = 13.6 \text{ TeV}$ during Run-III, the LHC will undergo upgrades for HL-LHC operation. The HL-LHC will achieve $\langle \mathcal{L}_{inst} \rangle = 5 \times 10^{34} \text{ cm}^{-2}\text{s}^{-1}$ and $\langle \mu \rangle = 140$, with a potential increase to $\langle \mathcal{L} \rangle = 7.5 \times 10^{34} \text{ cm}^{-2}\text{s}^{-1}$ and $\langle \mu \rangle = 200$ [252, 253]. These ambitious goals will be achieved through various upgrades, such as the introduction of stronger Nb_3Sn quadrupole bunch focusing magnets that can produce a magnetic field of 12 T, compared to the current 8 T. Additionally, ‘crab cavities’ will be introduced to provide a slight transverse momentum to the proton bunches, which will increase the overlap area. The HL-LHC is expected to collect 3000 fb^{-1} of data at $\sqrt{s} = 14 \text{ TeV}$ over 10 years of operation, providing an unprecedented dataset for analysis compared to what is currently available.

The proposed conditions of the HL-LHC are beyond the detection capabilities of the current ATLAS detector, making the Phase-II upgrade of the detector essential. The current Inner Detector was designed for radiation tolerance over a 10-year period with $\langle \mathcal{L} \rangle = 1 \times 10^{34}$ and $\langle \mu \rangle = 23$ at $\sqrt{s} = 14$ TeV [253]. The pixel detector was designed to withstand up to 400 fb^{-1} of collisions, which will be surpassed before the start of Run-IV. The increased μ at the HL-LHC will require higher detector granularity and more advanced electronics to maintain an adequate track finding efficiency.

The entirely silicon semiconductor based ITk will be installed to cope with the expected data rates and extreme conditions at the HL-LHC and will fill the entire area of the current Inner Detector. The trigger system will also undergo significant improvements to handle the much busier environment. A two-level hardware trigger system is proposed, starting at an accept rate of 1 MHz (level-0), which will consider tracking information at high μ . The current ATLAS L1 trigger cannot provide such tracking information. The upgraded trigger and increased flux of particles will also require the replacement of the LAr calorimeter electronics, which are at least 15 years old [254].

8.2 The ATLAS Inner Tracker Upgrade

The new ITk will be divided into two sub-parts, the silicon pixel and strip detectors, which will continue to operate in a 2 T magnetic field provided by the central solenoid. The ITk pixel detector will enable $|\eta| < 4.0$ coverage, improving track acceptance, forward jet reconstruction, E_T^{MISS} resolution, and pile-up rejection. A minimum of 9 hits across the entire $|\eta|$ acceptance will be ensured, except for some transition regions [255]. The ITk is illustrated in Figure 8.1, showing the separate pixel and strip detectors divided into their constituent barrel and end-cap parts.

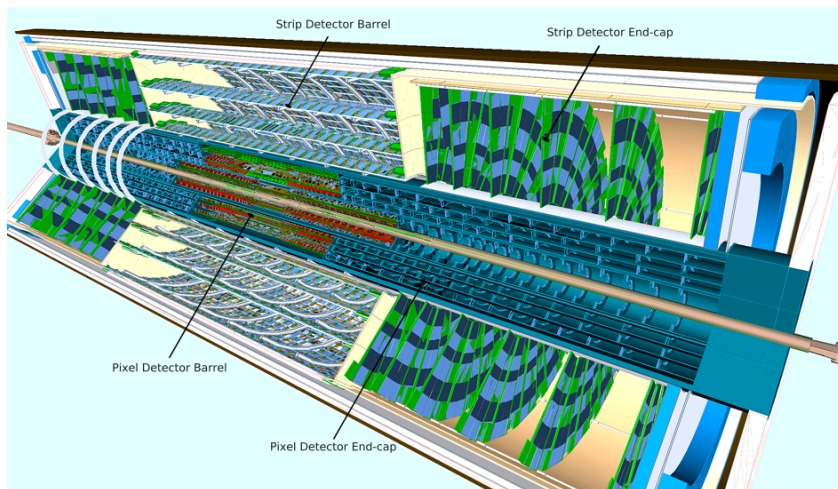


Figure 8.1: An illustration of the ATLAS Inner Tracker upgrade taken from [256], it is built to replace the current Inner Detector, the barrel and end-cap regions are labelled for the silicon pixel and strip based sub-detectors.

8.2.1 The Pixel Detector

The pixel detector will be formed of five layers broken up into three parts, the inner system, the outer barrel and the outer end-cap rings, as represented in Figure 8.2. The inner system forms the first two layers, the configuration is such that they are able to be replaced part way through the HL-LHC campaign. The outer barrel is composed of horizontal and inclined pixel modules, whereas the end-cap rings are orientated perpendicular to the beamline. The radial distance of the horizontal part of each barrel layer varies from 34 mm to 291 mm away from the beamline [255].

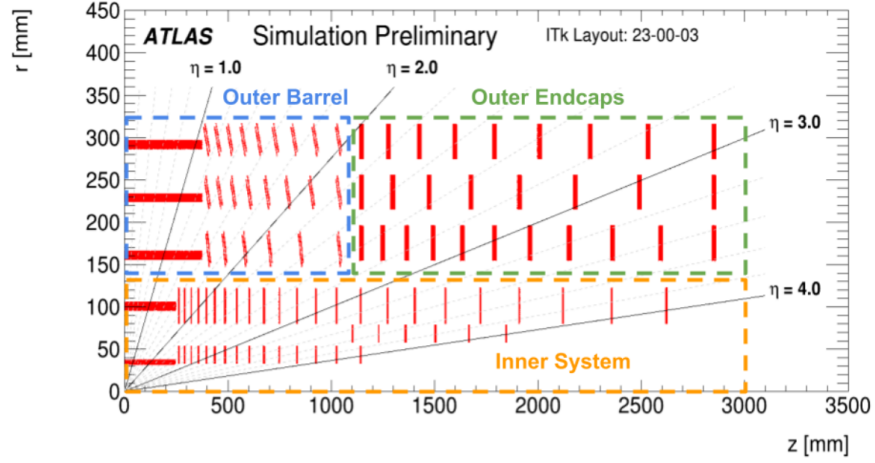


Figure 8.2: The decomposition of the ITk pixel detector as shown in $r - z$ space, taken from [257]. The inner system, outer barrel and outer end-cap regions are all shown. The inner system enable coverage up to $|\eta| < 4.0$ and can be replaced. The interaction point is located at the origin.

There are two types of pixel modules, named triplet and quad modules. Triplet modules are formed of three connected front-end $20 \times 21 \text{ mm}^2$ Application Specific Integrated Circuit (ASIC) read-out chips each connected to a $2 \times 2 \text{ cm}^2$ sensor, whilst quad modules are four read-out chips connected to one $4 \times 4 \text{ cm}^2$ sensor [257, 258]. An example of a quad module is shown in Figure 8.3, along with an illustration. The triplet modules are used for the innermost pixel layers and have pixel size $25 \times 100 \mu\text{m}^2$ in the barrel region, the quad modules have pixel size $50 \times 50 \mu\text{m}^2$ [255]. Each ASIC chip consists of 153,600 pixels [259]. In total around 10,000 pixel modules will be built at sites around the world, these will then be glued onto the corresponding local supports and installed into the detector. In total this will cover an active area of 13 m^2 and account for around 5 billion read-out channels [258].

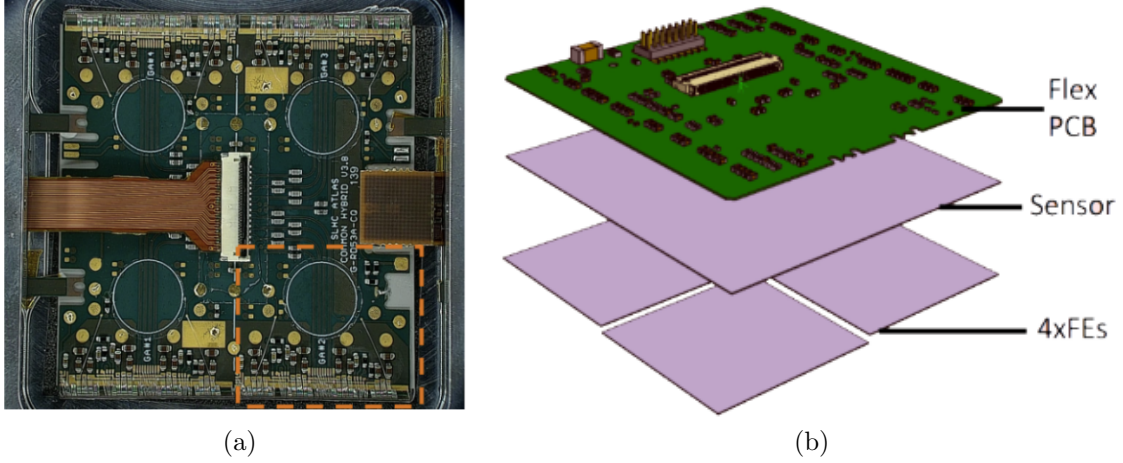


Figure 8.3: (a) A photograph of a quad module [257], four FE ASIC chips are bonded onto one $4 \times 4 \text{ cm}^2$ sensor. The orange dashed square shows where one of the $20 \times 21 \text{ mm}^2$ ASIC chips would be placed. (b) A schematic representation of a quad pixel module [260].

8.2.2 The Strip Detector

The strip detector, similar to the SCT, will be positioned immediately after the pixel layers. It consists of four barrel layers aligned parallel to the beam direction, as well as six end-cap disks on each side of the collision point, positioned perpendicular to the beam-pipe. The radial distance of the barrel layers from the beam-pipe ranges from 405 mm to 1000 mm. This configuration of barrel and end-cap layers enables effective tracking within the region $|\eta| < 2.7$ as shown in Figure 8.4 [261].

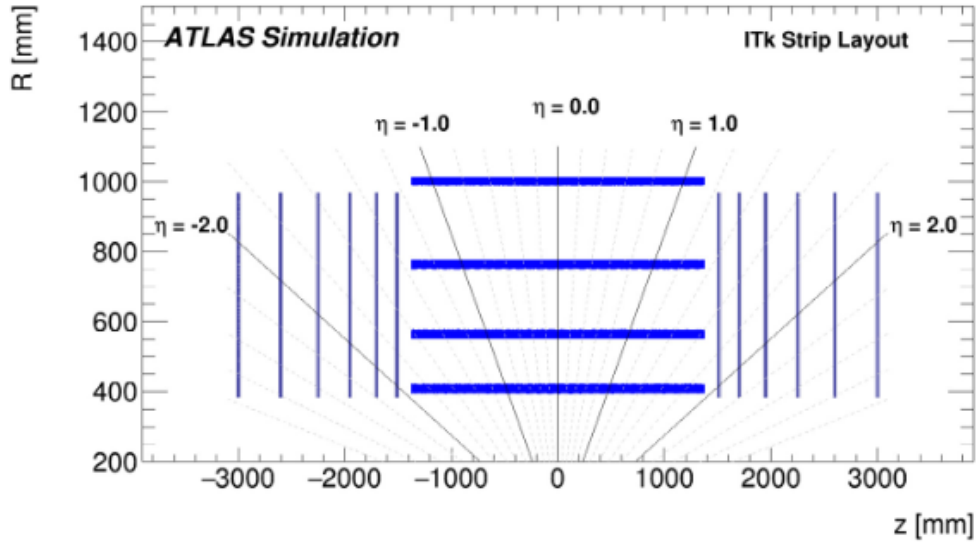


Figure 8.4: A schematic of the location of each strip barrel layer and end-cap disk situated within the ITk, taken from [261].

A barrel strip module is photographed and illustrated in Figure 8.5, they consist of several components. A given barrel module includes a $97 \times 97 \text{ mm}^2$ silicon strip semiconductor sensor, one or more hybrid circuits, and a powerboard (PB) circuit. The hybrids are flexible Printed Circuit Boards (PCBs) that incorporate ten ASIC ABCStar read-out chips and one HCCStar hybrid controller chip with the capability to communicate command and reject signals between the ASICs. Each ASIC provides various read-out services, such as pre-amplification, shaping, and buffering [256, 262]. Additionally, the powerboard contains a GaNFET transistor responsible for providing sensor bias. It also houses a DC-DC converter, which transforms an 11 V input into the necessary 1.5 V required by the ASICs. Furthermore, an AMACV2a chip handles voltage control and conditions monitoring within the module.

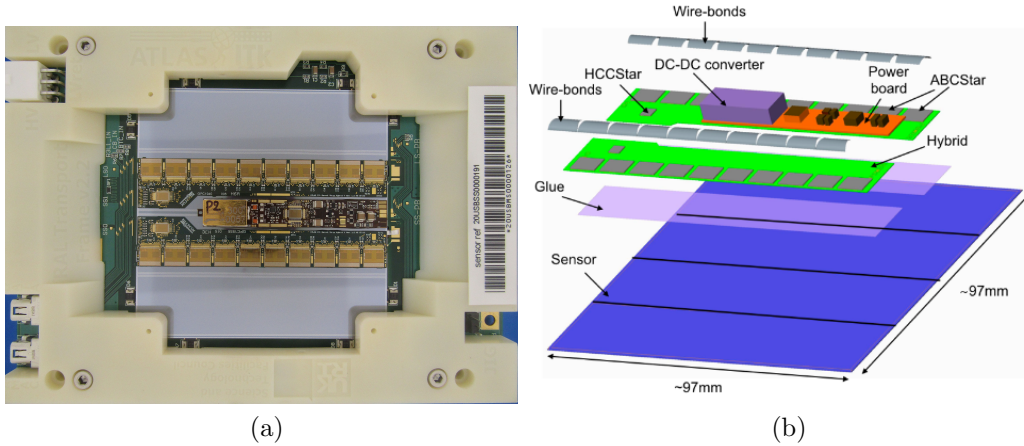


Figure 8.5: (a) A photograph of a prototype short strip barrel module constructed by the author, the photograph was taken before the front-end wire-bonds were applied. (b) An illustration of an exploded view of a short strip module, taken from [256].

A total of eight strip modules of similar design are used, with seven of them utilised in the end-cap region. To form complete modules, the constituents are glued together, and wire-bond connections are established between the read-out channels, ASICs, hybrids, and powerboard. During production, approximately 14,000 strip barrel modules will be manufactured by module building sites, accounting for the expected yield [263]. Once finished, the barrel and end-cap modules are affixed to 392 rectangular staves and 384 trapezoidal petals, respectively. This assembly process results in a combined sensor area of 190 m^2 and a total of around 60 million channels [253, 263, 264].

Within the strip detector barrel, the inner two layers consist of short strip (SS) modules. These modules are comprised of two hybrids and four rows of 1,280 strips with a length of 24.16 mm. An example of a prototype SS module, constructed by the author using the methods described in the following sections, is shown in Figure 8.5. On the other hand, the outermost two layers consist of long strip (LS) modules, which feature a single hybrid and two rows of 1,280 strips with a length of 48.35 mm [253].

8.3 Construction of Strip Barrel Modules

The construction of the ITk barrel modules is a collaborative effort involving multiple sites, each responsible for specific stages of the process. Generally, module parts are manufactured by an external contractor and passed through a chain of assembly focused or quality check (QC) focussed sites. Module assembly sites play a crucial role in the construction process. They receive detector quality hybrids, powerboards, and sensors from preceding sites in the chain. At the module assembly sites, gluing, wire-bonding, and quality checks are performed to ensure the completion and functionality of each module.

The production chain for sensors, leading up to their integration into modules, is illustrated in Figure 8.6. Initially, bare sensors are received from the vendor Hamamatsu (HPK), and they are subsequently transported to reception sites such as CERN or the High Energy Accelerator Research Organisation (KEK). From there, the sensors are dispatched to dedicated sensor QC and high voltage tabbing (HV-tab) sites. Here, a metallic tab for supplying high voltage is welded on and a comprehensive range of quality control measures is performed to ensure that the sensors meet the required standards. Following the completion of the quality checks, the sensors are shipped to the module building sites for assembly [265]. A similar network and production chain are established for the hybrids and powerboards involved in the module construction process.

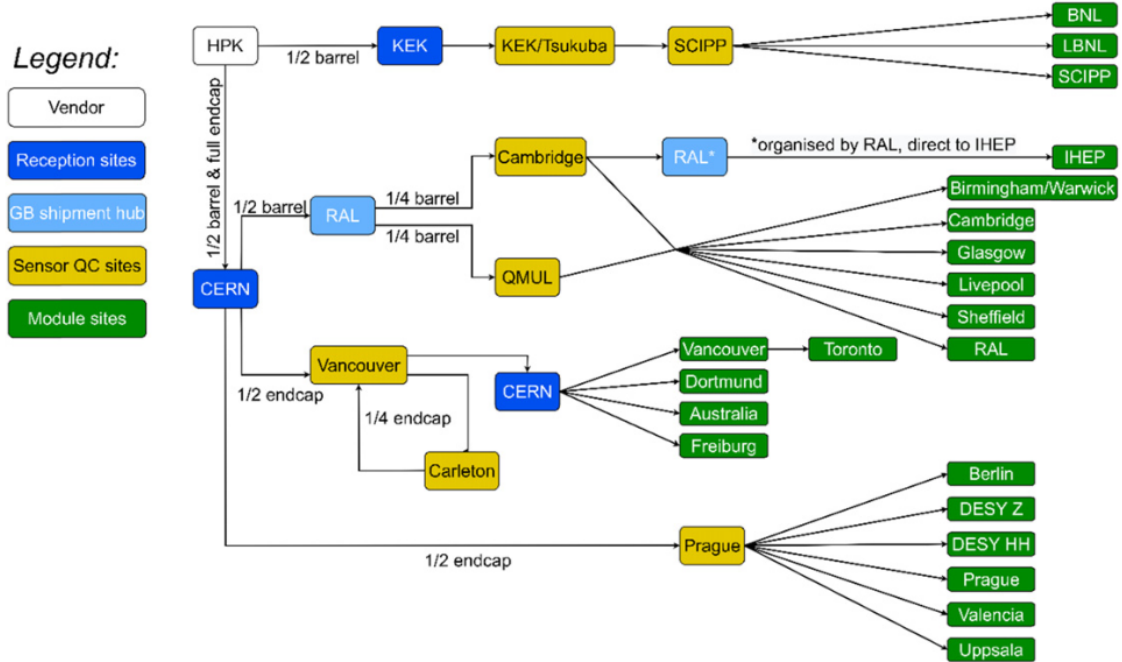


Figure 8.6: The production chain for the silicon sensors used for the strip modules, as described in [265].

The University of Sheffield is assigned a module production quota. Using the techniques outlined in the following sections, the modules are constructed and tested within a part class 5, part class 7 ISO 14644-1 accredited clean room [266]. This specialised environment suitable for module gluing ensures minimal contamination from particulate matter, maintains a consistent temperature of approximately $19 \pm 1^\circ\text{C}$, and regulates relative humidity at around $52 \pm 4\%$.

8.3.1 Module Assembly Procedure

Every assembly step followed by the author to construct the module shown in Figure 8.5(a) is detailed in this section. The gluing stage of module assembly can be divided into three key stages: sensor preparation, hybrid gluing, and powerboard gluing. This section provides an account of each stage based on a prototype short strip module constructed by the author, the same one as depicted in Figure 8.5. The module was created as part of the pre-production A (PPA) prototype campaign conducted in mid-2022. During the PPA phase, components very close to production level were used, with only minor adjustments anticipated for the gluing procedure during mass production. Following successful QC tests, the PPA modules were shipped to a stave installation site for integration onto a prototype stave. The prototype stave was built to conduct a system test, a comprehensive milestone test involving the complete stave powering and read-out chain. The PPA modules were also instrumental in qualifying the University of Sheffield for module building.

Sensors are securely shipped to Sheffield from either Cambridge or Queen Mary University of London (QMUL) using specialised sensor transport frames. These frames are equipped with shock watches as depicted in Figure 8.7(a). These act as indicators to harsh impacts such as contact with the floor, triggering if the sensor has been subject to a g-force of size 25 G. Upon arrival, the transport frame is screwed into the module bonding jig, typically used to secure the module during the bonding process. In this case, the jig is used to secure the sensor to be picked up for weighing. The sensor is connected to the transport frame using a few wire-bonds, facilitating easy electrical testing upon reception (as discussed in the next section). These bonds must be manually removed using Electro-static Discharge (ESD) safe tweezers. Once the bonds are removed, the sensor can be gently lifted off the transport frame using a vacuum tool, and its weight is measured using a 1 mg precision KERN EWJ 300-3 weighing scale. All tooling and jigs involved in this process are meticulously visually inspected and cleaned with isopropanol alcohol prior to coming into contact with the sensor. The vacuum tool is employed once again to position the sensor onto the module assembly jig, as depicted in Figure 8.7(a). Small metallic pins are used for precise alignment, while the vacuum ensures the fixed placement of the sensor. Furthermore, a grounding port is utilised to maintain ESD safety throughout the process.

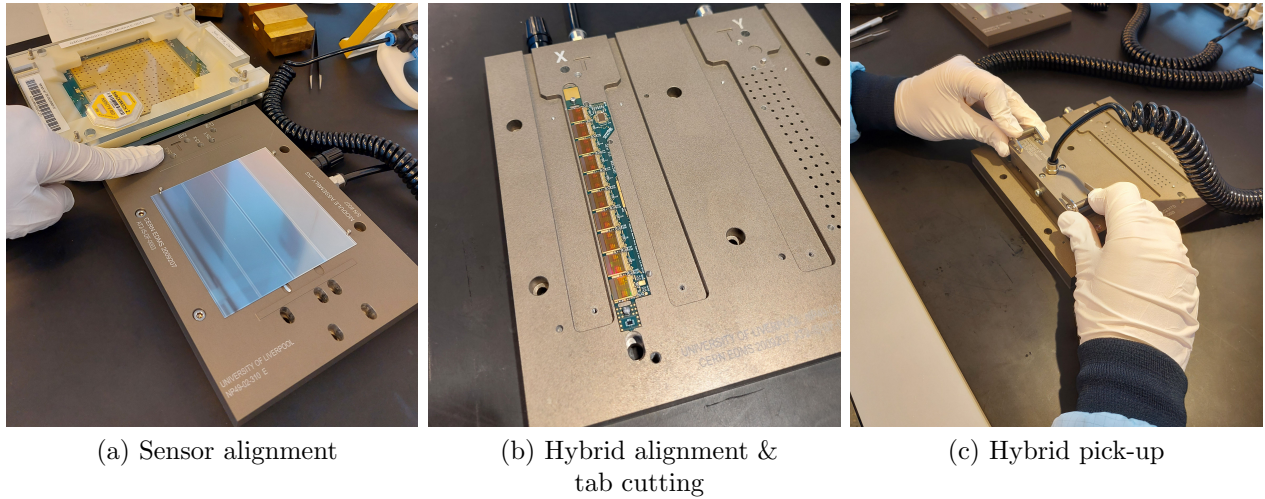


Figure 8.7: (a) A sensor on the module assembly jig ready for gluing, also shown is the sensor transport frame complete with shock watch. (b) An X-hybrid on the hybrid alignment jig, ready for the hybrid tabs to be cut off. (c) A hybrid pick-up tool being used on an X-hybrid.

After handling the sensor, the hybrid is ready for gluing. The hybrids, received from the hybrid population site (Liverpool), are part of a panel that can accommodate up to nine hybrids. To secure the panel for hybrid extraction, it is screwed onto the hybrid testing jig, primarily used for hybrid panel testing. The hybrids are connected to the panel using a few wire-bonds, which are manually removed using ESD safe tweezers. The hybrids also have tabs on both sides of the PCB, allowing them to be attached to the panel using Kapton tape. To remove the hybrid, the tape is carefully peeled off using tweezers, and then the hybrid is weighed. Using tweezers, the hybrid is placed on the hybrid alignment jig, the pins shown in Figure 8.7(b) are used to ensure proper alignment. The jig includes a vacuum and grounding port for hybrid fixing and ESD safety, respectively. For an SS module with two hybrids, referred to as the X-hybrid and Y-hybrid, the process is repeated for the other hybrid. Once both hybrids are aligned on the jig, the tabs on either side of each hybrid are manually removed by applying a downward force using an X-ACTO scalpel with a blade size 7. Finally, the weight of each tab is measured to determine the weight of each hybrid.

Next, the hybrid must then be picked up ready for gluing using a hybrid pick-up tool. In Figure 8.7(c), an X-hybrid pick-up tool is shown, they have pins on their front side that align with the holes in the hybrid alignment jig. The pick-up tool is placed over the front side of the hybrid, and with moderate force, it is pushed downwards. The vacuum is turned on for the pick-up tool and off for the jig. Once secured, the pick-up tool is attached to the gluing stand depicted in Figure 8.8(a), and a gluing sample is prepared. During the prototype phase, different types of glue were used due to supplier issues and increased electrical noise with certain glues. However, for this module, the previously approved Polaris PF-7006 glue was utilised [267]. This involved depositing 0.9 g of hardener and 10 g of epoxy into a small plastic glue boat, as shown in Figure 8.8(a). The mixture was thoroughly mixed for 2 minutes using a plastic straw. After the mixing process, a mandatory waiting time of 20

minutes was required for pre-curing, followed by a 40-minute window for gluing the module. For production, a different glue will be used as the Polaris glue has been discontinued. Currently, the ‘True Blue’ (ECCOBOND F 112) [268] is favoured for usage since it gives reduced electrical noise compared to other trialled candidates. This means that the mixing and curing times during production will be different to those mentioned above.

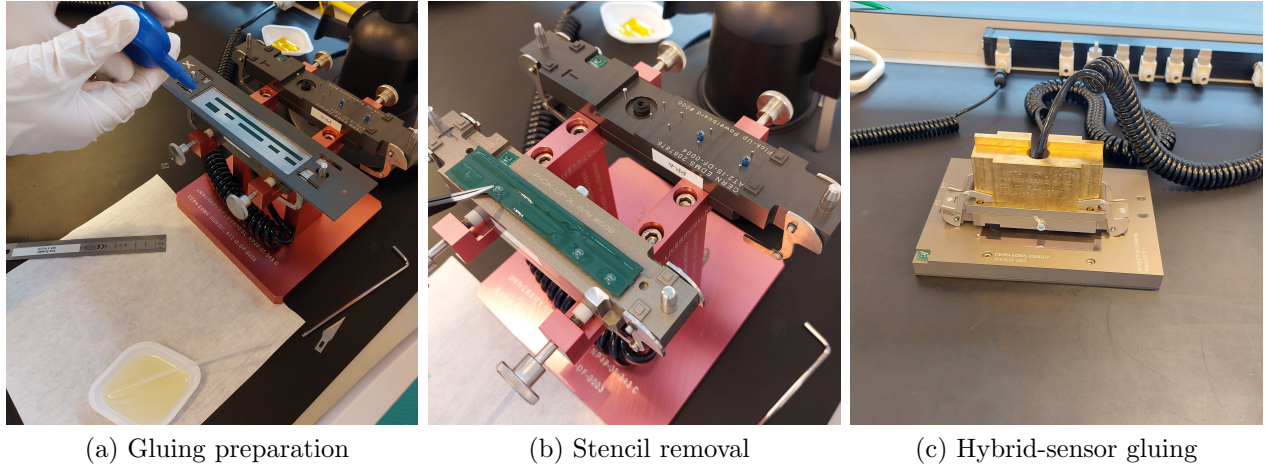


Figure 8.8: The hybrid pick-up tool placed onto the gluing rack and the stencil placed over the back of the hybrid, ready for the glue to be scraped along the back. (b) The back of the hybrid once the stencil is removed, showing the glue pattern, tweezers are used to pop any air bubbles. (c) The hybrid placed over the top of the sensor on the module assembly jig, a weight is applied to ensure close connection.

After allowing time for the glue to cure, the builder places the stencil, as depicted in Figure 8.8(a), onto the back of the hybrid. It is crucial to ensure alignment of the stencil and to remove any dust from the hybrid’s back surface. A 15 cm stainless steel metal ruler is used to scrape glue. The builder holds the scraper at a 45-degree angle after retrieving a modest amount of glue from the sample. By making a scrape to the left of the stencil and then returning to the starting position, the glue is evenly spread along the back of the hybrid. When the stencil is pulled directly upwards, a visible glue pattern remains on the hybrid. Sometimes, the glue pattern may contain bubbles, which can be popped using tweezers, as demonstrated in Figure 8.8(b). After a few seconds, the glue pattern takes its expected shape. The glue boat is set aside to monitor the setting process.

The pick-up tool is detached from the gluing stand and positioned over the prepared sensor. The pins of the pick-up tool are aligned with the holes of the module assembly jig. The back of the hybrid is brought into contact with the sensor, and a weight is applied to ensure optimal contact. The vacuum connections are kept engaged. The glue is left to set for at least 6 hours in the configuration shown in Figure 8.8(c). After the elapsed time, the glue boat is inspected to confirm that the glue has hardened. The vacuum is disconnected from the pick-up tool, which is carefully removed. These steps can be repeated for the Y-hybrid.

The gluing protocol for powerboards, which arrive on a panel from the powerboard population site at Lawrence Berkeley National Laboratory (LBNL), is largely similar, with the main differences being the use of different jigs, tools, stencils, and glue patterns due to the distinct geometry of the powerboard compared to the hybrid. There is also no tab cutting stage for the hybrids.

After the gluing process, the module is weighed to determine the mass of the glue applied to the sensor surface. The glue weight target is 147 ± 20 mg, significant deviation of this may lead to failed QC tests and rejected modules. Following this, several quality checks are conducted, which are elaborated upon in the subsequent section. To finalise the module assembly, the required wire-bond connections are established between the sensor, ASICs, hybrid, and powerboard. This is accomplished using a Hesse Bondjet BJ820 automatic wire-bonder, employing a $25\ \mu\text{m}$ diameter aluminium spool for the bonding wires. Figure 8.9 showcases the wire-bonder along with the sensor to ASIC wire-bonds attached to the ASIC bond pads.



Figure 8.9: (a) The Hesse Bondjet BJ820 wire-bonder situated in the University of Sheffield clean room. (b) Sensor to ASIC wire-bonds shown for the module assembled in this section.

8.4 Quality Assurance of Strip Barrel Modules

To ensure the production of high-quality modules for the ITk, a meticulous system of QC steps and checks is implemented. These checks cover a wide range of activities, starting from thorough inspections of the equipment and components involved. The electrical and thermomechanical performance of the modules is rigorously evaluated, along with the quality of wire-bonds and gluing. Each module must successfully pass multiple tests in order to meet the necessary standards and avoid rejection.

8.4.1 Visual Inspection

A thorough visual inspection of tooling and parts is a crucial aspect of the assembly pipeline, with more detailed inspections required at specific milestone stages. Visual inspection plays a vital role in identifying potential issues that could lead to module failure. Initially, sensors, hybrids, and powerboards undergo inspection after the HV-tab attachment and chip population stages at their respective QC sites. Microscopic inspection is utilised at the module sites to check for any broken bonds or scratches on the sensors. Following the gluing of the hybrid and powerboard, a detailed inspection is carried out to ensure that there is no excess glue seeping onto the sensor from beneath the PCB. It is crucial that the glue does not cover any FE bond pads or the (guard) ring surrounding the sensor, which prevents leakage current into the active region. Additionally, the hybrid must not overhang the sensor edges, and all chips on the PCB must remain intact. Any deviations from the accepted standards are documented in the ITk production database, which will be detailed in the Section 8.5. After wire-bonding, the wire-bonds are inspected for signs of looseness, detachment, or touching bonds. If any issues are found, rework is performed using the bonder, and the details are recorded in the database. Before shipping the finished module to the stave loading site, a final inspection is conducted. A photograph is taken, which serves as a reference for comparison upon inspection at the receiving site.

8.4.2 Pull Testing

Pull testing is a crucial quality control step that evaluates the bond weld quality between surfaces such as ASICs, hybrids, sensors, and powerboards. To conduct these tests, a Dage 4000+ bond tester, located in the University of Sheffield clean room and shown in Figure 8.10 is employed. This bond tester measures the bond breakage strength by applying a pulling force using a small metallic hook. Upon receiving sensors, hybrids, and powerboards, the module sites receive additional test structures that accurately represent the materials used. These test structures are used for monthly pull tests. In the case of hybrids, the test structure is the tab that is cut off during the assembly process. Additionally, bonding test cards, which provide a similar material composition to the bond pads, are used for testing the bonder after calibration or on a monthly basis. To pass a pull test, certain criteria must be met. A minimum mean pull strength of 8 G is required, with each wire having a minimum strength of 5 G. The maximum standard deviation of the pull strengths should also not exceed 1.5 G. Additionally, it is expected that 90% of bond breaks occur via the heel, indicating a strong bond, as the bond foot should not be peeled off during the test.

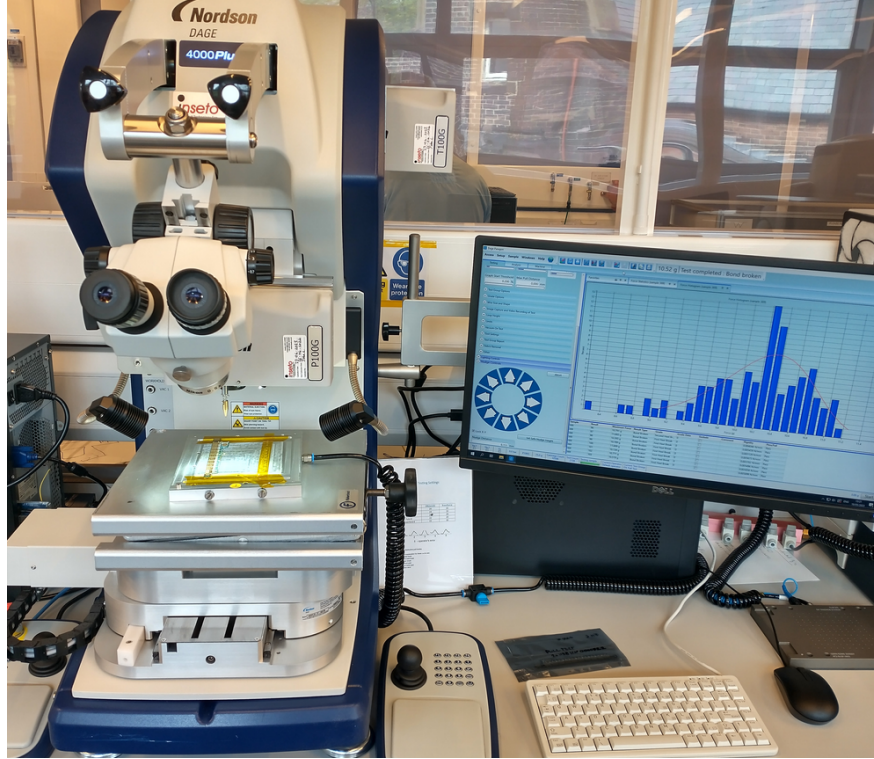


Figure 8.10: The Dage 4000+ bond tester located in the University of Sheffield clean room and used for pull tests.

8.4.3 Metrology

Metrology is the QC procedure which ensures that the hybrids and powerboards are in their correct positions on the sensor, the glue heights are within tolerance and the bow of the module is within specifications. It is a vital part of the QC procedure to ensure that the module will work correctly under the challenging detector conditions. For example, modules with large glue heights will potentially fail during the thermal cycling QC step mentioned in Section 8.4.5. The metrology is performed before wire-bonding because the bare bond pads are used as part of the metrology procedure. The module is placed onto a flat surface such as the module building jig and the metrology is performed using an OGP SmartScope Flash CNC 200 located in the University of Sheffield clean room and shown in Figure 8.11. The SmartScope uses a laser and microscope to automatically locate fiducial marks on the module, yielding three spatial coordinates [269]. It is necessary to define a coordinate system of which the origin is defined to be the top left hand corner of the sensor. The SmartScope data is then fed into the ATLAS metrology analysis software which calculates and plots the required variables.

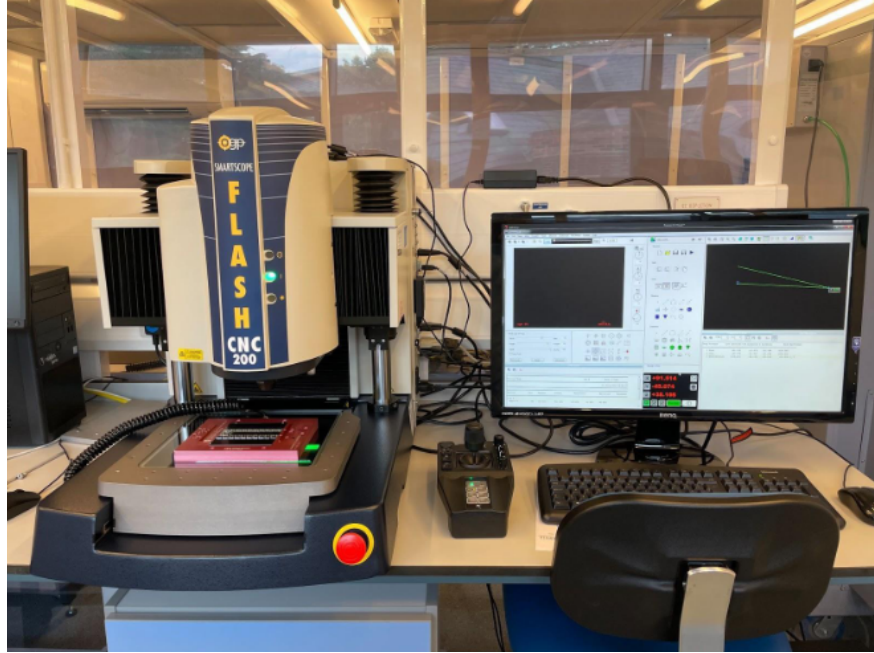


Figure 8.11: The OGP SmartScope Flash CNC 200 device located in the University of Sheffield clean room and used for module metrology.

To assess the positional accuracy of the hybrids and powerboards, fiducial marks are utilised. These marks can be either empty bond pads, intentionally printed symbols on the PCBs or alignment holes. The hybrids feature two crosses etched onto the PCB, while powerboards have two alignment holes. This results in both hybrids and powerboards having two fiducial marks each. The expected positions of each fiducial mark are known from the specifications of the module. The deviation in position is calculated by comparing the specification to the measured values using the defined metrology coordinate system. Figure 8.12 illustrates the positional deviation for each fiducial mark on the hybrids and powerboards of the SS module produced in the previous section. For the naming convention of the fiducials, 'HXP1', for example, represents the X-hybrid's first fiducial mark. The acceptable tolerances for the positional deviation are within 0.25 mm in both the x-direction and y-direction. From the plot, it is evident that the positions of the fiducial marks for this prototype SS module are well within the specified tolerance range for both the x and y-coordinates. This indicates that the hybrids and powerboard are aligned correctly.

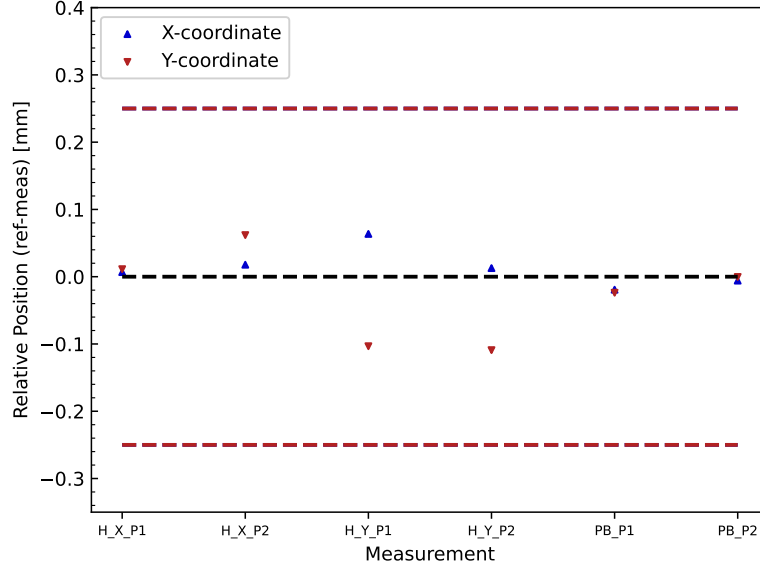


Figure 8.12: The deviation of the hybrid and powerboard fiducials from their expected values for the assembled SS module. The tolerance is 0.25 mm in the x and y-directions.

The metrology analysis software employs the SCIKIT-SPATIAL software [270] to conduct glue height metrology. This software utilises the SmartScope measurements to establish a sensor plane, where the plane is defined as the z -origin. To accurately define the plane, a minimum of four measurements is necessary. In order to capture more data points along the hybrid and powerboard, an increased number of fiducials are identified for this measurement process. For the hybrids, multiple exposed copper pads between each ASIC, as well as various points around the HCC chip and the bond pads connecting the hybrid and powerboard are used. Several measurements are taken around each fiducial, and their values are averaged. This results in a total of 14 measurements per hybrid: 10 ASIC measurements, 1 HCC measurement, and 3 bond pad measurements. Similarly, the powerboard follows a comparable approach by utilising additional bond pads located around the edge of the PCB, resulting in five measurements. To obtain accurate glue height measurements, the software subtracts the z -plane and the known thickness of the hybrids and powerboard from the fiducial measurements. For this prototype period, the X-hybrid had a thickness of $380\text{ }\mu\text{m}$, the Y-hybrid had a thickness of $360\text{ }\mu\text{m}$, and the powerboard had a thickness of $390\text{ }\mu\text{m}$.

Figure 8.13 illustrates the glue thicknesses for the X-hybrid, Y-hybrid, and powerboard, along with the agreed tolerance limits. The target glue height is $120^{+50}_{-80}\text{ }\mu\text{m}$, represented by the red upper and lower tolerance bounds. Additionally, a blue line indicates a target lower bound of $70\text{ }\mu\text{m}$. When determining the pass or fail decision, mean glue height values falling between the blue line and the bottom red line result in a ‘pass with problems’ verdict. The tolerance limits apply only to the fiducials around the ASICs and powerboard, excluding PB.5. The non-planar shapes of the hybrid can cause thinner glue heights for the HCC and bond pad

fiducials. The PB_5 fiducial is excluded from this consideration since it utilises a single measurement point in the height calculation. The green lines represent an alternative average calculation for the edge ASICs, where the measurement points closest to the hybrid's edge are not included. The alternative calculation has a significant impact on the central value for ABC_X_0, resulting in it falling out of tolerance. However, the alternative heights are not considered for the pass or fail verdict, unless a metrology failure is specifically attributed to these ASICs. The uncertainty bars in the plot indicate the maximum and minimum values used in the average calculation. Taking into account the caveats mentioned above regarding the pass or fail verdict, all the necessary points fall within the strict tolerances. However, the ABC_X_0 and PB_4 fiducials fall outside the target. Therefore, this module under the current guidance is categorised as 'pass with problems' indicating the module is suitable for use. Finally, the total package height, measured as the height of the powerboard shield box, is evaluated. The specifications allow for a height of up to 5.71 mm, and in this case, the measured height was found to be within the specification at 5.50 mm.

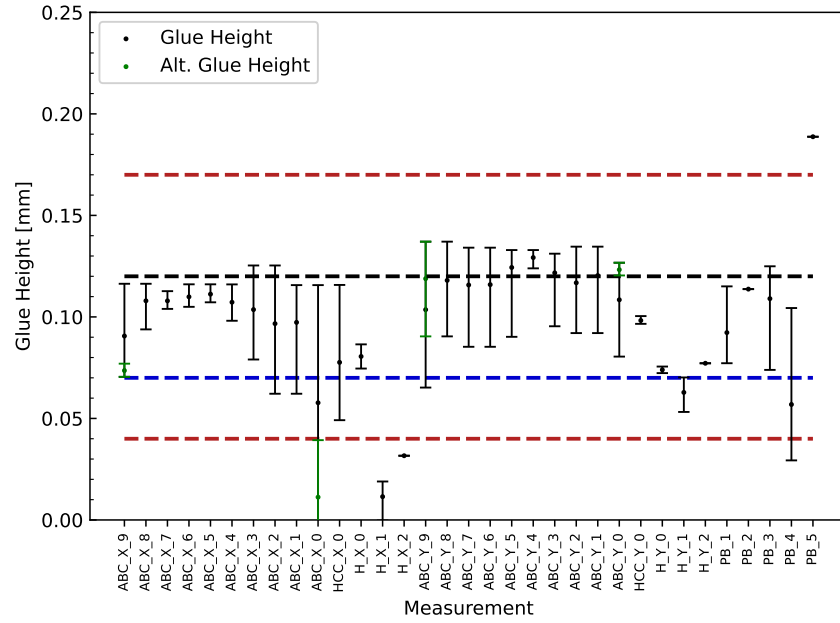


Figure 8.13: The glue heights for the X-hybrid, Y-hybrid and powerboard fiducials on the SS module. The target value for the glue height is $120\ \mu\text{m}$. The red lines indicate the hard tolerance cut-offs of $170\ \mu\text{m}$ and $40\ \mu\text{m}$ with a lower target of $70\ \mu\text{m}$. The alternative average height is performed for ASICs near the edge of the hybrid, where the points nearest to the edge are not considered. The uncertainty bars consider the maximum and minimum of the values used in the calculation of the average. Only the datapoints around the ASICs (ASIC_X) and powerboards (PB_X, excluding PB_5) are considered for the pass or fail decision. Therefore, this module is categorised at "pass with problems".

The module bow measurement is the final step in the metrology process. It involves using the two-dimensional sensor plane. By comparing the sensor height data with the plane,

deviations are determined, which provide insights into the module's bow. The resulting module bow measurement is depicted in Figure 8.14. The bow can be either concave or convex, and its value is determined by the distance between the lowest and highest points. Typically, one height amplitude will be near the centre of the module, while another will be closer to the edges. Consequently, the bow can have a negative sign if the centre is higher than the edges. In the case of Figure 8.14, the measured bow is approximately $+46 \mu\text{m}$, which falls within the specified tolerance range of $-50 \mu\text{m}$ to $+150 \mu\text{m}$. This means that the module's bow meets the required standards and demonstrates acceptable levels of curvature.

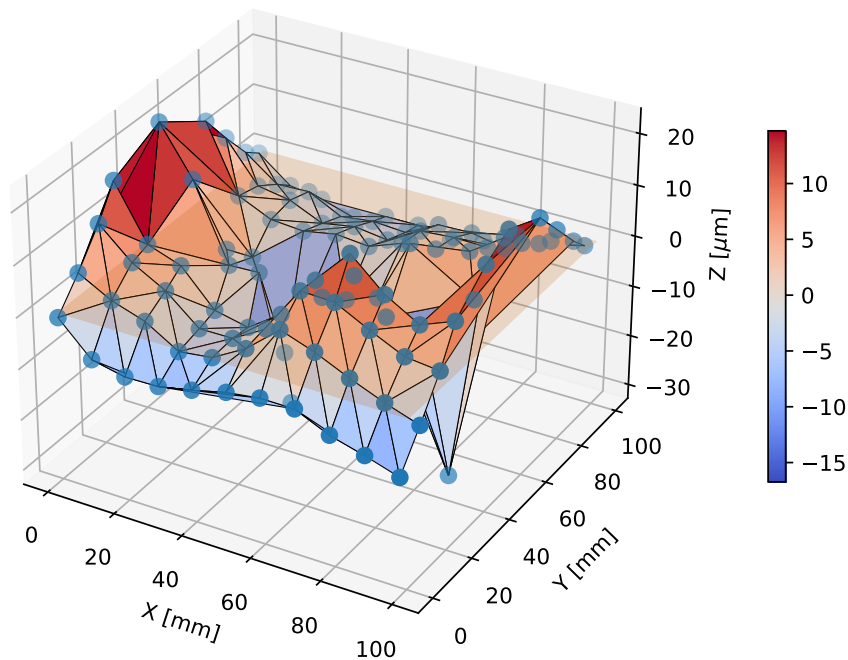


Figure 8.14: The sensor bow metrology measurement for the assembled SS module. The specified tolerance range for module bow is $-50 \mu\text{m}$ to $+150 \mu\text{m}$.

8.4.4 Electrical Testing

To ensure that the modules will work correctly within the detector, a series of electrical tests are performed at different stages of the module assembly process. These tests are categorised into two types, each requiring distinct electrical setup configurations: panel testing and module testing. Panel testing is conducted when hybrids and powerboards attached to their panels are received. This enables the electrical testing of individual hybrids and powerboards on the panel to verify their functionality before they are affixed to the sensor. Module testing, on the other hand, involves two different scenarios: HV-tabbed sensor and completed module testing.

For completed module and hybrid panel testing, a comprehensive series of individual tests are carried out using the ITSDAQ software, collectively they are referred to as a ‘FullTest’. The FullTest sequence is listed below [253], the setup used to complete these tests for each case will be discussed in the following sections.

- Strobe delay: Measures the delay in the read-out of the FE chip after a calibration pulse is applied. This allows for the necessary adjustments to ensure the synchronisation of signals through the circuit.
- Trim range / Pedestal trim: Used as a means to trim each channel’s response such as to remove excess variation. After trimming, the response of each channel should be roughly uniform with some masked channels if they were behaving spuriously.
- Three-point gain: Three different charges (0.5 fC, 1.0 fC and 1.5 fC) are injected into the FE chips and the response of each channel is observed for each charge. Analysis of the output yields input noise and gain values for that input charge and channel.
- Response curve: Similar to the three-point gain test but extended over ten charges ranging from 0.5 fC to 8.0 fC. This test happens after each channel has been trimmed. A more accurate account of the input noise and gain values are yielded from analysis of these data.
- Noise Occupancy: A measurement of the noise signals in each channel above a threshold level or as a function of the threshold level.

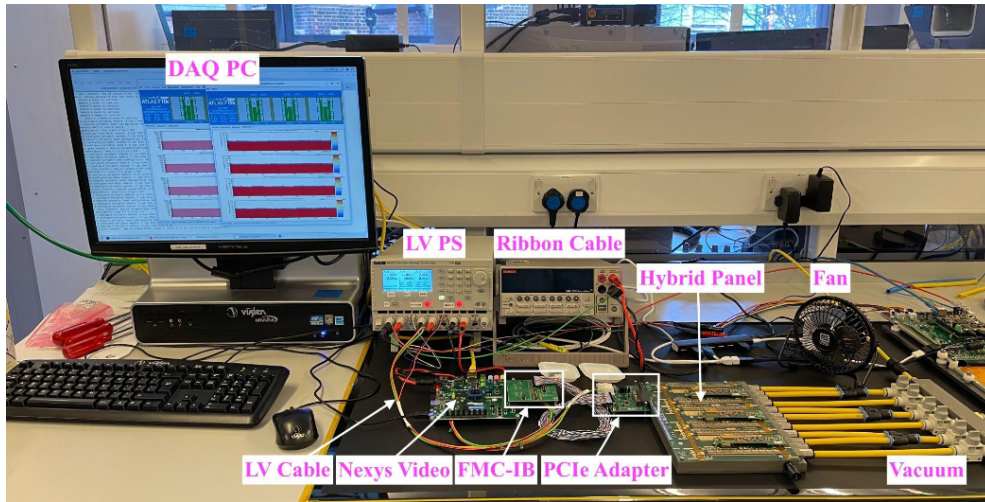
In addition to the tests listed above, an IV scan is generally conducted for module testing. This is when the current across the sensor is measured as the sensor bias is increased. The main objective of the test is to check for the presence of electrical breakdown from micro-discharges. Any breakdown by the HV-tabbed sensor should be compared with the IV curve done by the sensor QC sites. The IV scans for glued modules are performed for sensor biases up to 700 V with current compliance 2 A, bonded module IVs are performed up to 550 V with compliance $20\ \mu\text{A} + 1\ \mu\text{A per } 10\ \text{V}$, rising to $75\ \mu\text{A}$ at 550 V. The results are often split up into stream 0 and stream 1 results, where stream 0 refers to the half of the ASIC channels closest to the chip edge and stream 1 means the channels furthest from the chip edge.

For HV-tabbed sensor testing, the sensor is firstly received in the transport frame, the bonds between the sensor and the frame enable a preliminary IV curve to be established up to $-700\ \text{V}$. This step is crucial in confirming that the sensor is fully operational before proceeding further.

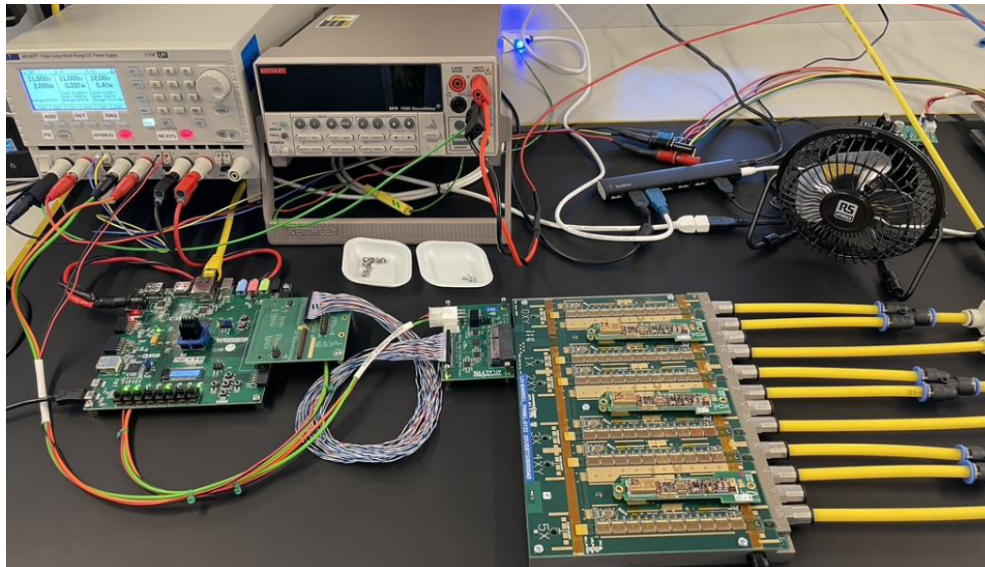
Hybrid Panel DAQ Testing

The setup used for hybrid panel testing is depicted in Figure 8.15, the received hybrid panel is shipped with attached powerboards necessary for the read-out. In the case of these prototypes, the powerboards were provided separately. The panel is securely fastened to the hybrid testing jig and the vacuum system is activated, while the jig itself is grounded through the grounding plug. The vacuum establishes a cooling contact between the panel and the jig,

and a fan is incorporated to assist with the cooling. To establish communication between the panel and the ItSDAQ software installed on the PC, a PCIe adapter is utilised, which is powered by a TTI MX180TP low voltage (LV) power supply delivering 11 V and a current compliance of 2.5 A. Data transfer is facilitated by a 50-way ribbon cable connecting the PCIe adapter to a FPGA Mezzanine Connector-Interface Board (FMC-IB). The FMC-IB adaptor is directly connected to the DAQ system, specifically the Digilent 410-316 Nexys Video Artix-7 FPGA board powered with 12 V and a current compliance of 1 A using the LV supply. The Nexys is connected to the PC via an ethernet cable. The FullTest is performed by ItSDAQ along with a series of smaller tests conducted to ensure successful communication with the chips integrated on the hybrid.



(a)

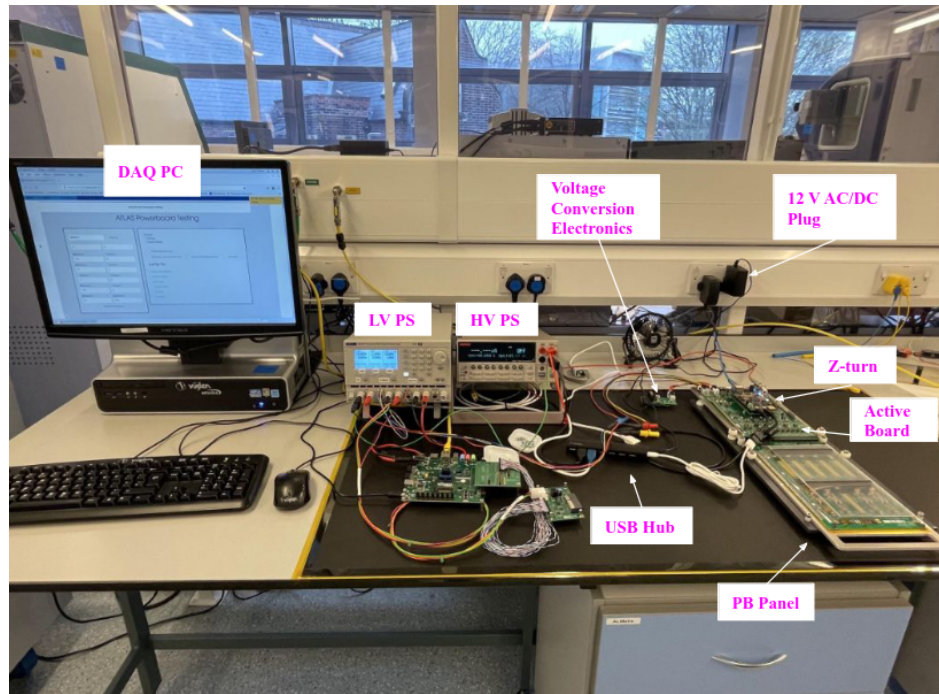


(b)

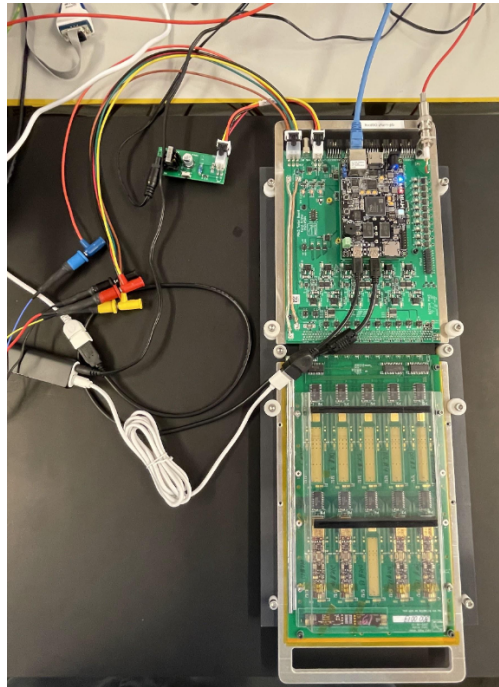
Figure 8.15: (a) The hybrid panel testing setup. (b) A zoomed in look at the hybrid panel testing setup, focusing on the hybrid panel and DAQ system.

Powerboard Panel DAQ Testing

The setup for powerboard electrical testing is depicted in Figure 8.16. Unlike hybrid panel testing, powerboard testing utilises an ATLAS developed DAQ system specifically designed for powerboards, rather than relying on commercially available FPGA based solutions like the Nexys. The powerboard testing system comprises several components. A sliding mechanism facilitates the connection of the powerboard panel. An active board (green PCB) enables the supply of HV and LV to the Z-turn circuit board, which serves as the control unit for LV and HV power supplies and facilitates read-out to the PC. The HV and LV control is achieved through a USB hub connected to the Z-turn. An additional USB port on the Z-turn is used for PC output, while an ethernet cable establishes network connectivity for the Z-turn. Power for the active board is provided by a 12 V AC/DC plug connected to the lab wall sockets. A custom electronics component is utilised between the wall plug and the active board to enable a 12 V to +5 V/−3 V conversion. The HV and LV power supplies are connected to the active board, with the HV and LV ground ports (black) interlinked. An ATLAS-based GUI facilitates communication with each power board.



(a)



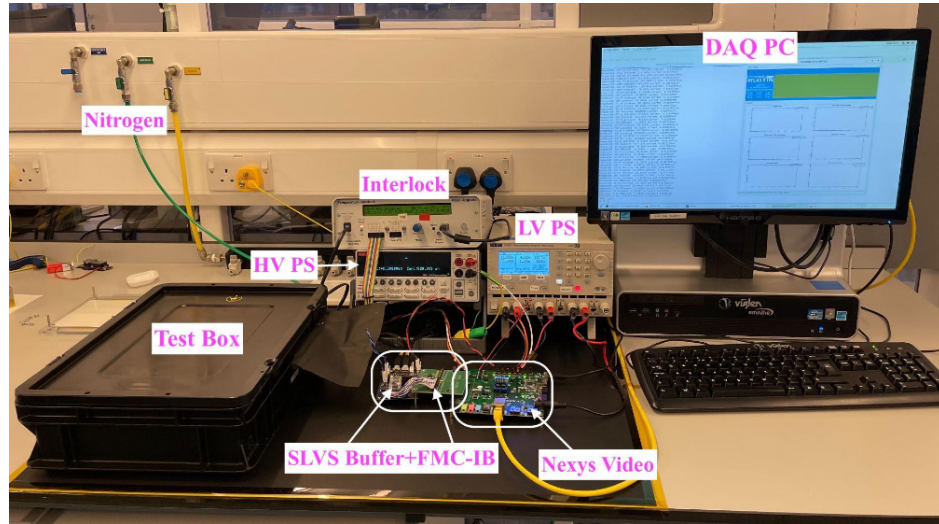
(b)

Figure 8.16: (a) The powerboard panel testing setup. (b) A zoomed in photograph of the Z-turn, active board, powerboard panel and the custom circuitry used to convert the voltage from the mains adapter.

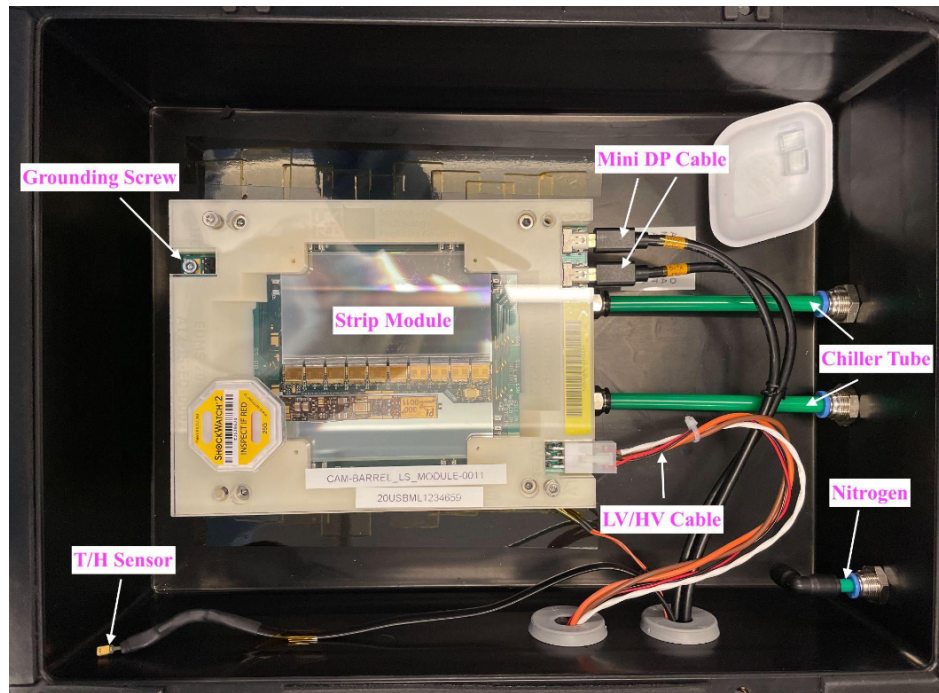
At a module building site, when testing a powerboard panel upon its reception, only a basic functionality test is necessary. This test focuses on verifying the output of different powerboard chips, ensuring successful communication with the AMACV2a, and checking the powerboard's control of the HV and LV power supplies. The functionality test is designed to be straightforward, requiring little input from the tester other than simply pressing the relevant button on the GUI. It provides a pass or fail verdict based on the test results.

Completed Module and Sensor DAQ Testing

Figure 8.17 illustrates the setup for conducting electrical testing on the completed module and HV tabbed sensor. A HV and LV power source is connected to the module to bias the sensor and power the module, respectively. A separate TTI MX180TP power supply is utilised to provide the LV supply, which delivers 11 V with a current compliance of 1 A. For the HV supply, a Keithley 2410 power supply is employed. The modules Mini Display Port (DP) cables are connected to a Scalable Low Voltage Signalling (SLVS) buffer board, which is further linked to a FMC-IB adapter through ribbon cables. The FMC-IB board is then connected to a Nexys FPGA board. The SLVS buffer board and Nexys board receive voltages of 4 V and 12 V from the LV supply, respectively, with current compliances of 0.5 A and 1 A. An ethernet cable establishes a connection between the Nexys board and a PC equipped with the ITSDAQ software.



(a)



(b)

Figure 8.17: (a) The completed module and sensor reception electrical testing setup. (b) The arrangement of the module in the test box.

The module is securely housed within an ESD safe box, designed to maintain an air and light tight environment. The module is mounted onto a dedicated module testing jig that offers provisions for cooling and grounding. Cooling is achieved through chiller tubes connected to the module testing jig. These tubes circulate deionised water, maintained at a controlled temperature of 21 ± 2 °C, sourced from a custom-built chiller system. In addition to cooling, the testing jig also features a dry nitrogen input pipe, regulating the humidity level below 10% to prevent electrical breakdown. To monitor the operating conditions, the temperature and humidity of the air in the dark box is monitored using a sensor. The temperature of the jig is also monitored using an attached thermocouple in tandem with the interlock box.

The testing procedure begins by verifying communication with the AMACV2a and an IV scan is performed up to -550 V to check for early sensor breakdown. The HV supply is then used to bias the sensor to its depletion voltage, which is set to -350 V. The FullTest procedure is then enacted. After conducting the tests, the ITSDAQ software generates a comprehensive report comprising various diagnostic plots related to the read-out. Additionally, a JSON file is produced, summarising the key results and providing a pass or fail verdict for the module. To assess the test outcomes, the ITSDAQ software utilises predefined tolerances. These tolerances are periodically modified as the collaboration advances towards full scale production. The adjustments are made to accommodate the evolving expected yield. Consequently, the validity of tested parts may vary over time, reflecting the dynamic nature of the production process.

The figures below present a selection of the most noteworthy plots obtained from the FullTest of the constructed SS module. Figure 8.18 illustrates the stream 1 strobe delay from the X-hybrid, which exhibits minimal variation, with each chip’s strobe delay aligning closely to the expected value of around $20 \mu\text{s}$. In Figure 8.19, the noise occupancy per channel and its dependence on the threshold are depicted for the X-hybrid. Figure 8.20 represents the X-hybrid gain and input noise per channel from an input charge of 1 fC. Figures 8.19 and 8.20 reveal that the rightmost ASIC chip exhibits some noise, as there are points significantly above the expectation of around 800 ENC (Equivalent Noise Charge). The noise coincides with marks on the sensor surface spotted during the VI, these are caused by the suction cups used for fixation during transportation. These marks are common occurrences for modules and their treatment is under investigation. Additionally, Figure 8.21 displays the resulting IV curve following module wire-bonding. Notably, the IV curve demonstrates continuity without any breakdown, indicating a satisfactory IV test.

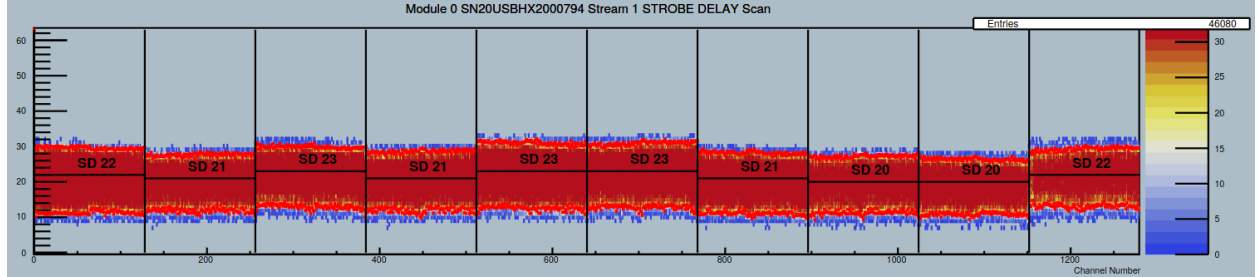


Figure 8.18: The results for the strobe delay test from the ITSDAQ software. The plot is shown for stream 1 of the X-hybrid for the SS module assembled in the previous section.

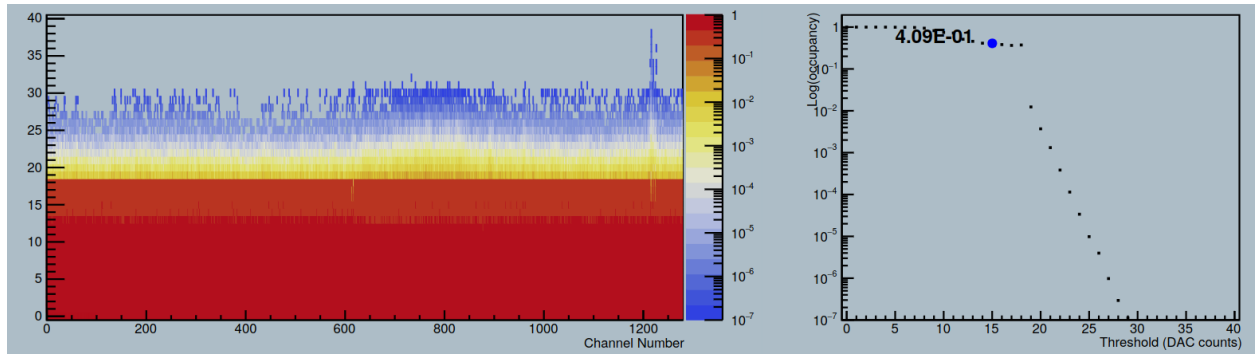
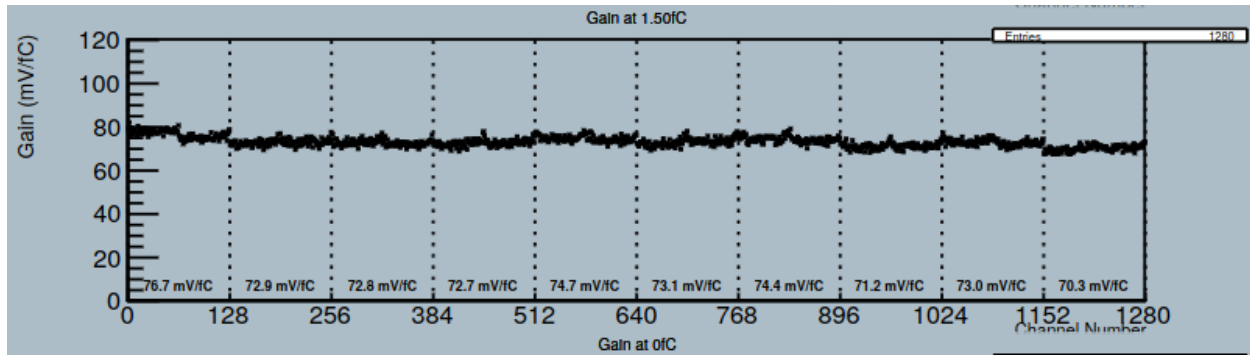
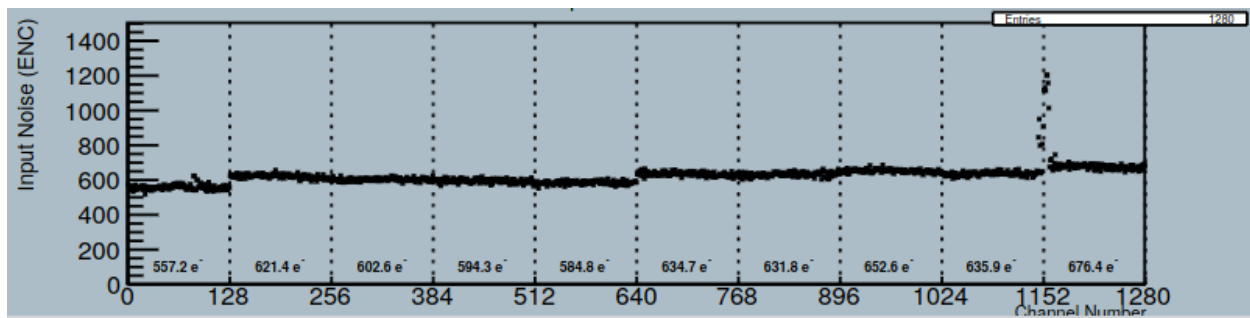


Figure 8.19: The results of the noise occupancy test for stream 1 of the X-hybrid situated on the SS module assembled in the previous section. The left plot shows the resulting threshold scan with respect to every channel showing how the noise occupancy changes as the threshold is varied, the right plot shows the occupancy as the threshold increases.



(a)



(b)

Figure 8.20: The results of the response curve tests for the stream 1 X-hybrid on the SS module assembled in the previous section. (a) The gain per channel shows a roughly uniform value across all channels. (b) The input noise per channel measured in Equivalent Noise Charge (ENC), which is the charge (number of electrons) at the input which would create the same output level as obtained from the noise.

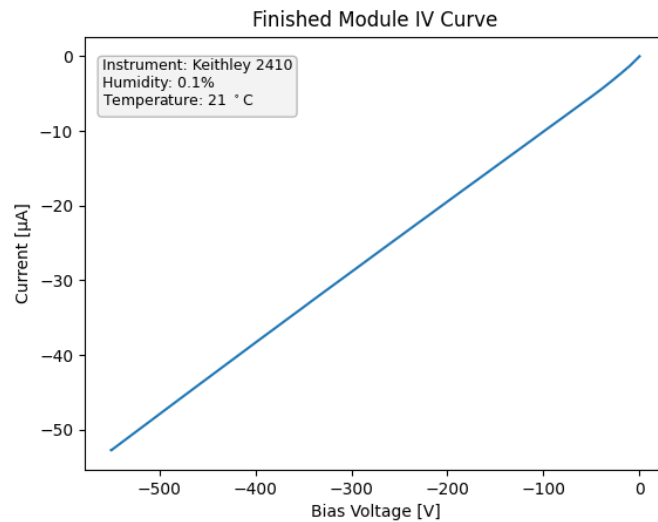


Figure 8.21: The current across the sensor as the sensor bias is ramped up to the maximum of -550 V for a wire-bonded module. The test looks for possible discontinuities which indicate electrical breakdown.

8.4.5 Thermal Cycling

To assess the thermomechanical properties of the completed modules, a thermal cycling QC step is performed. The setup for this thermal cycling process is shown in Figure 8.22, showcasing a cold jig provided by Warwick. The cold jig serves as a self-contained setup with five testing chucks and a cooling system. A Grant TXF200-R5 chiller is employed to circulate a 12 L coolant solution consisting of a 50% ethylene-glycol and water mixture, through a piping circuit. The chiller's output pipe is divided into five smaller pipes, each connected to an individual module testing jig. The pipes from each jig are then combined to form a single pipe returning to the chiller. Underneath each jig, a Peltier thermoelectric heat pump is positioned and powered by a dedicated power supply. The system is equipped with relays that facilitate current direction reversal, enabling both heating and cooling processes. Additionally, a supply of dry nitrogen is introduced into the system during operation to maintain a relative humidity below 10%. A DAQ system similar to the one used for module testing is used such that a FullTest can be performed like in the case of completed module tests.



Figure 8.22: A photograph of the cold jig setup showing the five jigs and piping used for module thermal cycling. One completed module is placed in the centre jig ready for thermal cycling.

The thermal cycling process involves subjecting the input modules to ten cycles, ranging from $-35\text{ }^{\circ}\text{C}$ to $+40\text{ }^{\circ}\text{C}$, within the cold jig. To ensure the module's safety, each cycle is conducted over a minimum duration of 30 minutes. At the temperature extremes of each cycle, an ITSDAQ FullTest is performed. Following the completion of the thermal cycling, the module is gradually warmed up to $+20\text{ }^{\circ}\text{C}$, where a two-hour HV stability test is conducted. Subsequently, the module is further warmed up to $+22\text{ }^{\circ}\text{C}$, and the results are assessed for any failures flagged by the ITSDAQ software, employing the same evaluation criteria as for single module testing.

8.5 The ITk Production Database

To ensure accurate tracking of parts within the large-scale ITk project, an ITk production database (ITkPD) is being developed. The ITkPD serves as a comprehensive repository for logging all actions related to part shipment, assembly, and testing. It enables detailed tracking of a module's specific state, stage history, current location, test history, and other relevant descriptors.

In the context of module building, when the sensor reception site produces HV-tabbed sensors from an ITkPD registered batch of bare sensors, the modified sensors act as the first stage of a module in the ITkPD. Therefore, the sensor site is responsible for registering 'HV-tab attached' modules using sensors in the 'Ready for module' stage and shipping them to Sheffield using the ITkPD. Upon delivery, the Sheffield based module builder accepts the shipment, assuming ownership and responsibility for the module. The module's stage on the ITkPD is updated accordingly by the modules institute as the assembly chain progresses. This involves tagging it with the correct ITkPD registered hybrid, powerboard, tooling, glue, and other relevant components. Test results are also uploaded to the database using the output JSON files from ITSDAQ. Once a module reaches the 'Finished module' stage, it is shipped to the stave loading site.

Notably, the ITkPD incorporates prerequisites for many actions. For instance, a module cannot progress to the next stage unless all relevant tests for the current stage have been completed. Furthermore, the module must be properly assembled and in the correct location. Consequently, if another institute attempts to upload a test for a module that has not been properly registered or shipped in the ITkPD, the test will not be accepted. This feature encourages adherence to the correct usage of the ITkPD, ensuring the integrity and accuracy of the database.

The ITkPD offers an Application Programming Interface (API) as another noteworthy feature. This API allows users to retrieve analytical data related to module properties such as components, tests, and institutes. By utilising the API, conclusions can be drawn based on useful metrics such as the number of failed modules per institute or the institute with the highest frequency of metrology QC failures. The author actively participated in implementing analytic reports utilising the ITkPD API. Additionally, the author developed scripts that interface with the ITkPD API, enabling the command-line upload of ITSDAQ tests. This work was undertaken as part of the author's qualification for ATLAS authorship, a year-long project that all ATLAS affiliates must complete to qualify for paper authorship.

Chapter 9

Summary

The techniques employed in the 2020 Minimal Supersymmetric Standard Model $H/A/h \rightarrow \tau\tau$ (legacy) [8] ATLAS analysis were used consistently in this thesis to search for Beyond-the-Standard-Model particle decays to tau leptons with also the possible addition of b -quarks. Chapters 2, 3 and 4 detail the theoretical motivation supporting the legacy analysis, the ATLAS detector infrastructure and the legacy analysis techniques, respectively. Searches were made for heavy Z' bosons and third-generation leptoquarks. Exploratory research was also conducted with a view towards improving the search for heavy MSSM Higgs bosons. No statistically significant deviation from the Standard Model prediction was found for any of the searches. Therefore, 95% CL upper limits on the cross section \times branching ratio were derived for each theoretical model considered, setting tighter constraints on the available model parameters compared to what they were previously.

For the heavy Z' boson search, a direct re-interpretation of the legacy analysis was undertaken in Chapter 5 to search for the $Z' \rightarrow \tau\tau$ process within the Sequential Standard Model. Using the derived 95% CL $\sigma \times \mathcal{B}$ limits and the predicted Z' cross section, masses below 3.06 TeV are excluded for this model. This is an improved lower limit compared to the previously reported 2.42 TeV gathered from data corresponding to an integrated luminosity of 36 fb^{-1} [58]. The results are to be used in the upcoming ATLAS search for V' bosons within the Heavy Vector Triplet model [62] using a combination of ATLAS analyses with varying final states. The $Z' \rightarrow \tau\tau$ results contribute to the exclusion of the $\{g_{q3}, g_{\ell3}\}$, $\{g_q, g_\ell\}$ and $\{g_H, g_f\}$ HVT coupling parameter planes, the preliminary results are shown in Section 5.5.2.

The search for third-generation leptoquarks takes place in Chapter 6 with a search in the $b\tau\tau$ final state using a modified version of the techniques from the legacy result. Both scalar and vector leptoquarks are considered. The leptoquark analysis is complicated by interference effects from Standard Model backgrounds which can be neglected by selecting a high $p_T^{b\text{-jet}}$ signal region to derive the 96% CL upper limits. When considering the case where leptoquarks can be singly produced and also produced in pairs, the lower observed (expected) limit on the scalar leptoquark mass under the \tilde{S}_1 model is 1.28 (1.37) TeV for a Yukawa coupling of $\lambda = 1.0$. For the vector case, under the U_1 model, the limit is 1.58 (1.64) TeV for the Yang-Mills coupling scenario and 1.35 (1.44) TeV for the minimal coupling scenario,

using a Yukawa coupling of $\lambda = 1.0$. For consistency with similar leptoquark analyses which don't consider the interference, a model-independent interpretation is considered and a 95% CL upper limit on the visible cross section is derived which varies from 0.17 fb to 4.8×10^{-2} fb.

To improve the search for MSSM Higgs bosons, a number of analysis optimisation studies were conducted and a mass-parameterised neural network was developed and implemented, this is discussed in Chapter 7. Up to 4.2 (2.6) times improvement to the sensitivity is observed when implementing these improvements for the bbH (ggH) limit when considering the $\tau_{\text{lep}}\tau_{\text{had}}$ and $\tau_{\text{had}}\tau_{\text{had}}$ decay modes combined. The $\{m_A, \tan\beta\}$ exclusion plane is also considered for two popular MSSM benchmark scenarios: hMSSM and M_h^{125} . The analysis with the optimisations is shown to be up to 3.1 (2.9) times more sensitive than the legacy result for the hMSSM (M_h^{125}) benchmark scenario. The majority of the improvement was found to be at lower signal masses, at higher signal masses the $\sigma \times \mathcal{B}$ sensitivity tends towards the same values as the legacy analysis.

Finally, the construction of strip barrel modules for the ATLAS Inner Tracker upgrade is discussed in Chapter 8. The reader is guided through the recipe used to build and quality test an actual prototype module built by the author for a system test. As the prototyping phase comes to a close, this recipe will be used to mass produce modules for the detector.

Bibliography

- [1] BaBar Collaboration. “Evidence for an excess of $\bar{B} \rightarrow D^{(*)}\tau^{-}\bar{\nu}_{\tau}$ decays”. In: *Phys. Rev. Lett.* 109 (2012), p. 101802. DOI: [10.1103/PhysRevLett.109.101802](#). arXiv: [1205.5442 \[hep-ex\]](#).
- [2] BaBar Collaboration. “Measurement of an Excess of $\bar{B} \rightarrow D^{(*)}\tau^{-}\bar{\nu}_{\tau}$ Decays and Implications for Charged Higgs Bosons”. In: *Phys. Rev. D* 88.7 (2013), p. 072012. DOI: [10.1103/PhysRevD.88.072012](#). arXiv: [1303.0571 \[hep-ex\]](#).
- [3] Belle Collaboration. “Measurement of the branching ratio of $\bar{B} \rightarrow D^{(*)}\tau^{-}\bar{\nu}_{\tau}$ relative to $\bar{B} \rightarrow D^{(*)}\ell^{-}\bar{\nu}_{\ell}$ decays with hadronic tagging at Belle”. In: *Phys. Rev. D* 92.7 (2015), p. 072014. DOI: [10.1103/PhysRevD.92.072014](#). arXiv: [1507.03233 \[hep-ex\]](#).
- [4] LHCb Collaboration. “Measurement of the ratio of branching fractions $\mathcal{B}(\bar{B}^0 \rightarrow D^{*+}\tau^{-}\bar{\nu}_{\tau}) / \mathcal{B}(\bar{B}^0 \rightarrow D^{*+}\mu^{-}\bar{\nu}_{\mu})$ ”. In: *Phys. Rev. Lett.* 115.11 (2015), p. 111803. DOI: [10.1103/PhysRevLett.115.111803](#). arXiv: [1506.08614 \[hep-ex\]](#).
- [5] LHCb Collaboration. “Measurement of the ratios of branching fractions $\mathcal{R}(D^{*})$ and $\mathcal{R}(D^0)$ ”. In: *Submitted to Phys. Rev. Lett.* (2023). arXiv: [2302.02886 \[hep-ex\]](#). Pre-published.
- [6] Muon $g - 2$ Collaboration. “Final Report of the Muon E821 Anomalous Magnetic Moment Measurement at BNL”. In: *Phys. Rev. D* 73 (2006), p. 072003. DOI: [10.1103/PhysRevD.73.072003](#). arXiv: [hep-ex/0602035](#).
- [7] Muon $g - 2$ Collaboration. “Measurement of the Positive Muon Anomalous Magnetic Moment to 0.46 ppm”. In: *Phys. Rev. Lett.* 126.14 (2021), p. 141801. DOI: [10.1103/PhysRevLett.126.141801](#). arXiv: [2104.03281 \[hep-ex\]](#).
- [8] ATLAS Collaboration. “Search for heavy Higgs bosons decaying into two tau leptons with the ATLAS detector using pp collisions at $\sqrt{s} = 13$ TeV”. In: *Phys. Rev. Lett.* 125.5 (2020), p. 051801. DOI: [10.1103/PhysRevLett.125.051801](#). arXiv: [2002.12223 \[hep-ex\]](#).
- [9] P. Higgs. “Broken Symmetries and the Masses of Gauge Bosons”. In: *Phys. Rev. Lett.* 13 (1964), pp. 508–509. DOI: [10.1103/PhysRevLett.13.508](#).
- [10] ATLAS Collaboration. “Observation of a new particle in the search for the Standard Model Higgs boson with the ATLAS detector at the LHC”. In: *Phys. Lett. B* 716 (2012), pp. 1–29. DOI: [10.1016/j.physletb.2012.08.020](#). arXiv: [1207.7214 \[hep-ex\]](#).

- [11] CMS Collaboration. “Observation of a New Boson at a Mass of 125 GeV with the CMS Experiment at the LHC”. In: *Phys. Lett. B* 716 (2012), pp. 30–61. DOI: [10.1016/j.physletb.2012.08.021](https://doi.org/10.1016/j.physletb.2012.08.021). arXiv: [1207.7235](https://arxiv.org/abs/1207.7235) [hep-ex].
- [12] Quanta Magazine. *A New Map of All the Particles and Forces*. 2020. URL: <https://www.quantamagazine.org/a-new-map-of-the-standard-model-of-particle-physics-20201022/>.
- [13] M. Thomson. *Modern particle physics*. New York: Cambridge University Press, 2013. ISBN: 978-1-107-03426-6. DOI: [10.1017/CB09781139525367](https://doi.org/10.1017/CB09781139525367).
- [14] C. S. Wu et al. “Experimental Test of Parity Conservation in β Decay”. In: *Phys. Rev.* 105 (1957), pp. 1413–1414. DOI: [10.1103/PhysRev.105.1413](https://doi.org/10.1103/PhysRev.105.1413).
- [15] J. H. Christenson et al. “Evidence for the 2π Decay of the K_2^0 Meson”. In: *Phys. Rev. Lett.* 13 (1964), pp. 138–140. DOI: [10.1103/PhysRevLett.13.138](https://doi.org/10.1103/PhysRevLett.13.138).
- [16] D. J. Gross and F. Wilczek. “Ultraviolet Behavior of Non-Abelian Gauge Theories”. In: *Phys. Rev. Lett.* 30 (26 1973), pp. 1343–1346. DOI: [10.1103/PhysRevLett.30.1343](https://doi.org/10.1103/PhysRevLett.30.1343).
- [17] H. D. Politzer. “Reliable Perturbative Results for Strong Interactions?” In: *Phys. Rev. Lett.* 30 (26 1973), pp. 1346–1349. DOI: [10.1103/PhysRevLett.30.1346](https://doi.org/10.1103/PhysRevLett.30.1346).
- [18] S. L. Glashow. “Partial-symmetries of weak interactions”. In: *Nuclear Physics* 22.4 (1961), pp. 579–588. DOI: [https://doi.org/10.1016/0029-5582\(61\)90469-2](https://doi.org/10.1016/0029-5582(61)90469-2).
- [19] S. Weinberg. “A Model of Leptons”. In: *Phys. Rev. Lett.* 19 (1967), pp. 1264–1266. DOI: [10.1103/PhysRevLett.19.1264](https://doi.org/10.1103/PhysRevLett.19.1264).
- [20] A. Salam. “Weak and Electromagnetic Interactions”. In: *Conf. Proc. C* 680519 (1968), pp. 367–377. DOI: [10.1142/9789812795915_0034](https://doi.org/10.1142/9789812795915_0034).
- [21] M. K. Gaillard, P. D. Grannis, and F. J. Sciulli. “The Standard Model of particle physics”. In: *Rev. Mod. Phys.* 71 (1999), S96–S111. DOI: [10.1103/RevModPhys.71.S96](https://doi.org/10.1103/RevModPhys.71.S96). arXiv: [hep-ph/9812285](https://arxiv.org/abs/hep-ph/9812285).
- [22] I. J. R. Aitchison and A. J. G. Hey. *Gauge Theories in Particle Physics: A Practical Introduction, Volume 1 : From Relativistic Quantum Mechanics to QED, Fourth Edition*. Taylor & Francis, 2013. ISBN: 978-1-4665-1302-0. DOI: [10.1201/b13717](https://doi.org/10.1201/b13717).
- [23] S. Tomonaga. “On a Relativistically Invariant Formulation of the Quantum Theory of Wave Fields”. In: *Progress of Theoretical Physics* 1.2 (1946), pp. 27–42. DOI: [10.1143/PTP.1.27](https://doi.org/10.1143/PTP.1.27).
- [24] R. P. Feynman. “Space-Time Approach to Quantum Electrodynamics”. In: *Phys. Rev.* 76 (6 1949), pp. 769–789. DOI: [10.1103/PhysRev.76.769](https://doi.org/10.1103/PhysRev.76.769).
- [25] R. P. Feynman. “The Theory of Positrons”. In: *Phys. Rev.* 76 (6 1949), pp. 749–759. DOI: [10.1103/PhysRev.76.749](https://doi.org/10.1103/PhysRev.76.749).
- [26] R. P. Feynman. “Mathematical Formulation of the Quantum Theory of Electromagnetic Interaction”. In: *Phys. Rev.* 80 (3 1950), pp. 440–457. DOI: [10.1103/PhysRev.80.440](https://doi.org/10.1103/PhysRev.80.440).

- [27] J. Schwinger. “Quantum Electrodynamics. I. A Covariant Formulation”. In: *Physical Review* 74.10 (1948), pp. 1439–1461. DOI: [10.1103/PhysRev.74.1439](https://doi.org/10.1103/PhysRev.74.1439).
- [28] P. A. M. Dirac. “The quantum theory of the electron”. In: *Proc. Roy. Soc. Lond. A* 117 (1928), pp. 610–624. DOI: [10.1098/rspa.1928.0023](https://doi.org/10.1098/rspa.1928.0023).
- [29] M. Gell-Mann. “Symmetries of Baryons and Mesons”. In: *Phys. Rev.* 125 (3 1962), pp. 1067–1084. DOI: [10.1103/PhysRev.125.1067](https://doi.org/10.1103/PhysRev.125.1067).
- [30] R. L. Workman et al (Particle Data Group). “Review of Particle Physics”. In: *PTEP* 2022 (2022), p. 083C01. DOI: [10.1093/ptep/ptac097](https://doi.org/10.1093/ptep/ptac097).
- [31] F. Englert and R. Brout. “Broken Symmetry and the Mass of Gauge Vector Mesons”. In: *Phys. Rev. Lett.* 13 (1964), pp. 321–323. DOI: [10.1103/PhysRevLett.13.321](https://doi.org/10.1103/PhysRevLett.13.321).
- [32] J. Goldstone, A. Salam, and S. Weinberg. “Broken Symmetries”. In: *Phys. Rev.* 127 (3 1962), pp. 965–970. DOI: [10.1103/PhysRev.127.965](https://doi.org/10.1103/PhysRev.127.965).
- [33] S. Weinberg. “General Theory of Broken Local Symmetries”. In: *Phys. Rev. D* 7 (4 1973), pp. 1068–1082. DOI: [10.1103/PhysRevD.7.1068](https://doi.org/10.1103/PhysRevD.7.1068).
- [34] G. Bertone, D. Hooper, and J. Silk. “Particle dark matter: Evidence, candidates and constraints”. In: *Phys. Rept.* 405 (2005), pp. 279–390. DOI: [10.1016/j.physrep.2004.08.031](https://doi.org/10.1016/j.physrep.2004.08.031). arXiv: [hep-ph/0404175](https://arxiv.org/abs/hep-ph/0404175).
- [35] B. Bajc et al. “Threshold corrections to dimension-six proton decay operators in non-minimal SUSY SU (5) GUTs”. In: *Nucl. Phys. B* 910 (2016), pp. 1–22. DOI: [10.1016/j.nuclphysb.2016.06.017](https://doi.org/10.1016/j.nuclphysb.2016.06.017). arXiv: [1603.03568 \[hep-ph\]](https://arxiv.org/abs/1603.03568).
- [36] S. P. Martin. “A Supersymmetry primer”. In: *Adv. Ser. Direct. High Energy Phys.* 18 (1998), pp. 1–98. DOI: [10.1142/9789812839657_0001](https://doi.org/10.1142/9789812839657_0001). arXiv: [hep-ph/9709356](https://arxiv.org/abs/hep-ph/9709356).
- [37] LHCb Collaboration. *Test of Lepton Flavour Universality using a measurement of $R(D^*)$ with hadronic τ decays*. 2023. URL: <https://lhcb-outreach.web.cern.ch/2023/03/21/test-of-lepton-flavour-universality-using-a-measurement-of-rd-with-hadronic-%cf%84-decays/>.
- [38] K. R. Labe. “The Muon $g - 2$ Experiment at Fermilab”. In: *56th Rencontres de Moriond on Electroweak Interactions and Unified Theories*. 2022. arXiv: [2205.06336 \[hep-ex\]](https://arxiv.org/abs/2205.06336).
- [39] T. Aoyama et al. “Complete Tenth-Order QED Contribution to the Muon $g - 2$ ”. In: *Phys. Rev. Lett.* 109 (2012), p. 111808. DOI: [10.1103/PhysRevLett.109.111808](https://doi.org/10.1103/PhysRevLett.109.111808). arXiv: [1205.5370 \[hep-ph\]](https://arxiv.org/abs/1205.5370).
- [40] S. Borsanyi et al. “Leading hadronic contribution to the muon magnetic moment from lattice QCD”. In: *Nature* 593.7857 (2021), pp. 51–55. DOI: [10.1038/s41586-021-03418-1](https://doi.org/10.1038/s41586-021-03418-1). arXiv: [2002.12347 \[hep-lat\]](https://arxiv.org/abs/2002.12347).
- [41] S. Dimopoulos and H. Georgi. “Softly broken supersymmetry and SU(5)”. In: *Nuclear Physics B* 193.1 (1981), pp. 150–162. DOI: [https://doi.org/10.1016/0550-3213\(81\)90522-8](https://doi.org/10.1016/0550-3213(81)90522-8).

- [42] M. Carena and H. E. Haber. “Higgs Boson theory and phenomenology”. In: *Progress in Particle and Nuclear Physics* 50.1 (2003), pp. 63–152. DOI: [https://doi.org/10.1016/S0146-6410\(02\)00177-1](https://doi.org/10.1016/S0146-6410(02)00177-1).
- [43] M. Carena et al. “MSSM Higgs Boson Searches at the LHC: Benchmark Scenarios after the Discovery of a Higgs-like Particle”. In: *Eur. Phys. J. C* 73.9 (2013), p. 2552. DOI: [10.1140/epjc/s10052-013-2552-1](https://doi.org/10.1140/epjc/s10052-013-2552-1). arXiv: [1302.7033](https://arxiv.org/abs/1302.7033) [hep-ph].
- [44] A. Djouadi et al. “The post-Higgs MSSM scenario: Habemus MSSM?” In: *Eur. Phys. J. C* 73 (2013), p. 2650. DOI: [10.1140/epjc/s10052-013-2650-0](https://doi.org/10.1140/epjc/s10052-013-2650-0). arXiv: [1307.5205](https://arxiv.org/abs/1307.5205) [hep-ph].
- [45] H. Bahl, S. Liebler, and T. Stefaniak. “MSSM Higgs benchmark scenarios for Run 2 and beyond: the low $\tan\beta$ region”. In: *Eur. Phys. J. C* 79.3 (2019), p. 279. DOI: [10.1140/epjc/s10052-019-6770-z](https://doi.org/10.1140/epjc/s10052-019-6770-z). arXiv: [1901.05933](https://arxiv.org/abs/1901.05933) [hep-ph].
- [46] ATLAS Collaboration. *Summary plots for beyond Standard Model Higgs boson benchmarks for direct and indirect searches*. Tech. rep. Geneva: CERN, 2022. URL: <https://cds.cern.ch/record/2827098>.
- [47] J. L. Hewett and T. G. Rizzo. “Low-energy phenomenology of superstring-inspired E6 models”. In: *Physics Reports* 183.5 (1989), pp. 193–381. DOI: [https://doi.org/10.1016/0370-1573\(89\)90071-9](https://doi.org/10.1016/0370-1573(89)90071-9).
- [48] M. Cvetcic and S. Godfrey. “Discovery and identification of extra gauge bosons”. In: *Electroweak symmetry breaking and new physics at the TeV scale*. 1995, pp. 383–415. DOI: [10.1142/9789812830265_0007](https://doi.org/10.1142/9789812830265_0007). arXiv: [hep-ph/9504216](https://arxiv.org/abs/hep-ph/9504216).
- [49] P. Langacker. “The Physics of Heavy Z' Gauge Bosons”. In: *Rev. Mod. Phys.* 81 (2009), pp. 1199–1228. DOI: [10.1103/RevModPhys.81.1199](https://doi.org/10.1103/RevModPhys.81.1199). arXiv: [0801.1345](https://arxiv.org/abs/0801.1345) [hep-ph].
- [50] A. Leike. “The Phenomenology of extra neutral gauge bosons”. In: *Phys. Rept.* 317 (1999), pp. 143–250. DOI: [10.1016/S0370-1573\(98\)00133-1](https://doi.org/10.1016/S0370-1573(98)00133-1). arXiv: [hep-ph/9805494](https://arxiv.org/abs/hep-ph/9805494).
- [51] M. Cvetcic and P. Langacker. “ Z' Physics and Supersymmetry”. In: *Adv. Ser. Direct. High Energy Phys.* 18 (1998), pp. 312–331. DOI: [10.1142/9789812839657_0012](https://doi.org/10.1142/9789812839657_0012). arXiv: [hep-ph/9707451](https://arxiv.org/abs/hep-ph/9707451).
- [52] D. Pappadopulo et al. “Heavy Vector Triplets: Bridging Theory and Data”. In: *JHEP* 09 (2014), p. 060. DOI: [10.1007/JHEP09\(2014\)060](https://doi.org/10.1007/JHEP09(2014)060). arXiv: [1402.4431](https://arxiv.org/abs/1402.4431) [hep-ph].
- [53] J. de Blas, J. M. Lizana, and M. Perez-Victoria. “Combining searches of Z' and W' bosons”. In: *JHEP* 01 (2013), p. 166. DOI: [10.1007/JHEP01\(2013\)166](https://doi.org/10.1007/JHEP01(2013)166). arXiv: [1211.2229](https://arxiv.org/abs/1211.2229) [hep-ph].
- [54] M. J. Dugan, H. Georgi, and D. B. Kaplan. “Anatomy of a composite Higgs model”. In: *Nuclear Physics B* 254 (1985), pp. 299–326. DOI: [https://doi.org/10.1016/0550-3213\(85\)90221-4](https://doi.org/10.1016/0550-3213(85)90221-4).
- [55] M. Frigerio, J. Serra, and A. Varagnolo. “Composite GUTs: models and expectations at the LHC”. In: *JHEP* 06 (2011), p. 029. DOI: [10.1007/JHEP06\(2011\)029](https://doi.org/10.1007/JHEP06(2011)029). arXiv: [1103.2997](https://arxiv.org/abs/1103.2997) [hep-ph].

- [56] E. Farhi and L. Susskind. “Technicolour”. In: *Physics Reports* 74.3 (1981), pp. 277–321. DOI: [https://doi.org/10.1016/0370-1573\(81\)90173-3](https://doi.org/10.1016/0370-1573(81)90173-3).
- [57] ATLAS Collaboration. “Search for additional heavy neutral Higgs and gauge bosons in the ditau final state produced in 36 fb⁻¹ of pp collisions at $\sqrt{s} = 13$ TeV with the ATLAS detector”. In: *JHEP* 01 (2018), p. 055. DOI: [10.1007/JHEP01\(2018\)055](https://doi.org/10.1007/JHEP01(2018)055). arXiv: [1709.07242](https://arxiv.org/abs/1709.07242) [hep-ex].
- [58] ATLAS Collaboration. *Summary Plots for Heavy Particle Searches and Long-lived Particle Searches - March 2023*. Tech. rep. Geneva: CERN, 2023. URL: <http://cds.cern.ch/record/2853754>.
- [59] J. M. Cornwall, D. N. Levin, and G. Tiktopoulos. “Erratum: Derivation of gauge invariance from high-energy unitarity bounds on the S matrix”. In: *Phys. Rev. D* 11 (4 1975), pp. 972–972. DOI: [10.1103/PhysRevD.11.972](https://doi.org/10.1103/PhysRevD.11.972).
- [60] G. J. Gounaris, R. K  gerler, and H. Neufeld. “Relationship between longitudinally polarized vector bosons and their unphysical scalar partners”. In: *Phys. Rev. D* 34 (10 1986), pp. 3257–3259. DOI: [10.1103/PhysRevD.34.3257](https://doi.org/10.1103/PhysRevD.34.3257).
- [61] M. S. Chanowitz and M. K. Gaillard. “The TeV physics of strongly interacting W’s and Z’s”. In: *Nuclear Physics B* 261 (1985), pp. 379–431. DOI: [https://doi.org/10.1016/0550-3213\(85\)90580-2](https://doi.org/10.1016/0550-3213(85)90580-2).
- [62] ATLAS Collaboration. *Combination of searches for heavy resonances using 139 fb⁻¹ of proton–proton collision data at $\sqrt{s} = 13$ TeV with the ATLAS detector*. Tech. rep. Geneva: CERN, 2022. URL: <http://cds.cern.ch/record/2809967>.
- [63] V. Barger, W. Y. Keung, and E. Ma. “Gauge model with light W and Z bosons”. In: *Phys. Rev. D* 22 (3 1980), pp. 727–737. DOI: [10.1103/PhysRevD.22.727](https://doi.org/10.1103/PhysRevD.22.727).
- [64] F. del Aguila, J. de Blas, and M. Perez-Victoria. “Electroweak Limits on General New Vector Bosons”. In: *JHEP* 09 (2010), p. 033. DOI: [10.1007/JHEP09\(2010\)033](https://doi.org/10.1007/JHEP09(2010)033). arXiv: [1005.3998](https://arxiv.org/abs/1005.3998) [hep-ph].
- [65] H. Georgi and S. L. Glashow. “Unity of All Elementary-Particle Forces”. In: *Phys. Rev. Lett.* 32 (8 1974), pp. 438–441. DOI: [10.1103/PhysRevLett.32.438](https://doi.org/10.1103/PhysRevLett.32.438).
- [66] J. C. Pati and A. Salam. “Unified Lepton-Hadron Symmetry and a Gauge Theory of the Basic Interactions”. In: *Phys. Rev. D* 8 (4 1973), pp. 1240–1251. DOI: [10.1103/PhysRevD.8.1240](https://doi.org/10.1103/PhysRevD.8.1240).
- [67] J. C. Pati and A. Salam. “Lepton number as the fourth ‘color’”. In: *Phys. Rev. D* 10 (1 1974), pp. 275–289. DOI: [10.1103/PhysRevD.10.275](https://doi.org/10.1103/PhysRevD.10.275).
- [68] B. Schrempp and F. Schrempp. “Light leptoquarks”. In: *Physics Letters B* 153.1 (1985), pp. 101–107. DOI: [https://doi.org/10.1016/0370-2693\(85\)91450-9](https://doi.org/10.1016/0370-2693(85)91450-9).
- [69] D. Buttazzo et al. “B-physics anomalies: a guide to combined explanations”. In: *JHEP* 11 (2017), p. 044. DOI: [10.1007/JHEP11\(2017\)044](https://doi.org/10.1007/JHEP11(2017)044). arXiv: [1706.07808](https://arxiv.org/abs/1706.07808) [hep-ph].
- [70] I. Dor  ner et al. “Physics of leptoquarks in precision experiments and at particle colliders”. In: *Phys. Rept.* 641 (2016), pp. 1–68. arXiv: [1603.04993](https://arxiv.org/abs/1603.04993) [hep-ph].

- [71] W. Buchmüller, R. Rückl, and D. Wyler. “Leptoquarks in lepton-quark collisions”. In: *Physics Letters B* 191.4 (1987), pp. 442–448. DOI: [https://doi.org/10.1016/0370-2693\(87\)90637-X](https://doi.org/10.1016/0370-2693(87)90637-X).
- [72] M. J. Baker et al. “High- p_T signatures in vector leptoquark models”. In: *Eur. Phys. J. C* 79.4 (2019), p. 334. arXiv: [1901.10480 \[hep-ph\]](#).
- [73] A. Angelescu et al. “Closing the window on single leptoquark solutions to the B -physics anomalies”. In: *JHEP* 10 (2018), p. 183. DOI: [10.1007/JHEP10\(2018\)183](#). arXiv: [1808.08179 \[hep-ph\]](#).
- [74] ATLAS Collaboration. “Search for a scalar partner of the top quark in the all-hadronic $t\bar{t}$ plus missing transverse momentum final state at $\sqrt{s} = 13$ TeV with the ATLAS detector”. In: *Eur. Phys. J. C* 80.8 (2020), p. 737. arXiv: [2004.14060 \[hep-ex\]](#).
- [75] ATLAS Collaboration. “Search for new phenomena in final states with b -jets and missing transverse momentum in $\sqrt{s} = 13$ TeV pp collisions with the ATLAS detector”. In: *JHEP* 05 (2021), p. 093. arXiv: [2101.12527 \[hep-ex\]](#).
- [76] ATLAS Collaboration. “Search for new phenomena in pp collisions in final states with tau leptons, b -jets, and missing transverse momentum with the ATLAS detector”. In: *Phys. Rev. D* 104.11 (2021), p. 112005. arXiv: [2108.07665 \[hep-ex\]](#).
- [77] ATLAS Collaboration. “Search for pairs of scalar leptoquarks decaying into quarks and electrons or muons in $\sqrt{s} = 13$ TeV pp collisions with the ATLAS detector”. In: *JHEP* 10 (2020), p. 112. arXiv: [2006.05872 \[hep-ex\]](#).
- [78] ATLAS Collaboration. “Search for pair production of third-generation scalar leptoquarks decaying into a top quark and a τ -lepton in pp collisions at $\sqrt{s} = 13$ TeV with the ATLAS detector”. In: *JHEP* 06 (2021), p. 179. arXiv: [2101.11582 \[hep-ex\]](#).
- [79] CMS Collaboration. “Search for leptoquarks coupled to third-generation quarks in proton-proton collisions at $\sqrt{s} = 13$ TeV”. In: *Phys. Rev. Lett.* 121.24 (2018), p. 241802. arXiv: [1809.05558 \[hep-ex\]](#).
- [80] CMS Collaboration. “Search for third-generation scalar leptoquarks decaying to a top quark and a τ lepton at $\sqrt{s} = 13$ TeV”. In: *Eur. Phys. J. C* 78 (2018), p. 707. arXiv: [1803.02864 \[hep-ex\]](#).
- [81] CMS Collaboration. “Search for dark matter in events with a leptoquark and missing transverse momentum in proton-proton collisions at 13 TeV”. In: *Phys. Lett. B* 795 (2019), pp. 76–99. arXiv: [1811.10151 \[hep-ex\]](#).
- [82] Morad Aaboud et al. “Searches for third-generation scalar leptoquarks in $\sqrt{s} = 13$ TeV pp collisions with the ATLAS detector”. In: *JHEP* 06 (2019), p. 144. DOI: [10.1007/JHEP06\(2019\)144](#). arXiv: [1902.08103 \[hep-ex\]](#).
- [83] ATLAS Collaboration. “Search for leptoquarks decaying into the $b\tau$ final state in pp collisions at $\sqrt{s} = 13$ TeV with the ATLAS detector”. In: *Submitted to JHEP* (2023). arXiv: [2305.15962 \[hep-ex\]](#). Pre-published.

- [84] Albert M Sirunyan et al. “Search for singly and pair-produced leptoquarks coupling to third-generation fermions in proton-proton collisions at $\sqrt{s}=13$ TeV”. In: *Phys. Lett. B* 819 (2021), p. 136446. DOI: [10.1016/j.physletb.2021.136446](https://doi.org/10.1016/j.physletb.2021.136446). arXiv: [2012.04178](https://arxiv.org/abs/2012.04178) [hep-ex].
- [85] ATLAS Collaboration. “The ATLAS Experiment at the CERN Large Hadron Collider”. In: *JINST* 3 (2008), S08003. DOI: [10.1088/1748-0221/3/08/S08003](https://doi.org/10.1088/1748-0221/3/08/S08003). URL: <https://cds.cern.ch/record/1129811>.
- [86] L. Evans and P. Bryant. “LHC Machine”. In: *JINST* 3 (2008), S08001. DOI: [10.1088/1748-0221/3/08/S08001](https://doi.org/10.1088/1748-0221/3/08/S08001).
- [87] L. Evans and L. Evans. *The Large Hadron Collider: a marvel of technology; 2nd ed.* Physics (EPFL Press). Lausanne: EPFL Press, 2018. ISBN: 97829400222346. URL: <https://cds.cern.ch/record/2645935>.
- [88] CMS Collaboration. “The CMS Experiment at the CERN LHC”. In: *JINST* 3 (2008), S08004. DOI: [10.1088/1748-0221/3/08/S08004](https://doi.org/10.1088/1748-0221/3/08/S08004).
- [89] LHCb Collaboration. “The LHCb Detector at the LHC”. In: *JINST* 3 (2008), S08005. DOI: [10.1088/1748-0221/3/08/S08005](https://doi.org/10.1088/1748-0221/3/08/S08005). URL: <https://cds.cern.ch/record/1129809>.
- [90] ALICE Collaboration. “The ALICE experiment at the CERN LHC”. In: *JINST* 3 (2008), S08002. DOI: [10.1088/1748-0221/3/08/S08002](https://doi.org/10.1088/1748-0221/3/08/S08002).
- [91] CERN. *LHC Complex Schematic*. 2023. URL: <https://home.cern/resources/faqs/facts-and-figures-about-lhc>.
- [92] M. Vretenar et al. *Linac4 design report*. Vol. 6. CERN Yellow Reports: Monographs. Geneva: CERN, 2020. DOI: [10.23731/CYRM-2020-006](https://doi.org/10.23731/CYRM-2020-006). URL: <https://cds.cern.ch/record/2736208>.
- [93] ATLAS Collaboration. “Luminosity determination in pp collisions at $\sqrt{s} = 13$ TeV using the ATLAS detector at the LHC”. In: *Submitted to Eur. Phys. J. C* (2022). arXiv: [2212.09379](https://arxiv.org/abs/2212.09379) [hep-ex]. Pre-published.
- [94] The ATLAS Collaboration. *Public ATLAS Luminosity Results for Run-2 of the LHC*. 2023. URL: <https://twiki.cern.ch/twiki/bin/view/AtlasPublic/LuminosityPublicResultsRun2>.
- [95] T. G. Rizzo. “ Z' phenomenology and the LHC”. In: *Theoretical Advanced Study Institute in Elementary Particle Physics: Exploring New Frontiers Using Colliders and Neutrinos*. 2006, pp. 537–575. arXiv: [hep-ph/0610104](https://arxiv.org/abs/hep-ph/0610104).
- [96] M. Capeans et al. *ATLAS Insertable B-Layer Technical Design Report*. Tech. rep. 2010. URL: <https://cds.cern.ch/record/1291633>.
- [97] The ATLAS Collaboration. “Operation of the ATLAS trigger system in Run 2”. In: *Journal of Instrumentation* 15.10 (2020), P10004. DOI: [10.1088/1748-0221/15/10/P10004](https://doi.org/10.1088/1748-0221/15/10/P10004).
- [98] ATLAS Collaboration. “The ATLAS Fast TracKer system”. In: *JINST* 16 (2021), P07006. arXiv: [2101.05078](https://arxiv.org/abs/2101.05078) [physics.ins-det].

- [99] ATLAS Collaboration. “Performance of electron and photon triggers in ATLAS during LHC Run 2”. In: *Eur. Phys. J. C* 80.1 (2020), p. 47. DOI: [10.1140/epjc/s10052-019-7500-2](https://doi.org/10.1140/epjc/s10052-019-7500-2). arXiv: [1909.00761](https://arxiv.org/abs/1909.00761) [hep-ex].
- [100] M. Elsing et al. “The ATLAS Tier-0: Overview and operational experience”. In: *Journal of Physics: Conference Series* 219.7 (2010), p. 072011. DOI: [10.1088/1742-6596/219/7/072011](https://doi.org/10.1088/1742-6596/219/7/072011).
- [101] G. Barrand et al. “GAUDI — A software architecture and framework for building HEP data processing applications”. In: *Computer Physics Communications* 140.1 (2001). CHEP2000, pp. 45–55. DOI: [https://doi.org/10.1016/S0010-4655\(01\)00254-5](https://doi.org/10.1016/S0010-4655(01)00254-5).
- [102] ATLAS Collaboration. “Electron reconstruction and identification in the ATLAS experiment using the 2015 and 2016 LHC proton-proton collision data at $\sqrt{s} = 13$ TeV”. In: *Eur. Phys. J. C* 79.8 (2019), p. 639. DOI: [10.1140/epjc/s10052-019-7140-6](https://doi.org/10.1140/epjc/s10052-019-7140-6). arXiv: [1902.04655](https://arxiv.org/abs/1902.04655) [physics.ins-det].
- [103] W. Lampl et al. *Calorimeter Clustering Algorithms: Description and Performance*. Tech. rep. Geneva: CERN, 2008. URL: <https://cds.cern.ch/record/1099735>.
- [104] ATLAS Collaboration. “Performance of the ATLAS Track Reconstruction Algorithms in Dense Environments in LHC Run 2”. In: *Eur. Phys. J. C* 77.10 (2017), p. 673. DOI: [10.1140/epjc/s10052-017-5225-7](https://doi.org/10.1140/epjc/s10052-017-5225-7). arXiv: [1704.07983](https://arxiv.org/abs/1704.07983) [hep-ex].
- [105] T. G. Cornelissen et al. “The global χ^2 track fitter in ATLAS”. In: *J. Phys. Conf. Ser.* 119 (2008), p. 032013. DOI: [10.1088/1742-6596/119/3/032013](https://doi.org/10.1088/1742-6596/119/3/032013).
- [106] ATLAS Collaboration. *Low- p_T tracking for ATLAS in nominal LHC pileup*. Tech. rep. Geneva: CERN, 2020. URL: <https://cds.cern.ch/record/2718583>.
- [107] ATLAS Collaboration. “Muon reconstruction and identification efficiency in ATLAS using the full Run 2 pp collision data set at $\sqrt{s} = 13$ TeV”. In: *Eur. Phys. J. C* 81.7 (2021), p. 578. DOI: [10.1140/epjc/s10052-021-09233-2](https://doi.org/10.1140/epjc/s10052-021-09233-2). arXiv: [2012.00578](https://arxiv.org/abs/2012.00578) [hep-ex].
- [108] ATLAS Collaboration. “Topological cell clustering in the ATLAS calorimeters and its performance in LHC Run 1”. In: *Eur. Phys. J. C* 77 (2017), p. 490. DOI: [10.1140/epjc/s10052-017-5004-5](https://doi.org/10.1140/epjc/s10052-017-5004-5). arXiv: [1603.02934](https://arxiv.org/abs/1603.02934) [hep-ex].
- [109] M. Cacciari, G. P. Salam, and G. Soyez. “The anti- k_t jet clustering algorithm”. In: *JHEP* 04 (2008), p. 063. DOI: [10.1088/1126-6708/2008/04/063](https://doi.org/10.1088/1126-6708/2008/04/063). arXiv: [0802.1189](https://arxiv.org/abs/0802.1189) [hep-ph].
- [110] ATLAS Collaboration. “Jet energy scale measurements and their systematic uncertainties in proton-proton collisions at $\sqrt{s} = 13$ TeV with the ATLAS detector”. In: *Phys. Rev. D* 96.7 (2017), p. 072002. DOI: [10.1103/PhysRevD.96.072002](https://doi.org/10.1103/PhysRevD.96.072002). arXiv: [1703.09665](https://arxiv.org/abs/1703.09665) [hep-ex].
- [111] ATLAS Collaboration. “Performance of pile-up mitigation techniques for jets in pp collisions at $\sqrt{s} = 8$ TeV using the ATLAS detector”. In: *Eur. Phys. J. C* 76.11 (2016), p. 581. DOI: [10.1140/epjc/s10052-016-4395-z](https://doi.org/10.1140/epjc/s10052-016-4395-z). arXiv: [1510.03823](https://arxiv.org/abs/1510.03823) [hep-ex].

- [112] ATLAS Collaboration. “Jet reconstruction and performance using particle flow with the ATLAS Detector”. In: *Eur. Phys. J. C* 77.7 (2017), p. 466. DOI: [10.1140/epjc/s10052-017-5031-2](https://doi.org/10.1140/epjc/s10052-017-5031-2). arXiv: [1703.10485](https://arxiv.org/abs/1703.10485) [hep-ex].
- [113] ATLAS Collaboration. *Selection of jets produced in 13 TeV proton-proton collisions with the ATLAS detector*. Tech. rep. Geneva: CERN, 2015. URL: <https://cds.cern.ch/record/2037702>.
- [114] ATLAS Collaboration. *Optimisation and performance studies of the ATLAS b-tagging algorithms for the 2017-18 LHC run*. Tech. rep. Geneva: CERN, 2017. URL: <https://cds.cern.ch/record/2273281>.
- [115] ATLAS Collaboration. *Identification of Jets Containing b-Hadrons with Recurrent Neural Networks at the ATLAS Experiment*. Tech. rep. Geneva: CERN, 2017. URL: <https://cds.cern.ch/record/2255226>.
- [116] ATLAS Collaboration. *Secondary vertex finding for jet flavour identification with the ATLAS detector*. Tech. rep. Geneva: CERN, 2017. URL: <https://cds.cern.ch/record/2270366>.
- [117] ATLAS Collaboration. *Topological b-hadron decay reconstruction and identification of b-jets with the JetFitter package in the ATLAS experiment at the LHC*. Tech. rep. Geneva: CERN, 2018. URL: <https://cds.cern.ch/record/2645405>.
- [118] ATLAS Collaboration. “ATLAS b-jet identification performance and efficiency measurement with $t\bar{t}$ events in pp collisions at $\sqrt{s} = 13$ TeV”. In: *Eur. Phys. J. C* 79.11 (2019), p. 970. DOI: [10.1140/epjc/s10052-019-7450-8](https://doi.org/10.1140/epjc/s10052-019-7450-8). arXiv: [1907.05120](https://arxiv.org/abs/1907.05120) [hep-ex].
- [119] ATLAS Collaboration. “ATLAS flavour-tagging algorithms for the LHC Run 2 pp collision dataset”. In: *Submitted to Eur. Phys. J. C* (2022). arXiv: [2211.16345](https://arxiv.org/abs/2211.16345) [physics.data-an]. Pre-published.
- [120] ATLAS Collaboration. “Reconstruction of hadronic decay products of tau leptons with the ATLAS experiment”. In: *Eur. Phys. J. C* 76.5 (2016), p. 295. DOI: [10.1140/epjc/s10052-016-4110-0](https://doi.org/10.1140/epjc/s10052-016-4110-0). arXiv: [1512.05955](https://arxiv.org/abs/1512.05955) [hep-ex].
- [121] P. Giovannini. *Local hadron calibration with ATLAS*. Tech. rep. Geneva: CERN, 2010. URL: <https://cds.cern.ch/record/1284955>.
- [122] ATLAS Collaboration. *Reconstruction, Energy Calibration, and Identification of Hadronically Decaying Tau Leptons in the ATLAS Experiment for Run-2 of the LHC*. Tech. rep. Geneva: CERN, 2015. URL: <https://cds.cern.ch/record/2064383>.
- [123] ATLAS Collaboration. “Identification and energy calibration of hadronically decaying tau leptons with the ATLAS experiment in pp collisions at $\sqrt{s}=8$ TeV”. In: *Eur. Phys. J. C* 75.7 (2015), p. 303. DOI: [10.1140/epjc/s10052-015-3500-z](https://doi.org/10.1140/epjc/s10052-015-3500-z). arXiv: [1412.7086](https://arxiv.org/abs/1412.7086) [hep-ex].
- [124] ATLAS Collaboration. *Identification of hadronic tau lepton decays using neural networks in the ATLAS experiment*. Tech. rep. Geneva: CERN, 2019. URL: <https://cds.cern.ch/record/2688062>.

- [125] S. Hochreiter and J. Schmidhuber. “Long Short-Term Memory”. In: *Neural Computation* 9.8 (1997), pp. 1735–1780. DOI: [10.1162/neco.1997.9.8.1735](https://doi.org/10.1162/neco.1997.9.8.1735).
- [126] ATLAS Collaboration. “Performance of missing transverse momentum reconstruction with the ATLAS detector using proton-proton collisions at $\sqrt{s} = 13$ TeV”. In: *Eur. Phys. J. C* 78.11 (2018), p. 903. DOI: [10.1140/epjc/s10052-018-6288-9](https://doi.org/10.1140/epjc/s10052-018-6288-9). arXiv: [1802.08168](https://arxiv.org/abs/1802.08168) [hep-ex].
- [127] D. Cavalli et al. *Reconstruction of Soft Missing Transverse Momentum with Inner Detector Tracks*. Tech. rep. Geneva: CERN, 2015. URL: <https://cds.cern.ch/record/2002888>.
- [128] C. Ay et al. “Monte Carlo generators in ATLAS software”. In: *Journal of Physics: Conference Series* 219.3 (2010), p. 032001. DOI: [10.1088/1742-6596/219/3/032001](https://doi.org/10.1088/1742-6596/219/3/032001).
- [129] T. Gleisberg et al. “Event generation with SHERPA 1.1”. In: *JHEP* 02 (2009), p. 007. DOI: [10.1088/1126-6708/2009/02/007](https://doi.org/10.1088/1126-6708/2009/02/007). arXiv: [0811.4622](https://arxiv.org/abs/0811.4622) [hep-ph].
- [130] E. Bothmann et al. “Event Generation with Sherpa 2.2”. In: *SciPost Phys.* 7.3 (2019), p. 034. DOI: [10.21468/SciPostPhys.7.3.034](https://doi.org/10.21468/SciPostPhys.7.3.034). arXiv: [1905.09127](https://arxiv.org/abs/1905.09127) [hep-ph].
- [131] S. Alioli et al. “A general framework for implementing NLO calculations in shower Monte Carlo programs: the POWHEG BOX”. In: *JHEP* 06 (2010), p. 043. DOI: [10.1007/JHEP06\(2010\)043](https://doi.org/10.1007/JHEP06(2010)043). arXiv: [1002.2581](https://arxiv.org/abs/1002.2581) [hep-ph].
- [132] J. Alwall et al. “The automated computation of tree-level and next-to-leading order differential cross sections, and their matching to parton shower simulations”. In: *JHEP* 07 (2014), p. 079. DOI: [10.1007/JHEP07\(2014\)079](https://doi.org/10.1007/JHEP07(2014)079). arXiv: [1405.0301](https://arxiv.org/abs/1405.0301) [hep-ph].
- [133] T. Sjöstrand et al. “An introduction to PYTHIA 8.2”. In: *Comput. Phys. Commun.* 191 (2015), pp. 159–177. DOI: [10.1016/j.cpc.2015.01.024](https://doi.org/10.1016/j.cpc.2015.01.024). arXiv: [1410.3012](https://arxiv.org/abs/1410.3012) [hep-ph].
- [134] ATLAS Collaboration. *ATLAS Pythia 8 tunes to 7 TeV data*. Tech. rep. Geneva: CERN, 2014. URL: <https://cds.cern.ch/record/1966419>.
- [135] S. Agostinelli et al. “GEANT4—a simulation toolkit”. In: *Nucl. Instrum. Meth. A* 506 (2003), pp. 250–303. DOI: [10.1016/S0168-9002\(03\)01368-8](https://doi.org/10.1016/S0168-9002(03)01368-8).
- [136] ATLAS Collaboration. “The ATLAS Simulation Infrastructure”. In: *Eur. Phys. J. C* 70 (2010), pp. 823–874. DOI: [10.1140/epjc/s10052-010-1429-9](https://doi.org/10.1140/epjc/s10052-010-1429-9). arXiv: [1005.4568](https://arxiv.org/abs/1005.4568) [physics.ins-det].
- [137] A. Dewhurst and F. Legger. “Distributed analysis in ATLAS”. In: *Journal of Physics: Conference Series* 664.3 (2015), p. 032020. DOI: [10.1088/1742-6596/664/3/032020](https://doi.org/10.1088/1742-6596/664/3/032020).
- [138] J. Catmore et al. *A New Petabyte-scale Data Derivation Framework for ATLAS*. Tech. rep. 7. Geneva: CERN, 2015. DOI: [10.1088/1742-6596/664/7/072007](https://doi.org/10.1088/1742-6596/664/7/072007). URL: <https://cds.cern.ch/record/2016628>.
- [139] A. Buckley et al. “Implementation of the ATLAS Run 2 event data model”. In: *Journal of Physics: Conference Series* 664.7 (2015), p. 072045. DOI: [10.1088/1742-6596/664/7/072045](https://doi.org/10.1088/1742-6596/664/7/072045).

- [140] M. Dobbs and J. B. Hansen. *The HepMC C++ Monte Carlo Event Record for High Energy Physics*. Tech. rep. Geneva: CERN, 2000. URL: <https://cds.cern.ch/record/684090>.
- [141] R. Brun, F. Rademakers, and S. Panacek. *ROOT, an object oriented data analysis framework*. 2000. URL: <http://cds.cern.ch/record/491486>.
- [142] CERN. *TTree Implementation in ROOT*. 2023. URL: <https://root.cern.ch/doc/master/classTTree.html>.
- [143] J. Elmsheuser et al. “Evolution of the ATLAS analysis model for Run-3 and prospects for HL-LHC”. In: *EPJ Web Conf.* 245 (2020), p. 06014. DOI: [10.1051/epjconf/202024506014](https://doi.org/10.1051/epjconf/202024506014).
- [144] ATLAS Collaboration. “Search for Minimal Supersymmetric Standard Model Higgs bosons H/A and for a Z' boson in the $\tau\tau$ final state produced in pp collisions at $\sqrt{s} = 13$ TeV with the ATLAS Detector”. In: *Eur. Phys. J. C* 76.11 (2016), p. 585. DOI: [10.1140/epjc/s10052-016-4400-6](https://doi.org/10.1140/epjc/s10052-016-4400-6). arXiv: [1608.00890](https://arxiv.org/abs/1608.00890) [hep-ex].
- [145] CDF and DØ Collaborations. *Combined CDF and DØ Upper Limits on MSSM Higgs Boson Production in tau-tau Final States with up to 2.2 fb^{-1}* . 2010. arXiv: [1003.3363](https://arxiv.org/abs/1003.3363) [hep-ex].
- [146] CMS Collaboration. “Search for additional neutral MSSM Higgs bosons in the $\tau\tau$ final state in proton-proton collisions at $\sqrt{s} = 13$ TeV”. In: *JHEP* 09 (2018), p. 007. DOI: [10.1007/JHEP09\(2018\)007](https://doi.org/10.1007/JHEP09(2018)007). arXiv: [1803.06553](https://arxiv.org/abs/1803.06553) [hep-ex].
- [147] CMS Collaboration. “Searches for additional Higgs bosons and for vector leptoquarks in $\tau\tau$ final states in proton-proton collisions at $\sqrt{s} = 13$ TeV”. In: *Submitted to J. High Energy Phys.* (2022). arXiv: [2208.02717](https://arxiv.org/abs/2208.02717) [hep-ex]. Pre-published.
- [148] CMS Collaboration. “Search for neutral MSSM Higgs bosons decaying to a pair of tau leptons in pp collisions”. In: *JHEP* 10 (2014), p. 160. DOI: [10.1007/JHEP10\(2014\)160](https://doi.org/10.1007/JHEP10(2014)160). arXiv: [1408.3316](https://arxiv.org/abs/1408.3316) [hep-ex].
- [149] S. Dittmaier, M. Krämer, and M. Spira. “Higgs radiation off bottom quarks at the Tevatron and the CERN LHC”. In: *Phys. Rev. D* 70 (2004), p. 074010. DOI: [10.1103/PhysRevD.70.074010](https://doi.org/10.1103/PhysRevD.70.074010). arXiv: [hep-ph/0309204](https://arxiv.org/abs/hep-ph/0309204).
- [150] S. Dawson et al. “Exclusive Higgs boson production with bottom quarks at hadron colliders”. In: *Phys. Rev. D* 69 (2004), p. 074027. DOI: [10.1103/PhysRevD.69.074027](https://doi.org/10.1103/PhysRevD.69.074027). arXiv: [hep-ph/0311067](https://arxiv.org/abs/hep-ph/0311067).
- [151] R. V. Harlander and W. B. Kilgore. “Higgs boson production in bottom quark fusion at next-to-next-to leading order”. In: *Phys. Rev. D* 68 (2003), p. 013001. DOI: [10.1103/PhysRevD.68.013001](https://doi.org/10.1103/PhysRevD.68.013001). arXiv: [hep-ph/0304035](https://arxiv.org/abs/hep-ph/0304035).
- [152] S. Forte, D. Napoletano, and M. Ubiali. “Higgs production in bottom-quark fusion: matching beyond leading order”. In: *Phys. Lett. B* 763 (2016), pp. 190–196. DOI: [10.1016/j.physletb.2016.10.040](https://doi.org/10.1016/j.physletb.2016.10.040). arXiv: [1607.00389](https://arxiv.org/abs/1607.00389) [hep-ph].
- [153] M. Bonvini, A. S. Papanastasiou, and F. J. Tackmann. “Resummation and matching of b-quark mass effects in $b\bar{b}H$ production”. In: *JHEP* 11 (2015), p. 196. DOI: [10.1007/JHEP11\(2015\)196](https://doi.org/10.1007/JHEP11(2015)196). arXiv: [1508.03288](https://arxiv.org/abs/1508.03288) [hep-ph].

- [154] M. Bonvini, A. S. Papanastasiou, and F. J. Tackmann. “Matched predictions for the $b\bar{b}H$ cross section at the 13 TeV LHC”. In: *JHEP* 10 (2016), p. 053. DOI: [10.1007/JHEP10\(2016\)053](#). arXiv: [1605.01733 \[hep-ph\]](#).
- [155] S. Forte, D. Napoletano, and M. Ubiali. “Higgs production in bottom-quark fusion in a matched scheme”. In: *Phys. Lett. B* 751 (2015), pp. 331–337. DOI: [10.1016/j.physletb.2015.10.051](#). arXiv: [1508.01529 \[hep-ph\]](#).
- [156] ATLAS Collaboration. “Search for neutral Higgs bosons of the minimal supersymmetric standard model in pp collisions at $\sqrt{s} = 8$ TeV with the ATLAS detector”. In: *JHEP* 11 (2014), p. 056. DOI: [10.1007/JHEP11\(2014\)056](#). arXiv: [1409.6064 \[hep-ex\]](#).
- [157] P. Nason. “A New method for combining NLO QCD with shower Monte Carlo algorithms”. In: *JHEP* 11 (2004), p. 040. DOI: [10.1088/1126-6708/2004/11/040](#). arXiv: [hep-ph/0409146](#).
- [158] S. Frixione, P. Nason, and C. Oleari. “Matching NLO QCD computations with Parton Shower simulations: the POWHEG method”. In: *JHEP* 11 (2007), p. 070. DOI: [10.1088/1126-6708/2007/11/070](#). arXiv: [0709.2092 \[hep-ph\]](#).
- [159] S. Alioli et al. “NLO vector-boson production matched with shower in POWHEG”. In: *JHEP* 07 (2008), p. 060. DOI: [10.1088/1126-6708/2008/07/060](#). arXiv: [0805.4802 \[hep-ph\]](#).
- [160] H. Lai et al. “New parton distributions for collider physics”. In: *Phys. Rev. D* 82 (2010), p. 074024. DOI: [10.1103/PhysRevD.82.074024](#). arXiv: [1007.2241 \[hep-ph\]](#).
- [161] T. Sjostrand, S. Mrenna, and P. Z. Skands. “A Brief Introduction to PYTHIA 8.1”. In: *Comput. Phys. Commun.* 178 (2008), pp. 852–867. DOI: [10.1016/j.cpc.2008.01.036](#). arXiv: [0710.3820 \[hep-ph\]](#).
- [162] C. Anastasiou et al. “High precision QCD at hadron colliders: Electroweak gauge boson rapidity distributions at NNLO”. In: *Phys. Rev. D* 69 (2004), p. 094008. DOI: [10.1103/PhysRevD.69.094008](#). arXiv: [hep-ph/0312266](#).
- [163] R. D. Ball et al. “Parton distributions for the LHC Run II”. In: *JHEP* 04 (2015), p. 040. DOI: [10.1007/JHEP04\(2015\)040](#). arXiv: [1410.8849 \[hep-ph\]](#).
- [164] S. Schumann and F. Krauss. “A Parton shower algorithm based on Catani-Seymour dipole factorisation”. In: *JHEP* 03 (2008), p. 038. DOI: [10.1088/1126-6708/2008/03/038](#). arXiv: [0709.1027 \[hep-ph\]](#).
- [165] S. Frixione, P. Nason, and G. Ridolfi. “A Positive-weight next-to-leading-order Monte Carlo for heavy flavour hadroproduction”. In: *JHEP* 09 (2007), p. 126. DOI: [10.1088/1126-6708/2007/09/126](#). arXiv: [0707.3088 \[hep-ph\]](#).
- [166] M. Beneke et al. “Hadronic top-quark pair production with NNLL threshold resummation”. In: *Nucl. Phys. B* 855 (2012), pp. 695–741. DOI: [10.1016/j.nuclphysb.2011.10.021](#). arXiv: [1109.1536 \[hep-ph\]](#).
- [167] M. Cacciari et al. “Top-pair production at hadron colliders with next-to-next-to-leading logarithmic soft-gluon resummation”. In: *Phys. Lett. B* 710 (2012), pp. 612–622. DOI: [10.1016/j.physletb.2012.03.013](#). arXiv: [1111.5869 \[hep-ph\]](#).

- [168] P. Bärnreuther, M. Czakon, and A. Mitov. “Percent Level Precision Physics at the Tevatron: First Genuine NNLO QCD Corrections to $q\bar{q} \rightarrow t\bar{t}+X$ ”. In: *Phys. Rev. Lett.* 109 (2012), p. 132001. DOI: [10.1103/PhysRevLett.109.132001](#). arXiv: [1204.5201 \[hep-ph\]](#).
- [169] M. Czakon and A. Mitov. “NNLO corrections to top pair production at hadron colliders: the quark-gluon reaction”. In: *JHEP* 01 (2013), p. 080. DOI: [10.1007/JHEP01\(2013\)080](#). arXiv: [1210.6832 \[hep-ph\]](#).
- [170] M. Czakon, Paul Fiedler, and Alexander Mitov. “Total Top-Quark Pair-Production Cross Section at Hadron Colliders Through $O(\alpha_s^4)$ ”. In: *Phys. Rev. Lett.* 110 (2013), p. 252004. DOI: [10.1103/PhysRevLett.110.252004](#). arXiv: [1303.6254 \[hep-ph\]](#).
- [171] M. Czakon and A. Mitov. “Top++: A Program for the Calculation of the Top-Pair Cross-Section at Hadron Colliders”. In: *Comput. Phys. Commun.* 185 (2014), p. 2930. DOI: [10.1016/j.cpc.2014.06.021](#). arXiv: [1112.5675 \[hep-ph\]](#).
- [172] E. Re. “Single-top Wt-channel production matched with parton showers using the POWHEG method”. In: *Eur. Phys. J. C* 71 (2011), p. 1547. DOI: [10.1140/epjc/s10052-011-1547-z](#). arXiv: [1009.2450 \[hep-ph\]](#).
- [173] R. Frederix, E. Re, and P. Torrielli. “Single-top t-channel hadroproduction in the four-flavour scheme with POWHEG and aMC@NLO”. In: *JHEP* 09 (2012), p. 130. DOI: [10.1007/JHEP09\(2012\)130](#). arXiv: [1207.5391 \[hep-ph\]](#).
- [174] S. Alioli et al. “NLO single-top production matched with shower in POWHEG: s- and t-channel contributions”. In: *JHEP* 09 (2009), p. 111. DOI: [10.1088/1126-6708/2009/09/111](#). arXiv: [0907.4076 \[hep-ph\]](#).
- [175] M. Aliev et al. “HATHOR: HAdronic Top and Heavy quarks crOss section calculator”. In: *Comput. Phys. Commun.* 182 (2011), pp. 1034–1046. DOI: [10.1016/j.cpc.2010.12.040](#). arXiv: [1007.1327 \[hep-ph\]](#).
- [176] P. Kant et al. “HatHor for single top-quark production: Updated predictions and uncertainty estimates for single top-quark production in hadronic collisions”. In: *Comput. Phys. Commun.* 191 (2015), pp. 74–89. DOI: [10.1016/j.cpc.2015.02.001](#). arXiv: [1406.4403 \[hep-ph\]](#).
- [177] J. M. Campbell, R. K. Ellis, and C. Williams. “Vector boson pair production at the LHC”. In: *JHEP* 07 (2011), p. 018. DOI: [10.1007/JHEP07\(2011\)018](#). arXiv: [1105.0020 \[hep-ph\]](#).
- [178] M. Wiesemann et al. “Higgs production in association with bottom quarks”. In: *JHEP* 02 (2015), p. 132. DOI: [10.1007/JHEP02\(2015\)132](#). arXiv: [1409.5301 \[hep-ph\]](#).
- [179] S. Alioli et al. “NLO Higgs boson production via gluon fusion matched with shower in POWHEG”. In: *JHEP* 04 (2009), p. 002. DOI: [10.1088/1126-6708/2009/04/002](#). arXiv: [0812.0578 \[hep-ph\]](#).
- [180] E. Bagnaschi et al. “Higgs production via gluon fusion in the POWHEG approach in the SM and in the MSSM”. In: *JHEP* 02 (2012), p. 088. DOI: [10.1007/JHEP02\(2012\)088](#). arXiv: [1111.2854 \[hep-ph\]](#).

- [181] R. V. Harlander, S. Liebler, and H. Mantler. “SusHi: A program for the calculation of Higgs production in gluon fusion and bottom-quark annihilation in the Standard Model and the MSSM”. In: *Comput. Phys. Commun.* 184 (2013), pp. 1605–1617. DOI: [10.1016/j.cpc.2013.02.006](#). arXiv: [1212.3249 \[hep-ph\]](#).
- [182] R. V. Harlander, S. Liebler, and H. Mantler. “SusHi Bento: Beyond NNLO and the heavy-top limit”. In: *Comput. Phys. Commun.* 212 (2017), pp. 239–257. DOI: [10.1016/j.cpc.2016.10.015](#). arXiv: [1605.03190 \[hep-ph\]](#).
- [183] M. Spira et al. “Higgs boson production at the LHC”. In: *Nucl. Phys. B* 453 (1995), pp. 17–82. DOI: [10.1016/0550-3213\(95\)00379-7](#). arXiv: [hep-ph/9504378](#).
- [184] R. V. Harlander and M. Steinhauser. “Supersymmetric Higgs production in gluon fusion at next-to-leading order”. In: *JHEP* 09 (2004), p. 066. DOI: [10.1088/1126-6708/2004/09/066](#). arXiv: [hep-ph/0409010](#).
- [185] R. Harlander and P. Kant. “Higgs production and decay: Analytic results at next-to-leading order QCD”. In: *JHEP* 12 (2005), p. 015. DOI: [10.1088/1126-6708/2005/12/015](#). arXiv: [hep-ph/0509189](#).
- [186] G. Degrandi and P. Slavich. “NLO QCD bottom corrections to Higgs boson production in the MSSM”. In: *JHEP* 11 (2010), p. 044. DOI: [10.1007/JHEP11\(2010\)044](#). arXiv: [1007.3465 \[hep-ph\]](#).
- [187] G. Degrandi, S. Di Vita, and P. Slavich. “NLO QCD corrections to pseudoscalar Higgs production in the MSSM”. In: *JHEP* 08 (2011), p. 128. DOI: [10.1007/JHEP08\(2011\)128](#). arXiv: [1107.0914 \[hep-ph\]](#).
- [188] G. Degrandi, S. Di Vita, and P. Slavich. “On the NLO QCD Corrections to the Production of the Heaviest Neutral Higgs Scalar in the MSSM”. In: *Eur. Phys. J. C* 72 (2012), p. 2032. DOI: [10.1140/epjc/s10052-012-2032-z](#). arXiv: [1204.1016 \[hep-ph\]](#).
- [189] C. Anastasiou and K. Melnikov. “Higgs boson production at hadron colliders in NNLO QCD”. In: *Nucl. Phys. B* 646 (2002), pp. 220–256. DOI: [10.1016/S0550-3213\(02\)00837-4](#). arXiv: [hep-ph/0207004](#).
- [190] V. Ravindran, J. Smith, and W. L. van Neerven. “NNLO corrections to the total cross-section for Higgs boson production in hadron hadron collisions”. In: *Nucl. Phys. B* 665 (2003), pp. 325–366. DOI: [10.1016/S0550-3213\(03\)00457-7](#). arXiv: [hep-ph/0302135](#).
- [191] R. V. Harlander and W. B. Kilgore. “Production of a pseudoscalar Higgs boson at hadron colliders at next-to-next-to leading order”. In: *JHEP* 10 (2002), p. 017. DOI: [10.1088/1126-6708/2002/10/017](#). arXiv: [hep-ph/0208096](#).
- [192] C. Anastasiou and K. Melnikov. “Pseudoscalar Higgs boson production at hadron colliders in NNLO QCD”. In: *Phys. Rev. D* 67 (2003), p. 037501. DOI: [10.1103/PhysRevD.67.037501](#). arXiv: [hep-ph/0208115](#).
- [193] U. Aglietti et al. “Two loop light fermion contribution to Higgs production and decays”. In: *Phys. Lett. B* 595 (2004), pp. 432–441. DOI: [10.1016/j.physletb.2004.06.063](#). arXiv: [hep-ph/0404071](#).

- [194] R. V. Harlander and W. B. Kilgore. “Next-to-next-to-leading order Higgs production at hadron colliders”. In: *Phys. Rev. Lett.* 88 (2002), p. 201801. DOI: [10.1103/PhysRevLett.88.201801](#). arXiv: [hep-ph/0201206](#).
- [195] R. Bonciani, G. Degrandi, and A. Vicini. “On the Generalized Harmonic Polylogarithms of One Complex Variable”. In: *Comput. Phys. Commun.* 182 (2011), pp. 1253–1264. DOI: [10.1016/j.cpc.2011.02.011](#). arXiv: [1007.1891 \[hep-ph\]](#).
- [196] S. Heinemeyer, W. Hollik, and G. Weiglein. “FeynHiggs: A Program for the calculation of the masses of the neutral CP even Higgs bosons in the MSSM”. In: *Comput. Phys. Commun.* 124 (2000), pp. 76–89. DOI: [10.1016/S0010-4655\(99\)00364-1](#). arXiv: [hep-ph/9812320](#).
- [197] S. Heinemeyer, W. Hollik, and G. Weiglein. “The Masses of the neutral CP - even Higgs bosons in the MSSM: Accurate analysis at the two loop level”. In: *Eur. Phys. J. C* 9 (1999), pp. 343–366. DOI: [10.1007/s100529900006](#). arXiv: [hep-ph/9812472](#).
- [198] G. Degrandi et al. “Towards high precision predictions for the MSSM Higgs sector”. In: *Eur. Phys. J. C* 28 (2003), pp. 133–143. DOI: [10.1140/epjc/s2003-01152-2](#). arXiv: [hep-ph/0212020](#).
- [199] T. Hahn et al. “High-Precision Predictions for the Light CP -Even Higgs Boson Mass of the Minimal Supersymmetric Standard Model”. In: *Phys. Rev. Lett.* 112.14 (2014), p. 141801. DOI: [10.1103/PhysRevLett.112.141801](#). arXiv: [1312.4937 \[hep-ph\]](#).
- [200] K. E. Williams, H. Rzehak, and G. Weiglein. “Higher order corrections to Higgs boson decays in the MSSM with complex parameters”. In: *Eur. Phys. J. C* 71 (2011), p. 1669. DOI: [10.1140/epjc/s10052-011-1669-3](#). arXiv: [1103.1335 \[hep-ph\]](#).
- [201] H. Bahl and W. Hollik. “Precise prediction for the light MSSM Higgs boson mass combining effective field theory and fixed-order calculations”. In: *Eur. Phys. J. C* 76.9 (2016), p. 499. DOI: [10.1140/epjc/s10052-016-4354-8](#). arXiv: [1608.01880 \[hep-ph\]](#).
- [202] H. Bahl et al. “Reconciling EFT and hybrid calculations of the light MSSM Higgs-boson mass”. In: *Eur. Phys. J. C* 78.1 (2018), p. 57. DOI: [10.1140/epjc/s10052-018-5544-3](#). arXiv: [1706.00346 \[hep-ph\]](#).
- [203] S. Dittmaier et al. *Handbook of LHC Higgs Cross Sections: 1. Inclusive Observables*. 2011. DOI: [10.5170/CERN-2011-002](#). URL: <http://cds.cern.ch/record/1318996>.
- [204] D. de Florian et al. *Handbook of LHC Higgs Cross Sections: 4. Deciphering the Nature of the Higgs Sector*. 2017. DOI: [10.23731/CYRM-2017-002](#). URL: <https://e-publishing.cern.ch/index.php/CYRM/issue/view/32>.
- [205] ATLAS Collaboration. “Performance of electron and photon triggers in ATLAS during LHC Run 2”. In: *Eur. Phys. J. C* 80.1 (2020), p. 47. DOI: [10.1140/epjc/s10052-019-7500-2](#). arXiv: [1909.00761 \[hep-ex\]](#).
- [206] ATLAS Collaboration. *2015 start-up trigger menu and initial performance assessment of the ATLAS trigger using Run-2 data*. Tech. rep. Geneva: CERN, 2016. URL: <https://cds.cern.ch/record/2136007>.

- [207] ATLAS Collaboration. *Trigger menu in 2018*. Tech. rep. Geneva: CERN, 2019. URL: <https://cds.cern.ch/record/2693402>.
- [208] G. Avoni et al. “The new LUCID-2 detector for luminosity measurement and monitoring in ATLAS”. In: *JINST* 13.07 (2018), P07017. DOI: [10.1088/1748-0221/13/07/P07017](https://cds.cern.ch/record/2633501). URL: <https://cds.cern.ch/record/2633501>.
- [209] ATLAS Collaboration. *Luminosity determination in pp collisions at $\sqrt{s} = 13$ TeV using the ATLAS detector at the LHC*. Tech. rep. Geneva: CERN, 2019. URL: <https://cds.cern.ch/record/2677054>.
- [210] J Butterworth et al. *Single Boson and Diboson Production Cross Sections in pp Collisions at $\sqrt{s} = 7$ TeV*. Tech. rep. Geneva: CERN, 2010. URL: <https://cds.cern.ch/record/1287902>.
- [211] G. Cowan. *Statistical data analysis*. 1998. ISBN: 978-0-19-850156-5.
- [212] M. Baak et al. “HistFitter software framework for statistical data analysis”. In: *Eur. Phys. J. C* 75 (2015), p. 153. DOI: [10.1140/epjc/s10052-015-3327-7](https://cds.cern.ch/record/14101280). arXiv: [1410.1280](https://arxiv.org/abs/1410.1280) [hep-ex].
- [213] K. Cranmer et al. *HistFactory: A tool for creating statistical models for use with RooFit and RooStats*. Tech. rep. New York: New York U., 2012. URL: <https://cds.cern.ch/record/1456844>.
- [214] L. Moneta et al. *The RooStats Project*. 2011. arXiv: [1009.1003](https://arxiv.org/abs/1009.1003) [physics.data-an].
- [215] G. Cowan et al. “Asymptotic formulae for likelihood-based tests of new physics”. In: *Eur. Phys. J. C* 71 (2011), p. 1554. DOI: [10.1140/epjc/s10052-011-1554-0](https://cds.cern.ch/record/10071727). arXiv: [1007.1727](https://arxiv.org/abs/1007.1727) [physics.data-an].
- [216] S. S. Wilks. “The Large-Sample Distribution of the Likelihood Ratio for Testing Composite Hypotheses”. In: *Annals Math. Statist.* 9.1 (1938), pp. 60–62. DOI: [10.1214/aoms/1177732360](https://cds.cern.ch/record/1214/aoms/1177732360).
- [217] A. Wald. “Tests of statistical hypotheses concerning several parameters when the number of observations is large”. In: *Transactions of the American Mathematical Society* 54 (1943), pp. 426–482.
- [218] O. Behnke. *Data analysis in high energy physics a practical guide to statistical methods*. eng. Weinheim an der Bergstrasse, Germany: Wiley-VCH Verlag GmbH, 2013. ISBN: 3-527-65343-0.
- [219] A. L. Read. “Modified frequentist analysis of search results (The CL(s) method)”. In: *Workshop on Confidence Limits*. 2000, pp. 81–101.
- [220] E. Bagnaschi et al. “MSSM Higgs Boson Searches at the LHC: Benchmark Scenarios for Run 2 and Beyond”. In: *Eur. Phys. J. C* 79.7 (2019), p. 617. DOI: [10.1140/epjc/s10052-019-7114-8](https://cds.cern.ch/record/180807542). arXiv: [1808.07542](https://arxiv.org/abs/1808.07542) [hep-ph].
- [221] ATLAS Collaboration. “Observation of a new particle in the search for the Standard Model Higgs boson with the ATLAS detector at the LHC”. In: *Phys. Lett. B* 716 (2012), pp. 1–29. DOI: [10.1016/j.physletb.2012.08.020](https://cds.cern.ch/record/12077214). arXiv: [1207.7214](https://arxiv.org/abs/1207.7214) [hep-ex].

- [222] Z. Czyżczula, T. Przedzinski, and Z. Was. “TauSpinner Program for Studies on Spin Effect in tau Production at the LHC”. In: *Eur. Phys. J. C* 72 (2012), p. 1988. DOI: [10.1140/epjc/s10052-012-1988-z](https://doi.org/10.1140/epjc/s10052-012-1988-z). arXiv: [1201.0117](https://arxiv.org/abs/1201.0117) [hep-ph].
- [223] T. Przedzinski, E. Richter-Was, and Z. Was. “Documentation of *TauSpinner* algorithms: program for simulating spin effects in τ -lepton production at LHC”. In: *Eur. Phys. J. C* 79.2 (2019), p. 91. DOI: [10.1140/epjc/s10052-018-6527-0](https://doi.org/10.1140/epjc/s10052-018-6527-0). arXiv: [1802.05459](https://arxiv.org/abs/1802.05459) [hep-ph].
- [224] T. Pierzchala et al. “Spin effects in tau lepton pair production at LHC”. In: *Acta Phys. Polon. B* 32 (2001), pp. 1277–1296. arXiv: [hep-ph/0101311](https://arxiv.org/abs/hep-ph/0101311).
- [225] S. Banerjee et al. “Ascertaining the spin for new resonances decaying into tau+ tau- at Hadron Colliders”. In: *Eur. Phys. J. C* 73.2 (2013), p. 2313. DOI: [10.1140/epjc/s10052-013-2313-1](https://doi.org/10.1140/epjc/s10052-013-2313-1). arXiv: [1212.2873](https://arxiv.org/abs/1212.2873) [hep-ph].
- [226] I. Deigaard. “Measurement of the Tau Polarization in $Z \rightarrow \tau\tau$ Decays with the ATLAS Detector”. Thesis. 2012. URL: <https://cds.cern.ch/record/1464097>.
- [227] D. U. Duschinger. “Search for neutral bosons decaying into the fully hadronic di-tau final state with the ATLAS detector at the LHC”. Thesis. 2018. URL: <https://cds.cern.ch/record/2673361>.
- [228] ATLAS Collaboration. *Search for scalar leptoquarks in the $b\tau\tau$ final state in pp collisions at $\sqrt{s} = 13$ TeV with the ATLAS detector*. Tech. rep. Geneva: CERN, 2022. URL: <https://cds.cern.ch/record/2812909>.
- [229] T. Mandal, S. Mitra, and S. Raz. “ $R_{D^{(*)}}$ motivated \mathcal{S}_1 leptoquark scenarios: Impact of interference on the exclusion limits from LHC data”. In: *Phys. Rev. D* 99.5 (2019), p. 055028. DOI: [10.1103/PhysRevD.99.055028](https://doi.org/10.1103/PhysRevD.99.055028). arXiv: [1811.03561](https://arxiv.org/abs/1811.03561) [hep-ph].
- [230] ATLAS Collaboration. *Search for leptoquark pair production in the $b\tau^-\bar{b}\tau^+$ final state with the ATLAS detector*. Tech. rep. Geneva: CERN, 2022. URL: <https://cds.cern.ch/record/2808368>.
- [231] I. Doršner and A. Greljo. “Leptoquark toolbox for precision collider studies”. In: *JHEP* 05 (2018), p. 126. arXiv: [1801.07641](https://arxiv.org/abs/1801.07641) [hep-ph].
- [232] T. Mandal, S. Mitra, and S. Seth. “Pair Production of Scalar Leptoquarks at the LHC to NLO Parton Shower Accuracy”. In: *Phys. Rev. D* 93.3 (2016), p. 035018. arXiv: [1506.07369](https://arxiv.org/abs/1506.07369) [hep-ph].
- [233] W. Beenakker et al. “NNLL-fast: predictions for coloured supersymmetric particle production at the LHC with threshold and Coulomb resummation”. In: *JHEP* 12 (2016), p. 133. DOI: [10.1007/JHEP12\(2016\)133](https://doi.org/10.1007/JHEP12(2016)133). arXiv: [1607.07741](https://arxiv.org/abs/1607.07741) [hep-ph].
- [234] W. Beenakker et al. “Stop production at hadron colliders”. In: *Nucl. Phys. B* 515 (1998), pp. 3–14. DOI: [10.1016/S0550-3213\(98\)00014-5](https://doi.org/10.1016/S0550-3213(98)00014-5). arXiv: [hep-ph/9710451](https://arxiv.org/abs/hep-ph/9710451).
- [235] W. Beenakker et al. “Supersymmetric top and bottom squark production at hadron colliders”. In: *JHEP* 08 (2010), p. 098. DOI: [10.1007/JHEP08\(2010\)098](https://doi.org/10.1007/JHEP08(2010)098). arXiv: [1006.4771](https://arxiv.org/abs/1006.4771) [hep-ph].

- [236] W. Beenakker et al. “NNLL resummation for stop pair-production at the LHC”. In: *JHEP* 05 (2016), p. 153. DOI: [10.1007/JHEP05\(2016\)153](https://doi.org/10.1007/JHEP05(2016)153). arXiv: [1601.02954](https://arxiv.org/abs/1601.02954) [hep-ph].
- [237] C. Borschensky et al. “Scalar leptoquark pair production at hadron colliders”. In: *Phys. Rev. D* 101.11 (2020), p. 115017. DOI: [10.1103/PhysRevD.101.115017](https://doi.org/10.1103/PhysRevD.101.115017). arXiv: [2002.08971](https://arxiv.org/abs/2002.08971) [hep-ph].
- [238] C. D. White et al. “Isolating Wt production at the LHC”. In: *JHEP* 11 (2009), p. 074. arXiv: [0908.0631](https://arxiv.org/abs/0908.0631) [hep-ph].
- [239] ATLAS Collaboration. “Measurements of Higgs boson production cross-sections in the $H \rightarrow \tau^+\tau^-$ decay channel in pp collisions at $\sqrt{s} = 13$ TeV with the ATLAS detector”. In: *JHEP* 08 (2022), p. 175. DOI: [10.1007/JHEP08\(2022\)175](https://doi.org/10.1007/JHEP08(2022)175). arXiv: [2201.08269](https://arxiv.org/abs/2201.08269) [hep-ex].
- [240] J. Aebischer et al. “Confronting the vector leptoquark hypothesis with new low- and high-energy data”. In: *Eur. Phys. J. C* 83.2 (2023), p. 153. DOI: [10.1140/epjc/s10052-023-11304-5](https://doi.org/10.1140/epjc/s10052-023-11304-5). arXiv: [2210.13422](https://arxiv.org/abs/2210.13422) [hep-ph].
- [241] A. Géron. *Hands-on machine learning with Scikit-Learn and TensorFlow : concepts, tools, and techniques to build intelligent systems*. O’Reilly Media, Inc., 2017. ISBN: 9781491962268.
- [242] I. Narsky. *Statistical analysis techniques in particle physics : fits, density estimation and supervised learning*. Wiley-VCH, 2014. ISBN: 3-527-67729-1.
- [243] L. Bottou, F. E. Curtis, and J. Nocedal. *Optimization Methods for Large-Scale Machine Learning*. 2018. arXiv: [1606.04838](https://arxiv.org/abs/1606.04838) [stat.ML].
- [244] A. F. Agarap. *Deep Learning using Rectified Linear Units (ReLU)*. 2019. arXiv: [1803.08375](https://arxiv.org/abs/1803.08375) [cs.NE].
- [245] F. Chollet et al. *Keras*. <https://keras.io>. 2015.
- [246] D. P. Kingma and J. Ba. *Adam: A Method for Stochastic Optimization*. 2017. arXiv: [1412.6980](https://arxiv.org/abs/1412.6980) [cs.LG].
- [247] N. Srivastava et al. “Dropout: A Simple Way to Prevent Neural Networks from Overfitting”. In: *Journal of Machine Learning Research* 15 (2014), pp. 1929–1958.
- [248] P. Baldi et al. “Parameterized neural networks for high-energy physics”. In: *Eur. Phys. J. C* 76.5 (2016), p. 235. DOI: [10.1140/epjc/s10052-016-4099-4](https://doi.org/10.1140/epjc/s10052-016-4099-4). arXiv: [1601.07913](https://arxiv.org/abs/1601.07913) [hep-ex].
- [249] F. Pedregosa et al. “Scikit-learn: Machine Learning in Python”. In: *Journal of Machine Learning Research* 12 (2011), pp. 2825–2830.
- [250] A. Elagin et al. “A New Mass Reconstruction Technique for Resonances Decaying to di-tau”. In: *Nucl. Instrum. Meth. A* 654 (2011), pp. 481–489. DOI: [10.1016/j.nima.2011.07.009](https://doi.org/10.1016/j.nima.2011.07.009). arXiv: [1012.4686](https://arxiv.org/abs/1012.4686) [hep-ex].
- [251] D. Buscher. “Search for Higgs bosons with b-jets in the final state in proton-proton collisions with the ATLAS experiment”. Thesis. 2016. URL: <https://cds.cern.ch/record/2232472>.

- [252] I. Z. Fernandez et al. “High-Luminosity Large Hadron Collider (HL-LHC): Technical design report”. In: 10/2020 (2020). DOI: [10.23731/CYRM-2020-0010](https://doi.org/10.23731/CYRM-2020-0010).
- [253] ATLAS Collaboration. *Technical Design Report for the ATLAS Inner Tracker Strip Detector*. Tech. rep. Geneva: CERN, 2017. URL: <https://cds.cern.ch/record/2257755>.
- [254] ATLAS Collaboration. *Letter of Intent for the Phase-II Upgrade of the ATLAS Experiment*. Tech. rep. Geneva: CERN, 2012. URL: <https://cds.cern.ch/record/1502664>.
- [255] ATLAS Collaboration. *Expected tracking and related performance with the updated ATLAS Inner Tracker layout at the High-Luminosity LHC*. Tech. rep. Geneva: CERN, 2021. URL: <https://cds.cern.ch/record/2776651>.
- [256] J. H. Arling et al. “Test beam measurement of ATLAS ITk Short Strip module at warm and cold operational temperature”. In: *JINST* 18.03 (2023), P03015. DOI: [10.1088/1748-0221/18/03/P03015](https://doi.org/10.1088/1748-0221/18/03/P03015). arXiv: [2302.10950](https://arxiv.org/abs/2302.10950) [hep-ex].
- [257] A. L. Heggelund. *Overview of the ATLAS ITk Pixel Detector*. Tech. rep. Geneva: CERN, 2022. URL: <https://cds.cern.ch/record/2834491>.
- [258] L. Meng. “ATLAS ITk Pixel Detector Overview”. In: *International Workshop on Future Linear Colliders*. 2021. arXiv: [2105.10367](https://arxiv.org/abs/2105.10367) [physics.ins-det].
- [259] ATLAS Collaboration. *Technical Design Report for the ATLAS Inner Tracker Pixel Detector*. Tech. rep. Geneva: CERN, 2017. DOI: [10.17181/CERN.FOZZ.ZP3Q](https://doi.org/10.17181/CERN.FOZZ.ZP3Q). URL: <https://cds.cern.ch/record/2285585>.
- [260] S. Mobius. “Module development for the ATLAS ITk pixel detector”. In: *JINST* 17.03 (2022), p. C03042. DOI: [10.1088/1748-0221/17/03/C03042](https://doi.org/10.1088/1748-0221/17/03/C03042). URL: <https://dx.doi.org/10.1088/1748-0221/17/03/C03042>.
- [261] F. Rühr et al. “Testbeam studies of barrel and end-cap modules for the ATLAS ITk strip detector before and after irradiation”. In: *Nucl. Instrum. Meth. A* 979 (2020), p. 164430. DOI: [10.1016/j.nima.2020.164430](https://doi.org/10.1016/j.nima.2020.164430).
- [262] L. Gonella. *The ATLAS ITk Detector System for the Phase-II LHC Upgrade*. Tech. rep. Geneva: CERN, 2023. DOI: [10.1016/j.nima.2022.167597](https://doi.org/10.1016/j.nima.2022.167597). URL: <https://cds.cern.ch/record/2816188>.
- [263] C. Haber et al. *Production and Testing of the Powerboard for ATLAS ITk Strip Barrel Modules*. Tech. rep. Geneva: CERN, 2022. URL: <https://cds.cern.ch/record/2837170>.
- [264] C. T. Klein et al. *ATLAS ITk Strip Sensor Quality Control and Review of ATLAS18 Pre-Production Sensor Results*. Tech. rep. Geneva: CERN, 2023. URL: <https://cds.cern.ch/record/2846511>.
- [265] M. Mikestikova et al. “ATLAS ITk strip sensor quality control procedures and testing site qualification”. In: *JINST* 17.12 (2022), p. C12013. DOI: [10.1088/1748-0221/17/12/C12013](https://doi.org/10.1088/1748-0221/17/12/C12013).

- [266] International Standards Organisation. *ISO 14644-1 Cleanrooms and Associated Controlled Environments Part 1: Classification of Air Cleanliness*. 2015. URL: <https://www.iso.org/standard/53394.html>.
- [267] Andover Corporation. *Polaris Polymers PF7006A Epoxy Resin*. OPTICAL EPOXY RESIN. 2016. URL: <https://www.andovercorp.com/content/uploads/Optical%20Epoxy%20Resin%20SDS.pdf>.
- [268] ThorLabs. *Eccobond F112*. TRA-BOND F112. 2012. URL: <https://www.thorlabs.com/drawings/e18406072e07bcb0-A7A7AB1D-C54C-3060-FF1BC2192DB935F1/F112-MFGSpec.pdf>.
- [269] OGP. *An Integrated Laser Sensor for OGP Measurement Systems*. URL: https://www.ogpnet.com/wp-content/uploads/TTL%5C_Laser%5C_OGP-NA%5C_794065-0422%5C_LR%5C_SECURED.pdf.
- [270] A. Hynes. *scikit-spatial: Spatial objects and computations based on NumPy arrays*. URL: <https://github.com/ajhynes7/scikit-spatial>.

Appendix A

Important Acronyms

Table A.1: A list of acronyms used throughout the thesis.

2HDM	2-Higgs Doublet Model	HVT	Heavy Vector Triplet	PPA	Pre-production A
ABC	Type of ASIC chip	IBL	Inner B-Layer	PS	Parton Shower
AMI	ATLAS Metadata Interface	ID	Identification	PSB	Proton Synchrotron Booster
AOD	Analysis Object Data	IO	Inside-out combined muons	QC	Quality Checks
ASG	Analysis Software Group	ISO	Isolated	QCD	Quantum Chromodynamics
ASIC	Application Specific Integrated Circuit	IV	Current-Voltage scan	QED	Quantum Electrodynamics
ATLFAST-II	Fast MC simulation software for ATLAS	JEP	Jet/Energy-sum Processor	QFT	Quantum Field Theory
AUC	Area under the ROC curve	JER	Jet energy smearing	RF	Radio-Frequency
BDT	Boosted Decision Tree	JES	Jet Energy Scale	RNN	Recurrent Neural Network
BSM	Beyond the Standard Model	JVT	Jet Vertex Tagger	RNNIP	Algorithm fed into the DL1r <i>b</i> -tagger
CB	Combined muons	LB	Lumi-Block	ROC	Receiver Operating Characteristic curve
CL	Confidence Limit	LC	Local hadronic calibration scale	ROD	Read-out Driver
CP	The combination of charge conjugation and parity symmetry	LFR	Lepton Fake Region	ROI	Region Of Interest
CPT	The combination of charge conjugation, parity and time reversal symmetry	LH	Likelihood	ROS	Read-out System
CR	Control Region	LO	Leading Order	RPC	Resistive Plate Chambers
CSC	Cathode Strip Chambers	LQ	Leptoquark	SCT	Semi-conductor Tracker
CT	Calorimeter Tagged muons	LQLQ	Pair produced leptoquark	SLVS	Scalable Low Voltage Signalling
CTP	Central Trigger Processor	LS	Long Strip	SM	Standard Model
DAOD	Derived Analysis Object Data	LSTM	Long-Short Term Memory	SPS	Super Proton Synchrotron
DP	Display Port cables	LV	Low Voltage	SR	Signal Region
DY	Drell-Yan production	MC	Monte Carlo	SS	Same-Sign
ECAL	Electromagnetic calorimeter	MDT	Monitored Drift Tube	SSM	Sequential Standard Model
EDM	Event Data Model	ME	Muon spectrometer extrapolated muons	ST	Segment Tagged muons
ENC	Equivalent Noise Charge	MFF	Multi-jet Fake Factor	SUSY	Supersymmetry
EVNT	File created after event generation	MFR	Multi-jet Fake Region	TCR	Top Control Region
FCAL	Forward calorimeter	MIN	Minimal coupling scenario for LQ	TDAQ	Trigger and data acquisition system
FF	Fake Factor	ML	Machine Learning	TGC	Thin Gap Chambers
FPGA	Field Programmable Gate Array	MMC	Missing Mass Calculator	TRT	Transition Radiation Tracker
FSR	Final State Radiation	MS	Muon Spectrometer	TST	Track-based Soft Term
GSW	Glashow-Salam-Weinberg theory	MSSM	Minimal Supersymmetric Standard Model	TTVA	Track-to-vertex association
GUT	Grand unified Theory	NLO	Next-to-Leading-Order	UEPS	Underlying event, parton showering and hadronisation
HCAL	Hadronic calorimeter	NNLL	Next-to-Next-to-Leading-Log-Order	VBF	Vector Boson Fusion
HCC	Hybrid chip used to communicate with ASICs	NNLO	Next-to-Next-to-Leading-Order	VR	Validation Region
HEC	Hadronic end-cap calorimeter	NP	Nuisance Parameter	VSF	Validation Scale Factor
ISR	Initial State Radiation	OLR	Overlap Removal	WFF	W+jets Fake Factor
HF	Heavy Flavour	PB	Powerboard	WFR	W+jets Fake Region
HLT	High Level Trigger	PCB	Printed Circuit Board	WLCG	Worldwide LHC Computing Grid
HRC	Heavy Resonance Combination	PDF	Parton Distribution Function	YM	Yang-Mills coupling scenario for LQ
HV	High Voltage	PNN	Parametric Neural Network		

Appendix B

The MSSM $H/A/h \rightarrow \tau\tau$ Full Run-II (Legacy) Analysis

B.1 Validation Region Scale Factors

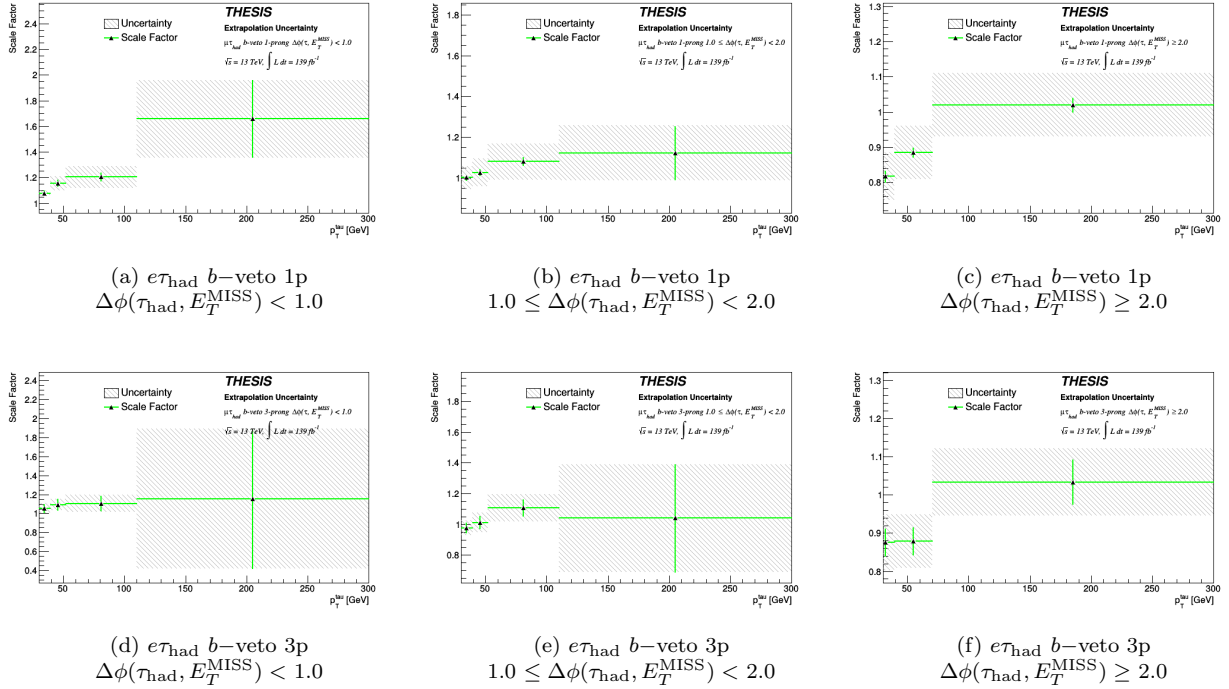
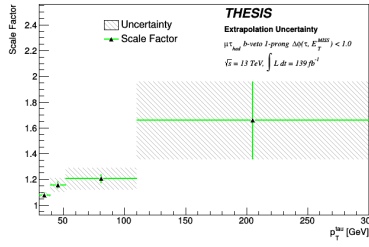
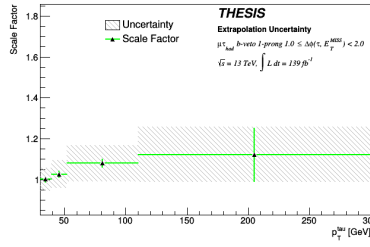


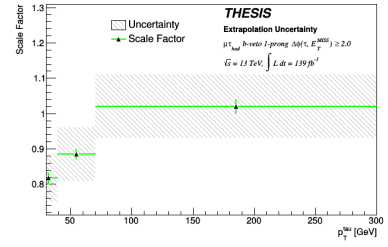
Figure B.1: The $e\tau_{\text{had}} b\text{-veto}$ validation region scale factors. The scale factors are parametrised in p_T^{τ} , the number of prongs and $\Delta\phi(\tau_{\text{had}}, E_T^{\text{MISS}})$. The uncertainty bar corresponds to the statistical uncertainty, whilst the uncertainty band considers also the assigned systematic uncertainty.



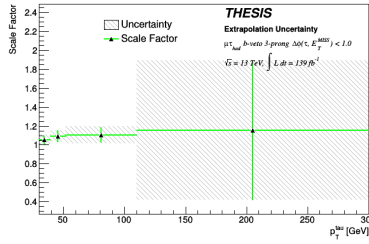
(a) $\mu\tau_{\text{had}} b\text{-veto } 1p$
 $\Delta\phi(\tau_{\text{had}}, E_T^{\text{MISS}}) < 1.0$



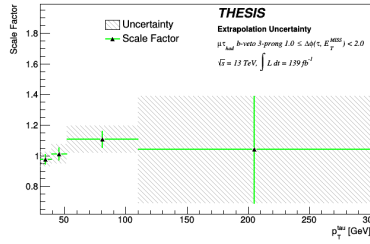
(b) $\mu\tau_{\text{had}} b\text{-veto } 1p$
 $1.0 \leq \Delta\phi(\tau_{\text{had}}, E_T^{\text{MISS}}) < 2.0$



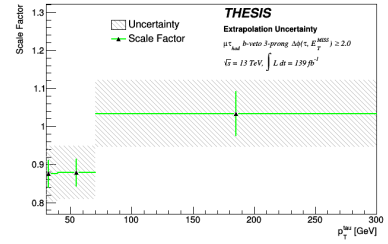
(c) $\mu\tau_{\text{had}} b\text{-veto } 1p$
 $\Delta\phi(\tau_{\text{had}}, E_T^{\text{MISS}}) \geq 2.0$



(d) $\mu\tau_{\text{had}} b\text{-veto } 3p$
 $\Delta\phi(\tau_{\text{had}}, E_T^{\text{MISS}}) < 1.0$

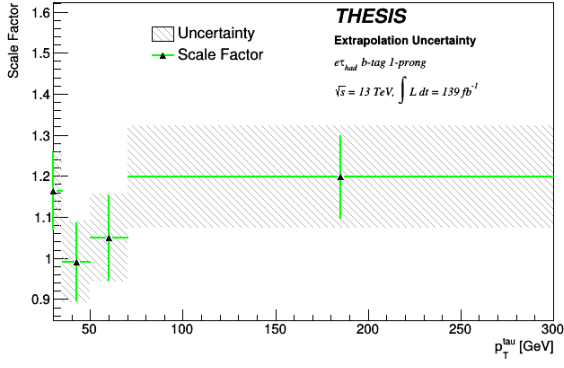


(e) $\mu\tau_{\text{had}} b\text{-veto } 3p$
 $1.0 \leq \Delta\phi(\tau_{\text{had}}, E_T^{\text{MISS}}) < 2.0$

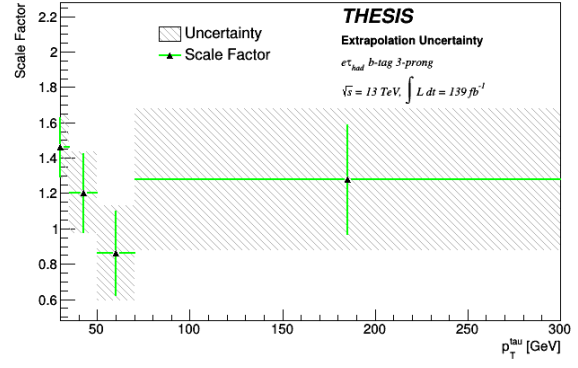


(f) $\mu\tau_{\text{had}} b\text{-veto } 3p$
 $\Delta\phi(\tau_{\text{had}}, E_T^{\text{MISS}}) \geq 2.0$

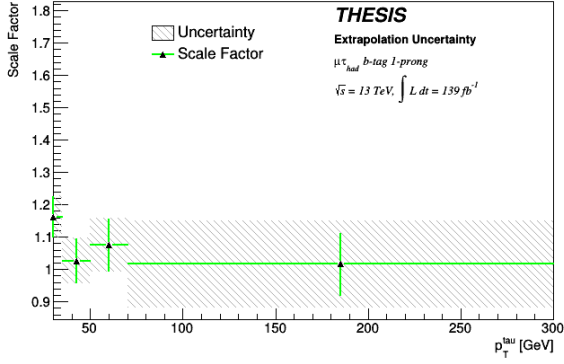
Figure B.2: The $\mu\tau_{\text{had}} b\text{-veto}$ validation region scale factors. The scale factors are parametrised in p_T^τ , the number of prongs and $\Delta\phi(\tau_{\text{had}}, E_T^{\text{MISS}})$. The uncertainty bar corresponds to the statistical uncertainty, whilst the uncertainty band considers also the assigned systematic uncertainty.



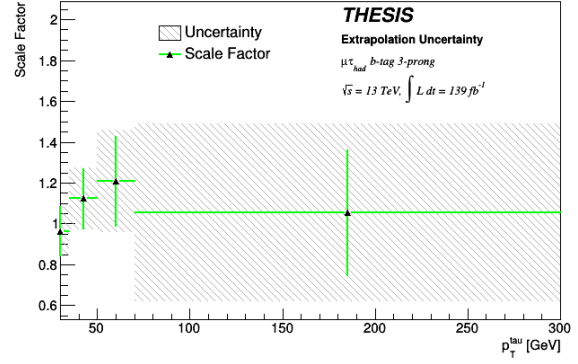
(a) $e\tau_{\text{had}}$
 $b\text{-tag 1p}$



(b) $e\tau_{\text{had}}$
 $b\text{-tag 3p}$



(c) $\mu\tau_{\text{had}}$
 $b\text{-tag 1p}$



(d) $\mu\tau_{\text{had}}$
 $b\text{-tag 3p}$

Figure B.3: The $e\tau_{\text{had}}$ and $\mu\tau_{\text{had}}$ b -tag validation region scale factors. The scale factors are parametrised in p_T^τ , the number of prongs and the b -veto scale factors. The uncertainty bar corresponds to the statistical uncertainty, whilst the uncertainty band considers also the assigned systematic uncertainty.

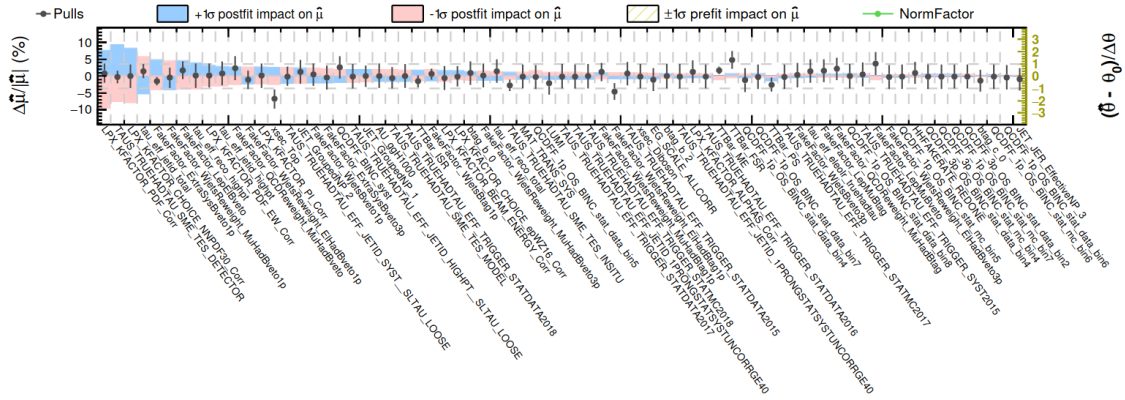
B.2 Statistical Fit and Systematic Uncertainty Diagnostic Plots

This appendix shows the associated plots used for inspecting the quality of the statistical fit and the impact of nuisance parameters on the upper limit. Generally, the best way to quote the individual nuisance parameters influence on the fit is via pulls, constraints and the impact on the post-fit μ . The pull is defined as the difference between the post-fit and pre-fit nuisance parameter central value, divided by the pre-fit central value. The constraint is the ratio of the post-fit and pre-fit uncertainty on μ . The post-fit (pre-fit) impact from each nuisance parameter is measured by fixing the NP value to the post-fit (pre-fit) central value with the post-fit (pre-fit) uncertainty added. The fit is then performed again but with N-1 variable parameters. The same procedure is done but with the post-fit (pre-fit) uncertainty subtracted to get the variation in the other direction. The impact is evaluated as the difference in the central value of μ .

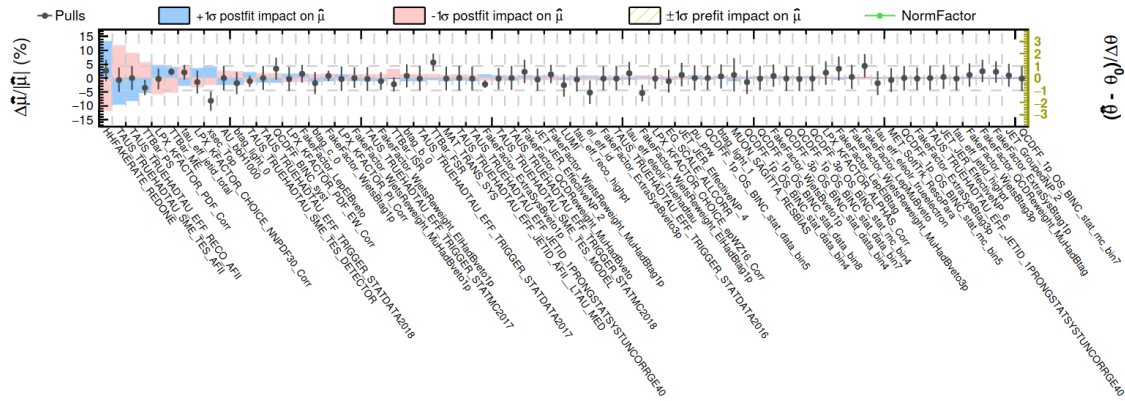
A pulled nuisance parameter can indicate that the pre-fit value is not reasonable and should be reviewed. A highly constrained nuisance parameter can indicate that the data contains enough information such that the precision of the nuisance parameter estimate can be improved, this is often not so helpful in BSM search analyses. For the Asimov dataset which matches the one predicted by MC, one should observe no pulls and zero constraints. The ranking plots show which systematics are most important to the determination of μ . It is also common to see the impact of nuisance parameters or nuisance parameter sets on the post-fit yield, which gives clues on how an analysis can be made more sensitive.

The ranking plots, with the pull and constraint overlaid are shown in Figure B.4 for a 1000 GeV bbH and ggH signal. There will be similar plots for all signals and mass points, creating a catalogue of plots to check. In general, only large pulls are a source of concern and usually trigger a study to try and better understand the pre-fit distribution. For the plots shown below, the top cross section uncertainty is one of the largest pulls. This was deemed satisfactory for the legacy analysis but for the improved MSSM and LQ analyses, it was one of the key reasons to introduce the t -quark correction in Sections 7.2.4 and 6.4.1.

The full picture can be observed by considering the correlation between different nuisance parameters. The correlations make it impossible to sum the uncertainties in quadrature and therefore the total post-fit uncertainty must be gained from the curvature of the profile likelihood. Where anti-correlations are present it is often the case that they can reduce the post-fit uncertainty. The correlation plots are shown in Figure B.5 for a 1000 GeV bbH and ggH mass point. If many nuisance parameters are strongly correlated, it may be necessary to try to decorrelate them in some way by modifying the analysis. For the analyses in this thesis, it was never deemed necessary.

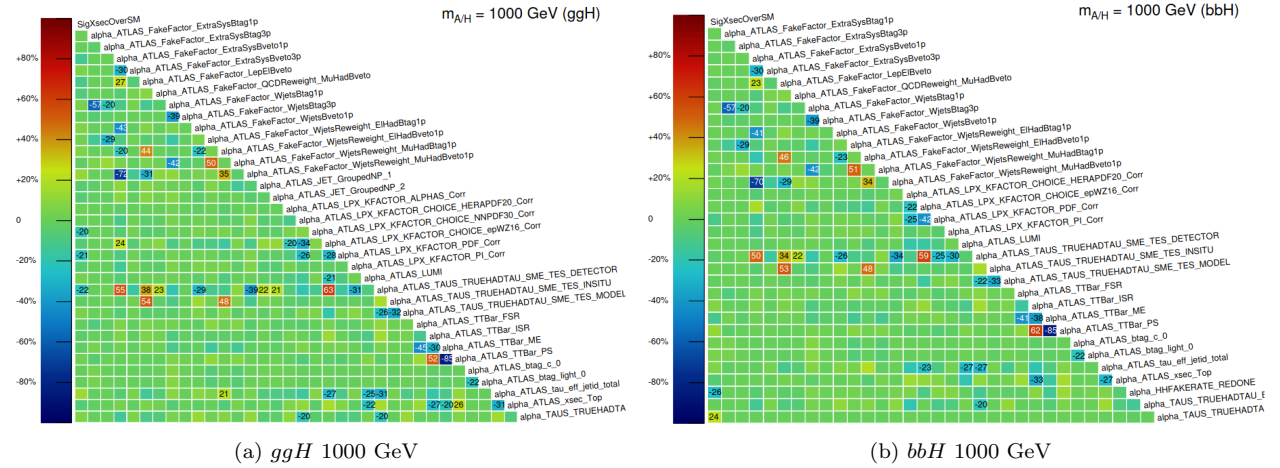


(a) ggH 1000 GeV



(b) bbH 1000 GeV

Figure B.4: The ranking plots for the 1000 GeV ggH and bbH signals with the pulls and constraints overlaid.



(a) ggH 1000 GeV

(b) bbH 1000 GeV

Figure B.5: The correlation plots for the 1000 GeV ggH and bbH signals.

Appendix C

Extra Information on Monte Carlo Samples and Triggers

C.1 Triggers Used

The definitions of the triggers used in the legacy analysis, Table C.1 shows the single lepton triggers used in the $\tau_{\text{lep}}\tau_{\text{had}}$ channel and Table C.2 shows the single tau triggers used in the $\tau_{\text{had}}\tau_{\text{had}}$. The same triggers are used in all analyses.

Table C.1: The $\tau_{\text{lep}}\tau_{\text{had}}$ single lepton triggers and the periods they were used for. An explanation of under which circumstances the trigger is fire for is given.

$\tau_{\text{lep}}\tau_{\text{had}}$		
Trigger	Period	Description
Single Electron Triggers		
e24_lhmedium_L1EM20VH	2015	$E_T > 24$ GeV, Medium LH, seeded by L1_EM20VH trigger
e60_lhmedium	2015	$E_T > 60$ GeV, Medium LH
e120_lhloose	2015	$E_T > 120$ GeV, Loose LH
e26_lhtight_nod0_ivarloose	2016-18	$E_T > 26$ GeV, Tight LH, No transverse impact parameter cuts, Variable sized cone isolation requirement
e60_lhmedium_nod0	2016-18	$E_T > 60$ GeV, Medium LH, No transverse impact parameter cuts
e140_lhloose_nod0	2016-18	$E_T > 140$ GeV, Loose LH, No transverse impact parameter cuts
Single Muon Triggers		
mu20_iloose_L1MU15	2015	$E_T > 20$ GeV, Loose isolation requirement using ID tracks, Seeded by L1MU15 trigger
mu50	All	$E_T > 50$ GeV, Seeded by L1MU20 trigger
mu26_ivarmedium	2016-18	$E_T > 26$ GeV, Medium isolation requirement using ID tracks in variable sized cone, Seeded by L1MU20 trigger

Table C.2: The $\tau_{\text{had}}\tau_{\text{had}}$ hadronic tau triggers and the periods they were used for.

$\tau_{\text{had}}\tau_{\text{had}}$		
Trigger	Period	Description
Single Tau Triggers		
HLT_tau80_medium1_tracktwo_L1TAU60	2015	$E_T > 80$ GeV, Medium BDT ID, seeded by L1_TAU60 trigger, tracktwo refers to the tracking algorithm used at trigger level
HLT_tau125_medium1_tracktwo	2015	$E_T > 125$ GeV, Medium BDT ID
HLT_tau160_medium1_tracktwo	2015-17	$E_T > 160$ GeV, Medium BDT ID
HLT_tau160_medium1_tracktwo_L1TAU100	2017	$E_T > 160$ GeV, Medium BDT ID, seeded by L1_TAU100 trigger,
HLT_tau160_medium1_tracktwoEF_L1TAU100	2018	$E_T > 160$ GeV, Medium BDT ID, seeded by L1_TAU100 trigger, tracktwoEF refers to the tracking algorithm used at trigger level

C.2 Monte Carlo Samples

The tables below show extra information on the MC samples used for the analyses mentioned in this thesis. The background samples are used for all analyses mentioned in this thesis. Tables are shown for the ggH and bbH signals used for the legacy and MSSM improved analysis mentioned in Chapters 4 and 7, the LQ signals used in the LQ analysis in Chapter 6 and the Z' signals used in Chapter 5.

For each sample, the cross section (σ), filter efficiency ($\epsilon_{\text{Filter Eff}}$) and k -factor is stated, where the cross section used in the analysis is equal to $\sigma \times \epsilon_{\text{Filter Eff}} \times k$ -factor. The number of events is also stated which refers to the number used by the event generator and available in the EVNT file. All information is gathered from the ATLAS Metadata Interface (AMI).

Table C.3: Extra information on Diboson samples used for all analyses in this thesis.

Diboson				
Process	σ [pb]	$\epsilon_{\text{Filter Eff}}$	k -factor	N_{events}
4ℓ	1.2523	1	1	79689700
$3\ell + \nu$	4.579	1	1	74649400
$2\ell + 2\nu$	12.501	1	1	69900000
$\ell + 3\nu$	3.2344	1	1	27960000
$W \rightarrow \ell\nu, Z \rightarrow qq$	11.42	1	1	40760000
$W^+ \rightarrow \ell\nu, W^- \rightarrow qq$	24.724	1	1	26324000
$W^+ \rightarrow qq, W^- \rightarrow \ell\nu$	24.708	1	1	40726000
$W \rightarrow qq, Z \rightarrow \ell\ell$	3.4328	1	1	30554000
$W \rightarrow qq, Z \rightarrow \nu\nu$	6.7975	1	1	15960000
$Z \rightarrow qq, Z \rightarrow \ell\ell$	15.564	0.14158	1	8970000
$Z \rightarrow qq, Z \rightarrow \nu\nu$	15.561	0.28003	1	14369000

Table C.4: Extra information on $t\bar{t}$ and single t -quark samples used for all analyses in this thesis. Information is shown also for the samples used to derive the top systematics in all analyses.

Single Top				
Process	σ [pb]	$\epsilon_{\text{Filter Eff}}$	k -factor	N_{events}
s-channel $t \rightarrow \ell$	2.027	1	1.017	7830000
s-channel $\bar{t} \rightarrow \ell$	1.2674	1	1.0167	7830000
Wt inclusive	37.935	1	0.945	39100000
$W\bar{t}$ inclusive	37.905	1	0.9457	39100000
t-channel $t \rightarrow \ell$	36.996	1	1.1935	106219500
t-channel $\bar{t} \rightarrow \ell$	22.173	1	1.1849	97932500
$t\bar{t}$				
hadronic with leptonic decay (non-all hadronic)	729.76	0.54385	1.13975636159	709060000
hadronic	729.77	0.45623	1.13974074379	271360000
di-lepton	729.77	0.10547	1.13975636159	554162000
Systematics				
non-all hadronic: varied $h_{\text{damp}}, \mu_r, \mu_f$	729.74	0.43852	1	376240000
hadronic: varied $h_{\text{damp}}, \mu_r, \mu_f$	729.74	0.45622	1	256805000
di-lepton: varied $h_{\text{damp}}, \mu_r, \mu_f$	729.74	0.10546	1	312904000
non-all hadronic: compare Powheg+Pythia8 with aMC@NLO+Pythia8	711.43	0.44037	1.1691	376985000
di-lepton: compare Powheg+Pythia8 with aMC@NLO+Pythia8	712.02	0.10717	1.1681	364951000
hadronic: compare Powheg+Pythia8 with aMC@NLO+Pythia8	711.38	0.45261	1.1692	249175000
non-all hadronic: compare Powheg+Pythia8 with PowHeg+Herwig7	730.14	0.43853	1	378265000
di-lepton: compare Powheg+Pythia8 with PowHeg+Herwig7	730.15	0.10547	1	312507000
hadronic: compare Powheg+Pythia8 with PowHeg+Herwig7	730.15	0.45624	1.1392	257780000

Table C.5: Extra information on W +jets samples used for all analyses in this thesis. These samples are split by whether they have b or c -jets present.

p_T Slice [GeV]	Selection	$W \rightarrow e\nu$ +jets				$W \rightarrow \mu\nu$ +jets				$W \rightarrow \tau\nu$ +jets			
		σ [pb]	$\epsilon_{\text{Filter Eff}}$	k -factor	N_{events}	σ [pb]	$\epsilon_{\text{Filter Eff}}$	k -factor	N_{events}	σ [pb]	$\epsilon_{\text{Filter Eff}}$	k -factor	N_{events}
0-70	c -veto, b -veto	19153	0.82467	0.9702	122776000	19151	0.82465	0.9702	97809000	19155	0.82462	0.9702	122553000
0-70	c -filter, b -veto	19146	0.13113	0.9702	327985500	19145	0.13031	0.9702	327705000	19153	0.13167	0.9702	78085800
0-70	b -filter	19143	0.044776	0.9702	318462600	19143	0.04421	0.9702	318291400	19152	0.045128	0.9702	73627400
70-140	c -veto, b -veto	944.98	0.67483	0.9702	57936500	945.89	0.6743	0.9702	73427000	945.58	0.6756	0.9702	73659000
70-140	c -filter, b -veto	946.37	0.24414	0.9702	43973300	946.12	0.24357	0.9702	48956200	946.49	0.24245	0.9702	44100000
70-140	b -filter	945.63	0.083353	0.9702	75259450	944.8	0.084525	0.9702	83103700	945.87	0.083903	0.9702	47499850
140-280	c -veto, b -veto	339.75	0.59858	0.9702	49248500	339.73	0.60009	0.9702	49269000	339.69	0.59884	0.9702	78309500
140-280	c -filter, b -veto	339.8	0.28805	0.9702	75704000	339.8	0.29256	0.9702	58830000	339.84	0.29032	0.9702	44029800
140-280	b -filter	339.7	0.11088	0.9702	103599500	339.68	0.1108	0.9702	107789500	339.68	0.10575	0.9702	103578600
280-500	c -veto, b -veto	72.077	0.54829	0.9702	24554800	72.084	0.54766	0.9702	24553600	72.078	0.56172	0.9702	122553000
280-500	c -filter, b -veto	72.105	0.31969	0.9702	14736800	72.103	0.32016	0.9702	14726400	71.99	0.31863	0.9702	17631000
280-500	b -filter	72.077	0.13865	0.9702	23518250	72.063	0.13137	0.9702	23533650	71.944	0.13597	0.9702	11733100
500-1000	None	15.05	1	0.9702	23468800	15.008	1	0.9702	29467000	15.052	1	0.9702	29430000
1000+	E.CMS	1.2344	1	0.9702	23639400	1.2349	1	0.9702	19650000	1.2342	1	0.9702	19639800

Table C.6: Extra information on $Z \rightarrow (\ell\ell/\tau\tau) + \text{jets}$ samples used for all analyses in this thesis. For these samples Drell-Yan mass slices are used along with mass inclusive samples corresponding to different production modes.

Mass Slice [GeV]	σ [pb]	$\epsilon_{\text{Filter Eff}}$	k -factor	N_{events}	σ [pb]	$\epsilon_{\text{Filter Eff}}$	k -factor	N_{events}	σ [pb]	$\epsilon_{\text{Filter Eff}}$	k -factor	N_{events}
Inclusive Z												
$Z \rightarrow ee$					$Z \rightarrow \mu\mu$				$Z \rightarrow \tau\tau$			
-	1901.1	1	1.02600047339	1213348000	1901.1	1	1.02605444217	1133262000	1901.1	1	1.02605444217	104229000
Drell-Yan												
$Z \rightarrow ee + \text{jets}$					$Z \rightarrow \mu\mu + \text{jets}$				$Z \rightarrow \tau\tau + \text{jets}$			
120-180	17.477	1	1	4600000	17.477	1	1	6320000	17.476	1	1	2100000
180-250	2.9215	1	1	2862000	2.9215	1	1	3700000	2.9213	1	1	1700000
250-400	1.0819	1	1	4140000	1.0819	1	1	4640000	1.082	1	1	2150000
400-600	0.19551	1	1	3120000	0.19551	1	1	3460000	0.19551	1	1	2150000
600-800	0.037403	1	1	1601000	0.037403	1	1	1995000	0.037403	1	1	2150000
800-1000	0.010607	1	1	832000	0.010607	1	1	995000	0.010608	1	1	2150000
1000-1250	0.0042586	1	1	212000	0.0042586	1	1	450000	0.0042586	1	1	2150000
1250-1500	0.001422	1	1	102000	0.001422	1	1	270000	0.001422	1	1	2150000
1500-1750	0.00054526	1	1	102000	0.00054526	1	1	270000	0.00054525	1	1	1690000
1750-2000	0.00022993	1	1	195000	0.00022992	1	1	270000	0.00022993	1	1	1150000
2000-2250	0.00010386	1	1	102000	0.00010386	1	1	270000	0.00010386	1	1	2150000
2250-2500	4.9403E-05	1	1	102000	4.9404E-05	1	1	270000	4.9403E-05	1	1	1690000
2500-2750	2.4454E-05	1	1	102000	2.4454E-05	1	1	270000	2.4454E-05	1	1	1690000
2750-3000	1.249E-05	1	1	102000	1.249E-05	1	1	270000	1.2489E-05	1	1	1765000
3000-3500	1.003E-05	1	1	170000	1.003E-05	1	1	270000	1.003E-05	1	1	1690000
3500-4000	2.9344E-06	1	1	102000	2.9344E-06	1	1	270000	2.9343E-06	1	1	1920000
4000-4500	8.9767E-07	1	1	102000	8.9767E-07	1	1	270000	8.9767E-07	1	1	1530000
4500-5000	2.8071E-07	1	1	102000	2.8071E-07	1	1	270000	2.8072E-07	1	1	1690000
5000+	1.2647E-07	1	1	102000	1.2648E-07	1	1	270000	1.2647E-07	1	1	1690000

Table C.7: Extra information on the ggH and bbH samples used for the legacy and MSSM improved analyses mentioned in chapters 4 and 7, respectively. For ggH samples, the signal width is also stated as this varies depending on the mass point.

ggH					
Mass [GeV]	Width [GeV]	σ [pb]	$\epsilon_{\text{Filter Eff}}$	k -factor	N_{events}
200	1	12.211	0.4549	1	350000
250	1	8.3951	0.45526	1	350000
300	2	6.6562	0.45554	1	350000
350	3	6.7896	0.45487	1	350000
400	5	6.2935	0.45461	1	350000
500	5	3.074	0.45539	1	350000
600	10	1.3801	0.45508	1	200000
700	20	0.64949	0.4555	1	200000
800	20	0.32277	0.45591	1	200000
1000	30	0.093746	0.4561	1	110000
1200	40	0.028722	0.45556	1	200000
1500	60	0.0061081	0.45554	1	210000
2000	80	0.00077942	0.45508	1	210000
2500	100	0.0001322	0.45559	1	210000
bbH					
125	-	0.42718	0.4546	1	1570000
150	-	0.23227	0.45448	1	1570000
200	-	0.084498	0.45558	1	1570000
300	-	0.017668	0.45424	1	1190000
400	-	0.005283	0.45665	1	1190000
600	-	0.00082623	0.45632	1	990000
1000	-	5.8262E-05	0.4553	1	3320000
1500	-	5.1141E-06	0.45591	1	600000
2000	-	7.2072E-07	0.45467	1	600000
2500	-	1.3099E-07	0.45658	1	600000

Table C.8: Extra information on singly produced scalar LQ samples used for the LQ analysis in Chapter 6. For each mass point there are five coupling (λ) points.

Mass [GeV]	Coupling (λ)	σ [pb]	$\epsilon_{\text{Filter Eff}}$	k -factor	N_{events}
400	0.5	0.047576	1	1	400000
	1.0	0.21539	1	1	400000
	1.5	0.5819	1	1	400000
	1.7	0.80683	1	1	400000
	2.0	1.2618	1	1	400000
	2.5	2.3409	1	1	400000
700	0.5	0.0028811	1	1	400000
	1.0	0.015676	1	1	400000
	1.5	0.05091	1	1	400000
	1.7	0.075764	1	1	400000
	2.0	0.12935	1	1	400000
	2.5	0.27171	1	1	400000
900	0.5	0.00073466,	1	1	400000
	1.0	0.0046685	1	1	400000
	1.5	0.016998	1	1	400000
	1.7	0.02614	1	1	400000
	2.0	0.046393	1	1	400000
	2.5	0.10269	1	1	400000
1100	0.5	0.00023888,	1	1	550000
	1.0	0.0017941	1	1	550000
	1.5	0.0071872	1	1	550000
	1.7	0.011322	1	1	550000
	2.0	0.020653	1	1	550000
	2.5	0.047226	1	1	550000
1300	0.5	9.339e-05,	1	1	550000
	1.0	0.00082709	1	1	550000
	1.5	0.0035648	1	1	550000
	1.7	0.0057106	1	1	550000
	2.0	0.010604	1	1	550000
	2.5	0.024755	1	1	550000
1600	1.0	0.000328	1	1	550000
	1.5	0.0015209	1	1	550000
	1.7	0.0024736	1	1	550000
	2.0	0.0046666	1	1	550000
	2.5	0.011097	1	1	550000
1900	1.0	0.00015768	1	1	800000
	1.5	0.00076201	1	1	800000
	1.7	0.0012492	1	1	800000
	2.0	0.0023771	1	1	800000
	2.5	0.0057067	1	1	800000
2200	1.0	8.6128E-05	1	1	800000
	1.5	0.00042551	1	1	800000
	1.7	0.00070068	1	1	800000
	2.0	0.0013397	1	1	800000
	2.5	0.0032321	1	1	800000
2500	1.0	5.1394E-05	1	1	800000
	1.5	0.00025702	1	1	800000
	1.7	0.00042391	1	1	800000
	2.0	0.00081247	1	1	800000
	2.5	0.0019655	1	1	800000

Table C.9: Extra information on singly produced vector Yang-Mills coupling scenario ($\kappa = 0$) LQ samples used for the LQ analysis in Chapter 6. For each mass point there are five coupling (λ) points.

Mass [GeV]	Coupling (λ)	σ [pb]	$\epsilon_{\text{Filter Eff}}$	k -factor	N_{events}
400	0.5	0.79075	1	1	400000
	1.0	3.4746	1	1	400000
	1.5	8.97	1	1	400000
	1.7	12.266	1	1	400000
	2.0	18.737	1	1	400000
	2.5	34.709	1	1	400000
700	0.5	0.035378	1	1	400000
	1.0	0.18546	1	1	400000
	1.5	0.58035	1	1	400000
	1.7	0.85257	1	1	400000
	2.0	1.4347	1	1	400000
	2.5	3.0369	1	1	400000
900	0.5	0.0080124	1	1	400000
	1.0	0.049285	1	1	400000
	1.5	0.17514	1	1	400000
	1.7	0.26722	1	1	400000
	2.0	0.47044	1	1	400000
	2.5	1.0512	1	1	400000
1100	0.5	0.0023821	1	1	550000
	1.0	0.017551	1	1	550000
	1.5	0.069497	1	1	550000
	1.7	0.10896	1	1	550000
	2.0	0.19792	1	1	550000
	2.5	0.45671	1	1	550000
1300	0.5	0.00087109	1	1	550000
	1.0	0.0076866	1	1	550000
	1.5	0.033059	1	1	550000
	1.7	0.052779	1	1	550000
	2.0	0.097813	1	1	550000
	2.5	0.23074	1	1	550000
1600	0.5	0.00026206	1	1	550000
	1.0	0.0029162	1	1	550000
	1.5	0.013546	1	1	550000
	1.7	0.021999	1	1	550000
	2.0	0.041501	1	1	550000
	2.5	0.099762	1	1	550000
1900	0.5	0.0001045	1	1	800000
	1.0	0.0013606	1	1	800000
	1.5	0.0066241	1	1	800000
	1.7	0.010865	1	1	800000
	2.0	0.020713	1	1	800000
	2.5	0.05024	1	1	800000
2200	0.5	5.0435E-05	1	1	800000
	1.0	0.00073163	1	1	800000
	1.5	0.0036569	1	1	800000
	1.7	0.0060218	1	1	800000
	2.0	0.011513	1	1	800000
	2.5	0.028071	1	1	800000
2500	0.5	2.8041E-05	1	1	800000
	1.0	0.00043448	1	1	800000
	1.5	0.002191	1	1	800000
	1.7	0.0036117	1	1	800000
	2.0	0.0069242	1	1	800000
	2.5	0.016905	1	1	800000

Table C.10: Extra information on singly produced vector Minimal coupling scenario ($\kappa = 1$) LQ samples used for the LQ analysis in Chapter 6. For each mass point there are five coupling (λ) points.

Mass [GeV]	Coupling (λ)	σ [pb]	$\epsilon_{\text{Filter Eff}}$	k -factor	N_{events}
400	0.5	0.31064	1	1	400000
	1.0	1.5686	1	1	400000
	1.5	4.7237	1	1	400000
	1.7	6.8429	1	1	400000
	2.0	11.331	1	1	400000
	2.5	23.393	1	1	400000
700	0.5	0.014828	1	1	400000
	1.0	0.10292	1	1	400000
	1.5	0.39444	1	1	400000
	1.7	0.61386	1	1	400000
	2.0	1.1043	1	1	400000
	2.5	2.5247	1	1	400000
900	0.5	0.0037046	1	1	400000
	1.0	0.031832	1	1	400000
	1.5	0.13529	1	1	400000
	1.7	0.21572	1	1	400000
	2.0	0.39845	1	1	400000
	2.5	0.93732	1	1	400000
1100	0.5	0.00125	1	1	550000
	1.0	0.012919	1	1	550000
	1.5	0.058708	1	1	550000
	1.7	0.094912	1	1	550000
	2.0	0.17805	1	1	550000
	2.5	0.42536	1	1	550000
1300	0.5	0.0005254	1	1	550000
	1.0	0.0062504	1	1	550000
	1.5	0.029621	1	1	550000
	1.7	0.048327	1	1	550000
	2.0	0.091509	1	1	550000
	2.5	0.22045	1	1	550000
1600	0.5	0.00019049	1	1	550000
	1.0	0.0026036	1	1	550000
	1.5	0.012818	1	1	550000
	1.7	0.021067	1	1	550000
	2.0	0.040153	1	1	550000
	2.5	0.097523	1	1	550000
1900	0.5	8.6406E-05	1	1	800000
	1.0	0.0012887	1	1	800000
	1.5	0.0064609	1	1	800000
	1.7	0.010647	1	1	800000
	2.0	0.020359	1	1	800000
	2.5	0.049601	1	1	800000
2200	0.5	4.5674E-05	1	1	800000
	1.0	0.00071483	1	1	800000
	1.5	0.0036104	1	1	800000
	1.7	0.0059506	1	1	800000
	2.0	0.011402	1	1	800000
	2.5	0.027848	1	1	800000
2500	0.5	2.7055E-05	1	1	800000
	1.0	0.00042981	1	1	800000
	1.5	0.0021734	1	1	800000
	1.7	0.0035879	1	1	800000
	2.0	0.0068796	1	1	800000
	2.5	0.016827	1	1	800000

Table C.11: Extra information on pair produced scalar LQ samples used for the LQ analysis in Chapter 6.

Mass [GeV]	σ [pb]	$\epsilon_{\text{Filter Eff}}$	k -factor	N_{events}
400	4.5	1	1	300000
700	0.2773	1	1	300000
900	0.0539	1	1	720000
1100	0.012754	1	1	210000
1300	0.003425	1	1	560000
1600	0.000555	1	1	30000
1900	0.0001015	1	1	30000

Table C.12: Extra information on pair produced vector Yang-Mills coupling scenario ($\kappa = 0$) LQ samples used for the LQ analysis in Chapter 6.

Mass [GeV]	σ [pb]	$\epsilon_{\text{Filter Eff}}$	k -factor	N_{events}
400	69.175	1	1	300000
700	2.1708	1	1	300000
900	0.37147	1	1	700000
1100	0.079631	1	1	210000
1300	0.019816	1	1	550000
1600	0.0029717	1	1	30000
1900	0.0005213	1	1	30000
2200	0.0001035	1	1	30000
2500	2.2857e-05,	1	1	30000

Table C.13: Extra information on pair produced vector Minimal coupling scenario ($\kappa = 1$) LQ samples used for the LQ analysis in Chapter 6.

Mass [GeV]	σ [pb]	$\epsilon_{\text{Filter Eff}}$	k -factor	N_{events}
400	17.861	1	1	300000
700	0.49781	1	1	300000
900	0.081445	1	1	700000
1100	0.016912	1	1	210000
1300	0.0041125	1	1	550000
1600	0.0006007	1	1	30000
1900	0.00010403	1	1	30000
2200	2.0577e-05	1	1	30000
2500	4.5937e-06	1	1	30000

Table C.14: Extra information on Drell-Yan mass sliced $Z \rightarrow \tau\tau + \text{jets}$ generated at leading order. The samples are reweighted to a Z' resonance. A generated inclusive Z' mass point was also generated to validate the procedure.

Mass Slice [GeV]	σ [pb]	$\epsilon_{\text{Filter Eff}}$	k -factor	N_{events}
Inclusive Z'				
3000	118	1	1	220000
Drell-Yan				
120-180	13.818	1	1	130000
180-250	2.3388	1	1	130000
250-400	0.8659	1	1	130000
400-600	0.15597	1	1	130000
600-800	0.029587	1	1	130000
800-1000	0.0083227	1	1	130000
1000-1250	0.0033045	1	1	130000
1250-1500	0.0010952	1	1	130000
1500-1750	0.00041723	1	1	130000
1750-2000	0.00017641	1	1	130000
2000-2250	7.9755E-05	1	1	130000
2250-2500	3.8209E-05	1	1	130000
2500-2750	1.9075E-05	1	1	130000
2750-3000	9.8749E-06	1	1	130000
3000-3500	8.0468E-06	1	1	130000
3500-4000	2.4165E-06	1	1	130000
4000-4500	7.5859E-07	1	1	130000
4500-5000	2.4352E-07	1	1	130000
5000+	1.1655E-07	1	1	130000